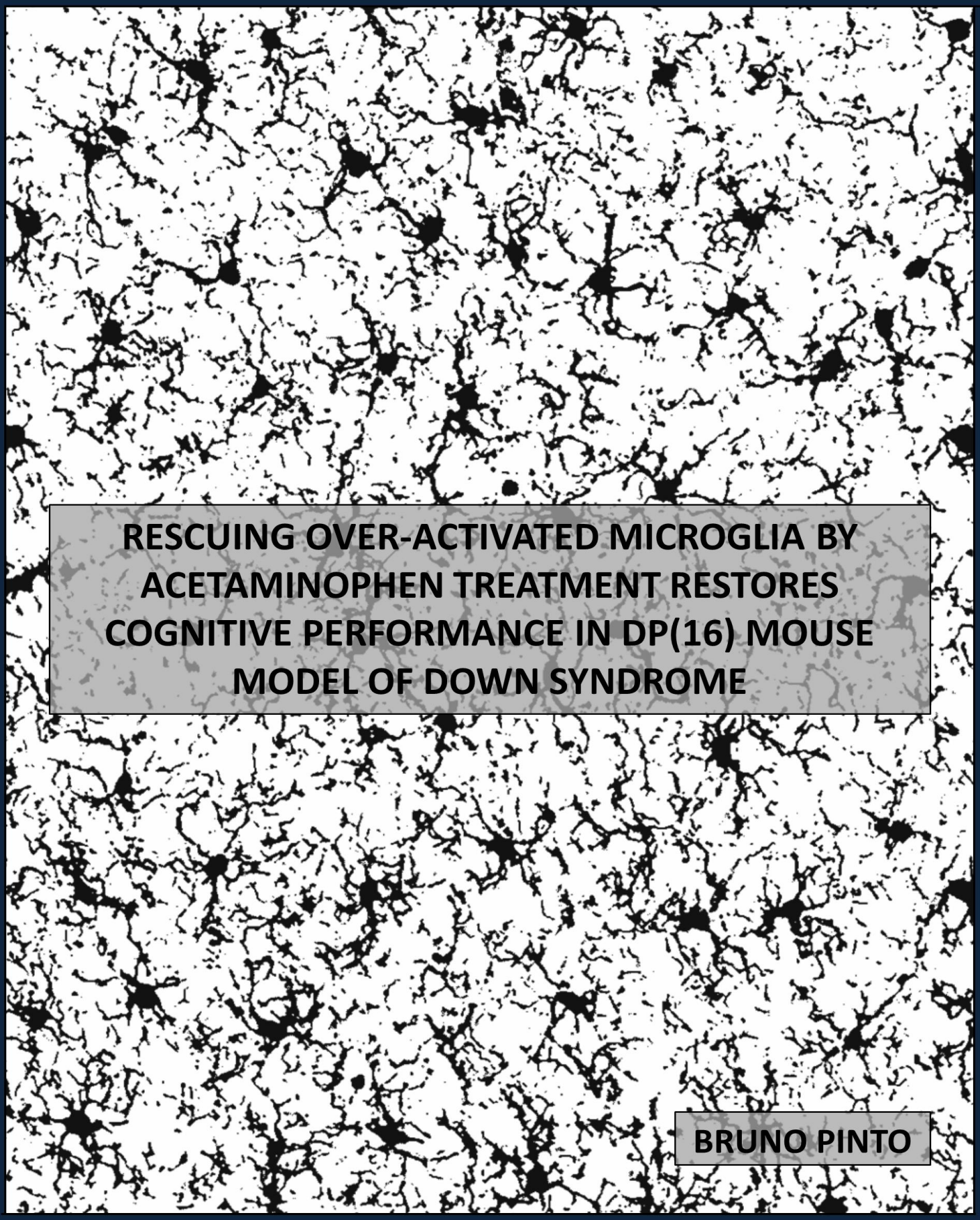

RESCUING OVER-ACTIVATED MICROGLIA BY ACETAMINOPHEN TREATMENT RESTORES COGNITIVE PERFORMANCE IN DP(16) MOUSE MODEL OF DOWN SYNDROME

BRUNO PINTO

SCUOLA NORMALE SUPERIORE

ISTITUTO ITALIANO DI TECNOLOGIA
NEUROSCIENCE AND BRAIN TECHNOLOGIES

SCUOLA NORMALE SUPERIORE DI PISA

CLASSE DI SCIENZE

PERFEZIONAMENTO (PhD) IN NEUROSCIENZE

BRUNO PINTO

Rescuing over-activated microglia by acetaminophen treatment restores cognitive performance in the Dp(16) mouse model of Down Syndrome

_____

TESI DI PERFEZIONAMENTO

_____

Relatore: Dott.ssa Laura Cancedda.

Domina omnium et regina ratio.

(La ragione sia padrona e regina di tutti)

Marco Tullio Cicerone

INDEX

ABSTRACT

Microglia are the resident immune cells of the brain and have been implicated in mechanisms essential for cognitive functions. Down syndrome (DS), the most frequent cause of genetic intellectual disability, is caused by the presence of a supernumerary chromosome 21, which contains genes essential for the function of the immune system. Here, we investigated the presence of microglial alterations and their implication for cognitive impairment in the Dp(16) mouse model of DS. In the hippocampus of Dp(16) mice and individuals with DS, we found microglial morphology indicative of an activated state. Accordingly, we found increased levels of pro-inflammatory cytokines and a phagocytosis marker in Dp(16) mice. In addition, Dp(16) mice showed decreased dendritic spine density and cognitive deficits. Remarkably, depletion of defective microglia by PLX3397 treatment or rescue of the microglia activated state by the commonly used anti-inflammatory drug acetaminophen fully rescued dendritic-spine density and cognitive deficits in Dp(16) mice.

Our data suggest an involvement of microglia in the cognitive impairment of DS animals and identify a new therapeutic approach for the potential rescue of cognitive disabilities in individuals with DS.

INTRODUCTION

Chapter I: Down Syndrome

Down syndrome (DS) is the main genetic cause of intellectual disability worldwide with a frequency of around 1 in 1000 live births (Khoshnood et al., 2011). It is caused by a supernumerary copy) or by a triplication of part of the human chromosome 21 (HSA21), usually due to meiotic non-disjunction during oogenesis (Dierssen, 2012; Hickey et al., 2012). Due to the fact that a long stretch of chromatin (~48 Mb) containing around 235 protein-coding genes is triplicated, this condition is very complex and characterized by a series of different symptoms (Colacurcio et al., 2018; Dierssen, 2012). Virtually all people with DS present some degree of cognitive impairment together with a wide range of other anomalies such as craniofacial deformations, congenital heart anomalies, thyroid diseases and immunological disorders (Dierssen, 2012; Hickey et al., 2012; Li et al., 2007; Sullivan et al., 2017). In addition, most individuals with DS by the age of 40 will develop Alzheimer's disease (AD; (Hickey et al., 2012). Although there is no cure for this condition, life quality of individuals with DS can be greatly improved with proper health care and education. Indeed, in developed countries the life expectancy of these individuals is around 55 years (Roizen and Patterson, 2003).

1.1 Cognitive impairments and pathophysiological changes

Cognitive impairments are the most common and also one of the most debilitating symptoms of DS (Parrini et al., 2017; Roizen and Patterson, 2003). Individuals with DS show deficits in many different cognitive domains with severe impairment in language and vocabulary development (Dierssen, 2012). Moreover, short-term memory as a whole is highly impaired as well as the acquisition and storage of explicit memory. Of note is the fact that DS individuals have an almost intact visuospatial memory (Dierssen, 2012). A wide range of pathophysiological changes in brains

from individuals with DS have been observed with an overall reduction of brain volume that comprises many of the brain areas (Fig. 1) together with extensive evidence showing that brain regions are wired atypically in the DS compared to non-DS individuals (Dierssen, 2012). For example, the corpus callosum is smaller in DS suggest an overall decreased of connectivity between brain hemispheres (Teipel et al., 2003). In addition, the frontal lobe have been extensively shown to have decreased connectivity with other brain areas considered important for learning and memory such as the hippocampus and the basal ganglia (Dierssen, 2012; Pujol et al., 2015). Interestingly, imbalances in excitation/inhibition (especially in the hippocampus), are present in DS and could be an interesting target for recovering cognition (Belichenko et al., 2009; Deidda et al., 2015; Parrini et al., 2017).

Brain region	Newborns	Adults (20–50 years of age)*	Elderly individuals (>50 years of age)*
Whole brain	Almost normal weight	Reduction in weight, brachycephalic	Smaller overall cerebral volumes
Prefrontal cortex	Reduction in volume	Reduction in volume	Reduction in volume
Parietal cortex	Normal or reduction in volume	Reduction in volume	Unknown
Temporal cortex	Narrow superior temporal gyrus	Reduction in volume of right middle or superior temporal gyrus	Decreased grey matter volume in posterior cingulate and entorhinal cortex
Hippocampus	Unknown	Reduction in volume	Unknown
Parahippocampal region	Unknown	Increase in size of the parahippocampal gyrus	Reduction in volume
Amygdala	Reduction in volume	Reduction in volume	Reduction in volume
Cerebellum	Reduction in volume	Reduction in volume	Reduction in volume
Brain stem	Reduction in volume	Increase in grey matter volume	Degeneration of locus coeruleus
Basal prosencephalon	Almost normal size	Normal	Degeneration of basal prosencephalon cholinergic nuclei (nucleus of Meynert)

*Adulthood begins later in people with trisomy 21 than in individuals without intellectual disability, although people with Down syndrome are considered to be elderly once they have reached 50 years of age.

Figure 1. Brain changes in individuals with Down syndrome (Adopted from **Dierssen, 2012**).

At a cellular level, neurons from individuals with DS as well as from DS animal models (i.e., Tc1, Ts1Rh1, Ts65Dn and Ts1Cje mice), show alterations in number and shape of dendritic spines (Belichenko et al., 2009; Haas et al., 2013; Herault et al., 2017; Torres et al., 2018).

Dendritic spines are structures on dendrites that protrude outwards and function as compartments for excitatory synaptic elements in excitatory synapses (Nakahata and Yasuda, 2018). Defective dendritic spine structure and number, together with their function are a very important feature of a wide range of neurodevelopmental disorders, including DS, and probably underlie alterations in neuronal and synaptic plasticity, ultimately having an impact on cognition (Torres et al., 2018). Dendritic spines are very dynamic structures that can assume a wide range of morphological states (Fig. 2) going from filiform (immature spines) to mushroom spines (mature, immobile spines) passing through more mobile shapes such as stubby and thin (mature, immobile spines; (Risher et al., 2014).

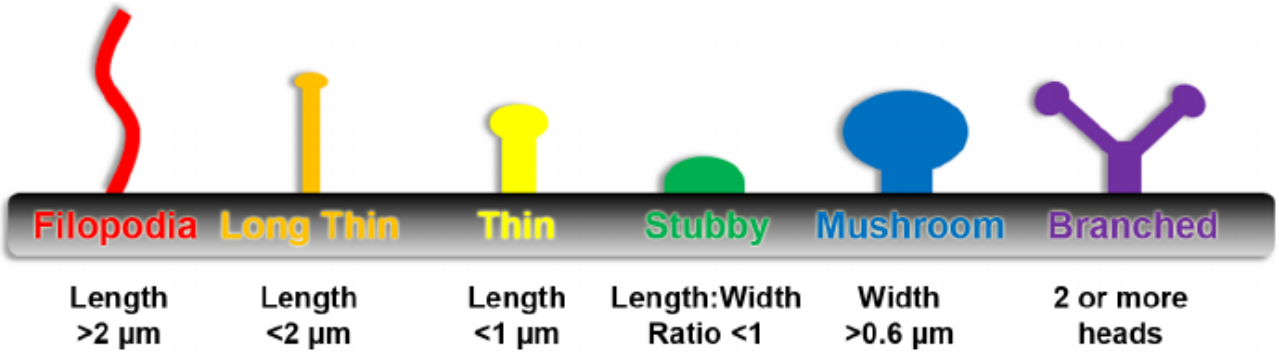

Figure 2. Dendritic spine morphologies. Dendritic spines can assume a wide range of morphological states (Adopted and adapted from **Risher et al. 2014**).

Spine dynamics are necessary for learning and memory (Bosch et al., 2014; Salter and Stevens, 2017) and its dynamicity is due to the actin cytoskeleton and a wide range of protein that can interact with actin itself stabilizing or destabilizing its structure (i.e., drebrin and profilin; (Nakahata and Yasuda, 2018); Fig. 3).

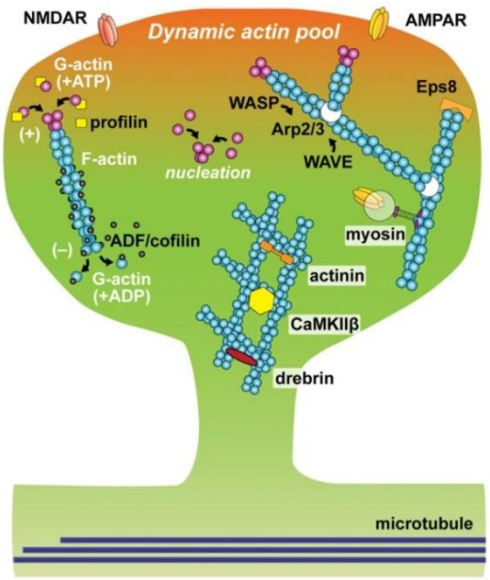

Figure 3. Dendritic spine structure. Dendritic spines are very dynamic structures. Their dynamicity is due to actin and its interactors, such as drebrin (DBN; Adopted from **Nakahata et al. 2018**).

Drebrin (DBN) is one of the most important actin-stabilizing proteins in dendritic spines where it is highly expressed and exerts a pivotal role in maintenance and maturation (Koganezawa et al., 2017). Interestingly, drebrin levels are drastically decreased in individuals with DS (Shim and Lubec, 2002; Weitzdoerfer et al., 2001).

1.2 Immune system dysregulation

In addition to cognitive disability, individuals with DS often suffer from intrinsic immunological dysfunctions such as an increased risk of infections, hematological and autoimmune disorders resulting in higher hospitalization and mortality rates (Guaraldi et al., 2017; Schoch et al., 2017). Accordingly, individuals with DS present dysregulation in a wide range of immune system-related cells and factors. Indeed, defects are present in both the innate (the first component of the immune system to activate upon pathogen presentation) and adaptive immune system (the component of the immune system that is activated after the activation of the innate immune system relies on tackling specific antigens; (Joseph et al., 2018). The adaptive immunity of individuals with DS show alterations typically seen in the elderly (i.e., lack of diversity among naive

circulating T and B cells and a dysregulated development of fully differentiated B and T cells; (Ram and Chinen, 2011; Schoch et al., 2017). In addition, immune response following vaccination is decreased probably due to a smaller number of circulating memory B cells (Schoch et al., 2017; Valentini et al., 2015). Circulating antibodies in individuals with DS are also strongly altered, with significant alteration of IgM, IgG and IgA (Eijsvoogel et al., 2017; Ram and Chinen, 2011). Interestingly, the acuteness of the changes in T and B cells have been correlated with prospectively identified infection-related hospitalizations in children with DS (Martinez et al., 2016). In addition, higher levels of circulating pro-inflammatory cytokines such as Tumor Necrosis Factor α (TNF-α), Interleukin-1 β (IL-1β), IL-6, Monocyte Chemoattractant Protein 1 (MCP-1), IL-22, Interferon γ (IFN-γ) as well as higher activation of the complement cascade are present in persons with DS (Sullivan et al., 2017; Zhang et al., 2017). Moreover, the interferon-response cascade is constantly activated in DS with a consequent decrease in protein synthesis and further release of pro-inflammatory molecules (Sullivan et al., 2017; Sullivan et al., 2016), or, as defined by Sullivan et al. 2016: "*(…) the cells of people with Down syndrome are constantly fighting a viral infection that does not exist*."

Although the brain is tightly sealed by the blood brain barrier (BBB), it partially touched by the immune system. The (only) representative of the immune system in the Central Nervous System (CNS) are the microglia (Kaur et al., 2017). Interestingly, together with higher level of neuroinflammation and increased pro-inflammatory cytokines levels persons with DS show microglial and astroglial activation (Rueda et al., 2018; Streit et al., 2014; Wilcock and Griffin, 2013; Xue and Streit, 2011). Finally, neurons from individuals with DS and the Ts65Dn mouse model overexpress the COX2 enzyme, one of the most prominent markers of inflammation (Mulet et al., 2017). This increase in neuroinflammation in DS may exacerbate the cognitive deficits in which pro-inflammatory molecules may affect neuronal proliferation, decrease neurogenesis, and

impair neuronal maturation and wiring (Rosi et al., 2012; Rueda et al., 2018; Salter and Stevens, 2017). Moreover, increased microglia-mediated synaptic synaptic elimination may underlie some of the defects observed (Salter and Stevens, 2017). Finally, neuroinflammation is one of the main contributors for the progression of AD. Interestingly, the Amyloid-Precursor Protein (APP) and the consequent Aβ aggregate promote neuroinflammation themselves. The higher level of basal neuroinflammation together with the triplication of the *App* gene could therefore explain the high susceptibility of DS persons to developing AD and dementia (Hartley et al., 2015; Rueda et al., 2018).

1.3 Animal models of Down Syndrome

Mice have around 158 genes that are orthologous to genes triplicated in people with DS. These orthologous genes lay on Murine Chromosome 10, 16, and 17, with most of them on Chromosome 16 (MMU16; (Herault et al., 2017). This lead researchers to develop a wide range of mice strains containing total or partial triplication of the MMU16 (Fig. 4). The first viable DS murine model ever developed was the Ts65Dn in 1990 (Davisson et al., 1990). Since then, the scientific community made huge efforts forward on the development of new and cleaner models. However, the Ts65Dn remains the most used and studied DS murine model (Herault et al., 2017).

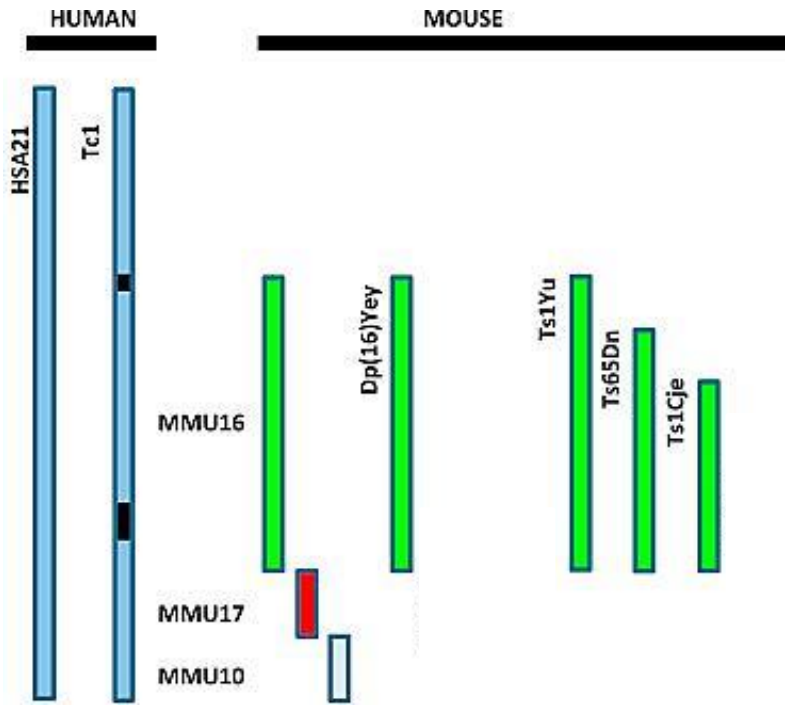

Figure 4. Diagram showing the chromosomic structure of the most commonly used DS mouse models with triplications on genes located in mouse Chromosome 16. The human chromosome 21 (HSA21) and the mouse chromosomes that contain genes orthologue to the HSA21 (Chr. 16, 17 and 10) are depicted. The Tc1 mouse is the only one that contains the whole HSA21 (black bars represent deletions included in the Tc1 chromosome), the other models bear a triplication or a partial triplication of the MMU16 (Adopted and adapted from Hartley et al. 2016).

The only model developed that contains the whole HSA21 is the Tc1 mouse (O'Doherty et al., 2005). In the Tc1 mouse however, during cell proliferation the HSA21 is stochastically lost generating at the end a mosaic animal: this huge drawback hindered a wider use of this model (Herault et al., 2017). With the development of a new genomic engineering technique, the Cre/Lox system, a wide range of partial MMU16-triplication bearing strains were developed (i.e. Dp(16)yey, Ts1Yu; (Herault et al., 2017); Fig. 4). The Dp(16)yey model of DS (hereafter referred to as Dp(16)), bears on one chromosome 16 a duplication orthologous to the region q11-q22.3 of HSA21 (Li et al., 2007). Therefore, Dp(16) mice have three copies of 113 genes orthologous to those overexpressed in DS and involved in the phenotype characteristic of this syndrome. Indeed,

Dp(16) mice recapitulate many of the characteristics of human syndrome such as craniofacial defects, gastrointestinal dysfunctions, and, most importantly, cognitive deficits (Goodliffe et al., 2016; Jiang et al., 2015; Li et al., 2007). Indeed, Dp(16) mice have defective behavior in many cognitive behaviors such as T-Maze test, Fear Conditioning and Morris Water Maze (Goodliffe et al., 2016; Jiang et al., 2015; Yu et al., 2010). Similar deficits have also been observed in the Ts65Dn mouse (Deidda et al., 2015; Parrini et al., 2017; Raveau et al., 2018). Interestingly, hippocampal Long Term Potentiation (LTP) in Dp(16) as well as in Ts65Dn are defective (Dierssen, 2012; Jiang et al., 2015). Moreover, an increased number of interneurons in the hippocampus of Dp(16) mice was observed together with significant decrease in the ability of bursting and producing complex spikes of CA1 pyramidal cells. This in turn may alter the ability of acquiring and consolidating spatial memories (Raveau et al., 2018).

Evidence from the study of postmortem fetal brains of individuals with DS and from animal models, namely Ts65Dn, Ts1Cje, and Ts16, have indicated a wide range of prenatal abnormalities such as reduced proliferation and neurogenesis, delayed neocortical expansion, and microcephaly (Contestabile et al., 2007; Goodliffe et al., 2016; Guidi et al., 2008). However, it has been unexpectedly shown that the Dp(16) mice present none of these neuron-related pre-natal defects (Goodliffe et al., 2016). On the other hand, at the second post-natal week Dp(16) animals presented delayed developmental milestones and deficits in motor and cognitive behavior, suggesting that the post-natal development is sufficient to generate most of the deficits that recapitulate the human condition (Goodliffe et al., 2016).

Nevertheless, to date, there is no extensive analysis of the immune system dysregulation in animal models of DS. However, in Ts65Dn it is possible to put together evidence showing that also in the animal model of DS the immunological deficits are recapitulated (Hartley et al., 2015). An early report reported that the treatment of pregnant Ts65Dn dams with an antibody against IFNγ was

able to rescue fetal growth (Maroun, 1995), which is in line with the more recent notion that in DS the IFNγ is abnormally activated (Sullivan et al., 2017; Sullivan et al., 2016). Interestingly, reports have shown that the Ts65Dn animals have smaller thymus, alterations in T and B cells, hematopoietic stem cells and lymphoid progenitor cell defects (Lorenzo et al., 2011; Lorenzo et al., 2013). Moreover, evidence point toward increased levels of neuroinflammation with increased microglia activation and overexpression of COX2 enzyme (Hunter et al., 2004; Mulet et al., 2017; Rueda et al., 2018). Remarkably, a recent report showed that blocking the action of the pro-inflammatory IL-17 was able to rescue hippocampal hypocellularity and neurogenesis together with an amelioration of cognitive abilities, APP expression and overall neuroinflammation, strongly suggesting that inflammation is indeed present in this mouse model and that it plays a very important role in exacerbating cognitive deficits (Rueda et al., 2018). To date there are no detailed reports on inflammation in Dp(16) mice. It was however shown that IFNα/β and IFNγ receptors are overexpressed in bone-marrow hematopoietic cells (Sullivan et al., 2016).

Chapter II: Microglia

The brain is isolated from the periphery by the BBB. This implies that macrophages cannot have access to the nervous tissue in a healthy state. However, there are resident immunological cells in the CNS, the microglia (Ginhoux et al., 2013), the brain macrophages. Microglia are cells mainly derived from a mesodermic structure called the yolk sack and very early in development (around E9 in mice and 4.5 gestational weeks in humans) they invade the neural tube (Ginhoux et al., 2013; Tay et al., 2017b). A second wave of invasion of macrophages (that later differentiate into microglia) deriving from the fetal liver happens at E13 in mice and the 12-13 gestational week in humans (Ginhoux et al., 2013; Tay et al., 2017b). Upon the closure of the neural tube, the microglial cells differentiate into a stable microglial population (Tay et al., 2017b). Although it is thought that all the microglia derives from c-kit^{+} cells from the yolk sack and fetal liver very early in development, the possibility that a second wave of microglial cells arrives in the CNS from the bone marrow postnatally still remains controversial (Fig. 5; (Tay et al., 2017b). In adults under physiological conditions, microglial cells show a ramified morphology, and they constantly surveil the brain parenchyma (Nimmerjahn et al., 2005; Tremblay et al., 2011). Then, in the case of injury and in the presence of pro-inflammatory molecules, microglial cells shift morphology to a mobile, more amoeboid (larger cell body and fewer ramifications) form (Fig. 6; (Cunningham et al., 2013). Together with their morphological change, microglia upregulate activation and phagocytosis markers (e.g., MHCII, Iba1 and LAMP1, respectively) during inflammation (Arcuri et al., 2017; Hanisch and Kettenmann, 2007; Shobin et al., 2017; Sipe et al., 2016). Moreover, in case of injury or systemic inflammation, the BBB allows the passage of macrophages from the periphery (Ginhoux et al., 2013).

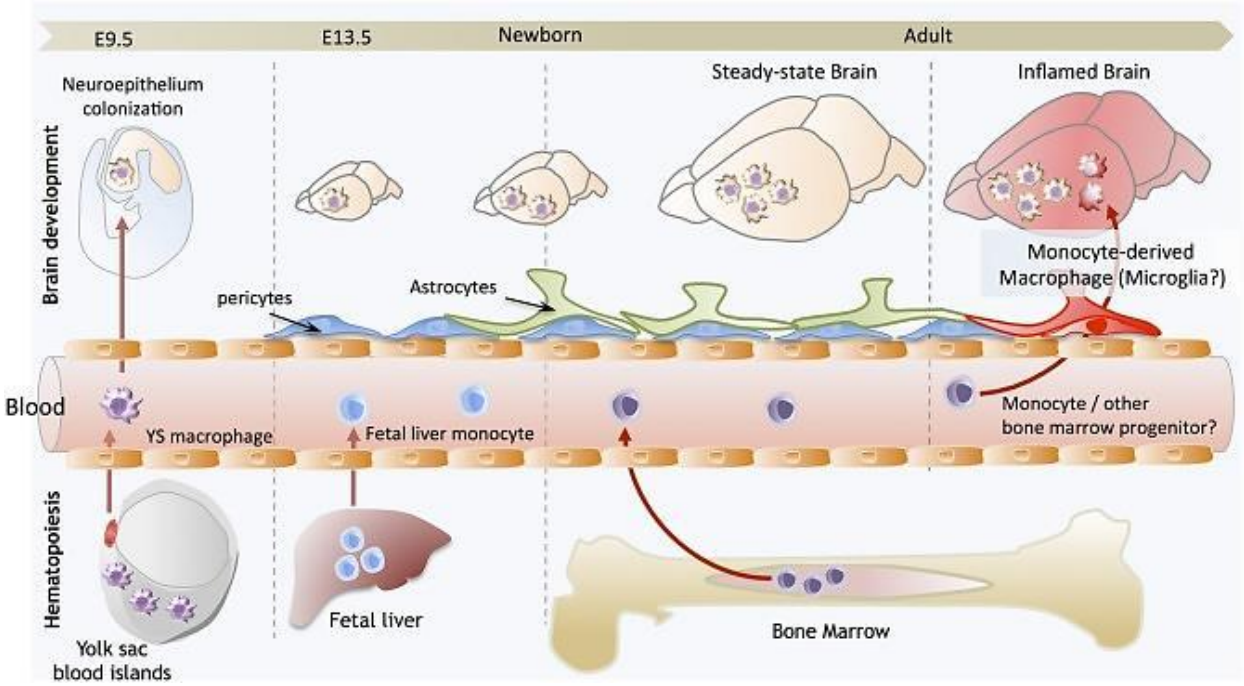

Figure 5. Microglia have a mesodermal origin. Microglia are mainly derived from c-kit^{+} cells from the yolk sack and later from the fetal liver. Before the closure of the neural tube the microglia population is isolated from the periphery reaching a steady-state. In case of inflammation or injury, macrophages derived from the bone marrow can cross the BBB and differentiate into microglia-like cells (Adopted from **Ginhoux et al. 2013**)

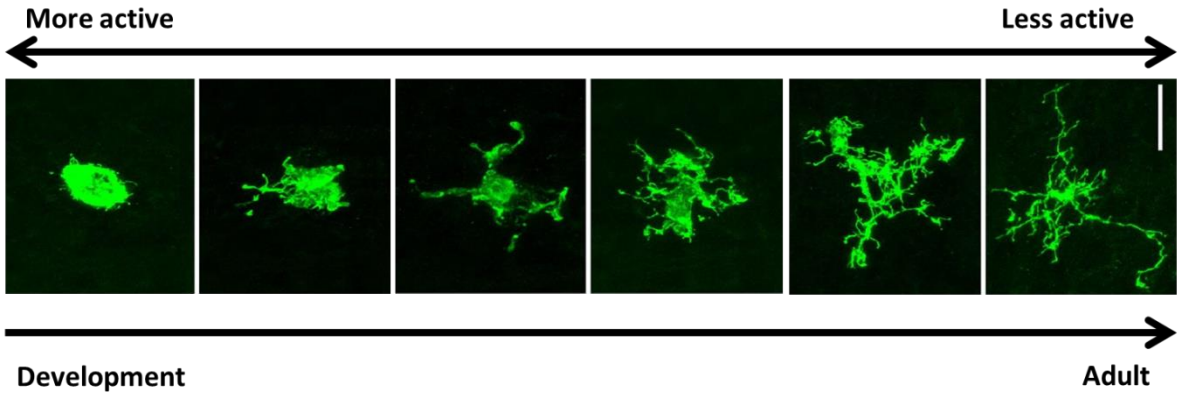

Figure 6. Microglia can drastically change morphology during development or inflammation. Diagram showing confocal images of different morphological states of microglia. From left to right the morphology changes from amoeboid to ramified. The same direction of the morphology change is observed during development or after inflammation (Adopted and adapted from **Cunningham et al. 2013**).

Interestingly, microglia also play an important role in brain development and plasticity (Arcuri et al., 2017; Tremblay et al., 2011). Microglia can regulate neuronal death and can phagocyte neuronal progenitors (Kaur et al., 2017). In addition, they play an essential role in phagocyting apoptotic cells in the developing brain. Indeed, apoptotic cells release factors such as the Macrophage Inflammatory Protein (MIP) that in turn activates and attracts microglia to the apoptosis site (Arno et al., 2014). Moreover, microglia are able to control the number of progenitor cells in the developing cortex and are sensitive to factors released by neural progenitor cells (Mosher et al., 2012; Tay et al., 2017b). Interestingly, microglia regulate neurogenesis also in the adult brain (in the Sub Ventricular Zone (SVZ) and sub granular zone in the hippocampus; (Sierra et al., 2010). In agreement with this notion, removal of microglia from the SVZ hampers the survival and the migration of neuroblasts destined to the olfactory bulb (Xavier et al., 2015). Moreover, microglia are very important for the correct wiring of neuronal circuits during development, giving support to growing axons and phagocyting debris (Tay et al., 2017b). Postnatally, microglia play a pivotal role in shaping circuits through synaptic elimination. Microglial activity is necessary for the correct formation of activity-driven synaptic maturation, critical period plasticity and physiological synaptic elimination during adolescence (Miyamoto et al., 2016; Paolicelli et al., 2011; Sipe et al., 2016; Squarzoni et al., 2015; Stevens et al., 2007; Tay et al., 2017b).

2.1 Microglia and cognition

Peripheral inflammation and inflammation of the nervous system have been extensively linked to decreased cognition in the young and physiologically aging brain, pointing toward a probable immunological regulation of learning and memory (Benson et al., 2017; Bharani et al., 2017; Marsland et al., 2015; Riazi et al., 2015; Salter and Stevens, 2017; Shobin et al., 2017; Todd, 2017). Interestingly, neurons and microglia are in constant communication and the contact between

microglial cells and neurons can result in changes of neuronal activity. In addition, pro-inflammatory cytokines released by microglia such as IL-1β, IL-6 and complement activation reduce LTP and reduce overall synaptic plasticity in the brain (Tchessalova et al., 2018; Wu et al., 2015). Moreover, activation of microglial activity with lipopolysaccharide (LPS) induces a decrease in LTP and an increase in Long-Term Depression (LTD) in hippocampal rat slices, strongly suggesting that microglia can interfere with mechanisms underlying cognition (Pascual et al., 2012; Wu et al., 2015). Remarkably, inhibition of microglial activity with minocycline (an anti-inflammatory tetracycline) is able to prevent inflammation-related cognitive impairments in rats (Wadhwa et al., 2017). Interestingly, deficiency in one of the main signaling pathways in microglial cells, the CX_3CR_1, deletion of microglia-produced Brain Derived Neurotrophic Factor (BDNF) or microglial depletion lead to cognitive impairment in mice when assessing fear conditioning and motor behavior (Parkhurst et al., 2013; Rogers et al., 2011; Tay et al., 2017b). In addition, $CX_3CR_1^{KO}$ animals present deficits in spatial memory (Rogers et al., 2011).

Chapter III: Microglia in Neurodevelopment Disorders

Neurodevelopmental disorders are a group of diseases which onset is early in life and often are characterized by deficits in sociability, cognitive problems, and obsessive/compulsive behavior and sometimes motor abnormalities (Arcuri et al., 2017). The pathophysiology of these disorders are very heterogeneous and therefore hard to study. However, deficits in synaptic maturation together with weak functional connectivity or an excess of weak excitatory synapses seem to play a very important role (Arcuri et al., 2017). Because microglia play an essential role in the synaptic pruning and shaping of circuits during development it has been proposed that the alteration of these cells may participate in the pathogenesis of these disorders (Salter and Stevens, 2017). Indeed, in the last 10 years there have been a significant increase in the number of findings showing that neurodevelopmental disorders such as autism, Down Syndrome, Rett Syndrome, Schizophrenia and Tourette Syndrome are accompanied by microglial disease. On the other hand, whether the microglial deficits are causing the disorder or if it is the diseased brain environment that is causing microglial dysfunction is still a matter of discussion (Salter and Stevens, 2017; Streit et al., 2014; Tay et al., 2017a). Interestingly, a number of post-mortem studies have shown alterations in microglia count and morphology together with a shift in the transcriptomics towards a more inflammatory state in the brains from individuals with autism (Gupta et al., 2014; Morgan et al., 2010; Suzuki et al., 2013; Tetreault et al., 2012; Vargas et al., 2005). Moreover, animal studies have shown that $CX_3CR_1^{KO}$ animals (which have decreased number of microglia), show insufficient pruning during development and display repetitive behavior and deficits in sociability, two behaviors that are believed to be related to autism (Salter and Stevens, 2017). Accordingly, treatment with a wide variety of anti-inflammatory molecules such as luteolin, minocycline and suramin attenuate the autistic-like behavior, especially in the social area (Kim et al., 2018). Interestingly, it has been proposed that microglia play an important role in shaping the autistic

brain. Indeed, the elevation of the levels of pro-inflammatory cytokines (i.e. IL-6, IL-1β, TNF-α) obtained by the treatment of pregnant dams with LPS or polinosinic:poly-cystidylic acid (poly I:C), strongly alter the brain wiring and induces the appearance of autistic-like behavior in the offspring (Kim et al., 2018). Likewise, schizophrenia and Tourette Syndrome have been also linked to increased microglial activation (Arcuri et al., 2017; Chung et al., 2015). Remarkably, individuals that suffer of schizophrenia show increased microglial activation in the whole gray matter of the brain (van Berckel et al., 2008), as shown by Positron Emission Tomography (PET) imaging. Indeed, the drug minocycline (which inhibits microglia activation) is currently under investigation as alternative antipsychotic (Inta et al., 2017). Interestingly, microglia play a role also in Rett syndrome (RTT). RTT is caused by the inactivation of the X-linked MeCp2 protein that is pivotal for the epigenetic regulation of the activation many genes (Xu and Pozzo-Miller, 2017). For long it was thought that MeCp2 was expressed only in the neurons but recent evidence show that microglia also express high levels of this protein (Maezawa and Jin, 2010). Accordingly, RTT microglia release toxic factors for neurons and potentially play a pivotal role in the synaptic and dendritic dysfunctions characteristics of this condition (Maezawa and Jin, 2010). Moreover, $MeCp2^{-/-}$ microglia show deficiency in phagocytosis and inability of debris clearance in the brain which could in turn contribute to neuronal toxicity (Arcuri et al., 2017). Interestingly, microgliosis is absent in RTT brains and the levels of pro-inflammatory cytokines seem to be normal, suggesting that in the case of RTT syndrome microglia acts through an intrinsic mechanism that is not related to chronic inflammation (Arcuri et al., 2017).

On what concerns DS the evidence is very fragmented. Early reports have shown that brains from individuals with DS show elevated expression of IL-1 in the microglia and astrocytes. The brains used for these analysis were however from DS persons that presented signs of AD (Griffin et al., 1989). In addition, a more recent study conducted on brains from aged DS individuals showed that

a large proportion of the microglia is in a senescent state, similar to AD patients (Xue and Streit, 2011). On the other hand, in another report, fetuses with DS showed increased microglial number, suggesting a role of these cells during development in DS (Wierzba-Bobrowicz et al., 1999). Accordingly, DS fetuses have increased number of infiltrating macrophages ($CD68^+$ cells) in the gray matter, CA1 and the subiculum regions of the hippocampus (Kanaumi et al., 2013). Interestingly, early *in vitro* studies have shown that microglial cultures from Ts16 mice show higher production of superoxide when exposed to Ts16 astrocyte-conditioned media, suggesting that trisomic microglia are hyperactive when insulted (Colton et al., 1990). In addition, the same group showed that trisomic microglia produce increased levels of IL1-β (Colton et al., 1991). More recently, work done on Ts65Dn animals have shown increased number and higher activation levels of microglia, deficit that could be rescued with treatment with minocycline together with the rescue of working memory in these animals (Hunter et al., 2004). Two remarkable studies conducted recently strongly support the idea that also in DS there is microglial pathology. It has been shown that microglia from DS patients and Ts65Dn mice show elevated levels of the COX2 enzyme. This enzyme is upregulated during inflammation and often is used as a marker of microglial activation (Mulet et al., 2017). In addition, treatment of 11 months-old Ts65Dn animals with anti-IL-17, a potent pro-inflammatory cytokine, was able to rescue the hyper activation of microglia together with cognitive abilities. These findings strongly support the idea that hyper active microglia might play a role in DS (Rueda et al., 2018). The active microglia in DS could potentially produce aberrant synaptic elimination of dendritic spines. Indeed, dendritic spine deficits have been extensively described in persons with DS and in DS murine models, and they have been suggested to play a role in DS cognitive disability (Belichenko et al., 2004; Dierssen, 2012; Dierssen et al., 2003; Haas et al., 2013; Takashima et al., 1994). An increased immunological activity with a subsequent increase in microglial activation and spine elimination could therefore

play a role in the cognitive deficits in DS (Kleschevnikov et al., 2004; Parrini et al., 2017). Taken together, a very clear picture starts to appear: the activation of the immune systems seems to be a common factor in neurodevelopmental disorders. However, the phenotype produced might be different than the simple acute inflammation. Indeed, the long-term increase of pro-inflammatory cytokines in the brain results in a notably different network of pro-inflammatory molecules and as a result in a different brain state when compared to an acute inflammatory situation (Tchessalova et al., 2018).

Chapter IV: Acetaminophen

Acetaminophen (APAP, Fig. 7) is an unconventional non-steroidal anti-inflammatory drug (NSAID) that likewise other traditional NSAIDs decreases the synthesis of prostaglandins (PGE) and has antipyretic and analgesic effects. Although APAP is considered to not have anti-inflammatory effect (Jozwiak-Bebenista and Nowak, 2014), it was shown that APAP is very active in the central nervous system on blocking the COX enzymes (Flower and Vane, 1972; Jozwiak-Bebenista and Nowak, 2014). Moreover, APAP has been shown to strongly act on microglial cells significantly diminishing the PGE production by microglial cells at low concentrations (Ajmone-Cat et al., 2010; Greco et al., 2003). Indeed, APAP could completely block the production of prostaglandin E_2 (PGE_2) even in microglia stimulated with LPS without having an effect on the COX2 protein synthesis (Fiebich et al., 2000; Greco et al., 2003; Saliba et al., 2018).

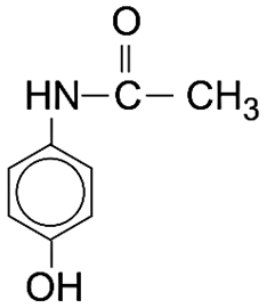

Figure 7. APAP Structure. Chemical structure of acetaminophen. The IUPAC chemical name is N-actetyl-para-aminophenol. (Adopted and adapted from **Jozwiak-Bebenista and Nowak, 2014**)

The mechanism of action of this drug is still matter of discussion although it is believed to have a blocking action on mainly the COX2 isoform likewise traditional NSAIDs with a great dependence on the reduction/oxidation state (redox) of the surrounding environment (Jozwiak-Bebenista and Nowak, 2014). Moreover, although acetaminophen is well known for being a potential hepatotoxic drug, it is extremely safe even at relatively high doses (up to 4 grams daily for adults) and it lacks the gastric side effects typical of the classical NSAIDs (Ajmone-Cat et al., 2010). However, on what concerns the effects on the brain, recent studies on animals and humans has begun to raise some

concerns about the safety of APAP during gestation and early postnatal stages because it can influence physiological brain development (Blecharz-Klin et al., 2015; Blecharz-Klin et al., 2018; Good, 2018; Philippot et al., 2017; Schultz and Gould, 2016; Viberg et al., 2014). Indeed, the administration of APAP to rats caused a significant decrease in spatial memory, social behavior and exploratory behavior (Blecharz-Klin et al., 2018; Ishida et al., 2007). Remarkably, recently it was discovered that a single administration of APAP (100mg/kg) caused object-recognition deficits and hyper-phosphorylation of extracellular signal-regulated kinase (ERK) in the dorsal mouse hippocampus (Milewski and Orr, 2018). On the other hand, APAP has positive effects on complex behaviors when administered postnatally to non-Wild-Type (WT) animals. For instance, the administration of 100mg/kg of APAP to BTBR mouse (a strain that is characterized by autistic-like behaviors such as decreased sociability) rescued the social deficits in these animals (Gould et al., 2012). Strikingly, a recent report showed that APAP treatment prevented the LPS-induced cognitive deficits in mice by means of Morris Water Maze and had a strong effect on decreasing the LPS-induced increase in pro-inflammatory molecules such as IL-1β, IL-6 and TNF-α. Notably, APAP acted mainly on microglia eliciting also a decrease in the LPS-induced microglial proliferation (Zhao et al., 2017). Remarkably, APAP can indeed change complex human behaviors such as social anxiety (Fung and Alden, 2017), empathy (Mischkowski et al., 2016) and social well-being (Chibnall et al., 2005). Interestingly, the only report that has studied the effects of APAP in cognition show that healthy volunteers treated once with 2g of APAP showed sharpened reflections and spatial memory (Pickering et al., 2016). This notable report supports the idea that APAP may have unexpected actions on complex behavior in humans and even on cognition. Altogether, these findings shed light on the role of inflammation and microglia in cognition and support the idea that APAP strongly acts on microglial cells in the brain.

RESULTS

Dp(16) microglia have larger cell bodies and fewer ramifications than WT microglia

To start our investigation on the role of microglia in DS, we first counted the number and analyzed the morphology of microglial cells in hippocampal brain slices (*stratum pyramidalis* of the CA1, CA3 and DG regions) from young adult animals (postnatal day (P)22) of the Dp(16) mouse model of DS and WT littermates (Fig. 8a). Whereas we found no difference in the number of microglia between the two strains (Fig. 8b-c), the whole microglial population of Dp(16) mice presented enlarged cell bodies (Fig. 8d-e). In addition, Dp(16) microglia exhibited a drastic impairment of branching, with a strong reduction in the median length of branching distribution starting from the cell body, as quantified by Sholl analysis (Sipe et al., 2016); Fig. 8f-h). A subsequent skeleton analysis performed on the same cells further revealed an significant decrease in branch numbers, with no changes in average branch length (Fig. 8i-k). When we compared the trisomic and WT microglia in the somatosensory cortex, we found a cell-body enlargement in trisomic microglia similar to that observed in the hippocampus (Fig. 9a-d), but no differences in branch number and distribution between the two strains (Fig. 9e-i). However, we observed a significant increase in the average length of the branches developed by trisomic microglia (Fig. 9j), suggesting that the area surveilled by each cell is larger in Dp(16) than in WT somatosensory cortices.

Altogether, these data show that microglia present a more amoeboid morphology in Dp(16) mice, suggesting a higher level of baseline activation than in WT littermates.

Dp(16) mice show increased levels of inflammation in the hippocampus

Activated microglia express high levels of MHCII and Iba1 (Arcuri et al., 2017; Hanisch and Kettenmann, 2007; Sipe et al., 2016) and secrete large amounts of pro-inflammatory cytokines (Ajmone-Cat et al., 2010; Kierdorf and Prinz, 2013). Thus, to quantify the level of activation of

microglia in the hippocampus of DS mice, we first analyzed the expression of MHCII (*via* immunohistochemistry) and of Iba1 (*via* western blot) in Dp(16) and WT littermates at P22. In the trisomic mice, we found no alterations in the MHCII levels (Figure 10), whereas we found increased Iba1 levels in comparison to WT mice (Fig. 11a). We then measured 40 cytokines using an antibody array. We found a significant increase in the levels of 15 cytokines (Fig. 11b-c, Fig. 12), suggesting that the basal level of microglial activation was increased in the hippocampus of Dp(16) mice. Since the phagocytic action of microglia is increased upon activation (Shobin et al., 2017) and this regulates neural activity and plasticity (Sipe et al., 2016; Wu et al., 2015), we next analyzed the overall level of phagocytosis *via* immunoblotting of the lysosomal marker LAMP1 in the hippocampus of Dp(16) and WT littermates. We found increased levels of LAMP1 in the Dp(16) hippocampi (Fig. 11d). To specifically analyze the levels of LAMP1 in microglial cells, we turned to immunohistochemistry. We found increased LAMP1 immunolabeling in trisomic microglia (Fig. 11e-f), suggesting increased phagocytosis.

Altogether, these results indicate a state of activation of trisomic microglia.

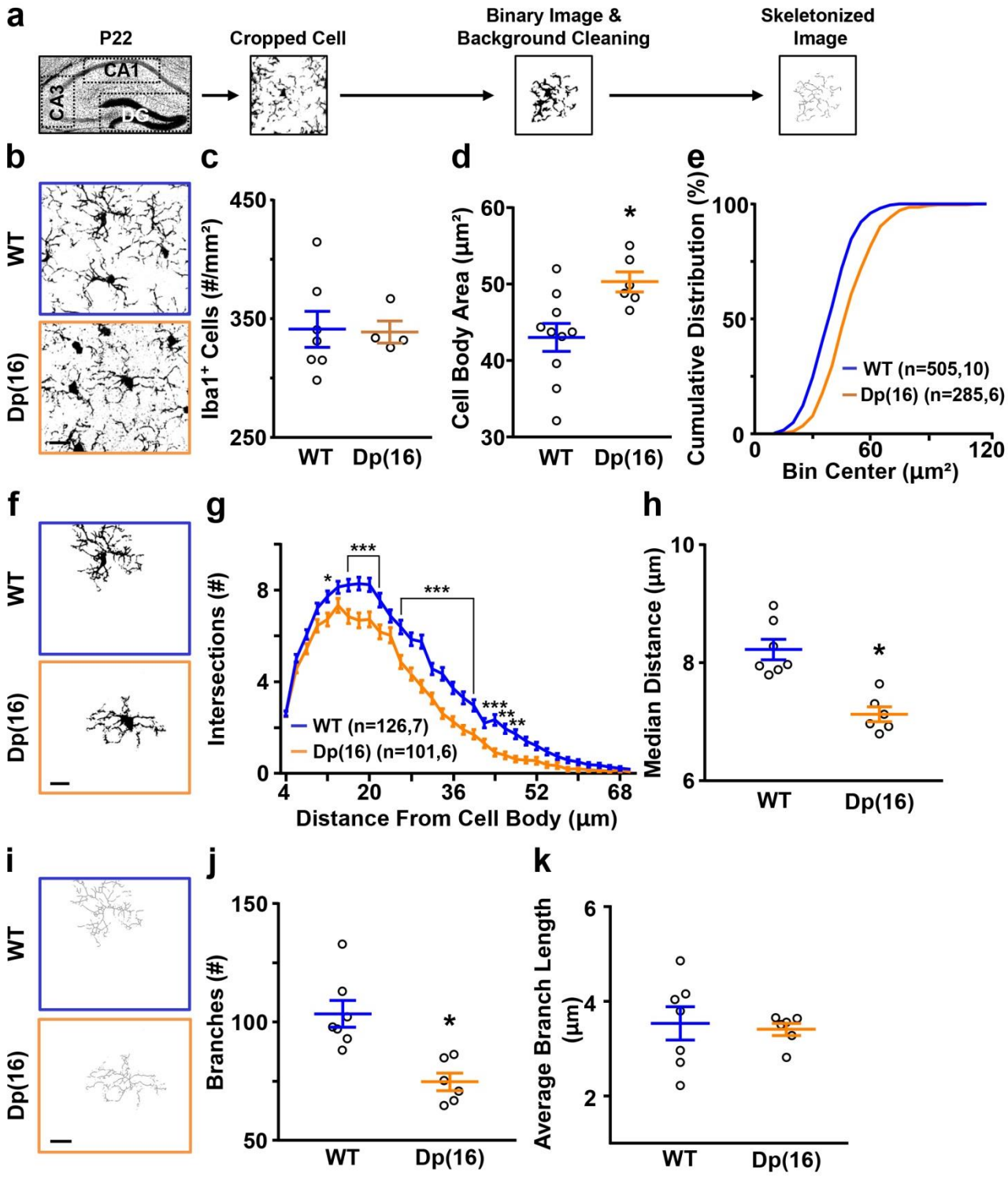

Figure 8. Microglial morphology is altered in Dp(16) hippocampi. (a) Experimental protocol used for analyzing the morphology of microglia in the CA1, CA3 and DG areas of the hippocampus (highlighted by the dotted lines). **(b)** Representative confocal images of Iba1-stained hippocampal slices from P22 WT (blue) and Dp(16) (orange) animals. Scale bar: 10µm. **(c)** Quantification of $Iba1^+$ cell density in the hippocampus in experiments as in b. Bars represent the average cell density of all analyzed animals ± SEM and circles represent the single data points for each animal (1 slice per

animal). **(d)** Quantification of the cell body area of microglial cells in experiments as in b. Bars represent the average of microglial cell body areas in all analyzed animals ± SEM and circles represent the single data points of the cell averages for each animal (38-73 cells/animal; 1 slice per animal). * p<0.05; Unpaired Two-tailed Student's *t*-test, t=2.8, df=14. **(e)** Cumulative distribution of the microglial cell body area of all analyzed cells, calculated as the percentages of the cells inside each bin area. The two distributions are significantly different (Kolmogorov-Smirnov Test, p<0.001). Numbers in parenthesis: analyzed cells, and animals. **(f)** Binary images of the fields shown in b. Scale bar: 10µm. **(g)** Sholl analysis of microglial cells in images as in f. Data are expressed as average number of intersections at each distance from the cell bodies of all analyzed cells ± SEM. * p<0.05, ** p<0.01, *** p<0.001; Two-Way ANOVA, F_{Strain} (33, 7650) = 317.5, p < 0.001; Holm-Sidak *post-hoc* test. Numbers in parenthesis: analyzed cells, and animals (1 slice per animal). **(h)** Quantification of the median distance of the intersections from the cell body, as obtained from the Sholl analysis in g. Bars represent the average of the median distances in all analyzed animals ± SEM, and circles represent the single data points of the median distance averages for each animal (12-21 cells/animal; 1 slice per animal). * p<0.05; Unpaired Two-tailed Student's *t*-test, t=4.98, df=11. **(i)** Representative skeleton images of binary images in f. Scale bar: 10µm. **(j)** Quantification of the number of branches per microglial cell in images as in i. Bars represent the average of the number of branches per microglial cell ± SEM in all analyzed animals, and circles represent the single data points of the cell averages for each animal (12-21 cells/animal; 1 slice per animal). * p<0.05; Unpaired Two-tailed Student's *t*-test, t=4.03, df=11. (k) Quantification of the average length of branches per microglial cell in images as in i. Bars represent the average of branch length per microglial cell ± SEM in all analyzed animals, and circles represent the single data points of the cell averages for each animal (12-21 cells/animal; 1 slice per animal).

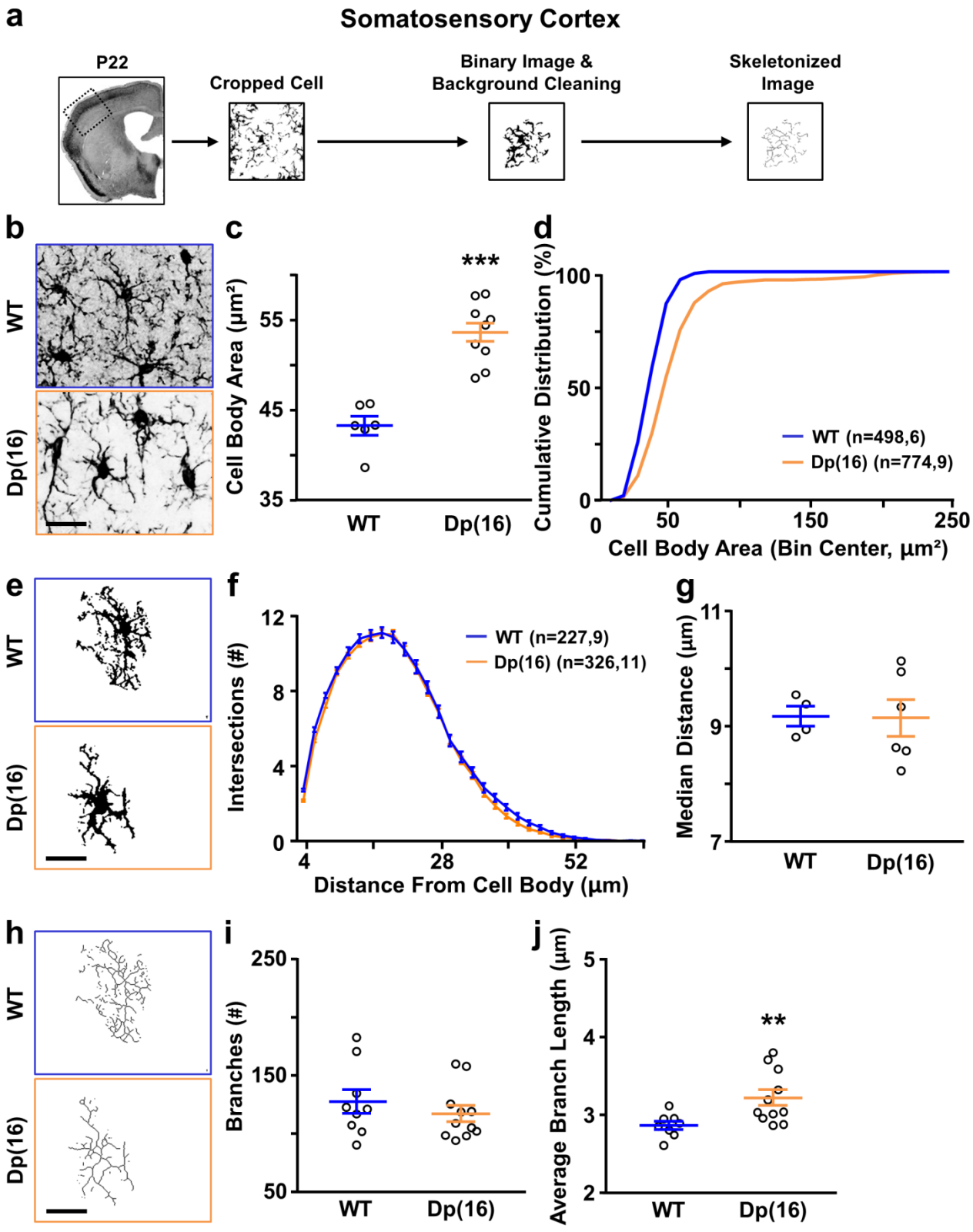

Figure 9. Microglial morphology is altered in the somatosensory cortex of Dp(16) mice.

(a) Experimental protocol used for analyzing the morphology of microglia in the somatosensory cortex (highlighted by the dotted lines). **(b)** Representative confocal images of Iba1-stained somatosensory cortices from P22 WT and Dp(16) animals. Scale bar: 20µm. **(c)** Quantification of

the cell body area of microglial cells in experiments as in b. Bars represent the average of microglial cell body areas in all analyzed animals ± SEM and circles represent single data points of the cell averages for each animal (72-126 cells/ animal; 1 slice per animal). *** p<0.001; Unpaired Two-tailed Student's t-test t=6.3, df=13. **(d)** Cumulative distribution of the microglial cell body area of all analyzed cells, calculated as the percentages of the cells inside each bin area. The two distributions are significantly different (Kolmogorov-Smirnov Test, p<0.001). Numbers in parenthesis: analyzed cells, and animals. **(e)** Binary images of the fields shown in b. Scale bar: 20µm. **(f)** Sholl analysis of microglial cells in images as in e. Data are expressed as average number of intersections at each distance from the cell bodies of all analyzed cells ± SEM. Numbers in parenthesis: analyzed cells, and animals (1 slice per animal). **(g)** Quantification of the median distance of the intersections from the cell body, as obtained from the Sholl analysis in f. Bars represent the average of the median distances in all analyzed animals ± SEM, and circles represent the single data points of the median distance averages for each animal (20-41 cells/animal; 1 slice per animal). **(h)** Representative skeleton images of binary images in e. Scale bar: 20µm. **(i)** Quantification of the number of branches per microglial cell in images as in h. Bars represent the average number of branches per microglial cell ± SEM in all analyzed animals, and circles represent the single data points of the cell averages for each animal (20-41 cells/animal; 1 slice per animal). **(j)** Quantification of the average length of branches per microglial cell in images as in h. Bars represent the average of branch length per microglial cell ± SEM in all analyzed animals, and circles represent the single data points of the cell averages for each animal (20-41 cells/animal; 1 slice per animal). ** p=0.0068; Mann-Whitney test, U=12.

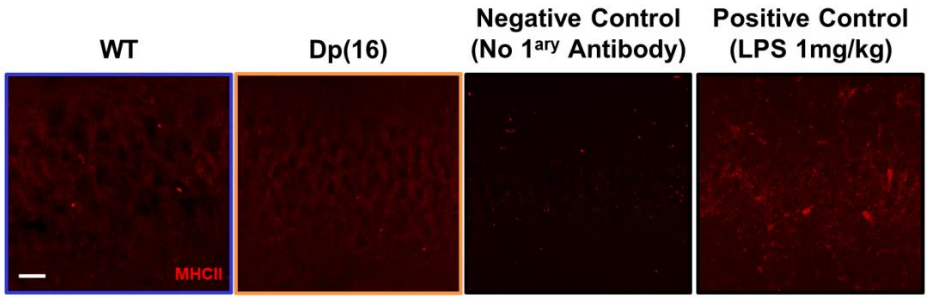

Figure 10. MHCII is not upregulated in Dp(16) animals. Representative confocal images of MHCII-stained (red) hippocampal slice from P22 WT and Dp(16) animals showing no immunoreactivity. In the negative control, the primary anti-MHCII antibody was omitted. Animals treated with 1mg/kg of LPS for 3 days were used as a positive control. Scale bar: 10µm.

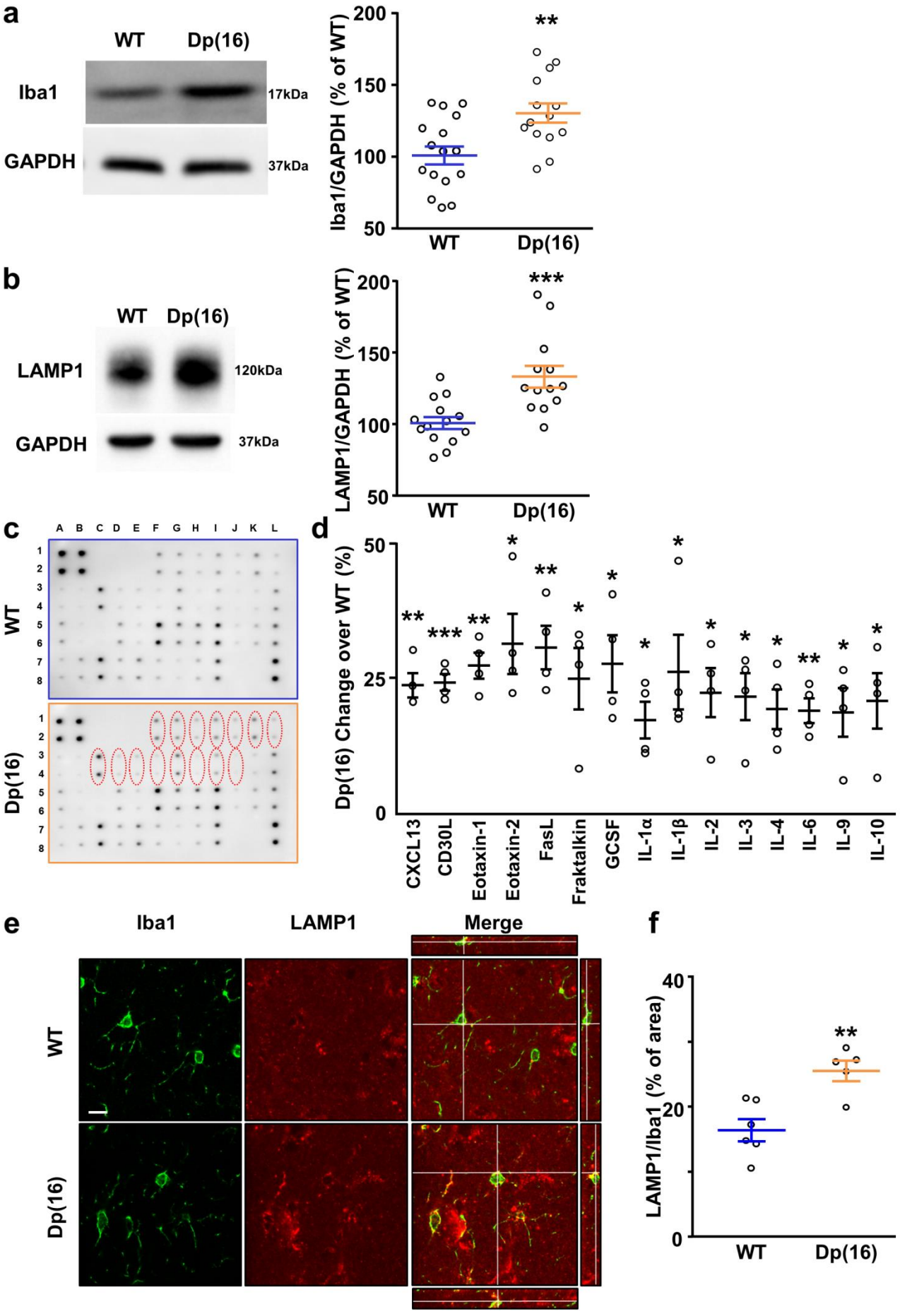
a
WT
Dp(16)
Iba1
17kDa
GAPDH
37kDa
Iba1/GAPDH (% of WT)
200
150
100
50
**
WT
Dp(16)
b
WT
Dp(16)
LAMP1
120kDa
GAPDH
37kDa
LAMP1/GAPDH (% of WT)
200
150
100
50
***
WT
Dp(16)
c
A B C D E F G H I J K L
1 2 3 4 5 6 7 8
WT
Dp(16)
d
Dp(16) Change over WT (%)
50
25
0
CXCL13
CD30L
Eotaxin-1
Eotaxin-2
FasL
Fraktalkin
GCSF
IL-1α
IL-1β
IL-2
IL-3
IL-4
IL-6
IL-9
IL-10
e
Iba1
LAMP1
Merge
WT
Dp(16)
f
LAMP1/Iba1 (% of area)
40
20
0
**
WT
Dp(16)

Figure 11. Hippocampi show increased levels of Iba1 and LAMP1 immunoreactivity, and cytokines in Dp(16) mice. (a) Representative immunoblots on protein extracts from lysates of hippocampi obtained from P22 WT and Dp(16) mice (*left)*. Quantification of Iba1 protein levels normalized to GADPH immunoreactivity (*right*). Bars represent the average percentage of Iba1 levels in Dp(16) over WT hippocampi for all the analyzed animals ± SEM, and circles represent the single data points for each animal. ** p<0.01; Unpaired Two-tailed Student's *t*-test, t=3.21, df=28. Data were averaged across 6 independent experiments. **(b)** Representative cytokines arrays performed on hippocampal lysates obtained from P22 WT and Dp(16) animals. The dashed circles show the cytokines significantly dysregulated between the two groups as quantified in d. **(c)** Quantification of all the cytokines significantly increased in Dp(16) *vs* WT hippocampi. Bars represent the average percentage of cytokine levels in Dp(16) over WT hippocampi of all independent experiments ± SEM, and circles represent the single data points of each independent experiment (1 animal per experiment). * p<0.05, ** p<0.01, *** p<0.001; Independent One-Sample *t*-test against 0. **(d)** Representative immunoblots on protein extracts from lysates of hippocampi obtained from P22 WT and Dp(16) mice (*left)*. Quantification of LAMP1 protein levels normalized to GADPH immunoreactivity (*right*). Bars represent the average percentage of LAMP1 levels in Dp(16) over WT hippocampi for all analyzed animals ± SEM, and circles represent the single data points for each animal. *** p<0.001; Unpaired Two-tailed Student's *t*-test, t=3.81, df=25. Data were collected from 5 independent experiments. **(e)** Representative single-plane confocal images of Iba1 (green) and LAMP1 (red)-stained hippocampal slices from P22 WT and Dp(16) animals, and the merging of the two channels showing Y-Z dimensions (*left*) and X-Z dimensions (*up in WT and below in Dp(16)*). Scale bar: 10µm. **(f)** Quantification of the $LAMP1^+$ area normalized on $Iba1^+$ area for microglial cell in experiments as in e. Bars represent the average LAMP1/Iba1 area for all analyzed animals ± SEM, and circles represent the average for all analyzed cells for each animal (4-9 cells/animal; 1 slice per animal). ** p=0.0038; Unpaired Two-tailed Student's *t*-test, t=3.87, df=9).

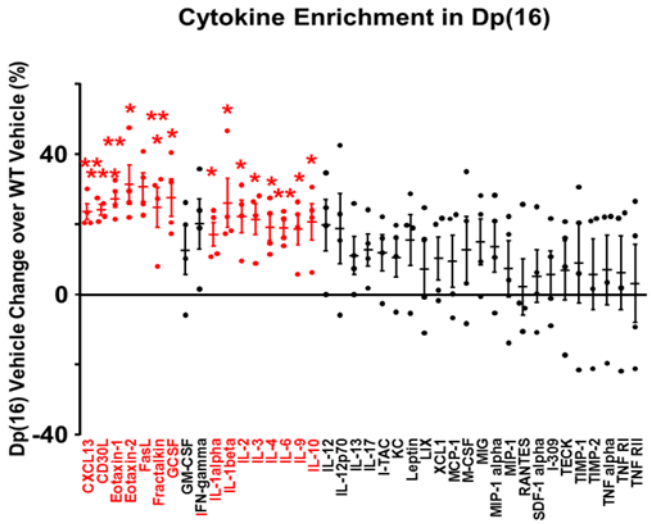

Figure 12. Cytokines are upregulated in Dp(16) animals. Quantification of the fold change of all the cytokines probed in vehicle-treated Dp(16) animals hippocampi when compared to vehicle-treated WT animals from the same experiments in figure 11b. Bars represent the average percentage of cytokine levels in Dp(16) over WT hippocampi of all independent experiments ± SEM, and circles represent the single data points of each independent experiment (1 animal per experiment). Statistically significant cytokines are highlighted in red. * $p<0.05$, ** $p<0.01$, *** $p<0.001$; Independent One-Sample t-test against 0.

The depletion of microglia recovers the cognitive deficits in Dp(16) mice

Microglial activation induced by inflammatory challenges or occurring in aging correlates with a decreased cognitive performance (Shobin et al., 2017; Tang et al., 2018). Since microglial cells in the hippocampus of Dp(16) mice show characteristics of activated microglia, we reasoned that they could play a role in cognitive deficits, which have already been described in this strain (Goodliffe et al., 2016). Dp(16) mice are a fairly recent model of DS, which has not been characterized thoroughly. Among the behavioral tests addressing hippocampus-dependent learning and memory, only the Morris water maze and fear conditioning have been performed on Dp(16) animals (Yu et al., 2010). Although these tests did reveal poor performance of the trisomic mice, both tests can be stressful for the mice (Carpenter and Summers, 2009; O'Connor and

Chipkin, 1984). Since stress *per se* may cause microglial activation (Delpech et al., 2016), we subjected Dp(16) animals and their WT littermates to two less stressful hippocampus-dependent cognitive tests (i.e., the novel object recognition (NOR) and object location test (OLT); (Deidda et al., 2015; Parrini et al., 2017), which had never been described for Dp(16) before. We found that trisomic animals presented cognitive deficits in NOR and OLT tests compared to their WT littermates (Fig. 13a, e-f). Interestingly, when we ran a proteomic analysis on the hippocampi of P22 Dp(16) animals and WT littermates followed by gene ontology (GO) analysis on the 169 differentially expressed proteins (Table 1), we found the term *Memory* among the first hits (Figure 14a-b; Table 2). This is in agreement with the idea that the trisomy interferes with hippocampal functions, affecting learning and memory.

To directly address whether defective microglia play a role in the low performance of Dp(16) mice in NOR and OLT, we took advantage of PLX3397. PLX3397 is a drug that selectively decreases the microglial population, without causing significant cognitive impairment in WT animals (Elmore et al., 2014). We thus treated P16 Dp(16) mice and their WT littermates with PLX3397 in their food supply (445 mg/kg of food available at *libitum*) for one week, and we then evaluated the impact of microglial depletion on cognitive performance at P22 (Fig. 13a). As expected, PLX3397 treatment sharply decreased the microglia count and Iba1 protein levels in the hippocampus of WT and Dp(16) mice (Fig. 13b-c). Remarkably, the treatment with PLX3397 fully rescued the cognitive deficit observed in the Dp(16) mice in the NOR and the OLT (Fig. 13e-f), supporting our hypothesis that activated microglia play a role in cognitive deficits.

Altogether, these data indicate that depletion of activated microglia can ameliorate the cognitive performance of trisomic mice.

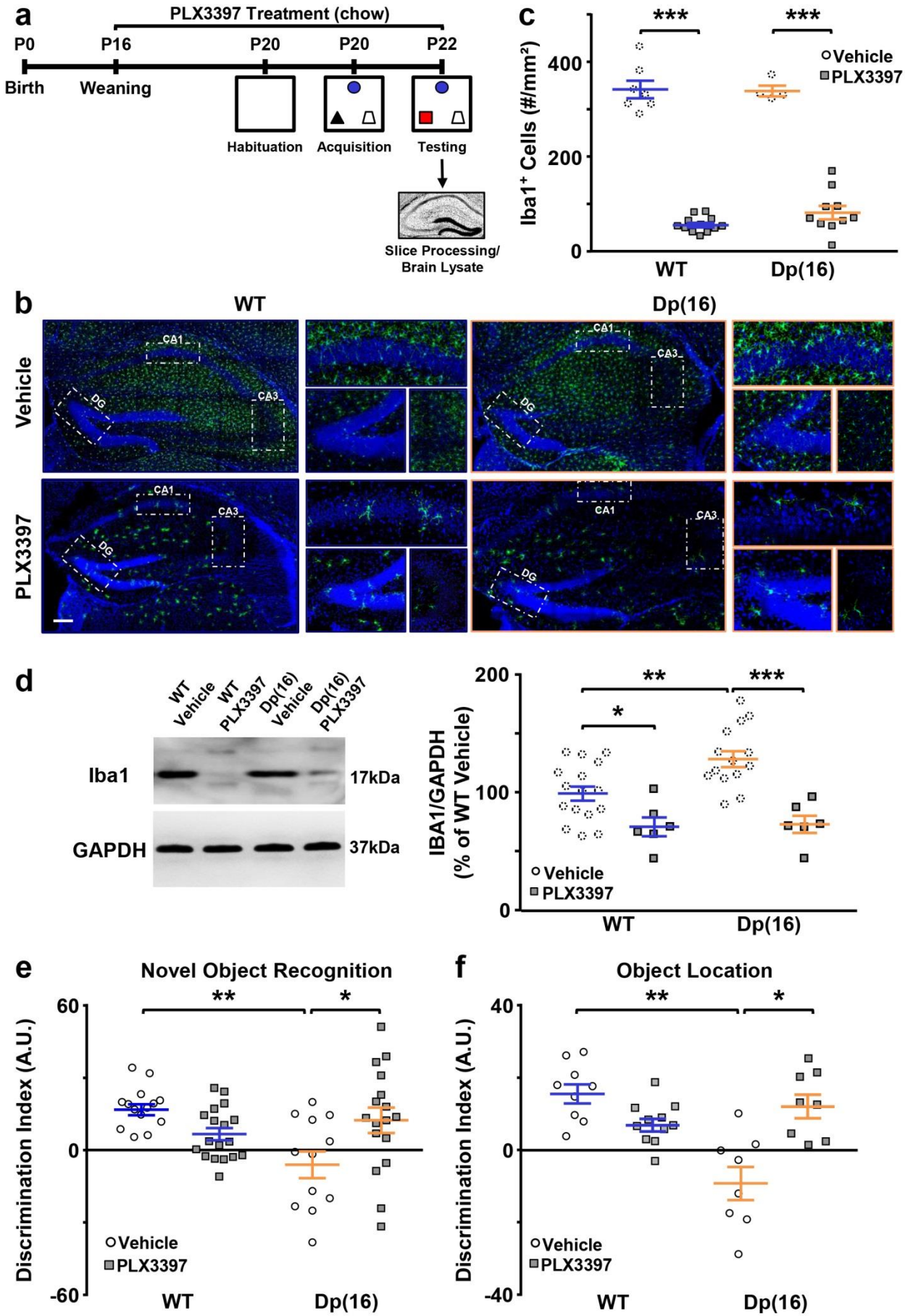
a
PLX3397 Treatment (chow)
P0
P16
P20
P20
P22
Birth
Weaning
Habituation
Acquisition
Testing
Slice Processing/
Brain Lysate
c
***
***
Iba1+ Cells (#/mm²)
400
200
0
Vehicle
PLX3397
WT
Dp(16)
b
WT
Dp(16)
Vehicle
PLX3397
CA1
CA3
DG
d
WT Vehicle
WT PLX3397
Dp(16) Vehicle
Dp(16) PLX3397
Iba1
17kDa
GAPDH
37kDa
IBA1/GAPDH (% of WT Vehicle)
200
100
0
**
***
*
Vehicle
PLX3397
WT
Dp(16)
e
Novel Object Recognition
Discrimination Index (A.U.)
60
0
-60
**
*
Vehicle
PLX3397
WT
Dp(16)
f
Object Location
Discrimination Index (A.U.)
40
0
-40
**
*
Vehicle
PLX3397
WT
Dp(16)

Figure 13. PLX3397 treatment depletes microglia and rescues cognitive deficits in Dp(16) mice.

(a) Experimental protocol used for PLX3397 treatment, histology/western-blotting and behavioral experiments. **(b)** Representative confocal images and higher magnifications from highlighted regions of Iba1-stained hippocampal slices from P22 WT and Dp(16) animals treated with either vehicle or PLX3397 in the chow. Scale bar: 100µm. **(c)** Quantification of the density of microglial cells in experiments as in b. Bars represent the average density of $Iba1^+$ cells of all the analyzed animals ± SEM, and symbols represent the single data points for each animal (1 slice per animal). *** p<0.001; Two-Way ANOVA, $F_{Treatment}$ (1, 29) = 642.6, p < 0.001; Holm-Sidak *post-hoc* test. The vehicle-treated animal data (dotted circles) were taken from Fig. 8c and shown here for comparison. **(d)** Representative immunoblots on protein extracts from lysates of hippocampi obtained from P22 WT and Dp(16) mice treated with either vehicle or PLX3397 in the chow (*left*). Quantification of Iba1 protein levels normalized to GADPH immunoreactivity (*right*). Bars represent the average percentage of Iba1 levels over WT vehicle of all analyzed animals ± SEM, and symbols represent the single data points for each animal. *p<0.05, **p<0.01, ***p < 0.001; Two-Way ANOVA, $F_{Treatment}$ (1, 38) = 27.26, Holm-Sidak *post-hoc* test. Data were averaged across 6 independent experiments. The vehicle-treated animal data (dotted circles) were taken from Fig. 11a and shown here for comparison. **(e)** Quantification of the discrimination index in the novel object recognition test in P22 WT and Dp(16) mice following vehicle or PLX3397 treatment. Bars represent the average discrimination index of all analyzed animals ± SEM, and symbols represent the single data points for each animal. *p<0.05, **p<0.01; Two-Way ANOVA, $F_{Interaction}$ (2, 84) = 11.52, p < 0.0001; Holm-Sidak *post-hoc* test. **(f)** Quantification of the discrimination index in the object location test in P22 WT and Dp(16) mice following vehicle or PLX3397 treatment. Bars represent the average discrimination index of all analyzed animals ± SEM, and symbols represent the single data points for each animal. *p<0.05, **p<0.01; Two-Way ANOVA, $F_{Interaction}$ (2, 52) = 8.76, p = 0.0005; Holm-Sidak *post-hoc* test.

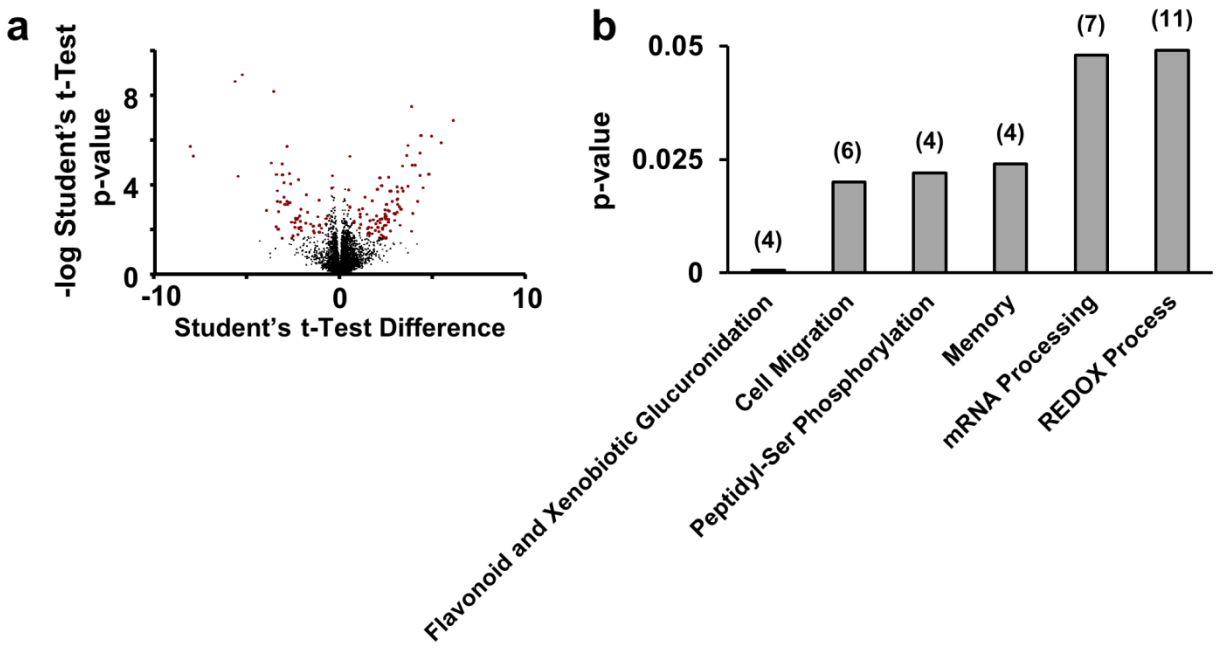

Figure 14. Proteomics analysis revealed differences in biological processes in hippocampi from Dp(16) mice. (a) Volcano plot depicting all the proteins (169) that were identified in the hippocampi of P22 WT and Dp(16) mice by proteomic analysis. The red dots represent the proteins that are significantly downregulated (Student's *t* test difference < 0) or upregulated (Student's *t* test difference > 0) in the hippocampus of Dp(16) compared to WT mice. The data were collected from 5 animals for each group. **(b)** Gene ontology terms on biological processes that are significantly altered in the hippocampi of Dp(16) *vs* WT mice. A p-value threshold of 0.05 was applied. The numbers on top of the histograms indicate the number of dysregulated proteins that generate the difference.

Microglial depletion restores the levels of the dendritic spine protein drebrin and rescues dendritic spine number and function in the hippocampus of Dp(16) mice

Since microglia play a crucial role in spine dynamics and in the synaptic elimination that occurs during plasticity (Garre et al., 2017; Miyamoto et al., 2016; Wu et al., 2015), we reasoned that the overactive microglia of the Dp(16) mice could impair the cognitive performance of Dp(16) animals by affecting the number and/or the level of maturation of spines. To test this hypothesis, we first

turned our attention to a dendritic spine marker, drebrin (DBN), which is downregulated by the activation of microglia (Kojima and Shirao, 2007; Ma et al., 2015; Xing et al., 2011) and it is decreased in brains of subjects with DS and in Alzheimer's disease (Kojima and Shirao, 2007; Ma et al., 2015; Xing et al., 2011). By western blotting with a specific antibody against DBN, we observed significantly decreased levels of this protein in the hippocampi of P22 Dp(16) mice in comparison to WT mice (Fig. 15a). Accordingly, when we ran a targeted proteomic protocol on hippocampi from Dp(16) and WT littermates, we found a sharp decrease in the levels of 4 different peptide fragments ascribed to DBN in trisomic mice (Figure 16a-b). Interestingly, PLX3397 treatment completely rescued the drebrin levels in Dp(16) mice, as assessed by western blotting (Fig. 15a). In agreement with our hypothesis, we found a decreased number of spines in CA1 hippocampal excitatory pyramidal neurons from Dp(16) mice counted after Golgi-Cox staining, which was fully rescued by the PLX3397 treatment (Fig. 15b-c). In particular, PLX3397 treatment had a significant effect on motile spines with a full rescue of the density of the thin-type (Majewska and Sur, 2003) in Dp(16) mice. Moreover, PLX3397 partially rescued the density of fully mature mushroom-type (Majewska and Sur, 2003) spines in Dp(16) mice and had no effect on immature spines (Figure 16a-c). Finally, depletion of microglial cells by PLX3397 treatment fully rescued the frequency and amplitude of miniature excitatory postsynaptic currents (mEPSCs; Fig. 15d-e), which suggests that the defective trisomic microglia also impinges on the correct functionality of dendritic spines. An increased number of contacts between microglia and synaptic elements is considered to be indicative of augmented synaptic elimination (Sipe et al., 2016). Thus, to further confirm that the overactive microglia in Dp(16) animals regulated the number of neuronal spines, we turned to electron microscopy. In P22 Dp(16) mice, we observed an increased number of contacts between microglia and surrounding cells -and specifically synaptic elements- compared to WT animals (Fig. 15f-g and Figure 17d).

Taken together, these data suggest that overactive microglia cause altered dendritic spine turnover and function in Dp(16) mice.

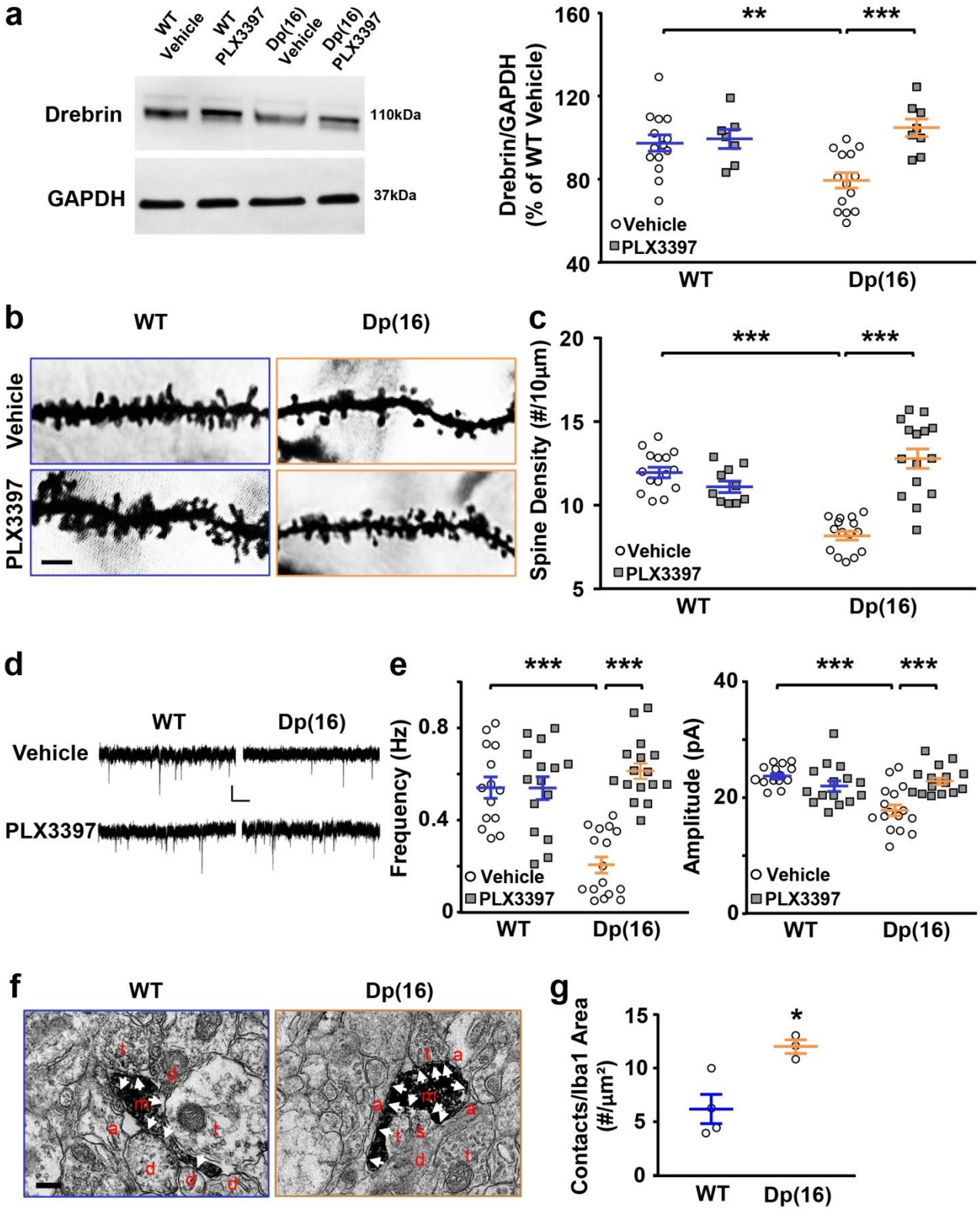

Figure 15. Drebrin levels, dendritic-spine density and miniature postsynaptic events are altered, and rescued by PLX3397 treatment in Dp(16) mice. (a) Representative immunoblots on protein extracts from lysates of hippocampi obtained from P22 WT and Dp(16) mice (*left)*. Quantification of Drebrin protein levels normalized to GADPH immunoreactivity (*right*). Bars represent the average percentage of Drebrin levels in Dp(16) over WT hippocampi for all analyzed animals ± SEM, and symbols represent the single data point for each animal. ** p<0.01, *** p<0.001; Two-Way ANOVA, $F_{Interaction}$ (1, 39) = 7.166, p = 0.0108; Holm-Sidak *post-hoc* test. Data were averaged across 6 independent experiments. **(b)** Representative light-transmitted images of dendritic spines from Golgi-Cox-stained slices of hippocampi from P22 WT and Dp(16) mice treated with vehicle or PLX3397. Scale bar: 4µm. **(c)** Quantification of the spine density in experiments as in b. Bars represent the average spine density of all analyzed cells ± SEM, and symbols represent the single data points for each cell (3 animals per condition). *** p<0.001; Two-Way ANOVA, $F_{Interaction}$ (1, 51) = 20.84, p < 0.0001; Holm-Sidak *post-hoc*. **(d)** Representative traces of mEPSC recordings in CA1 hippocampal pyramidal neurons from P22 WT and Dp(16) mice treated with vehicle or PLX3397. Scale bars: 10pA and 1s. **(e)** Quantification of the mEPSC frequency (*left)* and amplitude (*right*) in experiments as in d. Bars represent the average frequency and the average amplitude for all analyzed cells ± SEM, and symbols represent the single data points for each cell (3 WT vehicle-treated animals and 4 animals per each remaining conditions). *** p<0.001; For frequency: Two-Way ANOVA, $F_{Interaction}$ (2, 86) = 14.09, p < 0.0001; For amplitude Two-Way ANOVA, $F_{Interaction}$ (2, 86) = 20.61, p < 0.0001; Holm-Sidak *post-hoc* test. **(f)** Representative transmission electron microscopy images of hippocampal slices from P22 WT and Dp(16) mice. Scale bar: 500 nm. m: microglia, a: astrocytes, d: dendrite shaft, t: pre-synaptic element, s: post-synaptic element. **(g)** Quantification of the interaction between microglia and dendritic spines in experiments as in f. Bars represent the average number of contact points between microglia and spines of all animals analyzed ± SEM, and circles represent the average of all analyzed fields for each animal (20-44 fields/animal). *p<0.05; Unpaired Two-tailed Student's *t*-test, t=3.47, df=5.

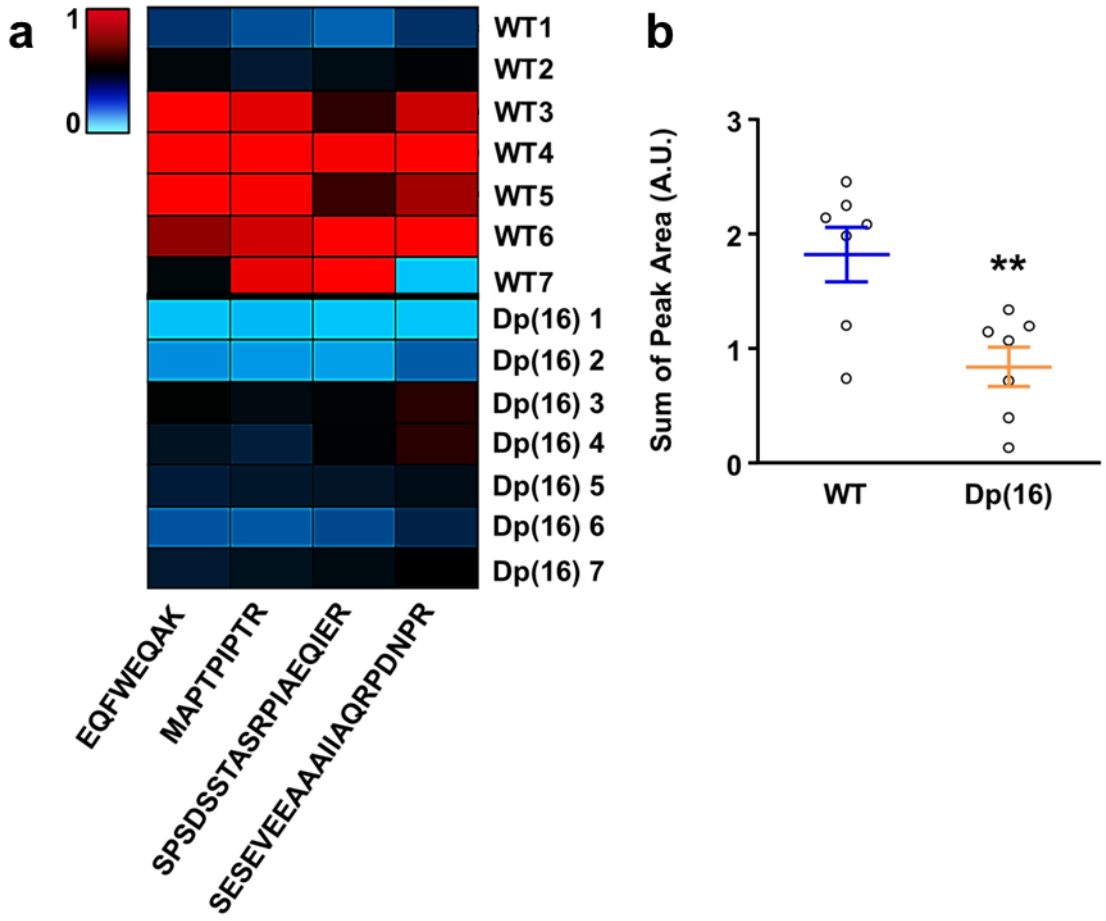

Figure 16. Proteomics analysis showed defects in the Drebrin protein levels in hippocampi from Dp(16) mice. (a) Heat-map from proteomic experiments of the peak area normalized to the maximum peak of Drebrin for the four peptides that can be ascribed to Drebrin (*vertical columns*). The data were collected from 7 animals per genotype (*horizontal lines*). **(b)** Quantification of the normalized peak area for each animal from experiments in a. For each animal, the reads from each peptide were summed together. Bars represent the average sum of the peak area of all analyzed animals ± SEM, and circles represent the single data points for each animal **p<0.01; Unpaired Two-tailed Student's *t*-test, t=3.37, df=12.

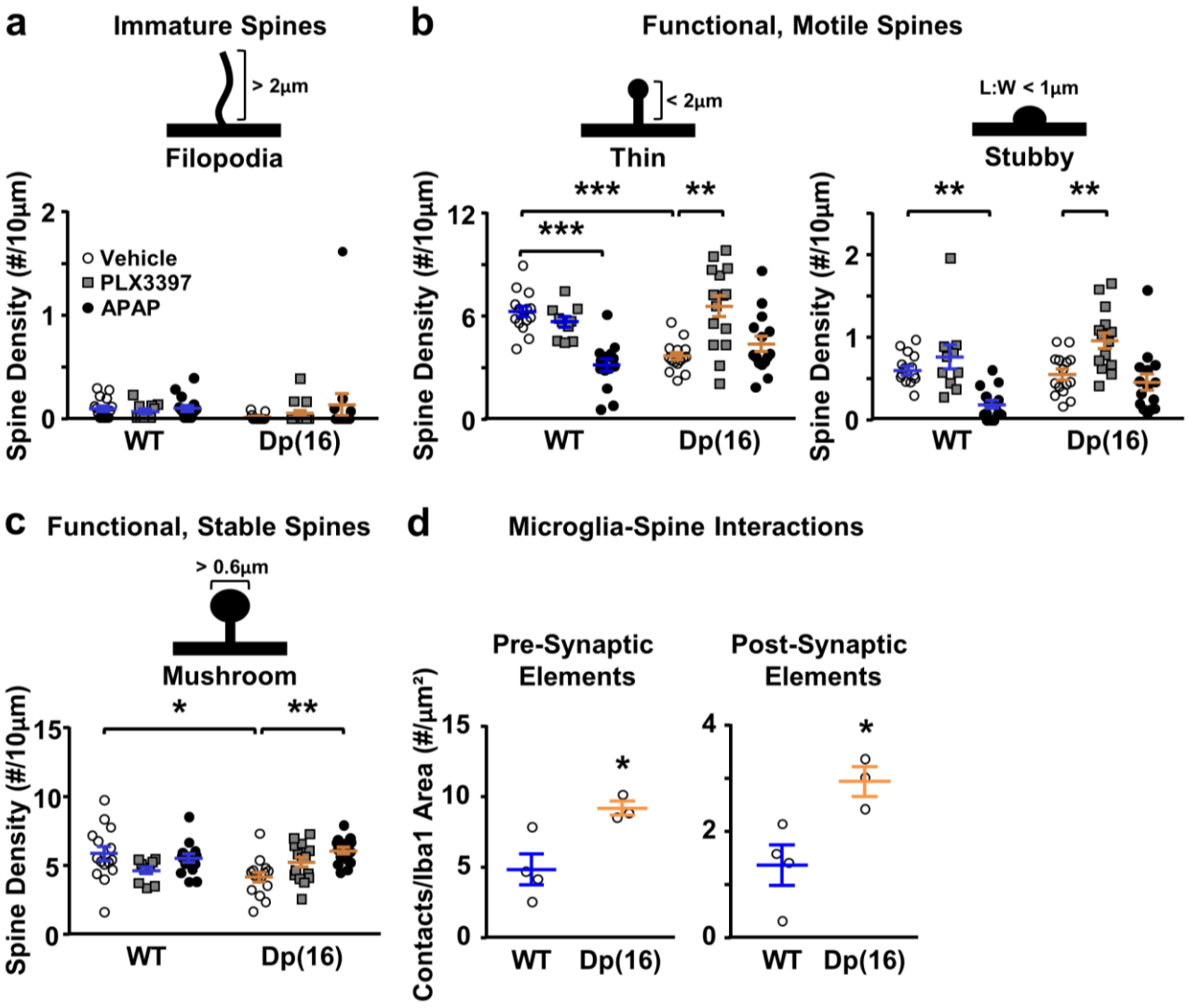

Figure 17. PLX3397 or APAP treatment rescues specific types of dendritic spines in Dp(16) mice. **(a)** Cartoon depicting the morphological characteristics of immature, filopodia spines (*top*). Quantification of the filopodia spine density (*bottom*) in P22 WT and Dp16 animals treated with vehicle, PLX3397, or APAP from experiments in Fig. 15c and Fig. 21a. Bars represent the average filopodia spine density of all analyzed cells ± SEM, and symbols represent the single data points for each cell. Data were collected from 3 animals per condition. **(b)** Cartoon depicting the morphological characteristics of the functional and motile, thin and stubby spines (*top*). Quantification of the thin or stubby spine density (*bottom*) in P22 WT and Dp16 animals treated with vehicle, PLX3397, or APAP from experiments in Fig. 15c and Fig. 21a. Bars represent the average thin or stubby spine density of all analyzed cells ± SEM, and symbols represent the single data points for each cell. For thin spines: ** $p<0.01$, *** $p<0.001$; Two-Way ANOVA $F_{Interaction}$ (2, 79) = 13.92, $p<0.001$. For stubby spines: **$p<0.01$; Two-Way ANOVA $F_{Treatment}$(2, 79) = 18.98,

p<0.001; Holm-Sidak *post-hoc* test. Data were collected from 3 animals per condition. **(c)** Cartoon depicting the morphological characteristics of the functional and stable, mushroom spines (*top*). Quantification of the mushroom spine density (*bottom*) in P22 WT and Dp16 animals treated with vehicle, PLX3397, or APAP from experiments in Fig. 15c and Fig. 21a. Bars represent the average mushroom spine density of all analyzed cells ± SEM, and symbols represent the single data points for each cell. * p<0.05, ** p<0.01; Two-Way ANOVA, $F_{Interaction}$ (2, 79) = 6.915, p = 0.0017; Holm-Sidak *post-hoc* test. Data were collected from 3 animals per condition. **(d)** Quantification of the number of physical interactions between the microglia and the pre-synaptic (left) or the post-synaptic (right) elements from experiments in Fig. 15f. Bars represent the average number of physical interactions between the microglia and the pre-synaptic or the post-synaptic element ± SEM in all analyzed animals, and circles represent the average of all the analyzed fields for each animal (Presynaptic interactions (20-44 fields/animal): *p<0.05; Unpaired Two-tailed Student's *t*-test, t=3.14, df=5. Post-synaptic interactions (20-44 fields/ animal): *p<0.05; Unpaired Two-tailed Student's *t*-test, t=3.09, df=5.

APAP treatment rescues microglial morphology, decreases cytokine levels and rescues spine density in the hippocampus of Dp(16) mice

Recent evidence in brains from the Ts65Dn mouse model of DS and from subjects with DS indicates increased expression of the inducible form of the cyclooxygenase enzymes (COX2) in microglia and neurons, which is a sign of increased immunological activity (Mulet et al., 2017). Indeed, activated microglia produce a large amount of the pro-inflammatory molecule PGE_2 (Zhang et al., 2009). Because COX2 inhibitors can decrease the production of PGE_2 by microglia (Villa et al., 2016; Zhang et al., 2009) decreasing overall inflammation, we hypothesized that the use of a COX2 inhibitor could rescue the microglial phenotype in Dp(16) mice. Among COX2 inhibitors, we chose to use APAP because it is one of the most widely used COX2 inhibitors; it readily crosses the blood-brain barrier and it has a very safe profile with few contraindications. Remarkably, after three daily doses of APAP (IP, 100 mg/kg, Fig. 18a), we completely rescued the

microglial morphology, measured as the cell-body area (Fig. 18b-c) and ramifications (Fig. 18d-g) in the hippocampi of Dp(16) mice at P22. APAP treatment also rescued the microglia cell body area in the somatosensory cortex (Fig. 19a-c). Importantly, APAP treatment also decreased the levels of all overrepresented cytokines in the Dp(16) mouse hippocampi (Fig. 18h, Fig. 20a-b). Interestingly, we were able to fully rescue the spine density with APAP treatment, with a full rescue of the mature mushroom-type and a partial rescue of motile thin-type in Dp16 mice (Fig. 21a-b, Fig. 17b-c). Accordingly, APAP treatment also rescued the frequency and amplitude of mEPSCs in Dp(16) animals (Fig. 21c-d).

Taken together, our data indicate that APAP treatment in Dp(16) animals is able to recover the activity state of microglia together with spine density and function, further strengthening the possible causal link between the two.

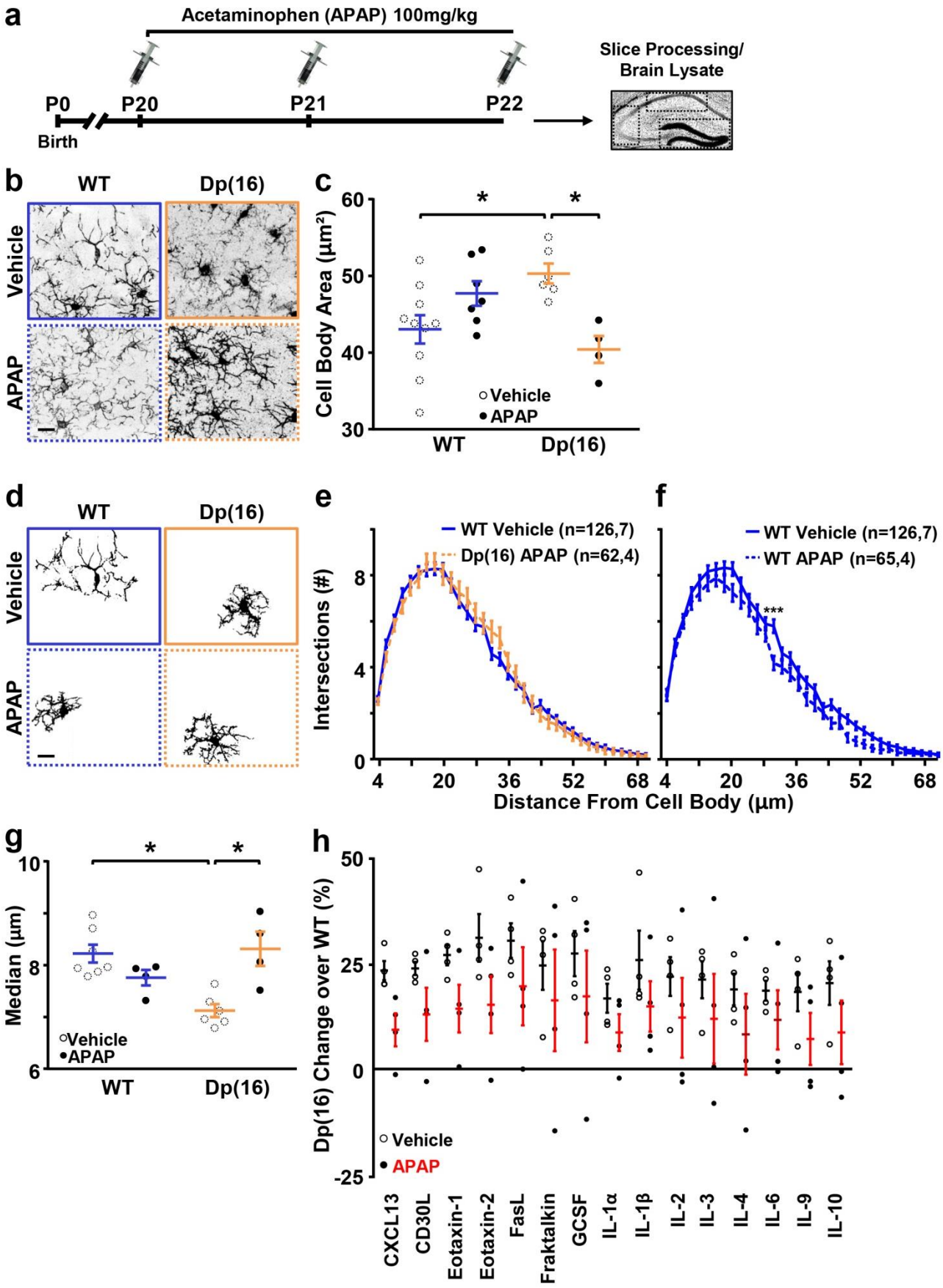
a
Acetaminophen (APAP) 100mg/kg
P0
Birth
P20
P21
P22
Slice Processing/
Brain Lysate
b
WT
Dp(16)
Vehicle
APAP
c
Cell Body Area (µm²)
60
50
40
30
*
*
Vehicle
APAP
WT
Dp(16)
d
WT
Dp(16)
Vehicle
APAP
e
WT Vehicle (n=126,7)
Dp(16) APAP (n=62,4)
Intersections (#)
8
4
0
4
20
36
52
68
Distance From Cell Body (µm)
f
WT Vehicle (n=126,7)
WT APAP (n=65,4)
***
4
20
36
52
68
g
Median (µm)
10
8
6
*
*
Vehicle
APAP
WT
Dp(16)
h
Dp(16) Change over WT (%)
50
25
0
-25
Vehicle
APAP
CXCL13
CD30L
Eotaxin-1
Eotaxin-2
FasL
Fraktalkin
GCSF
IL-1α
IL-1β
IL-2
IL-3
IL-4
IL-6
IL-9
IL-10

Figure 18. Acetaminophen (APAP) treatment rescues microglial morphology and cytokine levels in Dp(16) mice. (a) Experimental protocol used for APAP treatment and histology/western-blotting. **(b)** Representative confocal images of Iba1-stained hippocampal slices from WT and Dp(16) animals treated with either vehicle or APAP. Scale bar: 10µm. **(c)** Quantification of the cell body area of microglial cells in experiments as in b. Bars represent the average of microglial cell body areas in all analyzed animals ± SEM and circles represent the single data points of the cell averages for each animal (14-73 cells/ animal; 1 slice per animal). * $p<0.05$; Two-Way ANOVA $F_{Interaction}$ (1, 23) = 14.88 p = 0.0008; Holm-Sidak *post-hoc* test. The vehicle-treated animal data (dotted circles) were taken from Fig. 8d and shown here for comparison. **(d)** Binary images of the fields shown in b. Scale bar: 10µm. **(e)** Sholl analysis of microglial cells in images as in d. Data are expressed as average number of intersections at each distance from the cell bodies of all analyzed cells ± SEM. Numbers in parenthesis: analyzed cells, and animals. The vehicle-treated WT animal data were taken from Fig. 8g and shown here for comparison. **(f)** Sholl analysis of microglial cells in images as in d. Data are expressed as average number of intersections at each distance from the cell bodies of all analyzed cells ± SEM. Numbers in parenthesis: analyzed cells, and animals. *** $p<0.001$; Two-Way ANOVA, $F_{Treatment}$ (1, 6426) = 58.32, $p < 0.0001$; Holm-Sidak post-hoc test. The vehicle-treated WT animal data were taken from Fig.8g and shown here for comparison. **(g)** Quantification of the median distance of the intersections from the cell body, as obtained from the Sholl analysis in f. Bars represent the average of the median distances in all analyzed animals ± SEM, and circles represent the single data points of the median distance averages for each animal (12-21 cells/animal; 1 slice per animal). * $p<0.05$, Two-Way ANOVA, $F_{Interaction}$ (1, 17) = 17.41, p = 0.0006; Holm-Sidak *post-hoc* test). The vehicle-treated animal data (dotted circles) were taken from Fig. 8h and shown here for comparison. **(h)** Quantification of the rescue effect of APAP treatment (red) on all the cytokines significantly increased in Dp(16) *vs* WT hippocampi (black). Bars represent the average percentage of cytokine levels in APAP- or vehicle-treated Dp(16) hippocampi over WT hippocampi and of all independent experiments ± SEM, and circles represent the single data points of each independent experiment (1 animal per experiment). Two-Way ANOVA, $F_{Treatment}$ (1, 90) = 20.47, $p < 0.001$. The data of vehicle-treated Dp(16) animals normalized over WT levels were taken from Fig. 11d and shown here for comparison.

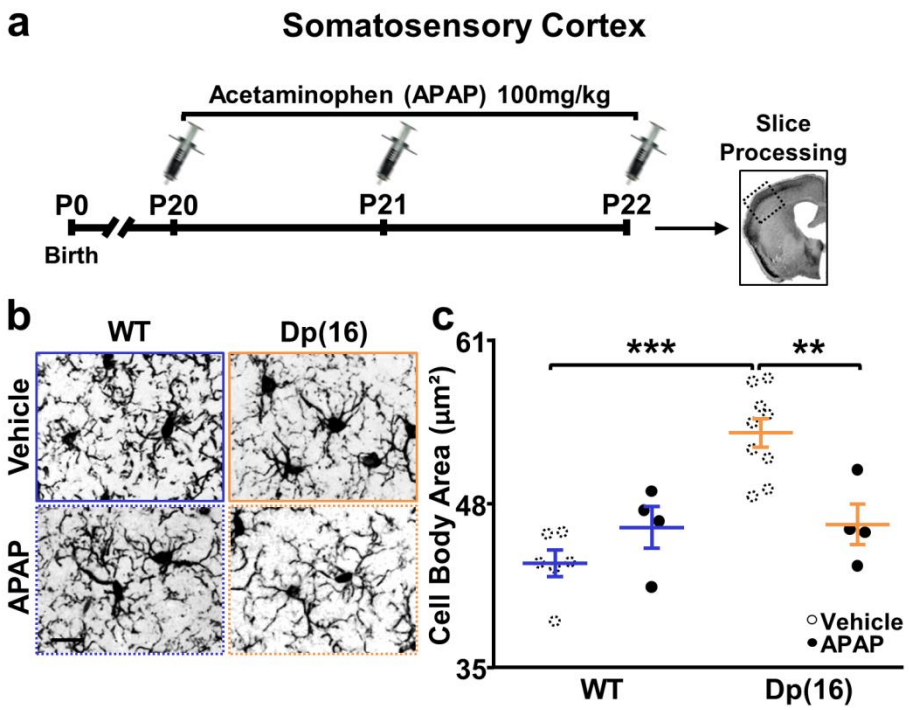

Figure 19. APAP treatment rescues microglial morphology in the somatosensory cortex of Dp(16) mice. (a) Experimental protocol used for APAP treatment and for analyzing the morphology of microglia. **(b)** Representative confocal images of Iba1-stained somatosensory cortices from P22 WT and Dp(16) animals treated with either vehicle or APAP. Scale bar: 20µm. **(c)** Quantification of the cell body area of microglial cells in experiments as in b. Bars represent the average of microglial cell body areas in all analyzed animals ± SEM and circles represent the single data points of the cell averages for each animal (72-126 cells/animal; 1 slice per animal). **p<0.01, *** p<0.001; Two-Way ANOVA $F_{Interaction}$ (1, 19) = 13.19, p = 0.0018; Holm-Sidak *post-hoc* test. The vehicle-treated animal data (dotted circles) were taken from Fig. 9c and shown here for comparison.

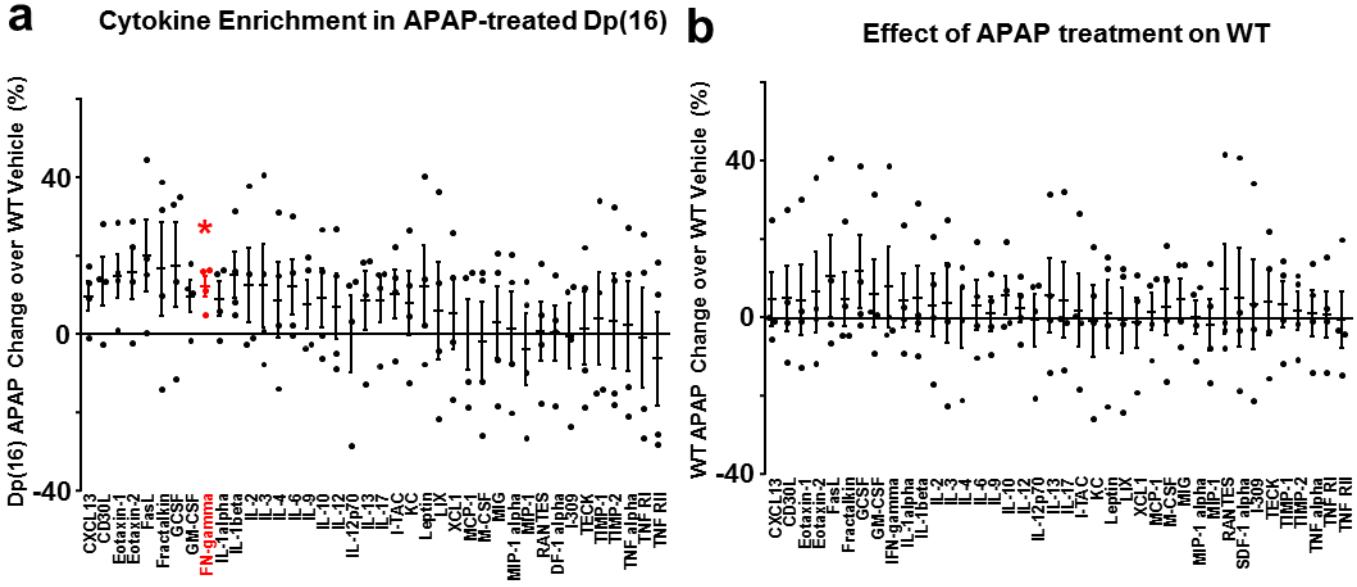

Figure 20. APAP affects cytokines levels. (a) Quantification of the fold change of all the cytokines probed in APAP-treated Dp(16) animals hippocampi when compared to vehicle-treated WT animals from the same experiments in Fig. 18g. Bars represent the average percentage of cytokine levels in APAP-treated Dp(16) over WT hippocampi of all independent experiments ± SEM, and circles represent the single data points of each independent experiment (1 animal per experiment). Statistically significant cytokines are highlighted in red. * $p<0.05$; Independent One-Sample t-test against 0. **(b)** Quantification of the fold change of all the cytokines probed in APAP-treated WT animals hippocampi when compared to vehicle-treated WT animals from the same experiments in figure 18g. Bars represent the average percentage of cytokine levels in APAP-treated WT over vehicle-treated WT animals of all independent experiments ± SEM, and circles represent the single data points of each independent experiment (1 animal per experiment).

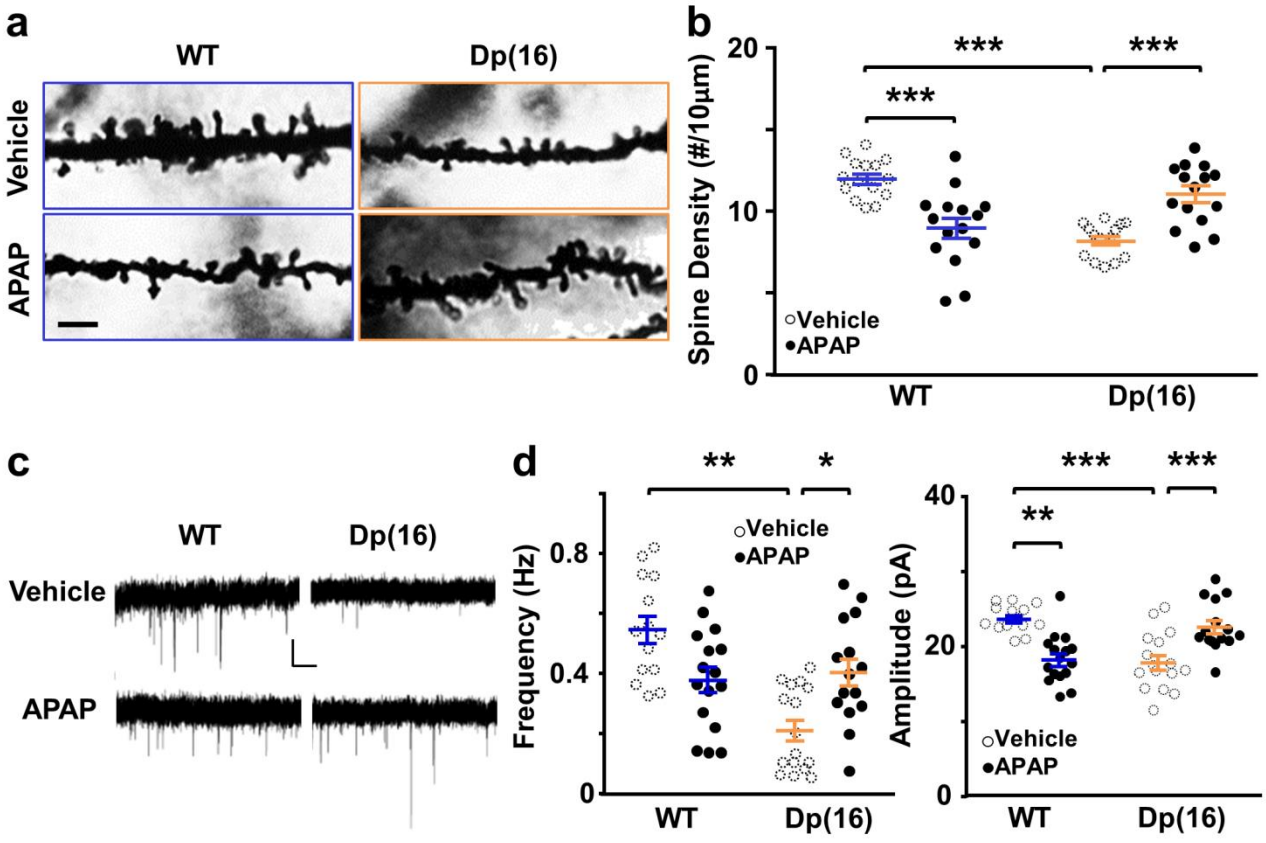

Figure 21. APAP rescues spine and electrophysiological deficits. (a) Representative light-transmitted images of dendritic spines from Golgi-Cox-stained slices of hippocampi from P22 WT and Dp(16) mice treated with vehicle or APAP. Scale bar: 4µm. **(b)** Quantification of the spine density in experiments as in a. Bars represent the average spine density of all analyzed cells ± SEM, and circles represent the single data points for each cell (3 animals per condition). *** p<0.001; Two-Way ANOVA, $F_{Interaction}$ (1, 56) = 42.99, p<0.001; Holm-Sidak *post-hoc* test. The vehicle-treated cell data (dotted circles) were taken from Fig. 15c and shown here for comparison. **(c)** Representative traces of mEPSC recordings in CA1 hippocampal pyramidal neurons from P22 WT and Dp(16) mice treated with vehicle or APAP. Scale bars: 10pA and 1s. **(d)** Quantification of the mEPSC frequency (*left)* and amplitude (*right*) in experiments as in d. Bars represent the average frequency and the average amplitude of mEPSCs for all analyzed cells ± SEM, and circles represent the single data points for each cell (4 Dp(16) vehicle-treated animals and 3 animals per each remaining condition). *p<0.05, ** p<0.01, *** p<0.001); For frequency: Two-Way ANOVA, $F_{Interaction}$(1, 57) = 18.51, p<0.001; For amplitude Two-Way ANOVA, $F_{Interaction}$ (1, 57) = 38.21, p<0.001; Holm-Sidak *post-hoc* test). The vehicle-treated animal data (dotted circles) were taken from Fig. 15e and shown here for comparison.

Acetaminophen treatment rescues cognitive deficits in Dp(16) mice and have opposite effects in WT mice

Our results on the rescue of cognitive impairment in Dp(16) mice upon depletion of microglia strongly suggest that these cells regulate learning and memory in trisomic animals. Thus, we investigated whether not only the complete depletion, but also the simple rescue of the activation state of microglia in Dp(16) mice was sufficient to restore their cognitive abilities. Thus, we treated Dp(16) and WT littermates with APAP from P20 to P22 and performed the NOR and OLT cognitive tests. APAP treatment completely recovered the cognitive deficits in Dp(16) animals (Figure 22a-c). In agreement with a hindering role of activated microglia in the cognitive abilities of Dp(16) mice, the administration of an inhibitor of the JAK1/2 pathway (ruxolitinib; 50 mg/kg twice a day for 3 consecutive days), whose activation is important for microglial activation (Qin et al., 2016), significantly rescued microglial branching (Figure 23a-g) together with cognitive performance in Dp(16) mice (Figure 23h-i). Notably, in WT animals, the treatment with APAP caused a decreased cognitive performance in both the NOR and OLT tests, together with a more amoeboid microglial morphology, and a significant decrease in the number of neuronal spines as well as in the mEPSC amplitude, but no significant effect on cytokine levels (Fig. 20; Fig. 21). These results indicate that the effects of APAP might be dependent on the genotype and that the behavioral cognitive outcome is strongly correlated with the microglia activated morphology as well as the spine density and function.

Altogether, our results indicate that APAP treatment influences spine density and function as well as cognitive performance, and that recovery of microglial activation state can have a positive impact on cognition.

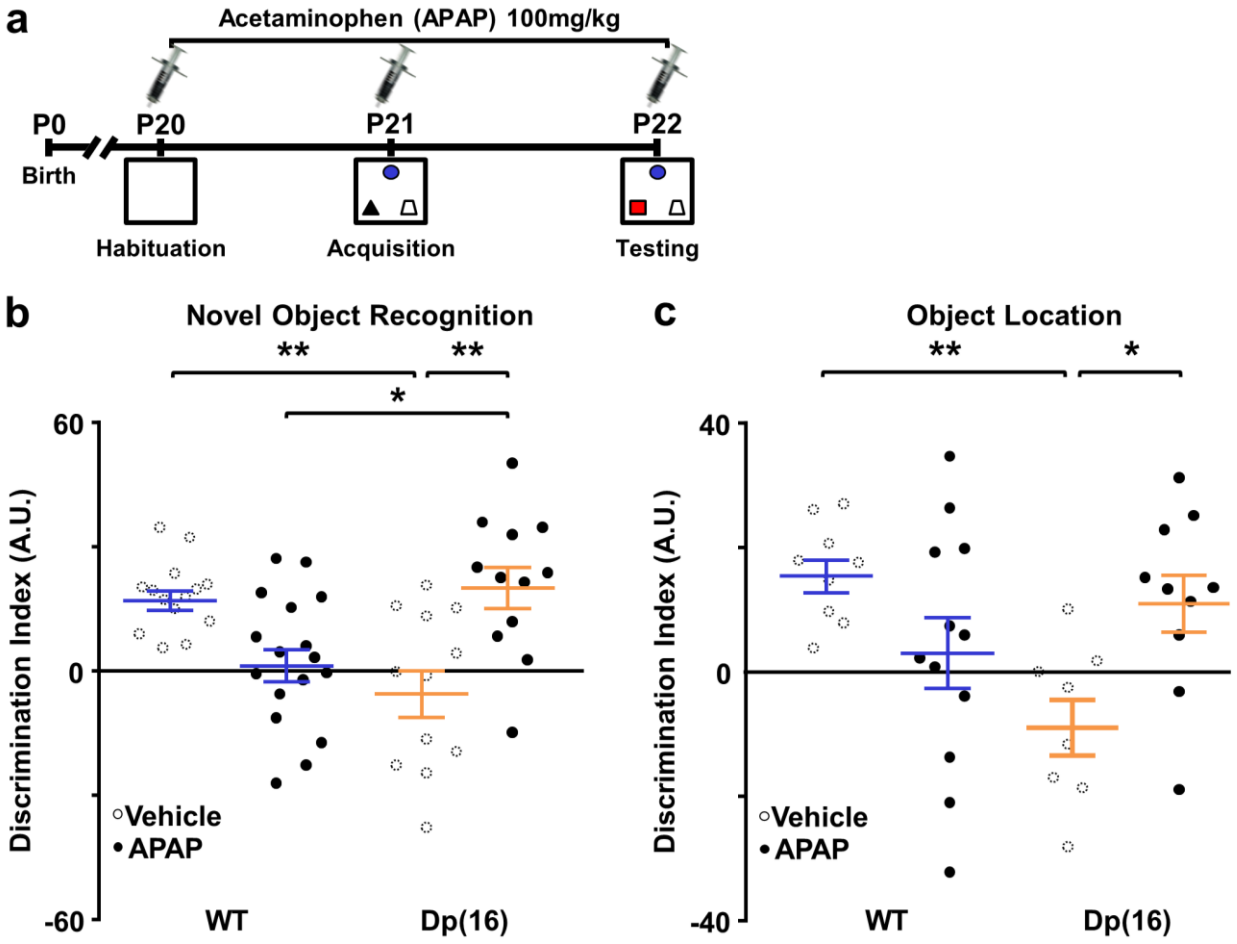

Figure 22. APAP treatment rescues cognitive deficits in Dp(16) mice. (a) Experimental protocol used for APAP treatment, histology and electrophysiology. **(b)** Quantification of the discrimination index in the novel object recognition test in P22 WT and Dp(16) mice following vehicle or APAP treatment. Bars represent the average discrimination index of all analyzed animals ± SEM, and circles represent the single data points for each animal. *p<0.05, **p<0.01; Two-Way ANOVA, $F_{Interaction}$ (1, 51) = 23.76, p<0.001; Holm-Sidak *post-hoc* test. The vehicle-treated animal data (dotted circles) were taken from Fig. 13e and shown here for comparison **(c)** Quantification of the discrimination index in the object location test in P22 WT and Dp(16) mice following vehicle or APAP treatment. Bars represent the average discrimination index of all analyzed animals ± SEM, and circles represent the single data points for each animal. * p<0.05, ** p<0.01; Two-Way ANOVA, $F_{Interaction}$ (1,35) = 11.24, p<0.002; Holm-Sidak *post-hoc* test. The vehicle-treated animal data (dotted circles) were taken from Fig. 13f and shown here for comparison.

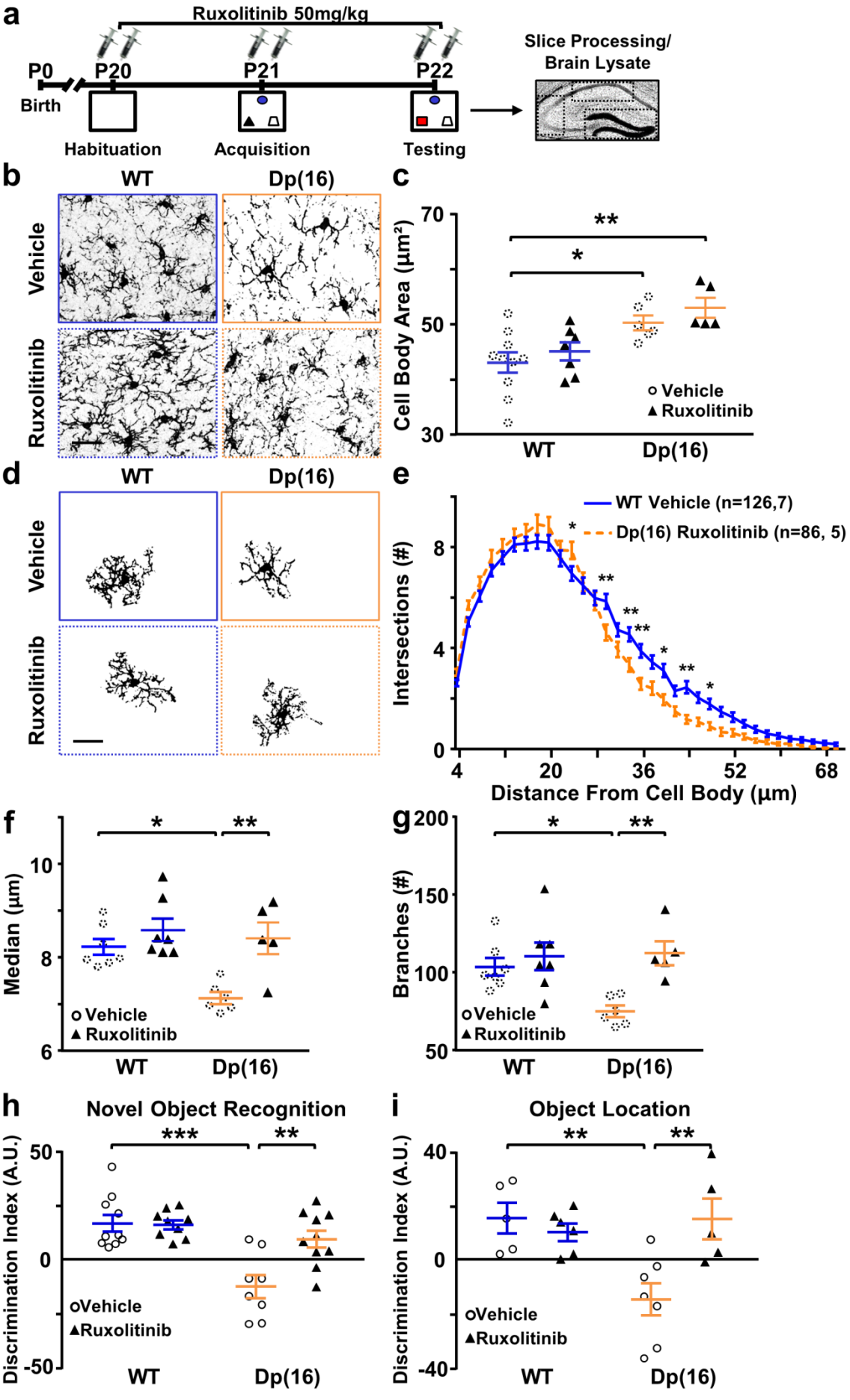
a
Ruxolitinib 50mg/kg
P0
Birth
P20
P21
P22
Habituation
Acquisition
Testing
Slice Processing/
Brain Lysate
b
WT
Dp(16)
Vehicle
Ruxolitinib
c
Cell Body Area (µm²)
70
50
30
**
*
Vehicle
Ruxolitinib
WT
Dp(16)
d
WT
Dp(16)
Vehicle
Ruxolitinib
e
WT Vehicle (n=126,7)
Dp(16) Ruxolitinib (n=86, 5)
Intersections (#)
8
4
0
4
20
36
52
68
Distance From Cell Body (µm)
f
Median (µm)
10
8
6
*
**
Vehicle
Ruxolitinib
WT
Dp(16)
g
Branches (#)
200
150
100
50
*
**
Vehicle
Ruxolitinib
WT
Dp(16)
h
Novel Object Recognition
Discrimination Index (A.U.)
50
0
-50
***
**
Vehicle
Ruxolitinib
WT
Dp(16)
i
Object Location
Discrimination Index (A.U.)
40
0
-40
**
**
Vehicle
Ruxolitinib
WT
Dp(16)

Figure 23. Ruxolitinib treatment rescues cognitive deficits and partially rescues microglial alterations in Dp(16) mice. (a) Experimental protocol used for Ruxolitinib treatment, and for analyzing the morphology of microglia and the behavior of mice. **(b)** Representative confocal images of Iba1-stained hippocampal slices from P22 WT and Dp(16) animals treated with either vehicle or Ruxolitinib. Scale bar: 20µm. **(c)** Quantification of the cell body area of microglial cells in experiments as in b. Bars represent the average of microglial cell body areas in all analyzed animals ± SEM and circles represent the single data points of the cell averages for each animal (38-73 cells/animal; 1 slice per animal). * p<0.05, **p<0.01; Two-Way ANOVA F_{Strain} (1, 24) = 17.35, p = 0.0003; Holm-Sidak *post-hoc* test. The vehicle-treated animal data (dotted circles) were taken from Fig. 8d and shown here for comparison. **(d)** Binary images of the fields shown in b. Scale bar: 20µm. **(e)** Sholl analysis of microglial cells in images as in d. Data are expressed as average number of intersections at each distance from the cell bodies of all analyzed cells ± SEM. * p<0.05, ** p<001; Two-Way ANOVA, F (33, 7140) = 3.352, p < 0.001; Holm-Sidak *post-hoc* test. Numbers in parenthesis: analyzed cells, and animals. The vehicle-treated WT animal data were taken from Fig. 8g and shown here for comparison. **(f)** Quantification of the median distance of intersections from the cell body, as obtained from the Sholl analysis in e. Bars represent the average of the median distances in all analyzed animals ± SEM, and circles represent the single data points of the median distance averages for each animal (12-21 cells/animal; 1 slice per animal). * p<0.05, **p<0.01; Two-Way ANOVA, $F_{Interaction}$ (1, 21) = 4.392, p = 0.048; Holm-Sidak *post-hoc* test). The vehicle-treated animal data (dotted circles) were taken from Fig. 8h and shown here for comparison. **(g)** Quantification of the number of branches per microglial cell in images as in d processed as in Fig 8i. Bars represent the average number of branches per microglial cell ± SEM of all analyzed animals, and circles represent the single data points of the cell averages for each animal (12-21 cell/animal; 1 slice per animal). * p<0.05, ** p<0.01; Two-Way ANOVA, $F_{Interaction}$ (1, 21) = 4.880 p = 0.0384, Holm-Sidak *post-hoc* test. The vehicle treated animals data was taken from Fig. 8j and shown here for comparison. **(h)** Quantification of the discrimination index in the novel object recognition test in P22 WT and Dp(16) mice following vehicle or Ruxolitinib treatment. Bars represent the average discrimination index of all analyzed animals ± SEM, and circles represent the single data points for each animal. **p<0.01, ***p<0.001; Two-Way ANOVA, $F_{Interaction}$ (1, 33) = 8.417, p=0.0066; Holm-Sidak *post-hoc* test. **(i)** Quantification of the discrimination index in the object location test in P22 WT and Dp(16) mice following vehicle or Ruxolitinib treatment. Bars represent the average discrimination index of all analyzed animals ± SEM, and circles represent the

single data points for each animal. **p<0.01; Two-Way ANOVA, $F_{Interaction}$ (1, 19) = 9.103, p=0.007; Holm-Sidak *post-hoc* test.

Microglial defects are also present in the brains of persons with DS

To verify whether our findings reflect the human condition, we analyzed the state of microglial activation in postmortem hippocampi from individuals with DS and age-matched controls (Table 3). We first investigated the expression of Iba1 as a marker of microglia activation (Arcuri et al., 2017; Hanisch and Kettenmann, 2007; Sipe et al., 2016) *via* western blot. We found increased expression of Iba1 in brain lysates from hippocampi of individuals with DS compared to controls (Fig. 24a), reflecting our findings in the Dp(16) mice (Fig. 11a). Next, to visualize the morphology of microglia, we took advantage of immunohistochemistry and stained brain slices from another set of individuals with DS and age-matched controls with an Iba1 antibody. This allowed us to perform the same analysis of microglial morphology already performed with Dp(16) animals (Fig. 8). Remarkably, we found that human DS microglia had enlarged cell bodies and, similar to Dp(16) animals, the enlargement concerned the whole microglial population (Fig. 24b-d). Moreover, the Sholl analysis revealed that human DS microglia also had ramification deficits (Fig. 24e), again in agreement with data in Dp(16) mice. A subsequent skeleton analysis revealed a decreased number of ramifications (Fig. 24f), which were, however, longer on average (Fig. 24g).

Altogether, these results suggest that the microglial dysfunction observed in Dp(16) mice is also present in persons with DS.

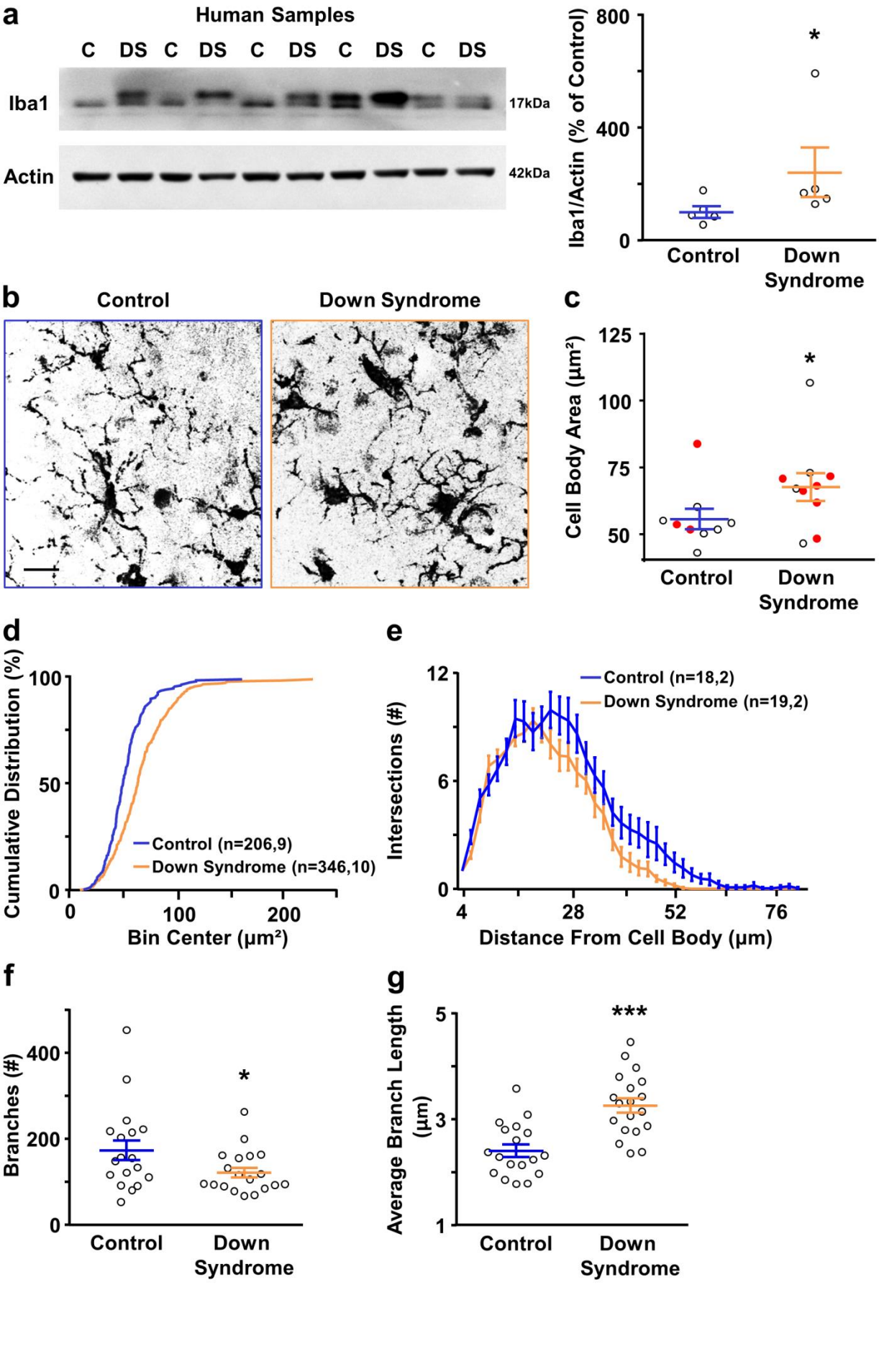
a
Human Samples
C DS C DS C DS C DS C DS
Iba1
17kDa
Actin
42kDa
Iba1/Actin (% of Control)
800
400
0
*
Control
Down Syndrome
b
Control
Down Syndrome
c
Cell Body Area (µm²)
125
100
75
50
*
Control
Down Syndrome
d
Cumulative Distribution (%)
100
50
0
Control (n=206,9)
Down Syndrome (n=346,10)
0
100
200
Bin Center (µm²)
e
Intersections (#)
12
6
0
Control (n=18,2)
Down Syndrome (n=19,2)
4
28
52
76
Distance From Cell Body (µm)
f
Branches (#)
400
200
0
*
Control
Down Syndrome
g
Average Branch Length (µm)
5
3
1
***
Control
Down Syndrome

Figure 24. Microglial alterations are present in brains from persons with DS. (a) Representative immunoblots on protein extracts from lysates of hippocampi obtained from age and sex-matched controls and persons with DS (*left)*. Quantification of Iba1 protein levels normalized to Actin immunoreactivity (*right*). Bars represent the average percentage of Iba1 levels in DS over control hippocampi in all individuals ± SEM, and circles represent the single data points for each person. Data were averaged across 3 independent experiments. * p = 0.027; Unpaired One-tailed Mann Whitney test U=3. **(b)** Representative confocal images of Iba1-stained hippocampal slices from a control and an individual with DS with no signs of amyloid deposition nor diagnosis of Alzheimer's disease (individual 13202 in Supplementary Table 3). Scale bar: 20µm. **(c)** Quantification of the cell body area of microglial cells in experiments as in b. Bars represent the average of the microglia cell body areas of all analyzed individuals ± SEM, and circles represent the single data points of the cell averages for each individual (24-60 cells, 3-7 slice per individual). Red circles represent people with hippocampal signs or diagnosis of Alzheimer's disease, as defined in Table 3. * p = 0.0423; Unpaired One-tailed Student's T-test, t=1.83, df=17. **(d)** Cumulative distribution of the microglial cell body area of all analyzed cells, calculated as the percentages of the cells inside each bin area. The two distributions are significantly different (Kolmogorov-Smirnov Test, p<0.001). Numbers in parenthesis: number of cells, and number of individuals analyzed. **(e)** Sholl analysis of microglial cells in images as in b processed as in Fig. 8f. Data are expressed as average number of intersections at each distance from the cell bodies of all analyzed cells ± SEM. The statistical analysis revealed a significant effect of the diagnosis of DS (Two-Way ANOVA, $F_{Diagnosis}$ (1, 1443) = 38.64, p < 0.0001). Numbers in parenthesis: cells, and analyzed individuals (4-10 slices per individual). Only slices from individuals 13149, 13202, 13235 and 13250 as in Table 3 had sufficient quality of Iba1 1 staining to ensure correct analysis of microglial ramifications and were analyzed. **(f)** Quantification of the number of branches per microglial cell in images as in b processed as in Fig. 8i. Bars represent the average number of branches per microglial cell ± SEM in all analyzed individuals, and circles represent the single data points of the cell averages for each individual (9-10 cell/individual; 4-10 slices per individual from the same individuals in e). * p<0.05; Unpaired One-tailed Mann-Whitney test, U=115. **(g)** Quantification of the average length of branches per microglial cell in images as in b processed as in Fig 8i. Bars represent the average of branch length per microglial cell ± SEM in all analyzed individuals, and circles represent the single data points of the cell averages for each individual (9-10 cells/individual; 4-10 slices per individual from the same individuals in e). ***p<0.01; Unpaired Two-Tailed *t*-test, t=4.69, df=35.

DISCUSSION

Microglial activation in DS

Recent evidence has indicated a high overall level of inflammation (Sullivan et al., 2017) and a high incidence of hematological and autoimmune diseases in DS (Alexander et al., 2016; Kinik et al., 2006). This is due to increased levels of circulating pro-inflammatory molecules, which is particularly marked in the brain (Wilcock and Griffin, 2013). Signs of high inflammation have also been observed in animal models of DS (Fructuoso et al., 2018; Gally et al., 2018; Guedj et al., 2015). However, a detailed investigation of microglia and their role in cognition in DS is still lacking. To address this issue in DS animal models, we preferred the Dp(16) mouse to the more commonly used Ts65Dn mouse. Indeed, contrary to Ts65Dn mice, Dp(16) mice do not show marked prenatal signs of defective neuronal precursor proliferation and neurogenesis (Goodliffe et al., 2016). These are *per se* a cause of cognitive defects in Ts65Dn mice (Parrini et al., 2017) and could be a confounding factor when investigating the role of microglia in cognitive performance. Indeed, we hypothesize that the alerted microglial phenotype we observed in Dp(16) might be exacerbated in Ts65Dn due to the increased amount of neuronal precursors phagocyted during development. We focused our investigation mostly on the hippocampus of Dp(16) mice, as microglia play a pivotal role in the correct formation and function of the hippocampus in WT animals (Riazi et al., 2015; Sierra et al., 2010; Tremblay et al., 2011), and this structure is strongly altered in DS (Alldred et al., 2018; Parrini et al., 2017; Raveau et al., 2018; Vacano et al., 2018; Velazquez et al., 2013). In addition, extensive evidence in the literature exists that hippocampal-related cognitive functions are the most impaired in people and animal models of DS (Deidda et al., 2015; Parrini et al., 2017). Here, we further characterized hippocampal cognitive function in the poorly investigated Dp(16) mouse. We restricted our investigation to the third postnatal week

of life (P22) because the main postnatal developmental stages are completed, but the brain still retains a good level of plasticity at this age (Le Magueresse and Monyer, 2013; Zhang, 2004).

At P22, the microglia in the Dp(16) hippocampus showed morphological signs of activation, such as enlarged cell bodies and decreased ramifications, when compared to those of WT littermates. This observation is consistent with the defects in microglial activation and branching area that have been previously described in Ts65Dn mice (Hunter et al., 2004; Mulet et al., 2017; Rueda et al., 2018). In Dp(16) mice, we also observed an active microglial phenotype in the somatosensory cortex, although to a milder extent than in the hippocampus. This could be due to the different gene expression profiles of the microglial populations residing in the two brain regions. Indeed, hippocampal microglia exist in a more immune vigilant state than their cortical counterparts (Grabert et al., 2016). Therefore, the hippocampal microglial population could possibly respond more strongly to the increased level of inflammation observed in DS (Broers et al., 2014; Fructuoso et al., 2018; Gally et al., 2018; Sullivan et al., 2017). Interestingly, microglial pathology (i.e., increased activation) is also present in other neurodevelopmental disorders, such as Rett Syndrome, autism and schizophrenia (Salter and Stevens, 2017). Indeed, elimination of the CX_3CR_1 signaling (and therefore altering microglia only) generates strong autistic-like behaviors.

Furthermore, in agreement with the idea that the peculiar morphology of the trisomic microglia is reflective of an activated state due to chronic inflammation in DS, we found increased levels of Iba1, cytokines and LAMP1 in the hippocampus of Dp(16) mice. Iba1 is a calcium-binding protein that is constitutively expressed by resting microglia. However, its expression is increased in concomitance with cytoskeletal remodeling and the consequent changes in cell morphology that occur during microglial activation. Thus, Iba1 is a reliable marker of microglia activation (Bosco et al., 2011; Imai and Kohsaka, 2002; Nilsson et al., 2008).

The overexpression of Iba1 was accompanied by increased levels of cytokines normally secreted by activated microglia, such as IL-1β and IL-6 (Wang et al., 2015). Interestingly, although the vast majority of the cytokines we found upregulated in the hippocampi of Dp(16) mice were pro-inflammatory, two anti-inflammatory cytokines (i.e., IL-4 and IL-10) were also upregulated. Notably, an increased production of IL-10, as a reaction to a chronic inflammatory state, has been described in subjects with DS (Broers et al., 2014). This observation also suggests that aberrant control of the production of anti-inflammatory molecules is present in DS, which contributes to the overall immunological dysregulation. In agreement with our findings, increased IL-1β and IL-6 can strongly alter hippocampal, LTP possibly acting through microglia activation (Riazi et al., 2015). However, we failed to detect any expression of the classical microglial activation marker MHCII (Hayes et al., 1987) in Dp(16) mice. Still, this is not the only example of microglial activation in the absence of increased expression of MHCII (Sipe et al., 2016). For instance, the same happens during the microglia-dependent synaptic elimination necessary for critical-period plasticity (Sipe et al., 2016). Moreover, a non-canonical activation of microglia is also caused by increased neuronal firing, which leads to changes in microglial morphology and physiology with no activation of MHCII (Hung et al., 2010; Kierdorf and Prinz, 2013; Sipe et al., 2016). Interestingly, in the Ts65Dn mouse, GABA signaling contributes to increased excitability of the hippocampus (Deidda et al., 2015). This increased level of excitability could lead to the morphological changes described in the literature in Ts65Dn mice and to the MHCII-independent microglial morphology alterations and increased activation markers described here in the Dp (16) mice. Nevertheless, whether GABAergic signaling positively regulates hippocampal excitability in Dp(16) mice is still unknown.

In agreement with the elevated levels of Iba1 and pro-inflammatory cytokines indicative of microglia activation, we also found increased levels of LAMP1. LAMP1 is a protein that is highly expressed in lysosomes and is upregulated when there is an increase in phagocytosis (Maxfield

and McGraw, 2004) in several cell types, including activated microglia (Tanaka et al., 2013). Interestingly, very prominent defects in the lysosomal pathways were observed in DS (Colacurcio et al., 2018).

Microglia, synaptic elimination and cognitive impairment in DS

Dendritic spine dynamics are necessary for learning and memory (Bosch et al., 2014; Salter and Stevens, 2017). Interestingly, recent evidence indicated that microglia play a pivotal role in remodeling dendritic spines and regulate their activity in brain development and plasticity (Kaur et al., 2017; Salter and Stevens, 2017). Moreover, individuals with DS and DS animal models (i.e., Tc1, Ts1Rh1, Ts65Dn and Ts1Cje mice (Belichenko et al., 2009; Haas et al., 2013; Herault et al., 2017; Torres et al., 2018) present altered spine density possibly due to increased synaptic elimination (Phillips and Pozzo-Miller, 2015). This experimental evidence prompted us to hypothesize that the link between the microglial changes observed in Dp(16) mice and their cognitive deficits may be the action of the hyperactive microglia on dendritic spines. Remarkably, the depletion of defective microglia from the brain parenchyma *via* administration of PLX3397 rescued the dendritic spine number of the functional subtypes, thin and mushroom (Majewska and Sur, 2003; Xu et al., 2018), together with the cognitive performance in Dp(16) mice. Consistently, PLX3397 treatment fully rescued the amplitude and frequency of mEPSCs, which we found altered in Dp(16) mice. Even if the mushroom spine density was not fully rescued, the mESPCs rescue can be explained by the fact that thin spines are also electrophysiologically active. Indeed, thin spines are also nicknamed “learning spines” because they are highly mobile and likely to change shape in response to activity, whereas mushroom spines, also called “memory spines,” are less mobile and more stable (Peebles et al., 2010) Notably, deficits in mEPSCs were observed in a wide number of animal models of neurodevelopmental disorders characterized by high inflammation levels and spine defects such as autism (Wu et al., 2018), Fragile X syndrome (Scharkowski et al., 2018), and Rett syndrome (Xu

and Pozzo-Miller, 2017) as well as the Ts65Dn mouse model of DS (Parrini et al., 2017). Moreover, microglial activation with LPS (a powerful microglia activator; (Chang et al., 2015) elicits deficits in mEPSCs together with a decrease in spine density. Thus, our results together with the literature indicate a relationship between microglial over-activation, spine impairments and cognitive disability in DS and suggest that similar microglia-dependent spine elimination may occur in other neurodevelopmental disorders. Interestingly, in a recent study Spangenberg et al. showed that depletion of microglia by PLX3397 treatment was able to rescue dendritic spine loss and neuronal death together with an overall decrease of neuroinflammation and increase in cognitive performance in a mouse model of AD. This could suggest that microglia may be a target for therapeutic intervention not only in young DS adults, but also later in life when these individuals become prone to developing AD (Spangenberg et al., 2016).

We decided to use drebrin (DBN) as a proxy to study spine density as previously done by other groups (Weitzdoerfer et al., 2001). DBN is an actin-binding protein highly expressed in spines where it exerts a pivotal role in maintenance and maturation, and its levels are drastically decreased in individuals with DS (Shim and Lubec, 2002; Weitzdoerfer et al., 2001) and during inflammation (Rao et al., 2012; Weitzdoerfer et al., 2001). Indeed, the activation of microglia with LPS in microglia-neuron co-cultures led to an extensive decrease in DBN levels in neurons (Xing et al., 2011). Moreover, decreased levels of DBN in experimental animals and in neurons *in vitro* caused a decrease in the density of spines and a shift toward more immature spinal states (Koganezawa et al., 2017; Rao et al., 2012; Takahashi et al., 2006). Accordingly, we found a significant decrease in the level of DBN accompanied by a decrease in the overall spine density, and particularly functional spines (thin, mushroom types; (Risher et al., 2014) in Dp(16) mice. The level of expression of DBN together with the spine density and the cognitive impairment were rescued upon depletion of the aberrant microglia by treatment of trisomic animals with PLX3397.

This result together with the increased interaction between microglia and spine elements we observed by electron microscopy in Dp (16) mice and the increased LAMP1 expression (i.e., increased phagocytic activity of trisomic microglia) sustain our hypothesis that the higher activation state of microglia leads to abnormal synaptic elimination of dendritic spines that in turn causes cognitive deficits in trisomic animals.

Additionally, the hippocampal proteome analysis we performed in Dp(16) and WT mice supports the idea that the difference in the cognitive behavior between the two strains may depend on a defect in spine elimination. Indeed, among the differentially expressed proteins, we singled out 4 significant proteins that fall into the gene ontology (GO) *Memory* category (i.e., integrin alpha 3 (Itga3), sodium/calcium exchanger member 3 (Slc8a3), sortilin-related VPS10 domain containing receptor 3 (Sorcs3) and kalirin (Kln)) and that are all involved in dendritic spine function and structure (Christiansen et al., 2017; Herring and Nicoll, 2016; Kerrisk et al., 2013; Minelli et al., 2007; Youn et al., 2007).

Possible sources of microglial defects in DS

DS is caused by the triplication of a very long stretch of DNA, comprising 110-150 genes in humans (many of which are expressed by microglia (Mrak and Griffin, 2004). In the Dp(16) mouse model, 113 genes are triplicated. Thus, it is very difficult to pinpoint the primary cause of the overall DS immunological dysfunction and the microglial defects we observed in this study. Nevertheless, at least 16 genes that are triplicated in both DS and Dp(16) mice are already known to play a direct role in the regulation of immune system activity (Li et al., 2007); Table 4). For example, the triplicated gene RUNX-1 encodes a transcription factor that plays a central role in microglia differentiation, proliferation and activation (Kierdorf and Prinz, 2013; Patel et al., 2011). In particular, RUNX-1 triplication could make the trisomic microglia highly sensitive to activating

stimuli such as IL-1, which we found increased in Dp(16) animals. Interestingly, the expression of IL-1 is constantly observed as increased also in DS individuals and can lead to microglia activation (Li et al., 1998; Liu et al., 2005; Wilcock and Griffin, 2013), which could generate a positive feedback loop in DS. Moreover, since microglial activation can indirectly lead (*via* IL-1) to an increased expression of the amyloid precursor protein (APP) gene (triplicated in DS and able to increase neuroinflammation *per se*), this would generate a second positive feedback loop that would further sustain microglia activation in the trisomic environment (Mrak and Griffin, 2004; Wilcock and Griffin, 2013).

Microglia in individuals with DS

Our results obtained from the analysis of postmortem brains of adult human subjects with DS suggest increased levels of hippocampal microglial activation, consistent with the chronic high level of inflammation reported in individuals with DS (Broers et al., 2014; Fructuoso et al., 2018; Gally et al., 2018; Sullivan et al., 2017). In particular, we found increased Iba1 expression and morphological alterations. These results were strikingly similar to the ones we observed in the Dp(16) mice. Only a limited number of studies have investigated microglia in individuals with DS, but they mostly focused on the effect of Alzheimer's Disease (AD) on microglia, as virtually all individuals with DS develop symptoms of AD by the age of 40 (Dekker et al., 2017). Thus, in the few studies investigating microglia in individuals with DS, brains with very advanced AD were purposely chosen, and investigations focused on the effect of the amyloid Aβ burden. In these studies, microglia were often found in a senescent state (dystrophic and less responsive to stimuli) similar to what is described in AD (Streit et al., 2014; Xue and Streit, 2011). Conversely, of our 15 brain samples of individuals with DS, only 3 presented diagnose of AD (no indication of the progression of the disease), and 3 presented only some anatomical signs of AD (low burden of Aβ or fibrillary tau). Notably, the presence or absence of AD or signs of AD did not influence the

morphological abnormalities we observed in our DS samples. Indeed, the microglia from the DS brains with AD or signs of AD showed the same level of impairment of the microglia from non-AD brains. This could be because the trisomy itself activates microglia, and a low burden of Aβ/ fibrillary tau or AD possibly not in a very advanced state cannot further change the morphology of those cells. On the other hand, the fact that we could not find any difference between the microglia of the 5 healthy controls and the 3 controls with some signs of AD would just favor the hypothesis that, unless AD is in a very late progression, microglia do not show signs of activation.

Our study investigated microglia only at late postnatal ages. Nevertheless, some scant evidence of defective microglia exists for DS fetuses. Indeed, only a few studies out of the many performed on DS fetuses addressed microglia. These studies showed a decreased microglia cell density in the developing temporal cortex and an increase in the developing prefrontal cortex (Kanaumi et al., 2013; Wierzba-Bobrowicz et al., 1999; Xue and Streit, 2011). Nevertheless, none of these studies addressed microglial morphology. Moreover, whether these changes in the density of microglia in DS fetuses could play a role in the paucity of neurons and the dendritic spine deficits characteristic of DS (Kanaumi et al., 2013) is still not known.

Anti-inflammatory treatments to improve cognitive impairment in DS

Our conclusions that the cognitive impairments in Dp(16) mice depended on the high inflammation levels in these animals were strengthened by the results in mice treated with an inhibitor of the JAK1/2 signaling cascade (ruxolitinib), an essential pathway for immunological activation. Treatment with ruxolitinib significantly rescued the behavioral phenotype in Dp(16) mice and the microglial branching phenotype. Nevertheless, ruxolitinib failed to rescue microglial cell/body size. Given its importance for immunological signaling, it is sensible to expect that there are mechanisms to compensate for a deficit of the JAK/STAT signaling (Seif et al., 2017). Therefore,

the only partial rescue of microglial morphology we observed upon ruxolitinib is not surprising. On the other hand, the fact that ruxolitinib treatment rescued the cognitive performances in Dp(16) animals (although seemingly to lower levels than APAP) may be because it is the physical interaction between the ramifications of the microglia and the dendritic spines themselves (rather than the activated state of microglia with increased body size) that is crucial for dendritic spine remodeling.

Acetaminophen as a treatment for cognitive impairment in DS

In this study, we showed that treatment with acetaminophen (APAP) fully rescued the morphological defects of trisomic microglia and concomitantly decreased the pro-inflammatory cytokines in the hippocampus of Dp(16) mice. Moreover, in our experiments, APAP treatment successfully rescued the spine density and mEPSCs, the levels of drebrin, and the cognitive performance of trisomic animals. APAP is a nonsteroidal anti-inflammatory drug (NSAID) that decreases the synthesis of prostaglandins (PGE) and has antipyretic and analgesic effects. Although APAP is considered not to have a solid anti-inflammatory effect (Jozwiak-Bebenista and Nowak, 2014), it strongly inhibits PGE production by microglial cells, already at low concentrations (Ajmone-Cat et al., 2010; Greco et al., 2003). In addition, APAP is active in the central nervous system (Flower and Vane, 1972; Jozwiak-Bebenista and Nowak, 2014), and although its effects on cognition in humans are not known, APAP can indeed change complex human behaviors such as social anxiety (Dewall et al., 2010; Fung and Alden, 2017), empathy (Mischkowski et al., 2016) and social well-being (Chibnall et al., 2005).

Although APAP is well known for being a potential hepatotoxic drug in the case of overdose, it is extremely safe even at relatively high doses (up to 4 grams daily for adults). Indeed, even at high doses, it lacks the gastric side effects typical of classical NSAIDs (Ajmone-Cat et al., 2010). Thus,

APAP is a good candidate for drug repurposing for long-term treatments (Strittmatter, 2014). In addition, APAP is considered so safe that it is routinely prescribed as an anti-inflammatory treatment to pregnant women. Therefore, APAP could also be a good candidate as a drug treatment at early stages of development. Interestingly, APAP was able to rescue ASD-like behaviors including sociability in animal models of DS, suggesting that it could be an interesting treatment for neurodevelopmental disorders (Gould et al., 2012; Kim et al., 2018). Since DS is a neurodevelopmental disorder, the treatment of DS subjects during gestation could potentially lead to even more positive outcomes on their cognitive performance. Nevertheless, our study only focused on late postnatal development, and further studies during perinatal ages will be necessary to address whether an earlier treatment with APAP could be beneficial in DS. Moreover, recent studies on WT animals and humans has begun to raise some concerns about the safety of APAP during gestation and early postnatal stages because it can influence physiological brain development (Blecharz-Klin et al., 2015; Blecharz-Klin et al., 2018; Good, 2018; Philippot et al., 2017; Schultz and Gould, 2016; Viberg et al., 2014). However, these detrimental effects on CNS development may be due to specific actions of APAP on WT embryos and may not apply to DS. Indeed, in our current study, APAP treatment had an opposite effect on the WT microglia, dendritic spines and mEPSCs in comparison to Dp(16) mice, and consistently decreased cognitive performance in WT mice. In line with our results, it was previously shown that the administration of APAP to WT rats caused a significant decrease in spatial memory, social behavior and exploratory behavior (Blecharz-Klin et al., 2018; Ishida et al., 2007). Moreover, it was recently shown that a single administration of APAP (100mg/kg) caused deficits in memory recognition and ERK phosphorylation in the hippocampus of mice (Milewski and Orr, 2018). Remarkably, Minocycline, a non-NSAID anti-inflammatory drug, administration causes a paradoxical increase in the alertness of microglial cells in a similar fashion we observed for APAP (Arnoux et al., 2014).

This could indicate the existence of a common mechanism of increased alertness in the presence of xenobiotics that is, at least in our case, genotype-dependent. The effect of APAP on WT animals may be due to unknown off-targets and may be independent of *a direct* effect on microglia. Accordingly, APAP had no effect on the levels of cytokines in WT animals. On the other hand, the correlation between overactive microglia, impaired spine density and function, and decreased cognition that we found in WT animals treated with APAP still suggests an active role of microglia at some level in the behavioral impairment. This active role of microglia in the defective cognition of APAP-treated WT animals could be *indirectly* caused by an off target effect of APAP treatment. For example, a high dose of APAP can be toxic to neurons, which in turn could activate microglia (Posadas et al., 2010). Thus, it is possible that the dose we used in our experiments (100 mg/kg/day for 3 days) had a toxic effect on a WT organism (perhaps through specific toxicity to neurons), although the same dose had a positive effect in a trisomic environment.

The different effects of APAP treatment on WT and trisomic animals call for some considerations on the current methods of validation of the efficacy of new pharmacological therapies (i.e., clinical trials). Indeed, according to the Food and Drug Administration (FDA), approximately 30% of new drugs are discontinued after phase I clinical trials (https://www.fda.gov/ForPatients/Approvals/Drugs/ucm405622.htm), which involves an initial testing of the safety, side effects, best dose, and formulation method for the drug in healthy volunteers. Based on our observations with APAP, drug treatments could have completely different outcomes based on the presence or absence of morbidity. This could mean that potentially valuable drugs for the treatment of certain conditions are erroneously discarded during phase I clinical trials because of the appearance of adverse effects in healthy volunteers, which might not be reproduced in patients.

Concluding remarks

Our study proposes microglial dysregulation as one of the causes of the cognitive deficits in DS. In particular, we hypothesize that the hyperactive state of microglia, on a background of chronic neuroinflammation, causes a profound alteration in the functionality of neuronal circuits *via* hyper-activation of synaptic elimination, thus leading to cognitive deficits. Remarkably, the use of APAP (an over-the-counter anti-inflammatory drug) is able to fully recover the aforementioned deficits in Dp(16) mouse model of DS. Thus, our results open up to the possibility of repurposing anti-inflammatory drugs for the treatment of cognitive deficits in persons with DS in the future.

MATERIALS AND METHODS

All care of animals and experimental procedures were conducted in accordance with IIT licensing and were approved by the Italian Ministry of Health. All animals were housed in a climate-controlled animal facility (22 ± 2°C) and maintained on a 12 h light/dark cycle with *ad libitum* access to food and water. The Dp(16)1Yey/+ animals were bought from The Jackson Laboratory (B6.129S7-Dp(16Lipi-Zbtb21)1Yey/J, catalog No 013530) and were used to create a colony by mating Dp(16) males with C57BL6/J females.

Drug treatments. PLX3397 (Pexidartinib) was purchased from Selleckem (catalog No. S7818). The powder was dissolved in Dimethyl Sulfoxide (DMSO; Sigma-Aldrich, catalog No 276855) to generate an 83mg/mL (198.65 mM) solution. The solution was then added to pulverized mouse chow at a concentration of 445 mg/kg of chow and given to animals *ad libitum* from P15 to P22. The final dosage of around 4.7 mg total of drug/mouse over the 7 days of treatment was calculated on an average of 1.5 g of chow consumed by each mouse/day (Bachmanov et al., 2002). Acetaminophen (APAP) was purchased from Sigma-Aldrich (catalog No A7085). The powder was dissolved in DMSO to generate a 500mg/mL (3.3M) stock solution and subsequently diluted in saline (NaCl 0.9% w/v) to generate a 10mg/mL (66.15 mM) solution. This solution was injected intraperitoneally (IP) to animals with a dosage of 100mg/kg (10µL/g of solution for a total of 2% DMSO) daily from P20 to P22. Ruxolitinib was purchased from Selleckem (catalog No. S1378). The powder was dissolved in DMSO to generate a 61mg/mL (199.1mM) stock solution and subsequently diluted in saline (NaCl 0.9% w/v) to generate a 1.25mg/mL (4.08 mM) solution. This solution was injected subcutaneously to animals with a dosage of 50mg/kg (40µL/g of solution for a total of 2% DMSO) twice a day from P20 to P22. Due to the insolubility of the Ruxolitinib-DMSO solution in saline, a light sonication was applied until full solubility was obtained. The solution was kept in ice during sonication to avoid overheating.

All injected drugs were dissolved in the same vehicle (2% DMSO v/v in Saline). To decrease the number of utilized animals in agreement with ethic directions from the Italian Ministry of Health, all vehicle treated animals from all experiments were pulled together. PLX3397-treated animals were compared to the 2% DMSO treated animals as well (refer to the Statistical methods section for further information on how these data were analyzed). For every acetaminophen or ruxolitinib-treated litter, at least one animal of each strain was treated with vehicle (except for 3 cases out of 19 total where the number of animals in a given litter did not allowed for such precaution and only 1 or no controls were assigned to the litter).

Slice histology, immunostaining, image acquisition and analysis. P22 brains were fixed by transcardial perfusion with PBS 1X followed by PFA solution (4% w/v in PB). Then, brains were cryopreserved in sucrose (30% w/v) and sectioned coronally in 50 µm thick slices with a microtome-refrigerator (Micron HM 450 Sliding Microtome equipped with Freezing Unit Micron KS34, Thermo Scientific).

For immunostaining, an antigen retrieval protocol was applied on free-floating slices. In brief, slices were incubated for 30 minutes in Sodium citrate buffer (10 mM Sodium citrate, 0.05% Tween 20, pH 6.0) at 90°C and subsequently let cool down to room temperature and washed in PBS1X. Slices were then permeabilized and blocked with PBS containing 0.3% Triton X-100 and 10% NGS. Primary antibodies were incubated in PBS containing 0.3% Triton X-100 and 5% NGS overnight [rabbit anti-Iba1, 1:300 (WAKO, catalog No. 019-19741), rat anti-LAMP1, 1:300 (Santa Cruz Biotechnology, catalog No. sc-19992), rat anti-MHCII, 1:100 (Santa Cruz Biotechnology, catalog No. sc-59322)]. Immunostaining was detected using Alexa 488 (for Iba1) or Alexa 543 (for LAMP1 and MHCII) fluorescent secondary antibody (Invitrogen), 1:600, incubated in PBS containing 0.3% Triton X-100 and 5% NGS. Slices were counterstained with Hoechst (2,5 µg/µL;

Sigma). All slices were mounted in Vectashield Mounting Medium (Vector Laboratories, Burlingame, CA).

For microglial cell count and morphology analysis, a stack of images spanning the whole thickness of the slice (1 µm thick z-stacks) from stained hippocampal slices were acquired using a confocal laser-scanning microscope (TCS SP5; Leica Microsystems, Milan, Italy) equipped with a 40x (NA 1.25) immersion objective and projected on a 2D image. One randomly chosen slice per animal was acquired and cells from DG, CA1 and CA3 areas from the hippocampus were chosen in a balanced manner. For the somatosensory cortex cells from all layers were selected in a balanced manner. For cell count, the number of cells was divided by the total area of the acquired field to represent cell density. For the calculation of the cell-body area, the measurements were performed using the freehand selection tool in ImageJ. Sholl analysis was performed as previously described (Sipe et al., 2016). Briefly, cells were cropped and thresholded to generate a binary (black and white) image. The background was manually cleaned for each cell and the ImageJ plugin Sholl Analysis (Ferreira et al., 2014) was used to perform the analysis (starting radius: 4µm, ending radius: 70µm, radius step size: 2µm, radius span: 0µm). For skeleton analysis, the same binary image created for Sholl Analysis was used. The image was skeletonized using the ImageJ Plugin Skeletonize3D (Lee T.C., 1994) and was subsequently analyzed using the plugin AnalyzeSkeleton (Arganda-Carreras et al., 2010).

For the analysis of MHCII/Iba1 staining co-localization area, a stack of images spanning the whole thickness of the slice (0.5 µm thick z-stacks) from stained hippocampal slices were acquired using a confocal laser-scanning microscope (TCS SP5; Leica Microsystems, Milan, Italy) equipped with a 63x (NA 1. 5) immersion objective and projected on a 2D image. Each channel (Iba1 and MHCII) was thresholded to generate a binary (black and white) image using ImageJ. The background of Iba1 binary image only was manually cleaned to ensure that only one cell was present.

Subsequently, the two images were merged, converted to 32-bit and thresholded again to generate a binary image of only the pixels that came from both MHCII and Iba1 images. The area of the double positive pixels was calculated and divided by the area of the Iba1 positive pixels only for normalization. One randomly chosen slice per animal was acquired.

Western Blotting. All hippocampus samples were lysed in RIPA buffer (150 mM NaCl, 50 mM HEPES, 0.5% NP40, 1% Sodiumdeoxycholate). After 30 minutes on ice, the lysates were clarified by centrifugation for 20 minutes at 16,000g. The protein samples were measured via Pierce BCA assay (Thermo-Fisher, Catalog No. 23225). For protein identification and relative quantification *via* Western blotting, a proper volume of sample containing an equal amount of proteins was diluted with 25% NuPAGE™ LDS Sample Buffer (4X; Thermo-Fisher, Catalog No. NP0007) and 5% 1,4-Dithiothreitol (DTT; equivalent of 50mM, Sigma-Aldrich, Catalog No. DTT-RO Roche) and loaded onto NuPAGE™ 4-12% Bis-Tris Midi Protein gels (Thermo-Fisher, Catalog No. WG1402BOX). The proteins were then transferred onto nitrocellulose membrane (Sigma-Aldrich, catalog No. GE10600001) at 200mA overnight at 4◦C. The primary antibodies [rabbit anti-Iba1 1:1000 (WAKO, catalog No. 016-20001), rat anti-LAMP1, 1:500 (Santa Cruz Biotechnology, catalog No. sc-19992), mouse anti-Drebrin 1:600 (Enzo Lifesciences, catalog No. ADI-NBA-110-E), chicken anti-GAPDH 1:2000 (Merck Millipore, catalog No AB2302) and rabbit anti-Actin 1:2500 (Sigma-Aldrich, catalog No A2066)] were then applied overnight in a blocking buffer (20 mM Tris, pH 7.4, 150 mM NaCl, 0.1% Tween 20, and 5% nonfat dry milk). The HRP-conjugated secondary antibodies [Thermo-Fisher, anti-mouse (catalog No 31430), anti-rabbit (catalog No 31460), anti-rat (catalog No 31470) or anti-chicken (catalog No PA1-28798)] were all used in a ratio of 1:2500. The signal was detected using the SuperSignal™ West Pico PLUS Chemiluminescent Substrate detection system (Thermo-Fisher, catalog No 34578). Images were acquired by the Image Quant LAS 4000 mini image system (General-Electrics Healthcare) and protein quantification was performed by measuring the optical

density of the specific bands with the Image Quant TL software (General-Electrics Healthcare). Samples from all experimental groups were loaded on each experiment and normalized to the WT treated with vehicle. For statistical analysis, normalized data across independent experiments were used together.

Cytokine assay. The mouse Inflammation Array C1 was purchased from Ray Biotech (catalog No AAM-INF-1). The hippocampal samples were lysed in RIPA buffer in the same way as for western-blotting. The protein quantification was performed by Pierce BCA assay (Thermo-Fisher, Catalog No. 23225), following manufacturer's instructions. The arrays were incubated with the hippocampal lysate over night at 4°C, then incubated with biotinylated secondary antibodies and HRP (both provided together with the arrays) following manufacturer's instructions. The bioluminescence emitted by the arrays were acquired by the Image Quant LAS 4000 mini image system (General-Electrics Healthcare) and dot quantification was performed by measuring the optical density of each dot using the oval tool in ImageJ. The same area was used to quantify all the arrays. The data were analyzed following manufacturer's instructions. In brief, the arrays were analyzed in pairs where one of the arrays was used as reference (array X below) and the other was expressed as fold change (array Y below). For each dot, the following formula was used: X(Ny) = X(y)*P1/P(y), where P1 is the mean signal for the positive control on the reference array (here called array X), P(y) is the mean signal for the positive control on the other array of the pair (here called array Y), X(y) is the raw quantification of a dot being analyzed and X(Ny) is the normalized quantification of the same dot. X(Ny) was then divided by the same dot's signal on array X giving a fold change quantification for each single dot.

Behavioral experiments. The behavioral experiments were performed between P20 and P22 on both male and female animals.

The *Novel Object Recognition test* (NOR) was performed as previously described(Deidda et al., 2015). In brief, a gray acrylic arena (44 × 44 cm) was used. On the day before the NOR test, the mice were allowed to become habituated to the apparatus by freely exploring the open arena for 15 min. During the acquisition sessions, three different objects different in shape, color, size and material were placed into the arena, and the mice were allowed to explore for 15 min (Fig. 25a). The object exploration and preference was evaluated during these sessions to rule out any eventual intrinsic bias (Fig. 25b-c). The testing occurred 24 h later in the same arena. In the test, one of the objects used in the acquisition session was replaced by a novel object, and the mice were allowed to explore freely for 15 min. The objects were counterbalanced between the sessions and were cleaned with 70% ethanol after each trial as well as the arena. The exploratory behavior toward an object was defined as direct contact with the object by the animal's mouth, nose or paws or as an instance when the animal approached the object so that its nose was within 1 cm of the object. Any indirect or accidental contact with the objects was not included in the scoring. The time spent exploring each object, expressed as a percentage of the total exploration time, was measured for each trial. The discrimination index was calculated as the difference between the percentage of time spent investigating the novel object and that of time spent investigating the familiar objects: Discrimination Index = ((Novel Object Exploration Time/Total Exploration Time) × 100) − ((Familiar Object Exploration Time/Total Exploration Time) × 100).

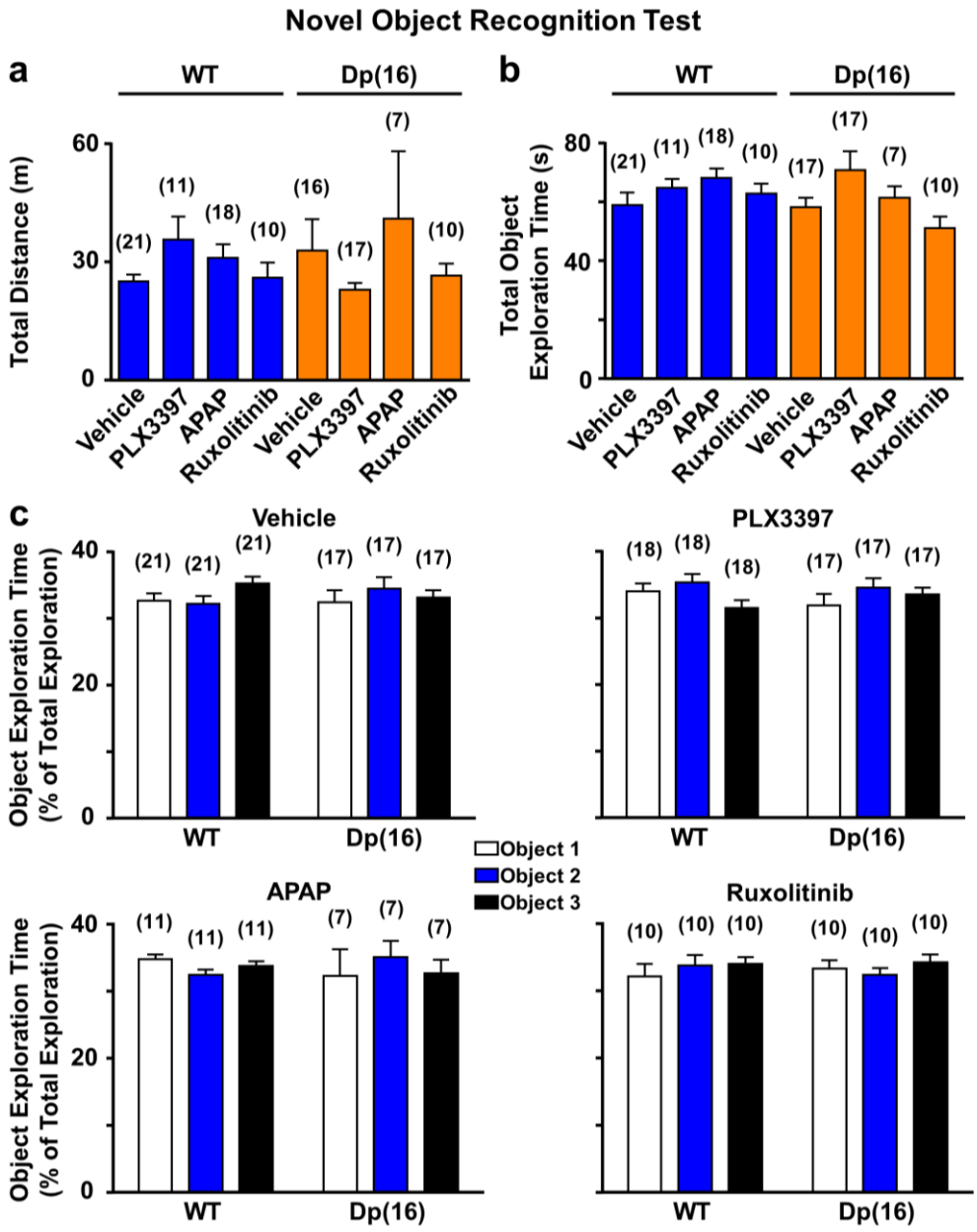

Figure 25. Covered distance, exploration time and object preference in the novel object recognition test. (a) Quantification of the total covered distance during the habituation phase of the novel object recognition test by animals treated with vehicle, PLX3397, APAP, or Ruxolitinib. No significant differences were found among the groups. Bar plots represent the average covered distance ± SEM. Numbers in parenthesis: analyzed animals. **(b)** Quantification of the total object exploration time in the acquisition phases of the novel object recognition test by animals treated with vehicle, PLX3397, APAP, or Ruxolitinib. No significant differences were found among the groups. Bar plots represent the average object exploration time ± SEM. Numbers in parenthesis: analyzed animals. **(c)** Quantification of the percentage of time spent exploring the three objects during the acquisition phase by animals treated with vehicle, PLX3397, APAP, or Ruxolitinib. No

significant biases were found among the groups. Bar plots represent the average percentage of exploration for each object ± SEM. Numbers in parenthesis: analyzed animals.

The *Object Location Test* (OLT) was performed as previously described (Deidda et al., 2015). In brief, a gray acrylic arena (44 × 44 cm) was used. On the day before the NOR test, the mice were allowed to become habituated to the apparatus by freely exploring the open arena for 15 min (Fig. 26a). The next day, the mice were exposed to two identical objects for 15 min during the acquisition phase. The object preference was evaluated during this session to rule out any eventual intrinsic bias (Fig. 26b-c). The testing occurred 24 h later in the same arena. During the trial session, one of the objects was moved to a novel location, and the mice were allowed to explore the objects for 15 min. The objects and the arena were cleaned with 70% ethanol after each trial. The time mice spent exploring each object was measured. The exploratory behavior toward an object was defined as direct contact with the object by the animal's mouth, nose or paws or as an instance when the animal approached the object so that its nose was within 1 cm of the object. Any indirect or accidental contact with the objects was not included in the scoring. The time spent exploring each object, expressed as a percentage of the total exploration time, was measured for each trial. The discrimination index was calculated as the percentage of time spent investigating the object in the new location minus the percentage of time spent investigating the object in the old location: Discrimination Index = ((New Object Location Exploration Time/Total Exploration Time) × 100) − ((Old Object Location Exploration Time/Total Exploration Time) × 100). The WT animals treated with APAP showed a small intrinsically preference for object 1 (on average animals explored 5.04% more object 1 than object 2 during acquisition). The bias did not affect the results on the testing day. The DI obtained from APAP treated WT animals in which the object in

the new location was object 1 as opposed to object 2 (3.43±SEM with N=5 vs. 7.73±SEM with N=7), was not significantly different.

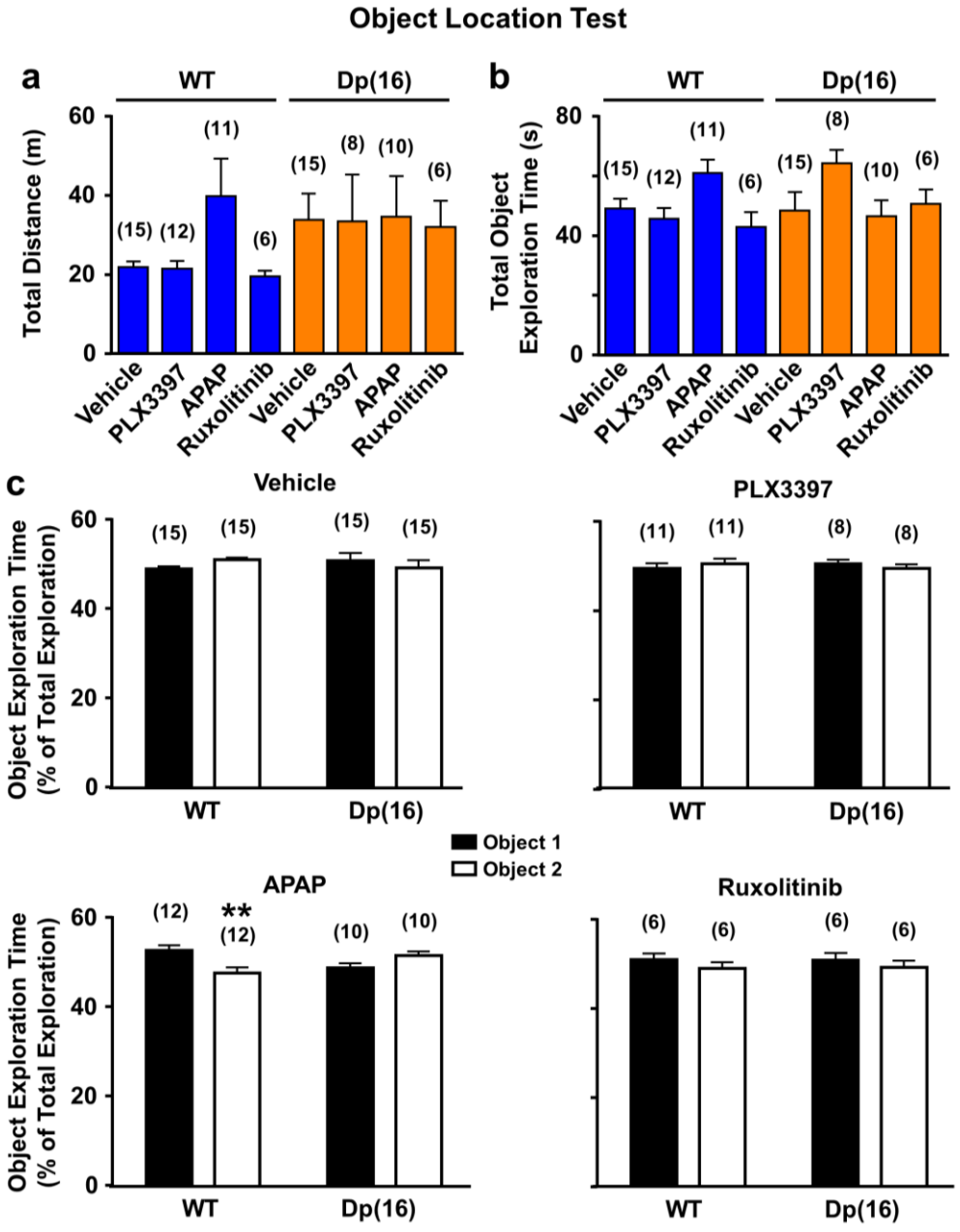

Figure 26. Covered distance, exploration time and object preference in the object location test. **(a)** Quantification of the total covered distance during the habituation phase of the object location test by animals treated with vehicle, PLX3397, APAP, or Ruxolitinib. No significant differences were found among groups. Bar plots represent the average covered distance ± SEM. Numbers in parenthesis: analyzed animals. **(b)** Quantification of the total object exploration time in the acquisition phases of the object location test by animals treated with vehicle, PLX3397, APAP, or

Ruxolitinib. No significant differences were found among groups. Bar plots represent the average object exploration time ± SEM. Numbers in parenthesis: analyzed animals. **(c)** Quantification of the percentage of time spent exploring the three objects during the acquisition phase by animals treated with vehicle, PLX3397, APAP, or Ruxolitinib. Bar plots represent the average percentage of exploration for each object ± SEM. Only WT animals treated with APAP showed a significant bias *vs* object 1 (** $p<0.01$; Two-Way ANOVA, $F_{Interaction}$ (1, 40) = 10.95, p=0.0022; Holm-Sidak *post-hoc* test). Numbers in parenthesis: analyzed animals.

In all the behavioral tests, both male and female animals were used. No difference in performance based on the sex of the animals was observed. Different sets of animals were used for NOR and OLT.

Golgi-Cox staining, image acquisition and analysis. The animals were perfused transcardially with 0.9% saline. Whole brains were dissected and immersed in the Golgi-Cox solution (5% potassium dichromate, 5% mercuric chloride and 5% potassium chromate) for 35 days. Then, the brains were transferred to a 30% sucrose solution and stored in the dark at 4°C. 200 µm-thick coronal slices were cut at room temperature with a microtome (Microm HM 450 Sliding Microtome) and transferred onto 1% gelatin-coated slides to initiate the staining process in humidified chambers. Ammonium hydroxide was applied for 10 minutes. Next, the slices were incubated in an increasing grade of ethanol (50%, 75%, 95% and 100%), then in xylene for 30 minutes, and finally mounted in DPX-Mounting medium (Sigma-Aldrich, Catalog No 06522). A stack of 80-150 focal images (1 µm thick z-stacks) per cell (for a total of 5 cells per animal) were acquired from randomly chosen cortical slices at the level of the somatosensory cortex on a Neurolucida microscope equipped with the software Neurolucida (MicroBrightField) and a 100X objective (NA 1.3). On each image stack, the apical dendrite of a neuron was visually identified, and spines were counted on the whole visible length of 3 collateral dendrites for each image and divided by this length using the

Reconstruct software, which allows for the measurement of spine length and width for an unbiased classification of spine types (Risher et al., 2014). The densities of spines for each dendrite were averaged per each image stack. All the chemicals were purchased from Sigma-Aldrich, unless otherwise specified.

***In vitro* electrophysiology.** P22-P30 mice were anesthetized with isoflurane and transcardially perfused with ice-cold cutting solution containing: 200 mM sucrose, 4 mM $MgCl_2$, 2.5 mM KCl, 1.25 mM NaH_2PO_4, 0.5 mM $CaCl_2$, 25 mM $NaHCO_3$ and 25 mM D-glucose (~300 mOsm, pH 7.4, oxygenated with 95% O2 and 5% CO2). Brains were removed and immersed in cutting solution. 270µm-thick coronal slices (cut with VT1000S Leica Microsystem vibratome) were allowed to recover for 1 hour at 35°C in a solution containing: 117 mM NaCl, 2.5 mM KCl, 1.25 mM NaH_2PO_4, 3 mM $MgCl_2$, 0.5 mM $CaCl_2$, 25 mM $NaHCO_3$ and 25 mM glucose (~310 mOsm, pH 7.4, oxygenated with 95% O_2 and 5% CO_2). Recordings were performed in visually-identified CA1 neurons of the hippocampus at room temperature in artificial cerebrospinal fluid (ACSF) composed of: 117 mM NaCl, 2.5 mM KCl, 1.25 mM NaH_2PO_4, 1 mM $MgCl_2$, 2 mM $CaCl_2$, 25 mM $NaHCO_3$ and 25 mM glucose (~310 mOsm, pH 7.4, oxygenated with 95% O_2 and 5% CO_2). Patch pipettes were made from thick-wall borosilicate glass capillaries (Sutter Instrument, catalog No B150-86-7.5). The pipettes (5-7 mΩ) were filled with intracellular solution containing: 130 mM K-gluconate, 10 mM HEPES, 7 mM KCl, 0.6 mM EGTA, 4 mM Mg2ATP, 0.3 Mm Na3GTP, 10 mM Phosphocreatine. The pH was adjusted to 7.3 with HCl. Whole-cell recordings from CA1 neurons were performed only when the series resistances were in the range of 10–25 mΩ. Three-minute recordings of mEPSCs were performed after a 10-minute bath application of 20 µM of Bicuculline methiodide (HelloBio, catalog No HB0893) and 1 µM Tetradotoxin (TTX; HelloBio, catalog No HB1035) to isolate excitatory events. Data, filtered at 0.1 Hz and 5 kHz and sampled at 10 kHz, were acquired by a

patch-clamp amplifier (Multiclamp 700B, Molecular Devices) and analyzed using MiniAnalysis (Synaptosoft). All the chemicals were purchased from Sigma-Aldrich, unless otherwise specified.

Electron microscopy. Pre-embedding immuno-labeling experiments were performed as previously described (Hebert-Chatelain et al., 2014). Briefly, P22 brains were fixed by transcardial perfusion with PBS 1X followed by PFA and Glutaraldehyde mixed solution (4% PFA, 0,2% Glutaraldehyde w/v in PB). Next, 70µm thick coronal sections were cut using a vibratome (VT1000S Leica Microsystem). After a pre-incubation in blocking solution (10% BSA, 0.1% sodium azide and 0.02% saponin in Tris-buffered saline (TBS), the sections were incubated with rabbit anti-Iba1, 1:300 (WAKO, catalog No. 019-19741) in blocking solution with 0.004% saponin overnight at 4°C. After several washes with 1% BSA in TBS, the sections were processed using the mouse specific HRP/DAB (ABC) Detection IHC Kit (Abcam, catalog No ab64259). In brief, the sections were incubated for 2 hours with a goat anti-rabbit biotinylated secondary antibody, then with avidin-biotin complex for 2 hours, and finally incubated in 0.05% diaminobenzidine (DAB) and 0.01% hydrogen peroxide mixed solution. After 10 minutes fixation with 1% glutaraldehyde solution, the sections were post-fixed in Osmium tetroxide 1% for 20 minutes, and stained 2h in aqueous 0.5% uranyl acetate solution. Then the samples were washed several times in distilled water, dehydrated in a graded ethanol series (50%, 75%, 95% and 100%) and then embedded in EPON resin. 70nm-thick sections of the CA1 hippocampal region were collected with a Leica EMU C6 ultra-microtome. Transmission electron microscopy (TEM) micrographs were collected with Jeol JEM 1011 (Jeol, Tokyo, Japan) electron microscope (Electron Microscopy Facility – Fondazione Istituto Italiano di Tecnologia, Genoa, Italy), operating at an acceleration voltage of 100 kV, and recorded with a 11 Mp fiber optical charge-coupled device (CCD) camera (Gatan Orius SC-1000, Gatan, USA) at 10,000x. The images were then quantified as previously described (Sipe et al., 2016). The post-synaptic elements were identified primarily by the presence of electron-dense

accumulations (postsynaptic densities) when contacting pre-synaptic elements, but also by the absence of mitochondria and rounded morphologies. The pre-synaptic elements were primarily identified by the presence of ~40nm-diameter synaptic vesicles, but also by synaptic contacts with dendritic shafts and post-synaptic elements and the often-present mitochondria. The interactions were calculated by dividing the number of contacts (per Iba1-labelled process) by the area of the microglial processes (expressed in μm^2) and averaging across processes (40-55 per animal).

Human Samples.

Western Blotting. Samples used for Western-Blot are the same used in Deidda et al. 2015 (Deidda et al., 2015). None of these samples All hippocampus samples were lysed in RIPA buffer (150 mM NaCl, 50 mM HEPES, 0.5% NP40, 1% Sodiumdeoxycholate). After 30 minutes on ice, the lysates were clarified by centrifugation for 20 minutes at 16,000g. The proteins were measured *via* Pierce BCA assay (Thermo-Fisher, Catalog No. 23225). For protein identification and relative quantification *via* Western blotting, a proper volume of sample containing an equal amount of proteins was diluted with 25% NuPAGE™ LDS Sample Buffer (4X; Thermo-Fisher, Catalog No. NP0007) and 5% 1,4-Dithiothreitol (DTT; equivalent of 50mM, Sigma-Aldrich, Catalog No. DTT-RO Roche), and loaded onto NuPAGE™ 4-12% Bis-Tris Midi Protein gels (Thermo-Fisher, Catalog No. WG1402BOX). The proteins were then transferred onto nitrocellulose membrane that was previously incubated with Transfer Buffer for 15 minutes (Sigma-Aldrich, catalog No. GE10600001) at 200mA overnight at 4◦C. The primary antibody [rabbit anti-Iba1 1:1000 (WAKO, catalog No. 016-20001)] was then applied overnight in a blocking buffer (20 mM Tris, pH 7.4, 150 mM NaCl, 0.1% Tween 20, and 5% nonfat dry milk). The HRP-conjugated secondary antibodies [Thermo-Fisher, anti-rabbit (catalog No 31460)] was used in a ratio of 1:2500. The signal was detected using the SuperSignal™ West Pico PLUS Chemiluminescent Substrate detection system (Thermo-Fisher, catalog No 34578). Images were acquired by the Image Quant LAS 4000 mini image system

(General-Electrics Healthcare) and protein quantification was performed by measuring the optical density of the specific bands with the Image Quant TL software (General-Electrics Healthcare). The samples were loaded in three independent gels and averaged across experiments.

Slice histology, immunostaining, image acquisition and analysis. Human samples used for immunohistochemistry (Supplementary Table 3) were obtained from two different sources: Biobank HCB – IDIBAPS (Barcelona, Spain) and NeuroBioBank (USA). Hippocampi were fixed (24h, PFA 4% (w/v) in PBS 1X), cryoprotected (sucrose 30%, w/v) and stored at -80°C. Samples from HCB – IDIBAPS were taken from 4 controls (40-86 years-old, postmortem interval (PMI) 7-16h) and 4 individuals with DS (36-67 years-old, PMI 9-22h). Samples from the NeuroBioBank were taken from 8 controls (36-56 years-old, PMI 8-21h) and 6 individuals with DS (25-57 years-old, PMI 3-22h). Tissue blocks were cut using a vibratome (VT1000S Leica Microsystem vibratome) into 8-10µm thick (samples from HCB-IDIBAPS) or 25 µm thick (samples from NeuroBioBank) sections. Sections were then incubated with citrate buffer (0.01M, pH 6.0) for 1 minute at 100 ºC. Next, sections were treated for 1 h with 5% normal donkey serum (NDS, Jackson Immuno-Research Laboratories, catalog No 017-000-121) in PBS 1X with 0.2% Triton- X100 and incubated overnight at room temperature with mouse monoclonal IgG anti-Iba1 1:500 (Chemicon, Catalog No MABN92). After washing, sections were incubated with secondary antibody (Alexa 488 donkey anti-mouse IgG 1:200 (Invitrogen, Catalog No. A-21202). After further washing, sections were then mounted using Dako fluorescent medium (Dako North America, Catalog No. S3023). For microglial morphology analysis, a stack of images spanning the whole thickness of the slice (1.15 µm thick z-stacks) from stained hippocampal slices were acquired using a confocal laser-scanning microscope (TSC-SPE; Leica Microsystems) equipped with a 40x (NA 1.25) immersion objective and projected on a 2D image. For calculation of the cell-body area, the measurements were performed using the freehand selection tool in ImageJ. Sholl analysis was performed as previously described(Sipe et al.,

2016). Briefly, cells were cropped and thresholded to generate a binary (black and white) image. The background was manually cleaned for each cell and the ImageJ plugin ShollAnalysis (Ferreira et al., 2014) was used to perform the analysis (starting radius: 4µm, ending radius: 70µm, radius step size: 2µm, radius span: 0µm). For skeleton analysis, the same binary image created for Sholl Analysis was used. The image was skeletonized using the ImageJ Plugin Skeletonize3D(Lee T.C., 1994) and was subsequently analyzed using the plugin AnalyzeSkeleton (Arganda-Carreras et al., 2010).

Mass-Spectrometry Based Proteomics.

*Sample preparation***.** Samples of hippocampi Dp(16) and WT littermates were lysed by FASP protocol(Wisniewski et al., 2009) using the FASP Protein Digestion Kit (Expedeon Inc, Cat. No. 44250). Briefly, the samples were mixed with 0.3ml of 8M Urea in 0.1M Tris/HCl pH 8.5 (UA solution), loaded into the filtration devices, alkylated in 0.1ml of 50mM iodoacetamide in UA solution for 1 h in darkness at RT. The samples were digested using sequentially 1 µg of LysC and 1µg of Trypsin in 50 mM NaHCO3 solution at 37°C overnight. The obtained peptides were collected by centrifugation of the filter units for 10 min and the filter devices were rinsed with two 40 µl washes 50mM $NaHCO_3$ and 50µl 0.5M NaCl to eliminate the hydrophobic interactions.

NanoLC and mass spectrometer setup. The prepared samples were loaded directly into the separation column and the peptides were eluted with a non-linear gradient of 5-65 % solution B (80% CAN and 20% H_2O, 5% DMSO, 0.1% FA) in 180min at a flow rate of 250nl/min. The peptide separations were carried out at 55°C by a 75-µm ID×50cm 2µm, 100 Å C18 column mounted in the thermostatic column compartment of the machine. Eluting peptides were electrosprayed and analyzed by tandem mass spectrometry on an Orbitrap Fusion Tribrid (Thermo Fischer Scientific) operating in positive ionization mode. The precursors were ionized using an EASY-spray source

held at +2.2kV and the inlet capillary temperature was held at 300°C. Single MS survey scans were performed in the Orbitrap, recording a mass window between 375 –1500 m/z with an AGC target of 250,000, at maximum injection time of 50ms, and a resolution of 120,000 at 200 m/z. Monoisotopic precursor selection was enabled for peptide isotopic distributions, precursors of z=2-5 were selected for 2 seconds of cycle time, and dynamic exclusion was set to 45 seconds with a ±10 ppm window set around the precursor. HCD (High-energy Collisional Dissociation) was performed with a target value of 10,000 ions in the linear ion trap, a maximal ion injection time of 45ms, normalized collision energy of 30%, a Q-value of 0.25 and the possibility to inject ions for all available parallelizable time was enabled. The mass spectrometry proteomic data were deposited to the ProteomeXchange Consortium via the PRIDE (Vizcaino et al., 2016) partner repository with the dataset identifier PXD000000.

Proteomic data analysis. The raw data were processed with MaxQuant software(Cox and Mann, 2008). The database used by the software was the Mouse human database (release 2016_02). For the search trypsin allowing for cleavage N-terminal to proline was chosen as enzyme specificity. A contaminants database by the Andromeda search engine (Cox et al., 2011), with cysteine carbamidomethylation as fixed modification and acetylation protein N-terminal methionine oxidation and deamidation (N, Q) as variable modifications, were selected. For the identification of proteins, a false discovery rate (FDR) of 0.01 was requested. For peptide identification, peptides and peptide-spectrum match (PSM) and a minimum length of 6 amino acids were requested. Quantification in MaxQuant was performed using the built-in label-free quantification algorithm (Luber et al., 2010), enabling the “Match Between Runs” (Nagaraj et al., 2012). All proteins and peptides matching to the reversed database were filtered out. Label-free protein quantitation (LFQ) was performed with a minimum ratio count of 1 (Cox et al., 2014).

Proteomic bioinformatic analysis. All bioinformatics analyses were performed with the Perseus software of the MaxQuant computational platform (Tyanova et al., 2016). Protein groups were filtered to require 100% valid values in at least one experimental group. The label-free intensities were expressed as base log2 and empty values were imputed with random numbers from a normal distribution for each column, to best simulate low abundance values close to the noise level. For each sample, a Student's t-test with permutation-based FDR statistics was run. 250 permutations were performed, with an s0 of 0.1 and required an FDR of 0.05.

Targeted Proteomics. Targeted Peptides for drebrin protein were selected based on the data-dependent analysis (DDA), experimental results and on the theoretical scores obtained by the Picky software (Zauber et al., 2018). Peptide samples were prepared using the same FASP protocol used for the discovery study and analyzed with an Orbitrap Fusion Tribrid mass spectrometer (Thermo Scientific) coupled to a Thermo/Dionex Ultimate 3000 Rapid Separation UPLC system and EasySpray nano source. Samples were separated on an EasySpray PepMap RSLC, C18, 2 µm particle, 75 µm x 50 cm column at a 250 nl/min flow rate. Solvent A was water and solvent B was a solution of acetonitrile, water and DMSO (80/20 at 5%, final v/v), each containing 0.1% (v/v) formic acid. After loading at 2% B for 5 min, peptides were separated using a 100-min gradient from 7-30% B and a 20-min gradient from 30-50% B, 5-min at 80% B, followed by a 20 min re-equilibration at 2% B. Peptides were analyzed using the targeted MS2 mode of the Xcalibur software in which the doubly or triply charged precursor ion corresponding to each peptide was isolated in the quadrupole, fragmented by HCD, and full m/z 300-1200 scans of fragment ions at 30,000 resolution collected in the Orbitrap. Targeted MS2 parameters included an isolation width of 1.8 m/z for each precursor of interest, collision energy of 28%, AGC target of 5 x 10e4, maximum ion injection time of 64 ms, spray voltage of 2200 V, and ion transfer temperature of 300°C. A number of 10 precursors were targeted in each run and no scheduling was used. We used

the software package Skyline (MacLean et al., 2010) to generate precursor isolation lists for all peptides of interest and export them into the Orbitrap. Skyline was used to analyze targeted MS/MS data. Chromatographic and spectral data from RAW files were loaded into Skyline and manually analyzed to identify fragment ion peaks corresponding to each peptide. RAW files were also processed using MaxQuant software in order to match MS/MS spectra to the drebrin proteotype sequence peptide. Peak areas for all selected precursors and transitions in Skyline were combined for quantitation. For transitions refinement, we checked if all transitions were of good quality and reproducible over the samples. If certain transitions were of low quality (low intensity, high CV (%)) or irreproducible over runs, we removed them from the analysis.

Statistical Analysis. For statistical analysis, the Graph Pad Prism 7 software (GraphPad Software, USA) was used. The statistical analysis was performed by Student's t test (comparisons between two-groups), one-way analysis of variance (ANOVA) followed by Holm-Sidak *post-hoc* (comparisons among three or more groups) or two-way analysis of variance (ANOVA) followed by Holm-Sidak *post hoc* comparison (comparisons among more four or more groups with two different variables (i.e. Strain and Treatment). For heteroskedastic datasets and/or for datasets of non-normal distribution, Mann-Whitney test comparison (comparisons between two-groups) or Kruskal-Wallis test followed by Dunn's *post-hoc* test (for comparison between three or more groups) were used. The Kolmogorov-Smirnov test was used to compare cumulative distributions. For datasets in Fig. 8e, 9d and 24d, independent One-Sample t-test against 0 for each cytokine was used. The outliers were excluded only from the final pool of data by a Grubb's test iteratively until no outliers were found. In all cases, where the datasets from vehicle-treated animals were reused for comparison in different graphs, the statistical significance depicted in the graphs derives from one single two-way ANOVA including all groups across all figures. The T or F statistics reported in the figure legends derive from statistical tests including only the groups shown in each individual

graph. The statistics from experiments where we could not detect statistically significant differences are reported in Table 5.

Table 1. Proteins significantly differentially expressed in WT and Dp(16) hippocampi.

Protein names	Gene names
ATP-binding cassette sub-family A member 5	Abca5
Multidrug resistance-associated protein 1	Abcc1
Alpha/beta hydrolase domain-containing protein 13	Abhd13
Acyl-CoA dehydrogenase family member 11	Acad11
Angiotensinogen;Angiotensin-1;Angiotensin-2;Angiotensin-3;Angiotensin-4;Angiotensin 1-9;Angiotensin 1-7;Angiotensin 1-5;Angiotensin 1-4	Agt
Apoptosis-inducing factor 2	Aifm2
A-kinase anchor protein 8-like	Akap8l
A-kinase anchor protein 9	Akap9
Archaemetzincin-2	Amz2
Anoctamin-8	Ano8
AP-4 complex subunit beta-1	Ap4b1
Arginase-2, mitochondrial	Arg2
Rho GTPase-activating protein 25	Arhgap25
Rho GTPase-activating protein 33	Arhgap33
BTB/POZ domain-containing protein At1g04390	At1g04390
Autophagy-related protein 2 homolog A	Atg2a
Plasma membrane calcium-transporting ATPase 3	ATP2B3
ATP synthase subunit beta, chloroplastic	atpB
Ataxin-1	Atxn1
Beta-2-microglobulin	B2m
Protein PTHB1	Bbs9
Vesicle transport protein SEC20	Bnip1
BRCA1-associated ATM activator 1	Brat1
Bromodomain-containing protein 4	Brd4
Uncharacterized protein C2orf72 homolog	C2orf72
Carbonic anhydrase 1	Ca1
Calmodulin-binding transcription activator 2	Camta2
Cullin-associated NEDD8-dissociated protein 2	Cand2
Calpain-7	Capn7
COBW domain-containing protein 1	Cbwd1
Chromobox protein homolog 1	Cbx1
CD151 antigen	Cd151
CD44 antigen	Cd44
CD82 antigen	Cd82
Cell division cycle protein 27 homolog	Cdc27
Cadherin-9	Cdh9
Cyclin-dependent kinase 2-associated protein 1	Cdk2ap1
Phosphatidate cytidylyltransferase 1	Cds1
Complement factor B;Complement factor B Ba fragment;Complement factor B Bb fragment	Cfb;CFB
Probable cytosolic iron-sulfur protein assembly protein CIAO1	Ciao1
COX assembly mitochondrial protein homolog	Cmc1
Conserved oligomeric Golgi complex subunit 8	Cog8
Collagen alpha-1(II) chain;Collagen alpha-1(II) chain;Chondrocalcin	COL2A1;Col2a1
Copine-3	Cpne3
Crooked neck-like protein 1	Crnkl1
Cleavage stimulation factor subunit 2 tau variant	Cstf2t
Protein DENND6A	Dennd6a
Deoxyhypusine hydroxylase	Dohh
Probable C-mannosyltransferase DPY19L1	Dpy19l1

Desmoplakin	Dsp
Egl nine homolog 1;Egl nine homolog 3	Egln1;Egln3
Eukaryotic translation initiation factor 5A-2	Eif5a2
Ephrin type-B receptor 6	Ephb6
Epiplakin	Eppk1
Endoplasmic reticulum-Golgi intermediate compartment protein 3	Ergic3
Ethanolamine-phosphate phospho-lyase	Etnppl
Exonuclease 3-5 domain-containing protein 2	Exd2
Exosome complex component RRP40	Exosc3
Protein FAM173A	Fam173a
Protein FAM185A	Fam185a
Protein FAM3C	Fam3c
Polyphosphoinositide phosphatase	Fig4
Filamin-C	Flnc
FERM domain-containing protein 5	Frmd5
Alpha-(1,3)-fucosyltransferase 11	Fut11
FXYD domain-containing ion transport regulator 7	Fxyd7
H/ACA ribonucleoprotein complex subunit 1	Gar1
Glycosyltransferase 1 domain-containing protein 1	Glt1d1
Phosphatidylinositol-glycan-specific phospholipase D	Gpld1
Probable G-protein coupled receptor 162	Gpr162
14-3-3-like protein GF14 omega	GRF2
General transcription factor 3C polypeptide 4	Gtf3c4
Translation factor Guf1, mitochondrial	Guf1
Protein Hook homolog 1	Hook1
11-beta-hydroxysteroid dehydrogenase-like 5	HSD5
Interferon-induced protein with tetratricopeptide repeats 3	Ifit3
Intraflagellar transport protein 172 homolog	Ift172
Integrin-linked kinase-associated serine/threonine phosphatase 2C	Ilkap
Type I inositol 3,4-bisphosphate 4-phosphatase	Inpp4a
Integrator complex subunit 7	Ints7
Interactor protein for cytohesin exchange factors 1	Ipcef1
Integrin alpha-3;Integrin alpha-3 heavy chain;Integrin alpha-3 light chain	Itga3
Kalirin	Kalrn
Pumilio domain-containing protein KIAA0020	Kiaa0020
Kelch-like protein 26	Klhl26
L-lactate dehydrogenase A chain	LDHA
Lysosomal acid lipase/cholesteryl ester hydrolase	Lipa
Leucine-rich repeat flightless-interacting protein 2	Lrrfip2
U6 snRNA-associated Sm-like protein LSm5	Lsm5
Lysophospholipid acyltransferase 2	Mboat2
Protein-methionine sulfoxide oxidase MICAL1	Mical1
Molybdopterin synthase sulfur carrier subunit	Mocs2
Vacuolar fusion protein MON1 homolog B	Mon1b
28S ribosomal protein S10, mitochondrial	Mrps10
Metastasis suppressor protein 1	Mtss1
Unconventional myosin-If;Unconventional myosin-Ie	Myo1f;Myo1e
N-alpha-acetyltransferase 20	Naa20
NADH dehydrogenase [ubiquinone] flavoprotein 3, mitochondrial	Ndufv3
Negative elongation factor D	Nelfcd
Merlin	Nf2
NudC domain-containing protein 2	Nudcd2
Peroxisomal NADH pyrophosphatase NUDT12	Nudt12
Nucleoporin p58/p45	Nupl1
NACHT domain- and WD repeat-containing protein 1	Nwd1
Peroxisomal N(1)-acetyl-spermine/spermidine oxidase	Paox
Presenilins-associated rhomboid-like protein, mitochondrial;P-beta	Parl
Pterin-4-alpha-carbinolamine dehydratase 2	Pcbd2
Protocadherin-8	Pcdh8
Neuroendocrine convertase 1	Pcsk1

cGMP-specific 3,5-cyclic phosphodiesterase	Pde5a
Serine/threonine-protein phosphatase PGAM5, mitochondrial	Pgam5
Phosphatase and actin regulator 3	Phactr3
PH domain leucine-rich repeat-containing protein phosphatase 1	Phlpp1
Podocalyxin	Podxl
Pogo transposable element with ZNF domain	Pogz
Phragmoplast orienting kinesin-1	POK1
Proteasome inhibitor PI31 subunit	Psmf1
Peroxisomal membrane protein 2	Pxmp2
Ras-related protein Rab-34	Rab34
Guanine nucleotide exchange factor for Rab-3A	Rab3il1
RNA-binding protein Raly	RALY
Rap guanine nucleotide exchange factor 5	Rapgef5
Regulating synaptic membrane exocytosis protein 3	Rims3
E3 ubiquitin-protein ligase RNF213	Rnf213
mRNA-capping enzyme;Polynucleotide 5-triphosphatase;mRNA guanylyltransferase	Rngtt
60S ribosomal protein L36	Rpl36
Ribosomal protein S6 kinase beta-1	Rps6kb1
Sphingomyelin synthase-related protein 1	Samd8
Serine dehydratase-like	Sdsl
Septin-10	Sept10
Pigment epithelium-derived factor	Serpinf1
Serine hydroxymethyltransferase, cytosolic	Shmt1
Solute carrier family 25 member 35	Slc25a35
4F2 cell-surface antigen heavy chain	Slc3a2
Anion exchange protein 2	Slc4a2
Protein SMG9	Smg9
Sphingomyelin phosphodiesterase 4	Smpd4
Single-strand selective monofunctional uracil DNA glycosylase	Smug1
Histone-lysine N-methyltransferase SMYD3	Smyd3
VPS10 domain-containing receptor SorCS3	Sorcs3
Sperm-associated antigen 7	Spag7
Spermatogenesis-associated serine-rich protein 2	Spats2
Cytospin-A	Specc1l
STAM-binding protein	Stambp
TBC1 domain family member 22A	Tbc1d22a
F-box-like/WD repeat-containing protein TBL1X	Tbl1x
T-cell activation inhibitor, mitochondrial	TCAIM
Transcription factor 4	Tcf4
Tudor domain-containing protein 7	Tdrd7
Thyroid hormone receptor alpha	Thra
Delta(14)-sterol reductase	Tm7sf2
Transmembrane protein 115	Tmem115
Transmembrane protein 151B;Transmembrane protein 151A	Tmem151a/b
Transmembrane protein 200A	Tmem200a
Macoilin	Tmem57
Transmembrane protein 70, mitochondrial	Tmem70
Transmembrane and ubiquitin-like domain-containing protein 1	Tmub1
Torsin-2A;Prosalusin;Salusin-beta	Tor2a
Ubiquitin-associated protein 1	Ubap1
Ubiquitin-conjugating enzyme E2 J1	Ube2j1
Ubiquitin-conjugating enzyme E2 R2	Ube2r2
E3 ubiquitin-protein ligase UBR2	Ubr2
UDP-glucuronosyltransferase 1-1;UDP-glucuronosyltransferase 1-9;UDP-glucuronosyltransferase 1-7C;UDP-glucuronosyltransferase 1-6;UDP-glucuronosyltransferase 1-2	Ugt1a1;Ugt1a9;Ugt1a7c;Ugt1a6;Ugt1a2
WD repeat-containing protein 34	Wdr34
WW domain-containing oxidoreductase	Wwox
Ubiquitin thioesterase OTU1	Yod1
Zinc finger CCCH domain-containing protein 14	Zc3h14
Zinc finger CCHC domain-containing protein 8	Zcchc8

Table 2. Gene Ontology Biological Process Between WT and Dp(16) hippocampi.

Flavonoid and Xenobiotic Glucuronidation

Official Gene Symbol	Gene Name	Species
394436	UDP glucuronosyltransferase 1 family, polypeptide A1(Ugt1a1)	Mus musculus
22236	UDP glucuronosyltransferase 1 family, polypeptide A2(Ugt1a2)	Mus musculus
394432	UDP glucuronosyltransferase 1 family, polypeptide A7C(Ugt1a7c)	Mus musculus
394434	UDP glucuronosyltransferase 1 family, polypeptide A9(Ugt1a9)	Mus musculus

Cell Migration

Official Gene Symbol	Gene Name	Species
231841	BRCA1-associated ATM activator 1(Brat1)	Mus musculus
12476	CD151 antigen(Cd151)	Mus musculus
12505	CD44 antigen(Cd44)	Mus musculus
27205	podocalyxin-like(Podxl)	Mus musculus
72508	ribosomal protein S6 kinase, polypeptide 1(Rps6kb1)	Mus musculus
74392	sperm antigen with calponin homology and coiled-coil domains 1-like(Specc1l)	Mus musculus

Peptidyl-Ser Phosphorylation

Official Gene Symbol	Gene Name	Species
100986	A kinase (PRKA) anchor protein (yotiao) 9(Akap9)	Mus musculus
12505	CD44 antigen(Cd44)	Mus musculus
69726	SET and MYND domain containing 3(Smyd3)	Mus musculus
11606	angiotensinogen (serpin peptidase inhibitor,clade A,8)(Agt)	Mus musculus

Memory

Official Gene Symbol	Gene Name	Species
16400	integrin alpha 3(Itga3)	Mus musculus
545156	kalirin, RhoGEF kinase(Kalrn)	Mus musculus
110893	solute carrier family 8 (sodium/calcium exchanger), member 3(Slc8a3)	Mus musculus
66673	sortilin-related VPS10 domain containing receptor 3(Sorcs3)	Mus musculus

mRNA Processing

Official Gene Symbol	Gene Name	Species
54194	A kinase (PRKA) anchor protein 8-like(Akap8l)	Mus musculus
66877	Crn, crooked neck-like 1 (Drosophila)(Crnkl1)	Mus musculus
66373	LSM5 homolog, U6 small nuclear RNA and mRNA degradation associated(Lsm5)	Mus musculus
24018	RNA guanylyltransferase and 5'-phosphatase(Rngtt)	Mus musculus
83410	cleavage stimulation factor, 3' pre-RNA subunit 2, tau(Cstf2t)	Mus musculus
19383	hnRNP-associated with lethal yellow(Raly)	Mus musculus
70650	zinc finger, CCHC domain containing 8(Zcchc8)	Mus musculus

REDOX Process

Official Gene Symbol	Gene Name	Species
78330	NADH dehydrogenase (ubiquinone) flavoprotein 3(Ndufv3)	Mus musculus
80707	WW domain-containing oxidoreductase(Wwox)	Mus musculus
102632	acyl-Coenzyme A dehydrogenase family, member 11(Acad11)	Mus musculus
71361	apoptosis-inducing factor, mitochondrion-associated 2(Aifm2)	Mus musculus
102115	deoxyhypusine hydroxylase/monooxygenase(Dohh)	Mus musculus
112405	egl-9 family hypoxia-inducible factor 1(Egln1)	Mus musculus
112407	egl-9 family hypoxia-inducible factor 3(Egln3)	Mus musculus
16828	lactate dehydrogenase A(Ldha)	Mus musculus
171580	microtubule associated monooxygenase, calponin and LIM domain containing 1(Mical1)	Mus musculus
212503	polyamine oxidase (exo-N4-amino)(Paox)	Mus musculus
73166	transmembrane 7 superfamily member 2(Tm7sf2)	Mus musculus

Table 3. Human samples used in this work for immunohistochemistry

Case Number	Diagnosis	Age (years)	Gender	AD Signs	Source
13250	Control	49	F	Absent	Neurobiobank USA
13149	Control	46	F	Beta-A4 plaques were present in the CA4 region of the hippocampus	Neurobiobank USA
1570	Control	86	F	Absent	Biobank Spain
2	Control	53	M	Absent	Neurobiobank USA
3	Control	46	M	Absent	Neurobiobank USA
5	Control	53	M	Absent	Neurobiobank USA
1169	Control	62	M	Vascular dementia	Biobank Spain
1434	Control	40	M	Neuroaxonal pathology	Biobank Spain
1468	Control	64	M	Few neurofibrillar tangles	Biobank Spain
13202	DS	43	F	Absent	Neurobiobank USA
13235	DS	44	F	Tangles in the medial temporal lobe were scant	Neurobiobank USA
5005	DS	39	F	Absent	Neurobiobank USA
714	DS	36	F	Minimal neurofibrillar pathology (Braak I)	Biobank Spain
1028	DS	67	F	E Alzheimer V	Biobank Spain
1335	DS	62	F	E Alzheimer VI	Biobank Spain
5439	DS	57	M	Senile cerebral disease diffuse Alzheimer's type severe	Neurobiobank USA
5713	DS	25	M	Amyloid-beta immunostaining shows rare neocortical diffuse plaques	Neurobiobank USA
6135	DS	55	M	Cerebral amyloid angiopathy present	Neurobiobank USA
974	DS	44	M	Some amiloid deposits	Biobank Spain

Table 4. Triplicated genes in Dp(16) mice that play a role in the function of the immune system (red). Table from Li et al. 2007.

Supplementary Table 1 From Li et al. 2007. Orthologous genes on HSA21 and MMU 16

Names of human genes	Genome coordinates (Start position)	Names of mouse genes	Genome coordinates (Start position)
LIPI	14403005	D930038D03Rik	75423194
RBM11	14510350	Rbm11	75475524
STCH	14665310	Stch	75637868
SAMSN1	14779428	Samsn1	75741474
NRIP1	15258908	Nrip1	76172581
USP25	16024215	Usp25	76896661
CXADR	**17807201**	**Cxadr**	**78184283**
BTG3	17887846	Btg3	78242452
C21orf91	18083163	D16Ertd472e	78426122
CHODL	18539021	Chodl	78813540
PRSS7	18563561	Prss7	78835600
NCAM2	21574767	Ncam2	81315299
MRPL39	25879843	Mrpl39	84600170
JAM2	25933515	Jam2	84657025
ATP5J	**26018663**	**Atp5j**	**84710458**
GABPA	26028752	Gabpa	84717716
APP	**26174733**	**App**	**84837873**
CYYR1	26760402	Cyyr1	85345428
ADAMTS1	**27130479**	**Adamts1**	**85683023**
ADAMTS5	**27212112**	**Adamts5**	**85751616**
HEMK2_HUMAN	29166400	Hemk2	87243381
ZNF294	29222337	Zfp294	87267869
CU006_HUMAN	29299953	ORF5	87322527
USP16	29318809	Usp16	87344207
CCT8	29350518	Cct8	87372523
TAK1L_HUMAN	29380053	ORF63	87442526
BACH1	29593091	Bach1	87588150
GRIK1	29831422	Grik1	87785053
CLDN17	30460132	Cldn17	88395024
CLDN8	30508196	Cldn8	88451217
KR241_HUMAN	30576357	Gm312	88500349
KR261_HUMAN	30613592	2310002B14Rik	88535943
KRTAP13-2	30665875	2310061N02Rik	88596242
KRTAP13-1	30690213	Krtap13-1	88617721
KRTAP13-3	30719583	Krtap13	88639864
KRTAP19-1	30774235	Krtap16-1	88762689
KRTAP19-2	30781380	Krtap16-5	88766578
KRTAP19-4	30791045	Krtap16-4	88773671
KRTAP19-5	30796061	Krtap8-2	88785093
KRTAP20-1	30910645	Krtap6-1	88930037
KRTAP6-2	30892876	Krtap16-8	88936466
KRTAP21-2	31041140	Krtap21-1	89292225
KRTAP21-1	31049328	Krtap6-2	89308469
KRTAP8-1	31107218	Krtap8-1	89376581
TIAM1	**31414352**	**Tiam1**	**89675970**
SOD1	31953954	Sod1	90109717
SFR15_HUMAN	31965223	Sfrs15	90118157
HUNK	32167499	Hunk	90275244
C21orf45	32562403	2610039C10Rik	90603533
MRAP_HUMAN	32593030	Mrap	90627183
NPA1P_HUMAN	32605200	4921511H13Rik	90640868
CU063_HUMAN	32706560	4931408A02Rik	90715578
C21orf59	32895848	1110004E09Rik	90814670
SYNJ1	32922944	Synj1	90827099

GCFC_HUMAN	33028081	1810007M14Rik	90903775
CU062_HUMAN	33087746	4932438H23Rik	90942794
OLIG2	33320023	Olig2	91114409
OLIG1	33364320	Olig1	91158628
IFNAR2	**33524076**	**Ifnar2**	**91261758**
IL10RB	**33560533**	**Il10rb**	**91295167**
IFNAR1	**33619079**	**Ifnar1**	**91374108**
IFNGR2	**33697072**	**Ifngr2**	**91435953**
TMEM50B	33743312	Tmem50b	91463367
CU055_HUMAN	33779707	ORF28	91504573
GART	33798108	Gart	91510268
SON	33836794	Son	91536739
DONSON	33869653	Donson	91568126
CRYZL1	33883517	Cryzl1	91578183
ITSN1	33936634	Itsn1	91618368
ATP5O	34197627	Atp5o	91814082
KCNE2	34658193	Kcne2	92181248
C21orf51	34669669	1190017O12Rik	92190162
KCNE1	34740858	Kcne1	92234860
DSCR1	34810656	Dscr1	92280810
CLIC6	34963558	Clic6	92386993
RUNX1	**35081975**	**Runx1**	**92492515**
SETD4	36328710	Setd4	93471997
CBR1	36364155	Cbr1	93496379
CBR3	36429080	Cbr3	93571755
DOPEY2	36458876	Dopey2	93600447
MORC3	36614376	Morc3	93720824
CHAF1B	36679559	Chaf1b	93772441
CLDN14	36754793	Cldn14	93807573
SIM2	36993851	Sim2	93974356
HLCS	37045066	Hlcs	94239207
DSCR6	37300733	Dscr6	94437218
PIGP	37359534	Pigp	94467561
TTC3	37367441	Ttc3	94479537
DSCR3	**37517598**	**Dscr3**	**94606586**
DYRK1A	37713077	Dyrk1a	94720258
KCNJ6	37918656	Kcnj6	94869867
KCNJ15	38550534	Kcnj15	95366449
ERG	38675671	Erg	95469604
ETS2	39099719	Ets2	95815219
DSCR2	39468565	Dscr2	96084845
BRWD1	39477972	Brwd1	96097357
HMGN1	39636111	Hmgn1	96225528
WRB	39674040	Wrb	96250329
CU013_HUMAN	39699640	4921526F01Rik	96263961
SH3BGR	39739651	Sh3bgr	96305581
B3GALT5	39850239	B3galt5	96420079
Q9NSI5_HUMAN	**40039204**	**Jam4**	**96466704**
PCP4	40161113	Pcp4	96572516
DSCAM	**40306831**	**Dscam**	**96697969**
BACE2	41462061	Bace2	97461672
MX1	**41725838**	**Mx1**	**97553052**
FAM3B	41610531	ORF9	97576044
MX2	**41655820**	**Mx2**	**97690999**
TMPRSS2	41758351	Tmprss2	97721930
RIPK4	42032614	Ripk4	97896851
PRDM15	42094394	Prdm15	97946794
CU025_HUMAN	42178290	5830404H04Rik	98010132
ZNF295	42280009	Zfp295	98102306

Table 5. Non-significant statistics

Figure	Test	Statistic Values
Fig. 8c	Two-Tailed Unpaired Student's t-test	t=0.13 df=9 p=0.898
Fig. 8k	Two-Tailed Mann-Whitney Test	U=17 p=0.628
Fig. 9f	Two-Way ANOVA	$F_{Interaction}$ (30, 17081) = 0.5774 p = 0.9684
Fig. 9g	Two-Tailed Unpaired Student's t-test	t=0.08 df=8 p=0.938
Fig. 9i	Two-Tailed Unpaired Student's t-test	t=0.86 df=18 p=0.397
Fig. 17a	Two-Way ANOVA	$F_{Interaction}$ (2, 79) = 0.661 p = 0.519
Fig. 18e	Two-Way ANOVA	$F_{Interaction}$ (33, 6324) = 0.9459 p = 0.5563
Fig. 25a	Two-Way ANOVA	$F_{Interaction}$ (3, 102) = 1.002 p = 0.3950
Fig. 25b	Two-Way ANOVA	$F_{Interaction}$ (3, 103) = 0.8147 p = 0.489
Fig. 25c Vehicle	Two-Way ANOVA	$F_{Interaction}$ (2, 108) = 1.393 p = 0.2527
Fig. 25c PLX3397	Two-Way ANOVA	$F_{Interaction}$ (2, 99) = 1.22 p = 0.3
Fig. 25c APAP	Two-Way ANOVA	$F_{Interaction}$ (2, 48) = 1.049 p = 0.35
Fig. 25c Ruxolitinib	Two-Way ANOVA	$F_{Interaction}$ (2, 54) = 0.45 p = 0.6365
Fig. 26a	Two-Way ANOVA	$F_{Interaction}$ (3, 75) = 0.8154 p = 0.4894
Fig. 26b	Two-Way ANOVA	$F_{interaction}$ (3, 75) = 0.2080 p = 0.8906
Fig. 26c Vehicle	Two-Way ANOVA	$F_{Interaction}$ (1, 56) = 2.019 p = 0.1609
Fig. 26c PLX3397	Two-Way ANOVA	$F_{Interaction}$ (1, 34) = 0.92 p = 0.3426
Fig. 26c Ruxolitinib	Two-Way ANOVA	$F_{Interaction}$ (1, 20) = 0.008 p = 0.9264

ABBREVIATION INDEX

AD – Alzheimer's Disease

APAP – Acetaminophen

APP – Amyloid Precursor Protein

BBB – Blood Brain Barrier

BDNF – Brain-Derived Neurotrophic Factor

CNS – Central nervous System

DS – Down Syndrome

ERK – Extracellular Signal-Regulated Kinase

HSA21 – Human Chromosome 21

IFN – Interferon

IL – Interleukin

LPS – Lipopolysaccharide

LTD – Long-Term Depression

LTP – Long-Term Potentiation

MCP – Monocyte Chemoattractant Protein-1

MIP – Macrophage Inflammatory Protein

MMU16 – Murine Chromosome 16

NOR – Novel Object Recognition

NSAID – Non-Steroidal Anti Inflammatory Drugs

OLT – Object Location Test

P – Postnatal Day

PET – Positron-Emission Tomography

PGE – Prostaglandin

Poly I:C – Polyinosinic:polycytidylic Acid

Redox – Reduction/Oxidation

RTT – Rett Syndrome

SVZ – Sub Ventricular Zone

TNF – Tumor Necrosis Factor

WT – Wild Type

REFERENCES

Ajmone-Cat, M.A., Bernardo, A., Greco, A., and Minghetti, L. (2010). Non-Steroidal Anti-Inflammatory Drugs and Brain Inflammation: Effects on Microglial Functions. Pharmaceuticals (Basel) *3*, 1949-1965.

Alexander, M., Petri, H., Ding, Y., Wandel, C., Khwaja, O., and Foskett, N. (2016). Morbidity and medication in a large population of individuals with Down syndrome compared to the general population. Dev Med Child Neurol *58*, 246-254.

Alldred, M.J., Chao, H.M., Lee, S.H., Beilin, J., Powers, B.E., Petkova, E., Strupp, B.J., and Ginsberg, S.D. (2018). CA1 pyramidal neuron gene expression mosaics in the Ts65Dn murine model of Down syndrome and Alzheimer's disease following maternal choline supplementation. Hippocampus *28*, 251-268.

Arcuri, C., Mecca, C., Bianchi, R., Giambanco, I., and Donato, R. (2017). The Pathophysiological Role of Microglia in Dynamic Surveillance, Phagocytosis and Structural Remodeling of the Developing CNS. Front Mol Neurosci *10*, 191.

Arganda-Carreras, I., Fernandez-Gonzalez, R., Munoz-Barrutia, A., and Ortiz-De-Solorzano, C. (2010). 3D reconstruction of histological sections: Application to mammary gland tissue. Microsc Res Tech *73*, 1019-1029.

Arno, B., Grassivaro, F., Rossi, C., Bergamaschi, A., Castiglioni, V., Furlan, R., Greter, M., Favaro, R., Comi, G., Becher, B.*, et al.* (2014). Neural progenitor cells orchestrate microglia migration and positioning into the developing cortex. Nat Commun *5*, 5611.

Arnoux, I., Hoshiko, M., Sanz Diez, A., and Audinat, E. (2014). Paradoxical effects of minocycline in the developing mouse somatosensory cortex. Glia *62*, 399-410.

Bachmanov, A.A., Reed, D.R., Beauchamp, G.K., and Tordoff, M.G. (2002). Food intake, water intake, and drinking spout side preference of 28 mouse strains. Behav Genet *32*, 435-443.

Belichenko, N.P., Belichenko, P.V., Kleschevnikov, A.M., Salehi, A., Reeves, R.H., and Mobley, W.C. (2009). The "Down syndrome critical region" is sufficient in the mouse model to confer behavioral,

neurophysiological, and synaptic phenotypes characteristic of Down syndrome. J Neurosci *29*, 5938-5948.

Belichenko, P.V., Masliah, E., Kleschevnikov, A.M., Villar, A.J., Epstein, C.J., Salehi, A., and Mobley, W.C. (2004). Synaptic structural abnormalities in the Ts65Dn mouse model of Down Syndrome. J Comp Neurol *480*, 281-298.

Benson, S., Brinkhoff, A., Lueg, L., Roderigo, T., Kribben, A., Wilde, B., Witzke, O., Engler, H., Schedlowski, M., and Elsenbruch, S. (2017). Effects of acute systemic inflammation on the interplay between sad mood and affective cognition. Transl Psychiatry *7*, 1281.

Bharani, K.L., Derex, R., Granholm, A.C., and Ledreux, A. (2017). A noradrenergic lesion aggravates the effects of systemic inflammation on the hippocampus of aged rats. PLoS One *12*, e0189821.

Blecharz-Klin, K., Joniec-Maciejak, I., Jawna, K., Pyrzanowska, J., Piechal, A., Wawer, A., and Widy-Tyszkiewicz, E. (2015). Developmental exposure to paracetamol causes biochemical alterations in medulla oblongata. Environ Toxicol Pharmacol *40*, 369-374.

Blecharz-Klin, K., Wawer, A., Jawna-Zboinska, K., Pyrzanowska, J., Piechal, A., Mirowska-Guzel, D., and Widy-Tyszkiewicz, E. (2018). Early paracetamol exposure decreases brain-derived neurotrophic factor (BDNF) in striatum and affects social behaviour and exploration in rats. Pharmacol Biochem Behav *168*, 25-32.

Bosch, M., Castro, J., Saneyoshi, T., Matsuno, H., Sur, M., and Hayashi, Y. (2014). Structural and molecular remodeling of dendritic spine substructures during long-term potentiation. Neuron *82*, 444-459.

Bosco, A., Steele, M.R., and Vetter, M.L. (2011). Early microglia activation in a mouse model of chronic glaucoma. J Comp Neurol *519*, 599-620.

Broers, C.J., Gemke, R.J., Morre, S.A., Weijerman, M.E., and van Furth, A.M. (2014). Increased production of interleukin-10 in children with Down syndrome upon ex vivo stimulation with Streptococcus pneumoniae. Pediatr Res *75*, 109-113.

Carpenter, R.E., and Summers, C.H. (2009). Learning strategies during fear conditioning. Neurobiol Learn Mem *91*, 415-423.

Chang, P.K., Khatchadourian, A., McKinney, R.A., and Maysinger, D. (2015). Docosahexaenoic acid (DHA): a modulator of microglia activity and dendritic spine morphology. J Neuroinflammation *12*, 34.

Chibnall, J.T., Tait, R.C., Harman, B., and Luebbert, R.A. (2005). Effect of acetaminophen on behavior, well-being, and psychotropic medication use in nursing home residents with moderate-to-severe dementia. J Am Geriatr Soc *53*, 1921-1929.

Christiansen, G.B., Andersen, K.H., Riis, S., Nykjaer, A., Bolcho, U., Jensen, M.S., and Holm, M.M. (2017). The sorting receptor SorCS3 is a stronger regulator of glutamate receptor functions compared to GABAergic mechanisms in the hippocampus. Hippocampus *27*, 235-248.

Chung, W.S., Welsh, C.A., Barres, B.A., and Stevens, B. (2015). Do glia drive synaptic and cognitive impairment in disease? Nat Neurosci *18*, 1539-1545.

Colacurcio, D.J., Pensalfini, A., Jiang, Y., and Nixon, R.A. (2018). Dysfunction of autophagy and endosomal-lysosomal pathways: Roles in pathogenesis of Down syndrome and Alzheimer's Disease. Free Radic Biol Med *114*, 40-51.

Colton, C.A., Yao, J., Taffs, R.E., Keri, J.E., and Oster-Granite, M.L. (1991). Abnormal production of interleukin-1 by microglia from trisomy 16 mice. Neurosci Lett *132*, 270-274.

Colton, C.A., Yao, J.B., Gilbert, D., and Oster-Granite, M.L. (1990). Enhanced production of superoxide anion by microglia from trisomy 16 mice. Brain Res *519*, 236-242.

Contestabile, A., Fila, T., Ceccarelli, C., Bonasoni, P., Bonapace, L., Santini, D., Bartesaghi, R., and Ciani, E. (2007). Cell cycle alteration and decreased cell proliferation in the hippocampal dentate gyrus and in the neocortical germinal matrix of fetuses with Down syndrome and in Ts65Dn mice. Hippocampus *17*, 665-678.

Cox, J., Hein, M.Y., Luber, C.A., Paron, I., Nagaraj, N., and Mann, M. (2014). Accurate proteome-wide label-free quantification by delayed normalization and maximal peptide ratio extraction, termed MaxLFQ. Mol Cell Proteomics *13*, 2513-2526.

Cox, J., and Mann, M. (2008). MaxQuant enables high peptide identification rates, individualized p.p.b.-range mass accuracies and proteome-wide protein quantification. Nat Biotechnol *26*, 1367-1372.

Cox, J., Neuhauser, N., Michalski, A., Scheltema, R.A., Olsen, J.V., and Mann, M. (2011). Andromeda: a peptide search engine integrated into the MaxQuant environment. J Proteome Res *10*, 1794-1805.

Cunningham, C.L., Martinez-Cerdeno, V., and Noctor, S.C. (2013). Microglia regulate the number of neural precursor cells in the developing cerebral cortex. J Neurosci *33*, 4216-4233.

Davisson, M.T., Schmidt, C., and Akeson, E.C. (1990). Segmental trisomy of murine chromosome 16: a new model system for studying Down syndrome. Prog Clin Biol Res *360*, 263-280.

Deidda, G., Parrini, M., Naskar, S., Bozarth, I.F., Contestabile, A., and Cancedda, L. (2015). Reversing excitatory GABAAR signaling restores synaptic plasticity and memory in a mouse model of Down syndrome. Nat Med *21*, 318-326.

Dekker, A.D., Fortea, J., Blesa, R., and De Deyn, P.P. (2017). Cerebrospinal fluid biomarkers for Alzheimer's disease in Down syndrome. Alzheimers Dement (Amst) *8*, 1-10.

Delpech, J.C., Wei, L., Hao, J., Yu, X., Madore, C., Butovsky, O., and Kaffman, A. (2016). Early life stress perturbs the maturation of microglia in the developing hippocampus. Brain Behav Immun *57*, 79-93.

Dewall, C.N., Macdonald, G., Webster, G.D., Masten, C.L., Baumeister, R.F., Powell, C., Combs, D., Schurtz, D.R., Stillman, T.F., Tice, D.M.*, et al.* (2010). Acetaminophen reduces social pain: behavioral and neural evidence. Psychol Sci *21*, 931-937.

Dierssen, M. (2012). Down syndrome: the brain in trisomic mode. Nat Rev Neurosci *13*, 844-858.

Dierssen, M., Benavides-Piccione, R., Martinez-Cue, C., Estivill, X., Florez, J., Elston, G.N., and DeFelipe, J. (2003). Alterations of neocortical pyramidal cell phenotype in the Ts65Dn mouse model of Down syndrome: effects of environmental enrichment. Cereb Cortex *13*, 758-764.

Eijsvoogel, N.B., Hollegien, M.I., Bok, V.L.A., Derksen Lubsen, A.G., Dikken, F.P.J., Leenders, S., Pijning, A., Post, E., Wojciechowski, M., Hilbink, M.*, et al.* (2017). Declining antibody levels after

hepatitis B vaccination in Down syndrome: A need for booster vaccination? J Med Virol *89*, 1682-1685.

Elmore, M.R., Najafi, A.R., Koike, M.A., Dagher, N.N., Spangenberg, E.E., Rice, R.A., Kitazawa, M., Matusow, B., Nguyen, H., West, B.L*., et al.* (2014). Colony-stimulating factor 1 receptor signaling is necessary for microglia viability, unmasking a microglia progenitor cell in the adult brain. Neuron *82*, 380-397.

Ferreira, T.A., Blackman, A.V., Oyrer, J., Jayabal, S., Chung, A.J., Watt, A.J., Sjostrom, P.J., and van Meyel, D.J. (2014). Neuronal morphometry directly from bitmap images. Nat Methods *11*, 982-984.

Fiebich, B.L., Lieb, K., Hull, M., Aicher, B., van Ryn, J., Pairet, M., and Engelhardt, G. (2000). Effects of caffeine and paracetamol alone or in combination with acetylsalicylic acid on prostaglandin E(2) synthesis in rat microglial cells. Neuropharmacology *39*, 2205-2213.

Flower, R.J., and Vane, J.R. (1972). Inhibition of prostaglandin synthetase in brain explains the anti-pyretic activity of paracetamol (4-acetamidophenol). Nature *240*, 410-411.

Fructuoso, M., Rachdi, L., Philippe, E., Denis, R.G., Magnan, C., Le Stunff, H., Janel, N., and Dierssen, M. (2018). Increased levels of inflammatory plasma markers and obesity risk in a mouse model of Down syndrome. Free Radic Biol Med *114*, 122-130.

Fung, K., and Alden, L.E. (2017). Once hurt, twice shy: Social pain contributes to social anxiety. Emotion *17*, 231-239.

Gally, F., Rao, D.M., Schmitz, C., Colvin, K.L., Yeager, M.E., and Perraud, A.L. (2018). The TRPM2 ion channel contributes to cytokine hyperproduction in a mouse model of Down Syndrome. Biochim Biophys Acta *1864*, 126-132.

Garre, J.M., Silva, H.M., Lafaille, J.J., and Yang, G. (2017). CX3CR1+ monocytes modulate learning and learning-dependent dendritic spine remodeling via TNF-alpha. Nat Med *23*, 714-722.

Ginhoux, F., Lim, S., Hoeffel, G., Low, D., and Huber, T. (2013). Origin and differentiation of microglia. Front Cell Neurosci *7*, 45.

Good, P. (2018). Evidence the U.S. autism epidemic initiated by acetaminophen (Tylenol) is aggravated by oral antibiotic amoxicillin/clavulanate (Augmentin) and now exponentially by herbicide glyphosate (Roundup). Clin Nutr ESPEN *23*, 171-183.

Goodliffe, J.W., Olmos-Serrano, J.L., Aziz, N.M., Pennings, J.L., Guedj, F., Bianchi, D.W., and Haydar, T.F. (2016). Absence of Prenatal Forebrain Defects in the Dp(16)1Yey/+ Mouse Model of Down Syndrome. J Neurosci *36*, 2926-2944.

Gould, G.G., Seillier, A., Weiss, G., Giuffrida, A., Burke, T.F., Hensler, J.G., Rock, C., Tristan, A., McMahon, L.R., Salazar, A.*, et al.* (2012). Acetaminophen differentially enhances social behavior and cortical cannabinoid levels in inbred mice. Prog Neuropsychopharmacol Biol Psychiatry *38*, 260-269.

Grabert, K., Michoel, T., Karavolos, M.H., Clohisey, S., Baillie, J.K., Stevens, M.P., Freeman, T.C., Summers, K.M., and McColl, B.W. (2016). Microglial brain region-dependent diversity and selective regional sensitivities to aging. Nat Neurosci *19*, 504-516.

Greco, A., Ajmone-Cat, M.A., Nicolini, A., Sciulli, M.G., and Minghetti, L. (2003). Paracetamol effectively reduces prostaglandin E2 synthesis in brain macrophages by inhibiting enzymatic activity of cyclooxygenase but not phospholipase and prostaglandin E synthase. J Neurosci Res *71*, 844-852.

Griffin, W.S., Stanley, L.C., Ling, C., White, L., MacLeod, V., Perrot, L.J., White, C.L., 3rd, and Araoz, C. (1989). Brain interleukin 1 and S-100 immunoreactivity are elevated in Down syndrome and Alzheimer disease. Proc Natl Acad Sci U S A *86*, 7611-7615.

Guaraldi, F., Rossetto Giaccherino, R., Lanfranco, F., Motta, G., Gori, D., Arvat, E., Ghigo, E., and Giordano, R. (2017). Endocrine Autoimmunity in Down's Syndrome. Front Horm Res *48*, 133-146.

Guedj, F., Pennings, J.L., Ferres, M.A., Graham, L.C., Wick, H.C., Miczek, K.A., Slonim, D.K., and Bianchi, D.W. (2015). The fetal brain transcriptome and neonatal behavioral phenotype in the Ts1Cje mouse model of Down syndrome. Am J Med Genet A *167A*, 1993-2008.

Guidi, S., Bonasoni, P., Ceccarelli, C., Santini, D., Gualtieri, F., Ciani, E., and Bartesaghi, R. (2008). Neurogenesis impairment and increased cell death reduce total neuron number in the hippocampal region of fetuses with Down syndrome. Brain Pathol *18*, 180-197.

Gupta, S., Ellis, S.E., Ashar, F.N., Moes, A., Bader, J.S., Zhan, J., West, A.B., and Arking, D.E. (2014). Transcriptome analysis reveals dysregulation of innate immune response genes and neuronal activity-dependent genes in autism. Nat Commun *5*, 5748.

Haas, M.A., Bell, D., Slender, A., Lana-Elola, E., Watson-Scales, S., Fisher, E.M., Tybulewicz, V.L., and Guillemot, F. (2013). Alterations to dendritic spine morphology, but not dendrite patterning, of cortical projection neurons in Tc1 and Ts1Rhr mouse models of Down syndrome. PLoS One *8*, e78561.

Hanisch, U.K., and Kettenmann, H. (2007). Microglia: active sensor and versatile effector cells in the normal and pathologic brain. Nat Neurosci *10*, 1387-1394.

Hartley, D., Blumenthal, T., Carrillo, M., DiPaolo, G., Esralew, L., Gardiner, K., Granholm, A.C., Iqbal, K., Krams, M., Lemere, C.*, et al.* (2015). Down syndrome and Alzheimer's disease: Common pathways, common goals. Alzheimers Dement *11*, 700-709.

Hayes, G.M., Woodroofe, M.N., and Cuzner, M.L. (1987). Microglia are the major cell type expressing MHC class II in human white matter. J Neurol Sci *80*, 25-37.

Hebert-Chatelain, E., Reguero, L., Puente, N., Lutz, B., Chaouloff, F., Rossignol, R., Piazza, P.V., Benard, G., Grandes, P., and Marsicano, G. (2014). Cannabinoid control of brain bioenergetics: Exploring the subcellular localization of the CB1 receptor. Mol Metab *3*, 495-504.

Herault, Y., Delabar, J.M., Fisher, E.M.C., Tybulewicz, V.L.J., Yu, E., and Brault, V. (2017). Rodent models in Down syndrome research: impact and future opportunities. Dis Model Mech *10*, 1165-1186.

Herring, B.E., and Nicoll, R.A. (2016). Kalirin and Trio proteins serve critical roles in excitatory synaptic transmission and LTP. Proc Natl Acad Sci U S A *113*, 2264-2269.

Hickey, F., Hickey, E., and Summar, K.L. (2012). Medical update for children with Down syndrome for the pediatrician and family practitioner. Adv Pediatr *59*, 137-157.

Hung, J., Chansard, M., Ousman, S.S., Nguyen, M.D., and Colicos, M.A. (2010). Activation of microglia by neuronal activity: results from a new in vitro paradigm based on neuronal-silicon interfacing technology. Brain Behav Immun *24*, 31-40.

Hunter, C.L., Bachman, D., and Granholm, A.C. (2004). Minocycline prevents cholinergic loss in a mouse model of Down's syndrome. Ann Neurol *56*, 675-688.

Imai, Y., and Kohsaka, S. (2002). Intracellular signaling in M-CSF-induced microglia activation: role of Iba1. Glia *40*, 164-174.

Inta, D., Lang, U.E., Borgwardt, S., Meyer-Lindenberg, A., and Gass, P. (2017). Microglia Activation and Schizophrenia: Lessons From the Effects of Minocycline on Postnatal Neurogenesis, Neuronal Survival and Synaptic Pruning. Schizophr Bull *43*, 493-496.

Ishida, T., Sato, T., Irifune, M., Tanaka, K., Nakamura, N., and Nishikawa, T. (2007). Effect of acetaminophen, a cyclooxygenase inhibitor, on Morris water maze task performance in mice. J Psychopharmacol *21*, 757-767.

Jiang, X., Liu, C., Yu, T., Zhang, L., Meng, K., Xing, Z., Belichenko, P.V., Kleschevnikov, A.M., Pao, A., Peresie, J.*, et al.* (2015). Genetic dissection of the Down syndrome critical region. Hum Mol Genet *24*, 6540-6551.

Joseph, A.M., Monticelli, L.A., and Sonnenberg, G.F. (2018). Metabolic regulation of innate and adaptive lymphocyte effector responses. Immunol Rev *286*, 137-147.

Jozwiak-Bebenista, M., and Nowak, J.Z. (2014). Paracetamol: mechanism of action, applications and safety concern. Acta Pol Pharm *71*, 11-23.

Kanaumi, T., Milenkovic, I., Adle-Biassette, H., Aronica, E., and Kovacs, G.G. (2013). Non-neuronal cell responses differ between normal and Down syndrome developing brains. Int J Dev Neurosci *31*, 796-803.

Kaur, C., Rathnasamy, G., and Ling, E.A. (2017). Biology of Microglia in the Developing Brain. J Neuropathol Exp Neurol *76*, 736-753.

Kerrisk, M.E., Greer, C.A., and Koleske, A.J. (2013). Integrin alpha3 is required for late postnatal stability of dendrite arbors, dendritic spines and synapses, and mouse behavior. J Neurosci *33*, 6742-6752.

Khoshnood, B., Greenlees, R., Loane, M., Dolk, H., Committee, E.P.M., and Group, E.W. (2011). Paper 2: EUROCAT public health indicators for congenital anomalies in Europe. Birth Defects Res A Clin Mol Teratol *91 Suppl 1*, S16-22.

Kierdorf, K., and Prinz, M. (2013). Factors regulating microglia activation. Front Cell Neurosci *7*, 44.

Kim, J.W., Hong, J.Y., and Bae, S.M. (2018). Microglia and Autism Spectrum Disorder: Overview of Current Evidence and Novel Immunomodulatory Treatment Options. Clin Psychopharmacol Neurosci *16*, 246-252.

Kinik, S.T., Ozcay, F., and Varan, B. (2006). Type I diabetes mellitus, Hashimoto's thyroiditis and celiac disease in an adolescent with Down syndrome. Pediatr Int *48*, 433-435.

Kleschevnikov, A.M., Belichenko, P.V., Villar, A.J., Epstein, C.J., Malenka, R.C., and Mobley, W.C. (2004). Hippocampal long-term potentiation suppressed by increased inhibition in the Ts65Dn mouse, a genetic model of Down syndrome. J Neurosci *24*, 8153-8160.

Koganezawa, N., Hanamura, K., Sekino, Y., and Shirao, T. (2017). The role of drebrin in dendritic spines. Mol Cell Neurosci *84*, 85-92.

Kojima, N., and Shirao, T. (2007). Synaptic dysfunction and disruption of postsynaptic drebrin-actin complex: a study of neurological disorders accompanied by cognitive deficits. Neurosci Res *58*, 1-5.

Le Magueresse, C., and Monyer, H. (2013). GABAergic interneurons shape the functional maturation of the cortex. Neuron *77*, 388-405.

Lee T.C., K.R.L., ChuC.N. (1994). Building Skeleton Models via 3-D Medial Surface Axis Thinning Algorithms. CVGIP: Graphical Models and Image Processing *56*, 462-478.

Li, Y., Wang, J., Sheng, J.G., Liu, L., Barger, S.W., Jones, R.A., Van Eldik, L.J., Mrak, R.E., and Griffin, W.S. (1998). S100 beta increases levels of beta-amyloid precursor protein and its encoding mRNA in rat neuronal cultures. J Neurochem *71*, 1421-1428.

Li, Z., Yu, T., Morishima, M., Pao, A., LaDuca, J., Conroy, J., Nowak, N., Matsui, S., Shiraishi, I., and Yu, Y.E. (2007). Duplication of the entire 22.9 Mb human chromosome 21 syntenic region on mouse chromosome 16 causes cardiovascular and gastrointestinal abnormalities. Hum Mol Genet *16*, 1359-1366.

Liu, L., Li, Y., Van Eldik, L.J., Griffin, W.S., and Barger, S.W. (2005). S100B-induced microglial and neuronal IL-1 expression is mediated by cell type-specific transcription factors. J Neurochem *92*, 546-553.

Lorenzo, L.P., Chen, H., Shatynski, K.E., Clark, S., Yuan, R., Harrison, D.E., Yarowsky, P.J., and Williams, M.S. (2011). Defective hematopoietic stem cell and lymphoid progenitor development in the Ts65Dn mouse model of Down syndrome: potential role of oxidative stress. Antioxid Redox Signal *15*, 2083-2094.

Lorenzo, L.P., Shatynski, K.E., Clark, S., Yarowsky, P.J., and Williams, M.S. (2013). Defective thymic progenitor development and mature T-cell responses in a mouse model for Down syndrome. Immunology *139*, 447-458.

Luber, C.A., Cox, J., Lauterbach, H., Fancke, B., Selbach, M., Tschopp, J., Akira, S., Wiegand, M., Hochrein, H., O'Keeffe, M.*, et al.* (2010). Quantitative proteomics reveals subset-specific viral recognition in dendritic cells. Immunity *32*, 279-289.

Ma, L., Li, Y., and Wang, R. (2015). Drebrin and cognitive impairment. Clin Chim Acta *451*, 121-124.

MacLean, B., Tomazela, D.M., Shulman, N., Chambers, M., Finney, G.L., Frewen, B., Kern, R., Tabb, D.L., Liebler, D.C., and MacCoss, M.J. (2010). Skyline: an open source document editor for creating and analyzing targeted proteomics experiments. Bioinformatics *26*, 966-968.

Maezawa, I., and Jin, L.W. (2010). Rett syndrome microglia damage dendrites and synapses by the elevated release of glutamate. J Neurosci *30*, 5346-5356.

Majewska, A., and Sur, M. (2003). Motility of dendritic spines in visual cortex in vivo: changes during the critical period and effects of visual deprivation. Proc Natl Acad Sci U S A *100*, 16024-16029.

Maroun, L.E. (1995). Anti-interferon immunoglobulins can improve the trisomy 16 mouse phenotype. Teratology *51*, 329-335.

Marsland, A.L., Gianaros, P.J., Kuan, D.C., Sheu, L.K., Krajina, K., and Manuck, S.B. (2015). Brain morphology links systemic inflammation to cognitive function in midlife adults. Brain Behav Immun *48*, 195-204.

Martinez, E., Castaneda, D., Jaramillo, S., Iregui, A., Quinonez, T., Rodriguez, J.A., Herrera, E., Gomez, A.M., Rondon, M.A., Prieto, J.C*., et al.* (2016). Altered immune parameters correlate with infection-related hospitalizations in children with Down syndrome. Hum Immunol *77*, 594-599.

Maxfield, F.R., and McGraw, T.E. (2004). Endocytic recycling. Nat Rev Mol Cell Biol *5*, 121-132.

Milewski, T.M., and Orr, P.T. (2018). Acetaminophen disrupts memory in object recognition and increases extracellular signal-regulated kinase phosphorylation in male mice. Behav Neurosci.

Minelli, A., Castaldo, P., Gobbi, P., Salucci, S., Magi, S., and Amoroso, S. (2007). Cellular and subcellular localization of Na+-Ca2+ exchanger protein isoforms, NCX1, NCX2, and NCX3 in cerebral cortex and hippocampus of adult rat. Cell Calcium *41*, 221-234.

Mischkowski, D., Crocker, J., and Way, B.M. (2016). From painkiller to empathy killer: acetaminophen (paracetamol) reduces empathy for pain. Soc Cogn Affect Neurosci *11*, 1345-1353.

Miyamoto, A., Wake, H., Ishikawa, A.W., Eto, K., Shibata, K., Murakoshi, H., Koizumi, S., Moorhouse, A.J., Yoshimura, Y., and Nabekura, J. (2016). Microglia contact induces synapse formation in developing somatosensory cortex. Nat Commun *7*, 12540.

Morgan, J.T., Chana, G., Pardo, C.A., Achim, C., Semendeferi, K., Buckwalter, J., Courchesne, E., and Everall, I.P. (2010). Microglial activation and increased microglial density observed in the dorsolateral prefrontal cortex in autism. Biol Psychiatry *68*, 368-376.

Mosher, K.I., Andres, R.H., Fukuhara, T., Bieri, G., Hasegawa-Moriyama, M., He, Y., Guzman, R., and Wyss-Coray, T. (2012). Neural progenitor cells regulate microglia functions and activity. Nat Neurosci *15*, 1485-1487.

Mrak, R.E., and Griffin, W.S. (2004). Trisomy 21 and the brain. J Neuropathol Exp Neurol *63*, 679-685.

Mulet, M., Blasco-Ibanez, J.M., Crespo, C., Nacher, J., and Varea, E. (2017). Early increased density of cyclooxygenase-2 (COX-2) immunoreactive neurons in Down syndrome. Folia Neuropathol *55*, 154-160.

Nagaraj, N., Kulak, N.A., Cox, J., Neuhauser, N., Mayr, K., Hoerning, O., Vorm, O., and Mann, M. (2012). System-wide perturbation analysis with nearly complete coverage of the yeast proteome by single-shot ultra HPLC runs on a bench top Orbitrap. Mol Cell Proteomics *11*, M111 013722.

Nakahata, Y., and Yasuda, R. (2018). Plasticity of Spine Structure: Local Signaling, Translation and Cytoskeletal Reorganization. Front Synaptic Neurosci *10*, 29.

Nilsson, I., Lindfors, C., Fetissov, S.O., Hokfelt, T., and Johansen, J.E. (2008). Aberrant agouti-related protein system in the hypothalamus of the anx/anx mouse is associated with activation of microglia. J Comp Neurol *507*, 1128-1140.

Nimmerjahn, A., Kirchhoff, F., and Helmchen, F. (2005). Resting microglial cells are highly dynamic surveillants of brain parenchyma in vivo. Science *308*, 1314-1318.

O'Connor, P., and Chipkin, R.E. (1984). Comparisons between warm and cold water swim stress in mice. Life Sci *35*, 631-639.

O'Doherty, A., Ruf, S., Mulligan, C., Hildreth, V., Errington, M.L., Cooke, S., Sesay, A., Modino, S., Vanes, L., Hernandez, D.*, et al.* (2005). An aneuploid mouse strain carrying human chromosome 21 with Down syndrome phenotypes. Science *309*, 2033-2037.

Paolicelli, R.C., Bolasco, G., Pagani, F., Maggi, L., Scianni, M., Panzanelli, P., Giustetto, M., Ferreira, T.A., Guiducci, E., Dumas, L.*, et al.* (2011). Synaptic pruning by microglia is necessary for normal brain development. Science *333*, 1456-1458.

Parkhurst, C.N., Yang, G., Ninan, I., Savas, J.N., Yates, J.R., 3rd, Lafaille, J.J., Hempstead, B.L., Littman, D.R., and Gan, W.B. (2013). Microglia promote learning-dependent synapse formation through brain-derived neurotrophic factor. Cell *155*, 1596-1609.

Parrini, M., Ghezzi, D., Deidda, G., Medrihan, L., Castroflorio, E., Alberti, M., Baldelli, P., Cancedda, L., and Contestabile, A. (2017). Aerobic exercise and a BDNF-mimetic therapy rescue learning and memory in a mouse model of Down syndrome. Sci Rep *7*, 16825.

Pascual, O., Ben Achour, S., Rostaing, P., Triller, A., and Bessis, A. (2012). Microglia activation triggers astrocyte-mediated modulation of excitatory neurotransmission. Proc Natl Acad Sci U S A *109*, E197-205.

Patel, A., Rees, S.D., Kelly, M.A., Bain, S.C., Barnett, A.H., Thalitaya, D., and Prasher, V.P. (2011). Association of variants within APOE, SORL1, RUNX1, BACE1 and ALDH18A1 with dementia in Alzheimer's disease in subjects with Down syndrome. Neurosci Lett *487*, 144-148.

Peebles, C.L., Yoo, J., Thwin, M.T., Palop, J.J., Noebels, J.L., and Finkbeiner, S. (2010). Arc regulates spine morphology and maintains network stability in vivo. Proc Natl Acad Sci U S A *107*, 18173-18178.

Philippot, G., Gordh, T., Fredriksson, A., and Viberg, H. (2017). Adult neurobehavioral alterations in male and female mice following developmental exposure to paracetamol (acetaminophen): characterization of a critical period. J Appl Toxicol *37*, 1174-1181.

Phillips, M., and Pozzo-Miller, L. (2015). Dendritic spine dysgenesis in autism related disorders. Neurosci Lett *601*, 30-40.

Pickering, G., Macian, N., Dubray, C., and Pereira, B. (2016). Paracetamol sharpens reflection and spatial memory: a double-blind randomized controlled study in healthy volunteers. Drug Des Devel Ther *10*, 3969-3976.

Posadas, I., Santos, P., Blanco, A., Munoz-Fernandez, M., and Cena, V. (2010). Acetaminophen induces apoptosis in rat cortical neurons. PLoS One *5*, e15360.

Pujol, J., del Hoyo, L., Blanco-Hinojo, L., de Sola, S., Macia, D., Martinez-Vilavella, G., Amor, M., Deus, J., Rodriguez, J., Farre, M.*, et al.* (2015). Anomalous brain functional connectivity contributing to poor adaptive behavior in Down syndrome. Cortex *64*, 148-156.

Qin, H., Buckley, J.A., Li, X., Liu, Y., Fox, T.H., 3rd, Meares, G.P., Yu, H., Yan, Z., Harms, A.S., Li, Y.*, et al.* (2016). Inhibition of the JAK/STAT Pathway Protects Against alpha-Synuclein-Induced Neuroinflammation and Dopaminergic Neurodegeneration. J Neurosci *36*, 5144-5159.

Ram, G., and Chinen, J. (2011). Infections and immunodeficiency in Down syndrome. Clin Exp Immunol *164*, 9-16.

Rao, J.S., Kellom, M., Kim, H.W., Rapoport, S.I., and Reese, E.A. (2012). Neuroinflammation and synaptic loss. Neurochem Res *37*, 903-910.

Raveau, M., Polygalov, D., Boehringer, R., Amano, K., Yamakawa, K., and McHugh, T.J. (2018). Alterations of in vivo CA1 network activity in Dp(16)1Yey Down syndrome model mice. Elife *7*.

Riazi, K., Galic, M.A., Kentner, A.C., Reid, A.Y., Sharkey, K.A., and Pittman, Q.J. (2015). Microglia-dependent alteration of glutamatergic synaptic transmission and plasticity in the hippocampus during peripheral inflammation. J Neurosci *35*, 4942-4952.

Risher, W.C., Ustunkaya, T., Singh Alvarado, J., and Eroglu, C. (2014). Rapid Golgi analysis method for efficient and unbiased classification of dendritic spines. PLoS One *9*, e107591.

Rogers, J.T., Morganti, J.M., Bachstetter, A.D., Hudson, C.E., Peters, M.M., Grimmig, B.A., Weeber, E.J., Bickford, P.C., and Gemma, C. (2011). CX3CR1 deficiency leads to impairment of hippocampal cognitive function and synaptic plasticity. J Neurosci *31*, 16241-16250.

Roizen, N.J., and Patterson, D. (2003). Down's syndrome. Lancet *361*, 1281-1289.

Rosi, S., Belarbi, K., Ferguson, R.A., Fishman, K., Obenaus, A., Raber, J., and Fike, J.R. (2012). Trauma-induced alterations in cognition and Arc expression are reduced by previous exposure to 56Fe irradiation. Hippocampus *22*, 544-554.

Rueda, N., Vidal, V., Garcia-Cerro, S., Narcis, J.O., Llorens-Martin, M., Corrales, A., Lantigua, S., Iglesias, M., Merino, J., Merino, R*., et al.* (2018). Anti-IL17 treatment ameliorates Down syndrome phenotypes in mice. Brain Behav Immun.

Saliba, S.W., Marcotegui, A.R., Fortwangler, E., Ditrich, J., Perazzo, J.C., Munoz, E., de Oliveira, A.C.P., and Fiebich, B.L. (2018). Correction to: AM404, paracetamol metabolite, prevents prostaglandin synthesis in activated microglia by inhibiting COX activity. J Neuroinflammation *15*, 34.

Salter, M.W., and Stevens, B. (2017). Microglia emerge as central players in brain disease. Nat Med *23*, 1018-1027.

Scharkowski, F., Frotscher, M., Lutz, D., Korte, M., and Michaelsen-Preusse, K. (2018). Altered Connectivity and Synapse Maturation of the Hippocampal Mossy Fiber Pathway in a Mouse Model of the Fragile X Syndrome. Cereb Cortex *28*, 852-867.

Schoch, J., Rohrer, T.R., Kaestner, M., Abdul-Khaliq, H., Gortner, L., Sester, U., Sester, M., and Schmidt, T. (2017). Quantitative, Phenotypical, and Functional Characterization of Cellular Immunity in Children and Adolescents With Down Syndrome. J Infect Dis *215*, 1619-1628.

Schultz, S.T., and Gould, G.G. (2016). Acetaminophen Use for Fever in Children Associated with Autism Spectrum Disorder. Autism Open Access *6*.

Seif, F., Khoshmirsafa, M., Aazami, H., Mohsenzadegan, M., Sedighi, G., and Bahar, M. (2017). The role of JAK-STAT signaling pathway and its regulators in the fate of T helper cells. Cell Commun Signal *15*, 23.

Shim, K.S., and Lubec, G. (2002). Drebrin, a dendritic spine protein, is manifold decreased in brains of patients with Alzheimer's disease and Down syndrome. Neurosci Lett *324*, 209-212.

Shobin, E., Bowley, M.P., Estrada, L.I., Heyworth, N.C., Orczykowski, M.E., Eldridge, S.A., Calderazzo, S.M., Mortazavi, F., Moore, T.L., and Rosene, D.L. (2017). Microglia activation and phagocytosis: relationship with aging and cognitive impairment in the rhesus monkey. Geroscience *39*, 199-220.

Sierra, A., Encinas, J.M., Deudero, J.J., Chancey, J.H., Enikolopov, G., Overstreet-Wadiche, L.S., Tsirka, S.E., and Maletic-Savatic, M. (2010). Microglia shape adult hippocampal neurogenesis through apoptosis-coupled phagocytosis. Cell Stem Cell *7*, 483-495.

Sipe, G.O., Lowery, R.L., Tremblay, M.E., Kelly, E.A., Lamantia, C.E., and Majewska, A.K. (2016). Microglial P2Y12 is necessary for synaptic plasticity in mouse visual cortex. Nat Commun *7*, 10905.

Spangenberg, E.E., Lee, R.J., Najafi, A.R., Rice, R.A., Elmore, M.R., Blurton-Jones, M., West, B.L., and Green, K.N. (2016). Eliminating microglia in Alzheimer's mice prevents neuronal loss without modulating amyloid-beta pathology. Brain *139*, 1265-1281.

Squarzoni, P., Thion, M.S., and Garel, S. (2015). Neuronal and microglial regulators of cortical wiring: usual and novel guideposts. Front Neurosci *9*, 248.

Stevens, B., Allen, N.J., Vazquez, L.E., Howell, G.R., Christopherson, K.S., Nouri, N., Micheva, K.D., Mehalow, A.K., Huberman, A.D., Stafford, B.*, et al.* (2007). The classical complement cascade mediates CNS synapse elimination. Cell *131*, 1164-1178.

Streit, W.J., Xue, Q.S., Tischer, J., and Bechmann, I. (2014). Microglial pathology. Acta Neuropathol Commun *2*, 142.

Strittmatter, S.M. (2014). Overcoming Drug Development Bottlenecks With Repurposing: Old drugs learn new tricks. Nat Med *20*, 590-591.

Sullivan, K.D., Evans, D., Pandey, A., Hraha, T.H., Smith, K.P., Markham, N., Rachubinski, A.L., Wolter-Warmerdam, K., Hickey, F., Espinosa, J.M.*, et al.* (2017). Trisomy 21 causes changes in the circulating proteome indicative of chronic autoinflammation. Sci Rep *7*, 14818.

Sullivan, K.D., Lewis, H.C., Hill, A.A., Pandey, A., Jackson, L.P., Cabral, J.M., Smith, K.P., Liggett, L.A., Gomez, E.B., Galbraith, M.D.*, et al.* (2016). Trisomy 21 consistently activates the interferon response. Elife *5*.

Suzuki, K., Sugihara, G., Ouchi, Y., Nakamura, K., Futatsubashi, M., Takebayashi, K., Yoshihara, Y., Omata, K., Matsumoto, K., Tsuchiya, K.J.*, et al.* (2013). Microglial activation in young adults with autism spectrum disorder. JAMA Psychiatry *70*, 49-58.

Takahashi, H., Mizui, T., and Shirao, T. (2006). Down-regulation of drebrin A expression suppresses synaptic targeting of NMDA receptors in developing hippocampal neurones. J Neurochem *97 Suppl 1*, 110-115.

Takashima, S., Iida, K., Mito, T., and Arima, M. (1994). Dendritic and histochemical development and ageing in patients with Down's syndrome. J Intellect Disabil Res *38 (Pt 3)*, 265-273.

Tanaka, Y., Matsuwaki, T., Yamanouchi, K., and Nishihara, M. (2013). Increased lysosomal biogenesis in activated microglia and exacerbated neuronal damage after traumatic brain injury in progranulin-deficient mice. Neuroscience *250*, 8-19.

Tang, H., Ji, M., Zong, M., Jia, M., Luo, D., Zhou, Z., and Yang, J. (2018). Individual differences in the brain are associated with resilience versus susceptibility to lipopolysaccharide-induced memory impairment. Neurosci Lett *662*, 361-367.

Tay, T.L., Bechade, C., D'Andrea, I., St-Pierre, M.K., Henry, M.S., Roumier, A., and Tremblay, M.E. (2017a). Microglia Gone Rogue: Impacts on Psychiatric Disorders across the Lifespan. Front Mol Neurosci *10*, 421.

Tay, T.L., Savage, J.C., Hui, C.W., Bisht, K., and Tremblay, M.E. (2017b). Microglia across the lifespan: from origin to function in brain development, plasticity and cognition. J Physiol *595*, 1929-1945.

Tchessalova, D., Posillico, C.K., and Tronson, N.C. (2018). Neuroimmune Activation Drives Multiple Brain States. Front Syst Neurosci *12*, 39.

Teipel, S.J., Schapiro, M.B., Alexander, G.E., Krasuski, J.S., Horwitz, B., Hoehne, C., Moller, H.J., Rapoport, S.I., and Hampel, H. (2003). Relation of corpus callosum and hippocampal size to age in nondemented adults with Down's syndrome. Am J Psychiatry *160*, 1870-1878.

Tetreault, N.A., Hakeem, A.Y., Jiang, S., Williams, B.A., Allman, E., Wold, B.J., and Allman, J.M. (2012). Microglia in the cerebral cortex in autism. J Autism Dev Disord *42*, 2569-2584.

Todd, M.A. (2017). Inflammation and Cognition in Older Adults: Evidence from Taiwan. Biodemography Soc Biol *63*, 309-323.

Torres, M.D., Garcia, O., Tang, C., and Busciglio, J. (2018). Dendritic spine pathology and thrombospondin-1 deficits in Down syndrome. Free Radic Biol Med *114*, 10-14.

Tremblay, M.E., Stevens, B., Sierra, A., Wake, H., Bessis, A., and Nimmerjahn, A. (2011). The role of microglia in the healthy brain. J Neurosci *31*, 16064-16069.

Tyanova, S., Temu, T., Sinitcyn, P., Carlson, A., Hein, M.Y., Geiger, T., Mann, M., and Cox, J. (2016). The Perseus computational platform for comprehensive analysis of (prote)omics data. Nat Methods *13*, 731-740.

Vacano, G.N., Gibson, D.S., Turjoman, A.A., Gawryluk, J.W., Geiger, J.D., Duncan, M., and Patterson, D. (2018). Proteomic analysis of six- and twelve-month hippocampus and cerebellum in a murine Down syndrome model. Neurobiol Aging *63*, 96-109.

Valentini, D., Marcellini, V., Bianchi, S., Villani, A., Facchini, M., Donatelli, I., Castrucci, M.R., Marasco, E., Farroni, C., and Carsetti, R. (2015). Generation of switched memory B cells in response to vaccination in Down syndrome children and their siblings. Vaccine *33*, 6689-6696.

van Berckel, B.N., Bossong, M.G., Boellaard, R., Kloet, R., Schuitemaker, A., Caspers, E., Luurtsema, G., Windhorst, A.D., Cahn, W., Lammertsma, A.A*., et al.* (2008). Microglia activation in recent-

onset schizophrenia: a quantitative (R)-[11C]PK11195 positron emission tomography study. Biol Psychiatry *64*, 820-822.

Vargas, D.L., Nascimbene, C., Krishnan, C., Zimmerman, A.W., and Pardo, C.A. (2005). Neuroglial activation and neuroinflammation in the brain of patients with autism. Ann Neurol *57*, 67-81.

Velazquez, R., Ash, J.A., Powers, B.E., Kelley, C.M., Strawderman, M., Luscher, Z.I., Ginsberg, S.D., Mufson, E.J., and Strupp, B.J. (2013). Maternal choline supplementation improves spatial learning and adult hippocampal neurogenesis in the Ts65Dn mouse model of Down syndrome. Neurobiol Dis *58*, 92-101.

Viberg, H., Eriksson, P., Gordh, T., and Fredriksson, A. (2014). Paracetamol (acetaminophen) administration during neonatal brain development affects cognitive function and alters its analgesic and anxiolytic response in adult male mice. Toxicol Sci *138*, 139-147.

Villa, V., Thellung, S., Bajetto, A., Gatta, E., Robello, M., Novelli, F., Tasso, B., Tonelli, M., and Florio, T. (2016). Novel celecoxib analogues inhibit glial production of prostaglandin E2, nitric oxide, and oxygen radicals reverting the neuroinflammatory responses induced by misfolded prion protein fragment 90-231 or lipopolysaccharide. Pharmacol Res *113*, 500-514.

Vizcaino, J.A., Csordas, A., del-Toro, N., Dianes, J.A., Griss, J., Lavidas, I., Mayer, G., Perez-Riverol, Y., Reisinger, F., Ternent, T.*, et al.* (2016). 2016 update of the PRIDE database and its related tools. Nucleic Acids Res *44*, D447-456.

Wadhwa, M., Prabhakar, A., Ray, K., Roy, K., Kumari, P., Jha, P.K., Kishore, K., Kumar, S., and Panjwani, U. (2017). Inhibiting the microglia activation improves the spatial memory and adult neurogenesis in rat hippocampus during 48 h of sleep deprivation. J Neuroinflammation *14*, 222.

Wang, W.Y., Tan, M.S., Yu, J.T., and Tan, L. (2015). Role of pro-inflammatory cytokines released from microglia in Alzheimer's disease. Ann Transl Med *3*, 136.

Weitzdoerfer, R., Dierssen, M., Fountoulakis, M., and Lubec, G. (2001). Fetal life in Down syndrome starts with normal neuronal density but impaired dendritic spines and synaptosomal structure. J Neural Transm Suppl, 59-70.

Wierzba-Bobrowicz, T., Lewandowska, E., Schmidt-Sidor, B., and Gwiazda, E. (1999). The comparison of microglia maturation in CNS of normal human fetuses and fetuses with Down's syndrome. Folia Neuropathol *37*, 227-234.

Wilcock, D.M., and Griffin, W.S. (2013). Down's syndrome, neuroinflammation, and Alzheimer neuropathogenesis. J Neuroinflammation *10*, 84.

Wisniewski, J.R., Zougman, A., and Mann, M. (2009). Combination of FASP and StageTip-based fractionation allows in-depth analysis of the hippocampal membrane proteome. J Proteome Res *8*, 5674-5678.

Wu, H.F., Chen, P.S., Hsu, Y.T., Lee, C.W., Wang, T.F., Chen, Y.J., and Lin, H.C. (2018). D-Cycloserine Ameliorates Autism-Like Deficits by Removing GluA2-Containing AMPA Receptors in a Valproic Acid-Induced Rat Model. Mol Neurobiol *55*, 4811-4824.

Wu, Y., Dissing-Olesen, L., MacVicar, B.A., and Stevens, B. (2015). Microglia: Dynamic Mediators of Synapse Development and Plasticity. Trends Immunol *36*, 605-613.

Xavier, A.L., Lima, F.R., Nedergaard, M., and Menezes, J.R. (2015). Ontogeny of CX3CR1-EGFP expressing cells unveil microglia as an integral component of the postnatal subventricular zone. Front Cell Neurosci *9*, 37.

Xing, B., Bachstetter, A.D., and Van Eldik, L.J. (2011). Microglial p38alpha MAPK is critical for LPS-induced neuron degeneration, through a mechanism involving TNFalpha. Mol Neurodegener *6*, 84.

Xu, B., Sun, A., He, Y., Qian, F., Xi, S., Long, D., and Chen, Y. (2018). Loss of thin spines and small synapses contributes to defective hippocampal function in aged mice. Neurobiol Aging *71*, 91-104.

Xu, X., and Pozzo-Miller, L. (2017). EEA1 restores homeostatic synaptic plasticity in hippocampal neurons from Rett syndrome mice. J Physiol *595*, 5699-5712.

Xue, Q.S., and Streit, W.J. (2011). Microglial pathology in Down syndrome. Acta Neuropathol *122*, 455-466.

Youn, H., Jeoung, M., Koo, Y., Ji, H., Markesbery, W.R., Ji, I., and Ji, T.H. (2007). Kalirin is under-expressed in Alzheimer's disease hippocampus. J Alzheimers Dis *11*, 385-397.

Yu, T., Liu, C., Belichenko, P., Clapcote, S.J., Li, S., Pao, A., Kleschevnikov, A., Bechard, A.R., Asrar, S., Chen, R.*, et al.* (2010). Effects of individual segmental trisomies of human chromosome 21 syntenic regions on hippocampal long-term potentiation and cognitive behaviors in mice. Brain Res *1366*, 162-171.

Zauber, H., Kirchner, M., and Selbach, M. (2018). Picky: a simple online PRM and SRM method designer for targeted proteomics. Nat Methods *15*, 156-157.

Zhang, D., Hu, X., Qian, L., Wilson, B., Lee, C., Flood, P., Langenbach, R., and Hong, J.S. (2009). Prostaglandin E2 released from activated microglia enhances astrocyte proliferation in vitro. Toxicol Appl Pharmacol *238*, 64-70.

Zhang, Y., Che, M., Yuan, J., Yu, Y., Cao, C., Qin, X.Y., and Cheng, Y. (2017). Aberrations in circulating inflammatory cytokine levels in patients with Down syndrome: a meta-analysis. Oncotarget *8*, 84489-84496.

Zhang, Z.W. (2004). Maturation of layer V pyramidal neurons in the rat prefrontal cortex: intrinsic properties and synaptic function. J Neurophysiol *91*, 1171-1182.

Zhao, W.X., Zhang, J.H., Cao, J.B., Wang, W., Wang, D.X., Zhang, X.Y., Yu, J., Zhang, Y.Y., Zhang, Y.Z., and Mi, W.D. (2017). Acetaminophen attenuates lipopolysaccharide-induced cognitive impairment through antioxidant activity. J Neuroinflammation *14*, 17.

APPENDIX I

NEGR1 and FGFR2 cooperatively regulate cortical development and core behaviours related to autism disorders in mice.

Joanna Szczurkowska*, Francesca Pischedda*, Bruno Pinto*, Francesca Managò, Carola A Haas, Maria Summa, Rosalia Bertorelli, Francesco Papaleo, Michael K Schäfer, Giovanni Piccoli, Laura Cancedda.

***Equal contribution.**

APPENDIX II

In vivo methods for acute modulation of gene expression in the central nervous system.

Andrzej W. Cwetsch*, Bruno Pinto*, Annalisa Savardi*, Laura Cancedda.

***Equal contribution.**

Europe PMC Funders Group
Author Manuscript
Prog Neurobiol. Author manuscript; available in PMC 2018 September 01.

Published in final edited form as:
Prog Neurobiol. 2018 September ; 168: 69–85. doi:10.1016/j.pneurobio.2018.04.008.

In vivo methods for acute modulation of gene expression in the central nervous system

Andrzej W. Cwetsch[#a,b], **Bruno Pinto**[#a,c], **Annalisa Savardi**[#a,b], and **Laura Cancedda**[a,d,*]

[a]Local Micro-environment and Brain Development Laboratory, Istituto Italiano di Tecnologia, via Morego, 30, 16163 Genova, Italy

[b]Università degli Studi di Genova, Via Balbi, 5, 16126 Genova, Italy

[c]Bio@SNS, Scuola Normale Superiore, Piazza dei Cavalieri 7, 56126, Pisa, Italy

[d]DulbeccoTelethon Institute, Italy

[#] These authors contributed equally to this work.

Abstract

Accurate and timely expression of specific genes guarantees the healthy development and function of the brain. Indeed, variations in the correct amount or timing of gene expression lead to improper development and/or pathological conditions. Almost forty years after the first successful gene transfection in *in vitro* cell cultures, it is currently possible to regulate gene expression in an area-specific manner at any step of central nervous system development and in adulthood in experimental animals *in vivo*, even overcoming the very poor accessibility of the brain. Here, we will review the diverse approaches for acute gene transfer *in vivo*, highlighting their advantages and disadvantages with respect to the efficiency and specificity of transfection as well as to brain accessibility. In particular, we will present well-established chemical, physical and virus-based approaches suitable for different animal models, pointing out their current and future possible applications in basic and translational research as well as in gene therapy.

Keywords

In vivo genetic manipulations; Nanoparticles; Polymers; Electroporation; Sonoporation; Viruses

1 Introduction

Proper development of the central nervous system (CNS) determines its function and consequent behaviors. Accordingly, numerous gene alterations during development lead to brain disorders characterized by a variety of abnormal behaviors, often depending on which brain area is mostly affected. On the other hand, gene alterations during adulthood may also lead to a variety of brain-related diseases and neurodegenerative disorders that vary in their symptoms, depending on the affected brain areas. This complexity highlights the need for

This is an open access article under the CC BY-NC-ND license (http://creativecommons.org/licenses/BY-NC-ND/4.0/).
*Corresponding author. laura.cancedda@iit.it (L. Cancedda).

Europe PMC Funders Author Manuscripts

Europe PMC Funders Author Manuscripts

temporal and spatial regulation of specific genes for proper brain function. Accordingly, the development of reliable techniques for gene transfection *in vivo* has recently attracted the attention of an increasing number of researchers as a means to study and understand the roles of the diverse genes underlying the basic mechanisms of CNS development and function (basic research) and to study genes involved in CNS disorders to find new possible treatments (translational research). In particular, in recent years, basic research has benefited from new tools for gene editing (*e.g.*, CRISPR-Cas9 technology; Ahmad et al., 2018) and neuronal-activity modulation (optogenetics and chemogenetics; Dobrzanski and Kossut, 2017; Towne and Thompson, 2016), which both need to be coupled to a nucleic acid delivery system. For translational research, a fast-growing field of study focuses on the possibility of treating CNS disorders by manipulating gene expression (gene therapy) rather than by classical pharmacology, which has proven highly ineffective in the last 10 years (Gribkoff and Kaczmarek, 2017). Thus, regardless of the final application, the development of novel methods for modulating gene expression *in vivo* has acquired increasing importance in recent years. This modulation can be achieved either by the generation of genetically modified animals or by acute procedures for gene expression modulation. Here, we will only review the latter.

Generally, an acute modulation of gene expression requires a transfection or transduction process (*i.e.*, a procedure that introduces foreign nucleic acids, such as DNA/RNA, into a cell) to produce genetically modified cells or organisms by nonviral or viral methods, respectively. Indeed, many molecules, such as nucleic acids and certain drugs, are not able to diffuse through the lipophilic cell membrane due to their physicochemical properties (*e.g.*, hydrophilicity, charge) and/or size. Thus, the support of specific carriers or chemical/physical stimulation is often necessary to increase the efficiency of the transfection process.

Although highly efficient, acute introduction of DNA into mammalian cells *in vitro* was achieved a long time ago (Graham and van der Eb, 1973), for the last four decades, scientists have struggled to increase the efficiency of this process *in vivo* (Crystal, 2014). For example, circulating nucleic acids for transfection have a very short half-life *in vivo* because they are degraded by circulating nucleases in the blood. Moreover, targeting specific organs and cell types at discrete times is generally challenging *in vivo* and is particularly difficult in the case of the brain for a number of reasons. First, the brain is an isolated, inaccessible environment due to the presence of the skull and the blood-brain barrier (BBB), which separates circulating blood from the brain's extracellular fluid. Second, the brain contains several different areas that are each characterized by specific functions, rendering area-specific transfection crucial in this organ. Third, the CNS contains hundreds of billions of neuronal and glial cells characterized by high diversity (*e.g.*, even among neurons, there is a wide variety of diverse types with diverse functions). Finally, neurons are postmitotic cells that do not divide, requiring a cell cycle-independent introduction of genetic material.

Since almost ninety-five percent of the animals used in research are mice and rats (Badyal and Desai, 2014), we will focus this review on rodents. For a long time, the dominant approach for acute gene transfer *in vivo* in rodents was the design of different viral vectors with increasingly higher efficiency of transfection and tissue specificity (see viral methods below). Nevertheless, due to limitations related to the safety of viral gene transfer, many

Europe PMC Funders Author Manuscripts

Europe PMC Funders Author Manuscripts

physical strategies have also been adopted, such as electroporation and sonoporation (see physical methods below). However, physical methods require strong conditions (*e.g.*, strong electric field or ultrasound) for efficient transfection, and thus a range of synthetic carriers for nucleic acids suited for chemical transfection have also been created (see chemical methods below; Yin et al., 2014). In recent years, different methods have also been combined (*e.g.*, physical and chemical methods or viruses and physical methods) to try to overcome the shortcomings of one method *vs* the other while taking advantage of the positive features of both.

In this review, we describe the currently available methods for the delivery of nucleic acids to the CNS *in vivo*. First, we focus on chemical methods, which include a wide selection of nucleic acid carriers that allow crossing of the cell membrane. Second, we describe physical methods, which take advantage of physical forces to increase membrane permeability and possibly direct nucleic acids to the desired location. Third, we address viral-based techniques, which explore the intrinsic transfection ability of viruses. Interestingly, all of the described techniques are very different, but they each present some level of overlap, creating a great portfolio to choose from when designing diverse experiments with gene transfer *in vivo*. Here, we will note the advantages and disadvantages of each described method and will indicate their best-suited applications.

2 Chemical methods for transfection

Chemical methods of transfection are a set of techniques that rely on external carriers characterized by specific chemical properties that are essential for transfection of the exogenous nucleic acids of interest (Table 1). In particular, chemical carriers are prepared to favor the formation of complexes with the nucleic acids and internalization by endocytosis in the target cells. There, the genetic material is released into the cytoplasm through endosomal escape and subsequently enters the nucleus for transcription into messenger RNA (mRNA), followed by translation into functional proteins in the cytoplasm (Fig. 1). Chemical methods often have good gene-packaging capacity and low immunogenicity and toxicity, and they are relatively safe for the operator (Zhi et al., 2018). Nevertheless, most chemical methods have low efficiency, and they still rely on invasive methods of administration for *in vivo* applications (*e.g.*, intrathecal/intraventricular injections). Only recently, the rapid development of materials science and nanoscience has allowed the construction of more efficient chemical vectors for *in vivo* transfection; these vectors are useful for not only basic research but also the biomedical field (Glover et al., 2005; Lu and Jiang, 2017; Ramamoorth and Narvekar, 2015; Yin et al., 2014). Here, we will focus on three main groups of chemicals that are often used as vectors.

2.1 Lipids

The use of lipid carriers for transfection (*i.e.*, lipofection) for *in vitro* cell delivery has been widespread since the 1980s (Fraley et al., 1980; Lu et al., 1989). Cationic lipids – the most commonly used lipids – are synthetic lipids with a positively charged hydrophilic domain connected by a linker to a long lipophilic tail. During transfection, the negatively charged phosphate on the backbone of the nucleic acids interacts with the hydrophilic domain on the

Europe PMC Funders Author Manuscripts

Europe PMC Funders Author Manuscripts

lipid, creating a structure called *lipoplex* (2–200 nm in diameter; (Higuchi et al., 2006; Inoh et al., 2017; Ramamoorth and Narvekar, 2015; Ross and Hui et al., 1999)). Once the lipoplex reaches the cell membrane, it is internalized by endocytosis, and the genetic material is then released from the endosomes inside the cell (Nayerossadat et al., 2012; Fig. 1). Although the highly positive charge on the surface of the lipids protects the genetic material from cleavage by circulating endonucleases (Ramamoorth and Narvekar, 2015), lipid-based vectors still suffer from a short half-life *in vivo* because. This is due to the rapid degradation of lipid particles by the reticuloendothelial system, which is composed of phagocytic cells located in connective tissues (Nayerossadat et al., 2012; Petschauer et al., 2015; Song et al., 2014). To overcome this issue, the DNA and cationic lipid mixture is often supplemented with so-called helper lipids (the most common being polyethylene glycol (PEG) and 1,2-dioleoyl-phosphatidyl-ethanolamine (DOPE)). These are neutral lipids that increase the lipoplex's stability, thus increasing its serum half-life. Moreover, the addition of helper lipids also increases the fusion between the lipid particle and the cell membrane and facilitates the movement of genetic material between the endosomes and the cell nucleus (Hassani et al., 2005; Nayerossadat et al., 2012; Yin et al., 2014; Zhi et al., 2018). Finally, depending on the composition of the cationic lipid mixture and the concentration of the genetic material, lipoplexes may assume different tertiary structures that may favor transfection efficiency. This structural variation is mainly due to different charge distributions on their surface and different areas of interaction with the cell. For example, the hexagonal phases of a lipoplex can spontaneously release the DNA content when these lipoplexes are in contact with an anionic vesicle, whereas a multilamellar vesicular structure (where the genetic material is sandwiched between lipid multilayers) tends not to release its contents. Interestingly, the transition from multilamellar to hexagonal structures is favored by the addition of DOPE to the lipid-DNA mixtures (Dan, 2015; Ma et al., 2007). Due to all these practices that increase transfection efficiency, lipids have proven to be efficient *in vivo* for gene transfection by direct injection in the ventricle or brain of mice (Hassani et al., 2005; Roessler and Davidson et al., 1994). Moreover, lipids have been used as a gene-delivery method for the treatment of glioblastomas by intratumoral injection (Cikankowitz et al., 2017; Lagarce and Passirani, 2016; Pulkkanen and Yla-Herttuala, 2005).

Another structural arrangement that may occur among cationic lipids is a *nanoemulsion*. A lipid nanoemulsion (LNE) is a dispersion of nanoparticles of lipids (100–400 nm in diameter) in a liquid phase that is obtained *in vitro* by the addition of a surfactant agent to prevent the lipids from coalescing into a macroscopic phase. The main advantages of LNEs include easy processing, low costs and easy scale up to large-scale production (Liu and Yu et al., 2010; Ramamoorth and Narvekar, 2015). LNEs have been successfully used *in vitro*, showing a higher efficiency than liposomes (Liu and Yu et al., 2010). The usage of nanoemulsions *in vivo* is becoming more popular due to their low toxicity and high stability (Ramamoorth and Narvekar, 2015). For example, successful delivery of tumor necrosis factor alpha (TNF-α) small interfering RNA (siRNA) to treat lipopolysaccharide (LPS)-induced neuroinflammation has been achieved in rats (Kim et al., 2010). Of note, the small dimension of the nanoparticles has also allowed intranasal delivery, a convenient way of overcoming the impermeability of the BBB and preventing the action of blood-circulating nucleases that may digest the DNA of interest (Yadav et al., 2016).

Europe PMC Funders Author Manuscripts

Europe PMC Funders Author Manuscripts

Lastly, lipid carriers have also been recently used in the form of *solid lipid nanoparticles* (SLNs). SLNs are lipid nanospheres (70–230 nm in diameter) with an outer hydrophilic shell made of a phospholipid double layer and an inner core containing long-chained lipids, generating particles that are solid and stable at body temperature (Kaur et al., 2008). In the last decade, there has been increased interest in the use of these nanoparticles for gene delivery, mainly due to their stability and biocompatibility (Pathak et al., 2017). Interestingly, SLNs were used to deliver siRNAs against c-met in a murine model of glioblastoma *via* intravenous injection *in vivo*, and the treatment showed positive outcomes (Jin et al., 2011). This result highlights the fact that SLNs are very stable and may cross the BBB, making them a very desirable vector for *in vivo* gene transfection in the brain.

2.2 Nanoparticles

With the rapid development of nanotechnology in the last decade, the use of nanoparticles as a gene-delivery tool has quickly grown. The main advantage of this kind of carrier is its high stability, great protection against circulating nucleases and low risk of toxicity (Bharali et al., 2005). Here, we will focus on the most studied nanoparticles.

2.2.1 Silica and gold nanoparticles—*Silica* (an oxide of silicon) is a very malleable material that finds applications in all realms of science and engineering. Silica nanoparticles are spheres (30 nm in diameter) that can be relatively easily made and modified during synthesis. In particular, silica nanoparticles coated with organic amino acids can interact with nucleic acids and can protect the genetic material from endonucleases. *In vitro* studies have shown that upon phagocytosis, coated silica nanoparticles can then be internalized, subsequently releasing DNA (Kneuer et al., 2000a, b). Interestingly, silica nanoparticles have also been used to study the development of newly born neurons *in vivo* by transfecting an EFGFR1-coding plasmid in the subventricular zone of adult mice with no signs of cell degeneration or systemic or brain-specific toxicity (Bharali et al., 2005; Luo and Saltzman, 2006). However, a recent report showed signs of neuroinflammation in rats following intranasal administration of silica nanoparticles (Parveen et al., 2017). Further studies on the effect of these vectors in the brain are necessary.

Gold nanoparticles are also used as vectors for gene delivery, as gold has been extensively studied in a biological context due to its very low toxicity and its capability to bind a wide array of organic molecules. In particular, some *in vitro* studies have shown that gold nanoparticles coated with organic cationic molecules are able to bind nucleic acids and are endocytosed, providing efficient delivery of the genetic material (Bishop et al., 2015; Connor et al., 2005; Ekin et al., 2014; Jensen et al., 2013; Levy et al., 2010; Peng et al., 2016). In addition, gold nanoparticles also display strong and tunable optical properties that have been tested *in vitro* (Pissuwan et al., 2011; Wijaya and Hamad-Schifferli, 2008). Interestingly, gold nanoparticles can possibly cross the BBB, as tested in not only an *in vitro* model of the BBB (Bonoiu et al., 2009) but also *in vivo* (Jensen et al., 2013). In particular, successful transfection of a siRNA against the antiapoptotic gene Bcl2 L12 was achieved in glioma cells upon systemic injection of gold nanoparticles in mice. Notably, the siRNA showed little enzymatic degradation (Jensen et al., 2013). Recently, gold nanoparticles functionalized with PEG or other long organic molecules showed much higher BBB

Europe PMC Funders Author Manuscripts

Europe PMC Funders Author Manuscripts

permeability (Escudero-Francos et al., 2017; Takeuchi et al., 2018). Remarkably, gold nanoparticles were also used to downregulate α-synuclein in a murine model of Parkinson's disease following intraperitoneal injection and had positive outcomes on anatomical landmarks of Parkinson's (Hu et al., 2018).

2.2.2 Fullerenes—Fullerenes are carbon molecules of various shapes and dimensions: spherical fullerenes (SFs) are called Buckminster fullerenes, whereas cylindrical fullerenes with a hollow core are called carbon nanotubes (CNTs). The incredible properties of fullerenes, such as high thermal and electrical conductivity, great strength, and rigidity, put these molecules at the forefront of the fast-developing nanoengineering industry (Yang et al., 2006). Moreover, *SF*s can be functionalized with cationic charges and thus can stably condense double-stranded DNA into globules (< 100 nm in diameter), which are protective against intracellular and circulating nucleases. Nevertheless, the only known *in vivo* application to date of SFs is the successful delivery of the Insulin 2 gene directly to the liver in mice with no signs of systemic toxicity (Maeda-Mamiya et al., 2010). Finally, it has been reported that SFs are able to cross the BBB, although there are no reports of their use to deliver genes to the CNS (Quick et al., 2008).

Additionally, *CNTs* have been studied as a possible vector for gene delivery. Nevertheless, applying their use to the biomedical realm has proven difficult because CNTs are poorly soluble in water. One strategy to increase their water solubility is functionalization of their surface. Indeed, CNTs functionalized with peptides and conjugated to DNA or RNA are able to successfully penetrate the cell membrane, and the DNA-functionalized CNTs are able translocate to the nucleus in *in vitro* systems (Lacerda et al., 2008; Pantarotto et al., 2004; Singh et al., 2005). Nevertheless, the *in vivo* application of CNTs is still in its early stages (Lacerda et al., 2008; Zhang et al., 2014). Notably, Khuloud et al. transfected the brain cortex in a rat model of ischemia with CNTs functionalized with siRNA for Caspase 3. This treatment successfully decreased the apoptotic cells around the lesion, with amelioration of motor deficits in the operated rats (Al-Jamal et al., 2011; Costa et al., 2016). Thus, although the application of fullerenes in biology is still in its infancy, it is clear that these carbon nanomolecules offer a new, interesting perspective on the upcoming development of gene-delivery vectors (Montellano et al., 2011)

2.3 Polymers

Polymers are macromolecules composed of repeated units. Similar to lipoplexes, the polymers used for gene delivery have a positively charged surface that interacts with the negatively charged backbone of nucleic acids to form complexes called polyplexes. Among the polymer materials used for transfection, *polyethylenimine* (PEI) is one of the most effective vectors *in vitro* and *in vivo* (Pack et al., 2005). PEI is a synthetic, water-soluble polymer (0.8 −1000 kDa in molecular weight), and its structural complexity can vary from linear to highly branched (Ewe et al., 2016; Ramamoorth and Narvekar, 2015). PEIs are internalized through phagocytosis by cells and can avoid endosome digestion/degradation *via* a proton-sponge effect. Due to their highly positive charge (derived from the large number of partially protonated amino groups that they possess), PEIs can stop the natural acidification of the endosome, generating strong osmotic imbalances, ultimately causing

Europe PMC Funders Author Manuscripts

Europe PMC Funders Author Manuscripts

endosome rupture and release of the polymer and the conjugated genetic material into the cytoplasm. Moreover, the highly positive charge acts as a protective factor against the action of cytoplasmatic nucleases (Ewe et al., 2016). Interestingly, many studies showed promising prospects for the use of PEI *in vivo*. For example, in a classic study, PEI-based vectors were used to successfully and safely deliver luciferase DNA to the brain through intracortical and intrahippocampal injections with no animal morbidity (Abdallah et al., 1996). Since then, PEI-based vectors have been used to deliver genetic material to different CNS regions, such as the spinal cord (Shi et al., 2003; Shimamura et al., 2004), the cortex in a murine model of ischemia (Oh et al., 2017) and stem cells located in the subventricular zone (Lemkine et al., 2002). The delivery occurred by direct brain injection since PEI-based vectors were believed not to cross the BBB (Lungwitz et al., 2005). Recently, a PEI-based vector was used to successfully downregulate α-synuclein using a specific siRNA in a rat model of Parkinson's disease after one single intraventricular injection (Helmschrodt et al., 2017).

To overcome the potential low BBB permeability, PEI was linked to a peptide from the rabies virus (RVG), and this method was used to successfully deliver microRNA to the brain *in vivo* following tail injection (Hwang et al., 2011). Moreover, PEI functionalized with PEG was used to deliver a plasmid coding the gene CD200 in a mouse model of multiple sclerosis (CD200 shows decreased expression in this condition). Notably, the PEI-based carrier functionalized with PEG was able to cross the BBB (Nouri et al., 2017). Remarkably, the transfection of hypoglossal motor neurons was achieved by retrograde axonal transport, which followed the injection of PEI complexed with DNA into the tongue of an experimental rat (Wang et al., 2001).

Despite the abovementioned successes, further use of PEI for *in vivo* transfection has been hindered by the relatively high toxicity of this polymer and its low rate of uptake by living cells, leading to low transfection efficiency. Thus, in the past few years, attention has turned to less toxic polymers, such as *chitosans*. Chitosans are natural polymers made of randomly distributed β-(1-4)-linked D-glucosamine and N-acetyl-D-glucosamine and are considered very attractive vectors for gene delivery *in vivo*. Indeed, chitosans are nontoxic at all concentrations and can be efficiently functionalized (Duceppe and Tabrizian, 2010; Ramamoorth and Narvekar, 2015). For example, PEGylated chitosan polymers were used to deliver siRNA against Galectine-1 and EGFR, two genes known to increase the resistance of glioblastoma cells to treatment with temozolomide. The delivery, which was performed by intratumoral injection, resulted in an increased survival rate of the animals (Danhier et al., 2015). Although chitosan-based polymers cannot readily cross the BBB, this issue was overcome by extensively modifying the chitosan structure. In particular, chitosans were first trimethylated, generating a trimethylated chitosan (TMC), which increased the solubility and siRNA binding to the polymer. Subsequently, PEG was conjugated to TMC. Similar to the reports for lipid-based delivery methods, the addition of PEG increased the biocompatibility and serum stability of the construct. Notably, upon intravenous administration, the specific delivery of Cy5.5-siRNA (a fluorescent probe used to visualize RNA) to the brain *in vivo* was obtained by adding a fragment derived from a rabies virus glycoprotein to PEG-modified TMC (Gao et al., 2014). Remarkably, chitosan-based vectors were used to transfect HIV-infected astrocytes with siRNA against genes necessary for viral replication, successfully halting the HIV infection. In this study, the chitosan nanoparticles were

Europe PMC Funders Author Manuscripts

Europe PMC Funders Author Manuscripts

conjugated to antibodies that could bind to the transferrin receptor in the BBB strongly, increasing the permeability of the brain to the vectors (Gu et al., 2017).

Another class of polymers is *dendrimers*, highly branched synthetic polymers that have been growing in popularity in biomedical research. This interest is mainly due to their well-defined structure and high density of easily modifiable functional groups (Hu et al., 2016). Topologically, dendrimers are composed of a core, and the branching is organized around this core, forming a spherical structure that is usually positively charged with modifiable functional groups on the surface. Due to their high density of positive charges, dendrimers escape the endosome through the "proton sponge mechanism", similar to PEI-based polymers (Hu et al., 2016). Among the large array of dendrimers, the most commonly used and the best-characterized one is polyamidoamine (PAMAM; (Hu et al., 2016; Pack et al., 2005)). PAMAM has been extensively used *in vitro* due to its low cytotoxicity (Eichman et al., 2000). To increase gene transfer efficiency and biocompatibility, many functionalizations of PAMAM have been performed; these functionalizations include the substitution of positive charges with arginine groups (Choi et al., 2004), PEG (Luo and Saltzman, 2006; Wang et al., 2009), and pyridine/histidine (Hashemi et al., 2016) and the addition of hydrophobic chains, including lauroyl (Santos et al., 2010). Nevertheless, as a positively charged hydrophilic molecule, PAMAM cannot cross the BBB *in vivo*. To circumvent this problem, PAMAM was functionalized with PEG and SRL, a small, artificially generated peptide, and was able to cross the BBB. After internalization by phagocytosis and interaction with the low-density lipoprotein receptor-related protein (LRP) on the BBB, PAMAMs functionalized with SRL were able to efficiently transfect neurons *in vivo* with a plasmid DNA coding EGFP following their intravenous injection in the tail of mice (Zarebkohan et al., 2015). Similarly, different peptides that present high brain penetration, such as angiopep-2 (Ke et al., 2009), lactoferrin (Huang et al., 2008) and transferrin (Huang et al., 2007), were used to transfect brain cells *in vivo*. Thus, due to its possible functionalizations and increased BBB permeation, PAMAM potentially has great promise in applications as a gene-delivery vector *in vivo*.

3 Physical methods for transfection

Physical methods are a collection of nonviral techniques for cell transfection that rely on physical stimulation to deliver and direct genetic material inside the living cell (Table 2). Physical methods promote reversible alterations in the cell plasma membrane or endocytosis to allow the direct passage of the molecules of interest into the cell, either alone or with the support of chemical carriers, as described above (Fig. 2). Physical stimulations can, at least in part, overcome many of the side effects linked to biochemical or viral techniques. In particular, the lack of toxicity, the lack of limitations on the length of the coding sequence, and the low costs are among the main advantages. Physical methods have outstanding experimental value in basic brain research. On the other hand, their potential translational application in gene therapy is heavily hampered by the invasiveness of their procedures (*e.g.*, the application of strong electric fields and intraventricular injections) and their low efficiency when DNA delivery is performed systemically (*e.g.*, reduced brain accessibility through the BBB).

Europe PMC Funders Author Manuscripts

Europe PMC Funders Author Manuscripts

The first successful *in vitro* gene transfer supported by physical stimulation was performed in 1980 with transfers into mouse glioma cells by electroporation. The same approach was used for the first *in vivo* transfection in skin cells of mice (Titomirov et al., 1991). Over the years, other physical methods were proposed for *in vivo* gene transfer, including magnet-assisted transfection (Mah et al., 2002b; Scherer et al., 2002) and ultrasound application (Sheyn et al., 2008).

3.1 Electroporation

The electroporation technique was already used *in vitro* in the 1980s (Neumann et al., 1982; Potrykus et al., 1985; Potter, 1988) as an acute, quick, easy, highly efficient, low cost and mostly nontoxic procedure to transfect bacteria and most cell types and to create transgenic plants. Electroporation enables the transfection of large, highly charged molecules that cannot passively diffuse across the lipophilic cell membrane by creating temporary water-filled holes in the membrane (20–120 nm in diameter; (Chang and Reese et al., 1990)) through the application of a series of electric-field pulses. Moreover, application of the electric field also directs the charged molecules for transfection towards the anode side, thus driving them in the desired direction towards the area where the cells of interest are located. Conveniently, once the exposure to the electric pulse is completed, the cell membrane reorganizes by closing the temporary hydrophilic pores and returning to its physiological structure, which traps the exogenous material inside the cell. Recently, the electroporation technique has evolved into diverse applications *in vivo (in* and *ex ovo, in* and *ex utero*, as well as postnatal electroporation) with one of the main advantages being the fast onset of expression of the protein encoded by the transfected DNA. In general, all the *in vivo* electroporation methods for the CNS share the same concept: the DNA solution is injected into the lumen of the CNS ventricular system. Indeed, at the interface between the lumen of the ventricular system and the brain, there is a neuroepithelium where the neuronal progenitors of different brain areas are located. Thus, following exposure to an electric field applied by a multipolar electrode, negatively charged DNA is directed towards the positively charged electrode and incorporated in the specific populations of neuronal progenitor cells. Those progenitors will generate newly born neurons committed to different brain areas, where the neurons will start migrating upon birth, eventually allowing transfection of those discrete brain regions.

3.1.1 *In utero, exo utero* and postnatal electroporation—

In vivo electroporation was applied as a gene transfer method in 1997 in chick embryos *in ovo* (Muramatsu et al., 1997). Just four years later, the first CNS transfections of mouse and rat embryos were performed using *in utero* and *exo utero* electroporation (Fukuchi-Shimogori and Grove et al., 2001; Saito and Nakatsuji, 2001; Tabata and Nakajima, 2001).

The *in utero* electroporation (IUE) technique is based on the direct injection of exogenous nucleic acids into the ventricular system of embryos through the uterine wall of a pregnant dam. Then, the electric field is applied to the neuronal progenitors by means of two extrauterine forceps-type electrodes placed on the sides on the embryo head. Since the injection of the nucleic acid solution occurs through the uterine walls with no major damage to the *uterus*, the pregnant dam is able to deliver the pups. This process allows both

Europe PMC Funders Author Manuscripts

Europe PMC Funders Author Manuscripts

embryonal and postnatal studies of the electroporated pups. High efficiency with the two standard forceps-type paddle electrodes has been achieved for the electroporation of pyramidal neurons in the rodent somatosensory cortex (Saito, 2006). Since then, IUE has become the gold standard for studies on cortical development *ex vivo*, both at the anatomical and functional levels (LoTurco et al., 2009; Tabata and Nakajima, 2008; Taniguchi et al., 2012). Over the years, researchers have achieved targeting of many other brain regions by simply changing the orientation of the forceps-type electrodes. Indeed, by tilting the bipolar electrode, it is possible to target the visual cortex (Cang et al., 2005; Mizuno et al., 2007; Saito and Nakatsuji, 2001), hippocampus (Conrad et al., 2010; Saito and Nakatsuji, 2001; Tomita et al., 2011), olfactory bulb (Imamura and Greer et al., 2013), ganglionic eminence (Borrell et al., 2005; Tanaka et al., 2006), thalamus (Haddad-Tovolli et al., 2013), hypothalamus (Haddad-Tovolli et al., 2013), midbrain, amygdala (Remedios et al., 2007; Soma et al., 2009) cerebellum (dal Maschio et al., 2012; Kita et al., 2013; Szczurkowska et al., 2016; Yamada et al., 2014), spinal cord (Saba et al., 2003) and brainstem (David et al., 2014), but with a highly variable degree of efficiency (dal Maschio et al., 2012; Szczurkowska et al., 2016). Recently, the addition of a third electrode to the standard electroporation configuration has enabled highly reliable bilateral transfection of the hippocampus; the prefrontal, motor and visual cortices; and the cerebellum in a single electroporation episode (dal Maschio et al., 2012; Szczurkowska et al., 2016, 2013). Notably, although transfection is confined to a specific brain region and although not all cells in that region are transfected, successful behavioral studies have been performed. For example, animals have been transfected *in utero* with DISC1 cDNA, leading to amphetamine hypersensitivity (Vomund et al., 2013), and DCX KO mice have been transfected with DCX cDNA, leading to rescued epileptic-seizure susceptibility (Manent et al., 2009). Moreover, IUE has also been used in studies on psychiatric disorders, such as schizophrenia, indicating the molecular pathways that lead to cognitive deficits (Kamiya, 2009; Taniguchi et al., 2012).

One of the possible variations of the IUE technique is *exo utero* electroporation (EUE). In this case, during surgery, embryos are removed from the *uterus*. After DNA injection and delivery of the electric field with the forceps-type electrodes, the embryos are placed back inside the abdominal cavity of the dam without stitching the uterine walls. Since EUE guarantees better accessibility to the embryos than IUE, difficult-to-reach structures, such as the rhombencephalon (Akamatsu et al., 1999), spinal cord and caudal hindbrain (Saba et al., 2003), can be transfected with higher precision. *Exo utero* electroporation is mostly used for studying prenatal stages, as development of the embryos out of the uterus does not allow vaginal delivery. However, for postnatal studies, it is possible to rescue the electroporated embryos right before birth (E18.5) by Cesarean section, followed by immediate fostering with a stranger mother. Nevertheless, this procedure carries the risk of the pup's rejection by the foster mother.

It is possible to use the same principle of IUE to transfect animal brains after birth, enabling the study of postnatal brain development. In early postnatal electroporation, DNA is delivered to the brain ventricle or to the subventricular zone using a stereotactic microinjector (Boutin et al., 2008; Chesler et al., 2008), and the animal's head is conveniently placed between the plates of the forceps-type electrodes. This process allows

Europe PMC Funders Author Manuscripts

Europe PMC Funders Author Manuscripts

transfection of the progenitors located in the lateral, septal, and dorsal walls of the lateral ventricle, resulting in the transfection of different types of olfactory bulb neurons (Boutin et al., 2008; Chesler et al., 2008; De Vry et al., 2010; Fernandez et al., 2011; Sonego et al., 2013).

Finally, in adult rodents (up to 3,5 months old), DNA can be injected into the ventricle or directly into the targeted brain area to achieve the selective transfection of specific brain regions without affecting neurodevelopment. In the case of adult electroporation, the electric pulses can be applied with the standard forceps electrode (Chesler et al., 2008; Kitamura et al., 2008), or - for more precise and region-specific electroporation - a needle-like electrode can be inserted directly in the targeted brain region after local application of the DNA solution (Tanaka et al., 2000; Zhao et al., 2005). Late postnatal electroporation has been used to target the dentate gyrus (DG; (De Vry et al., 2010)) and the CA1 region (Tanaka et al., 2000) of the hippocampus, the prefrontal cortex (Zhao et al., 2005), the barrel cortex (Kitamura et al., 2008), and the cerebellum (Kitamura et al., 2008).

3.2 Sonoporation

Sonoporation takes advantage of temporary pores created in the cell membrane by ultrasound (US) exposure. The uptake of the DNA carriers during exposure to US occurs by mechanical stress, which causes endocytosis and/or large membrane wounds that are later closed by endogenous vesicle-based repair mechanisms (Fig. 2; Escoffre et al., 2013). US pulses can be delivered on their own, but their delivery in combination with a local application of microbubbles increases the efficiency of transfection (Taniyama and Morishita, 2006). Indeed, microbubbles are gas-filled structures (1–8 μm in diameter) that can react to the ultrasound waves by sequential expansion and compression (Lentacker et al., 2014), causing their own local oscillation close to the cell membrane and increasing the permeability to exogenous material (*e.g.*, DNA). Moreover, the physicochemical composition of the microbubbles can increase their chances of binding or capturing DNA. In particular, the most commonly used microbubbles are proteins, lipids or polymers (see chemical methods above). So far, the most suitable solution for microbubbles comprises cationic lipids, which can easily bind negatively charged plasmid DNA and are easily disrupted by US.

Although sonoporation is a promising technique that is well established for *in vitro* gene transfer (Fischer et al., 2006), its *in vivo* application is hindered by the possible aversive reactions of live tissue to US exposure (*e.g.*, increased temperature and production of reactive oxygen species; Juffermans et al., 2006; Wu, 1998). In the embryonic or newborn mouse, brain ultrasound was nevertheless used to attempt transfection of plasmid DNA in combination with microbubbles, both by intraventricular injection and systemically. However, the transfection efficiency was relatively low, and 50% of the injected embryos suffered from hydrocephaly (Endoh et al., 2002). On the other hand, microbubble-enhanced ultrasound improved gene transfer to the sub-ventricular zone after intraventricular injection in adult mice *in vivo* (Tan et al., 2016).

Europe PMC Funders Author Manuscripts

Europe PMC Funders Author Manuscripts

3.3 Magnet-assisted transfection

Magnetism-based targeted delivery was first described almost forty years ago (Widder et al., 1978) as a means to use magnetic micro- and nanoparticles for drug delivery to the circulatory system *in vivo*. The technique takes advantage of a magnetic field to direct magnetic nanoparticles (MNPs) containing nucleic acids into the target cells. The MNPs used as carriers are mostly composed of an iron oxide (magnetic) core with an additional organic or inorganic coating (*e.g.*, arabic gum ((Zhang et al., 2009), liposomes (Linemann et al., 2013), polymers, peptides and ligands/receptors (Estelrich et al., 2015)). Coated MNPs have major advantages (Chatterjee et al., 2001; Estelrich et al., 2015). Moreover, due to their positively charged magnetic core, the binding of negatively charged molecules (*e.g.*, DNA) is a relatively fast and easy process. Upon activation of the magnetic field, MNPs are drawn towards the target cells, where they undergo endocytosis or pinocytosis, followed by nucleic-acid release, leaving the membrane composition of the target cell intact (Fig. 2).

In *in vitro* studies, magnetofection has been commonly used due to its simplicity and high efficiency (Scherer et al., 2002). The application of a magnetic field, together with MNPs, is also a promising approach for *in vivo* gene transfer due to its noninvasive nature, ability to direct DNA to the region of interest and lack of toxicity. Nevertheless, magnetofection in the CNS is still in its infancy. Indeed, in one report describing MNPs functionalized with PEI that were administered in the rat spinal cord after lumbar intrathecal injection (Song et al., 2010), the experiment was not fully successful due to the dispersion of MNPs in the cerebrospinal fluid after exposure to the magnetic field. On the other hand, highly efficient and long-term magnetofection of complexes of EYFP channelrhodopsin and MNPs for optogenetic applications in the rat visual cortex *in vivo* has also been reported upon direct brain injection (Soto-Sanchez et al., 2015).

4 Virus-mediated trasduction

Viruses are nanometric infective agents composed of a protein capsid that protects their genetic material and, in some cases, a lipid envelope derived from the host cell membrane that protects the capsid. Viruses can therefore be classified as *naked* or *enveloped* based on the absence or presence of this lipid structure, respectively. All viruses are dependent on the host cell to successfully replicate: they hijack the replication machinery of the host cell and guide it to replicate the viral genetic material. Indeed, during laboratory synthesis of viral particles for experimental applications, cells are first infected with the aim of synthetizing high numbers of new viral particles that are subsequently purified and used at a high concentration in future experiments (Farson et al., 2004). Depending on the type of virus used for the transfection during experimental applications, the genetic material can be integrated in the host DNA or can be temporarily expressed (Fig. 3, Table 3). All cells can be infected by specific viruses (Koonin et al., 2006), and it is the capsid itself or in some cases, the envelope protein sequence and shape that determines what kind of cell a virus will infect, a property called *tropism*. As the genetic material carried by a virus can be modified or substituted by a synthetic construct altogether, viruses have been widely utilized as a means to perform genetic manipulations in live cells. Interestingly, the capsid can also be

Europe PMC Funders Author Manuscripts

Europe PMC Funders Author Manuscripts

artificially modified, thus generating viruses with a desired tropism for specific cell types (Freire et al., 2015).

The use of viral vectors for gene delivery into living cells dates back to 1976 when, for the first time, a DNA segment of a bacteriophage lambda was transfected into mammalian cells using a Simian Virus 40 (SV40) vector (Goff and Berg, 1976). Since then, the use of viruses in biological and biomedical research grew exponentially, and today, viral vectors are the most powerful technique for gene delivery *in vitro* and *in vivo*. The main advantages of the use of viral vectors are their extremely high specificity towards a certain cellular type and the high efficiency of reliable transfection. On the other hand, once engineered, the viral particle has to be purified. Easy and fast purification protocols are currently available. However, the process may sometimes damage the genomic material (Kay et al., 2001). Moreover, the size of the construct is limited by the packing capacity of the capsid. Furthermore, viruses are administered *via* intrathecal or intraventricular injection, which is extremely invasive (Artegiani and Calegari et al., 2013; Kotterman et al., 2015a; Thomas et al., 2003). Finally, most viruses require several days before transduction of the genetic material, although the precise expression timing varies for each type of viruses (*e.g.*, herpes simplex peaks at 24 h following infection; adeno-associated viruses require approximately 3 weeks to peak, although the expression is already visible as soon as 24 h following administration; Penrod et al., 2015; Reimsnider et al., 2007). Unlike the other methods for gene delivery, some viral vectors can lead to viral genetic material becoming stably integrated into the host genome (*e.g.*, Herpes Simplex viruses), which makes viral vectors particularly suited for the transfection of dividing cells. On the other hand, integrated viruses may be dangerous because the integration may occur in undesirable zones of the genome, leading to harmful mutations, which hinders their usage in biomedical research (Thomas et al., 2003). Conversely, with some other viral vectors (*e.g.*, adenoviruses), the genetic material remains in the nucleus as a so-called episome. Thus, nonintegrative viruses are safer but are mostly suitable only for nondividing cells, as the nonintegrated plasmid becomes too diluted in rapidly dividing cells to give the desired level of transfection (Kotterman et al., 2015a; Thomas et al., 2003). Here, we will review the four main viral classes that have *in vivo* applications in basic and biomedical research.

4.1 Lentiviruses

Lentiviruses are enveloped viruses belonging to the class of retroviruses (viruses bearing RNA genetic material) with the unique characteristic of being able to infect nondividing cells in a long-term manner. Being in the class of viruses bearing RNA, these viruses rely on retrotranscription to integrate their genetic material in the host genome (Fig. 3). Retrotranscription involves transcribing RNA into DNA with the help of a reverse transcriptase enzyme, which is encoded by the virus genome. Although lentiviruses are efficient viral vectors used for gene delivery, they were originally derived from pathogenic agents (*i.e.*, human immunodeficiency virus, HIV). This hampers their use *in vivo*, due to the risks of eliciting strong immunogenic responses or even reconversion to the wild-type pathogenic form (Cockrell and Kafri, 2007; Mah et al., 2002a). One important step made towards the development of safe lentiviral vectors was the substitution of the envelope protein of pathogenic viruses with one derived from a different virus (most commonly,

Europe PMC Funders Author Manuscripts

Europe PMC Funders Author Manuscripts

vesicular stomatitis virus G glycoprotein, VSV-G), which cannot successfully multiply after infection of the host cell and presents a wider *tropism* (Artegiani and Calegari et al., 2013; Mah et al., 2002b). Nevertheless, lentiviruses have been successfully used for efficient gene delivery *in vivo* for a long time (Bonci et al., 2003; Li et al., 2016; Qiao et al., 2016). Indeed, an HIV-based VSV-G-pseudotyped virus was used for the first time *in vivo* in 1996 to stably transfect fully differentiated neurons and glial cells and deliver β-galactosidase to the hippocampus of adult rats for up to three months after inoculation, without any evident immunogenic reaction. The stability of the infection depended on integration of the viral genome into the host-cell genetic material (Naldini et al., 1996a, b). Other applications in the CNS followed, and lentiviral vectors injected intracranially were used to study the effect of ApoE isoforms on amyloid plaque deposition in a mouse model, allowing the determination of the isoform-specific effects of ApoE on the amyloid burden in the hippocampus (Dodart et al., 2005). Moreover, modifications of the envelope of lentiviruses allowed preferential targeting of discrete populations of cells in the CNS with high flexibility. For example, lentiviruses pseudotyped with a modified envelope displayed anti-GLAST (an astrocyte-specific protein) IgG on their surfaces and preferential astrocyte targeting *in vivo* (Fassler et al., 2013). Interestingly, due to their ability to infect fully differentiated cells, lentiviruses find widespread usage in the study and development of therapies for neurodegenerative diseases, such as Parkinson's (Azzouz et al., 2004; Bensadoun et al., 2000; Yin et al., 2017) Alzheimer's (Li et al., 2017; Parsi et al., 2015; Tan et al., 2018) and Huntington's disease (Cui et al., 2006; Schwab et al., 2017).

4.2 Adenoviruses

Adenoviruses (ADVs) are nonintegrating naked viruses that bear double-stranded DNA. ADVs can transfect dividing and nondividing cells with fairly high efficiency (Mah et al., 2002a). ADVs have been successfully used *in vitro* to target neocortical and glial cells in culture (Morelli et al., 1999; Smith-Arica et al., 2000; Southgate et al., 2008). Nevertheless, their usage *in vivo* has been challenging due to their high virulence (Thomas et al., 2003). To overcome this issue, ADVs have been extensively engineered during the last 35 years with the aim of generating nonimmunogenic vectors. The first generation of modified ADVs had their viral genome deleted, generating replication-defective ADVs; nonetheless, these ADVs still exhibited potent T-cell-related immunogenicity. These first-generation viruses showed potent toxicity to the CNS, causing the transfected cells to be phagocyted. Nevertheless, usage of these vectors still led to the successful treatment of glioma in mice (Germano et al., 2003; Immonen et al., 2004; Lentz et al., 2012). Due to their capacity to infect dividing cells, replication-defective ADVs were also used to transfect neuronal precursors in the adult mouse brain following intraventricular injections (Yoon et al., 1996). In a great leap forward, safe ADV vectors were made with the development of helper-dependent ADVs (HD-ADV; Thomas et al., 2003). The HD-ADVs lacked any viral genes; thus, another virus (the helper virus) was needed to carry the information for their replication during the laboratory preparation of viruses for infection. This development enabled the synthesis of viral vectors with the ability to carry long constructs (up to 30 kB) that almost completely lacked virulence. Nevertheless, it is virtually impossible to completely eliminate the helper virus during the laboratory purification procedure, although currently, the amount of contamination can be reduced to less than 0,1%. This is a promising achievement for future

Europe PMC Funders Author Manuscripts

Europe PMC Funders Author Manuscripts

studies and applications using HD-ADVs (Kay et al., 2001). Indeed, HD-ADV has been recently used to perform manipulations of the DNA in human pluripotent stem cells and induced pluripotent stem cells (iPS), opening up the prospect of gene manipulation of pluripotent stem cells for therapeutic applications (Mitani, 2014).

4.3 Adeno-associated viruses

Adeno-associated viruses (AAVs) are viruses strictly related to ADVs. Indeed, AAVs were first isolated in 1965 as a contaminant in the preparation of ADV (Atchison et al., 1965; Kay et al., 2001). AAVs have a single-stranded DNA (ssDNA) genome composed of two genes, one for their replication (rep) and one for their encapsulation (cap), even though AAVs cannot replicate on their own. Similar to ADVs, AAVs require a helper virus to multiply. The AAV genome remains in the nucleus of host cells as an episome, or at a lower frequency, the AAV genome stably integrates in the host genome. The natural replication deficiency of AAVs in the absence of an HV gives them a natural safety mechanism in *in vivo* applications (Kay et al., 2001; Mah et al., 2002b; Samulski and Muzyczka, 2014; Yan et al., 2005). Indeed, these viruses have never been associated with any pathology, and they are the most studied viral vectors for gene delivery *in vivo* (Mah et al., 2000). Their main drawback is their small packing capacity (not exceeding 5 kb), which can nevertheless be increased by clever molecular biology tricks (*e.g.*, dividing the expression plasmid into two vectors and reconstituting a fully functional expression cassette after concatemerization of episomes in the nucleus (Thomas et al., 2003)). So far, AAVs are the method of choice for the study of *in vivo* brain physiology, since the transfection can be stable for strikingly long times. Moreover, different serotypes of AAVs can have different tropisms for discrete cell populations (Burger et al., 2004; Lentz et al., 2012). For example, an AAV infection was stably expressed up to six months in the rat brain (Klein et al., 1999) and up to 6 years in the bone marrow of nonhuman primates (Rivera et al., 2005). Moreover, due to their neurotropism and their ability to be transported along the axon, AAV9 and AAVrh10 may be used for the development of therapeutic approaches for local interventions of axonally connected structures (Choudhury et al., 2016b). Finally, different AAV serotypes can transfect different cell types (*e.g.*, astrocytes and oligodendrocytes) in the brain *in vivo* (Foust et al., 2009; Lawlor et al., 2009). This transfection was achieved by shuffling random pieces of the *cap* gene together to generate a large variety of different *cap* proteins and later screening for specific tropism for different cell types. Indeed, gene shuffling of the heparin-binding domain (HBD) in individual hybrid capsids of various AAV serotypes (AAV-type 2/type 8/type 9 chimera) helped in the creation of the AAV-DJ-derived viral peptide library for cell-specific tropism *in vivo* in mice (Grimm et al., 2008). The effect of the HBD on viral tropism was demonstrated by transduction to diverse tissues, including the brain (Grimm et al., 2008). Notably, cap-gene shuffling was also used to develop chimeric AAVs with the remarkable ability to pass through the seizure-compromised BBB in rats after kainic acid-induced seizures (Gray et al., 2010). In addition to capsid shuffling, packaged plasmids with specific promoters can also be used to achieve the goal of cell specificity (see the discussion section for further information about promoters). Interestingly, other AAV serotypes -when administered intravenously - were unexpectedly shown to cross even an intact BBB in young and adult animals (Bourdenx et al., 2014; Duque et al., 2009; Foust and Kaspar et al., 2009;

Europe PMC Funders Author Manuscripts

Europe PMC Funders Author Manuscripts

Foust et al., 2009). All these findings further fuel the interest in basic and biomedical research on AAVs.

4.4 Herpes simplex viruses

The herpes simplex viruses (HSVs) are enveloped viruses bearing double-stranded DNA genetic material. Their genome is relatively large, having a length of approximately 152 kb and containing more than 80 genes. Because many of the genes are not essential for viral replication, HSVs can carry at least 30 kb of nonviral DNA suitable for experimental purposes (Kay et al., 2001). The main advantages of HSVs are their high tropism for the CNS (for an unknown reason, especially sensory neurons; Menendez and Carr, 2017) and the fact that after infection, the HSV genome mostly remains in a latent form as a stable circular episome in the nucleus of fully differentiated cells for a very long time without eliciting any immunogenic response (Lentz et al., 2012). On the other hand, their strikingly complex envelope makes the development of cell-specific HSVs very challenging, although pseudotyping of HSV with the VSV-G protein can reduce off-target transfection *in vitro* (Andersen et al., 1982). Moreover, HSVs may still cause a massive activation of the immune system by starting replication in the host cell. This activation remains one of the main concerns for the use of HSV for gene delivery *in vivo*. One way to avoid self-replication is to delete some of the viral genetic material, generating nonself-replicating viral particles, which nevertheless need to be coupled to helper viruses for their replication during preparation (Kay et al., 2001; Spaete and Frenkel, 1982). With this process, cytotoxicity was strongly reduced, and neurons in culture were stably transfected for more than three weeks (Krisky et al., 1998). Although HSVs have been widely studied *in vivo* to treat glioblastoma in rodents (Nakashima et al., 2018; Ning and Wakimoto, 2014; Wollmann et al., 2005), their application to the transduction of neurons is still limited. Nevertheless, HSVs have been already used to transfect the striatum (for up to 7 months) in a rat model of Parkinson's disease with genes necessary for the functioning of dopaminergic neurons, providing significant recovery of the phenotype (Sun et al., 2003).

5 Discussion

5.1 Challenges of *in vivo* gene delivery to the brain

The study of the CNS through acute genetic manipulations *in vivo* to understand brain function in health and disease has always been a challenging issue for scientists. First, there are technical issues related to the inaccessibility of the brain due to the presence of the skull and the BBB. Additionally, the great complexity of brain circuits (*i.e.*, the variety of neuronal and nonneuronal cell types) and network functionality (*i.e.*, the long- and short-range connectivity among different brain regions) renders it difficult to establish causal relationships between genetic manipulations and cellular/behavioral outcomes in basic research. Finally, the invasiveness of surgical procedures and viral vector safety constitute additional challenges for translational applications. The various methods for *in vivo* gene manipulations highlighted above present positives and negatives in regard to applications for basic research or translational purposes in the difficult to access brain, which we will discuss below.

Europe PMC Funders Author Manuscripts

Europe PMC Funders Author Manuscripts

5.1.1 CNS penetration—The first difficulty in achieving acute gene manipulations in the brain *in vivo* is the need to bypass the skull or the BBB. To this end, tremendous efforts have been made to improve brain-delivery methods or maximize vector permeability. One of the first and simplest ideas developed in the past was the injection of DNA directly into the brain area of interest. The first studies in this regard were performed in the late 1980s and early 1990s (Breakefield and Geller, 1987), when different groups performed genetic manipulations by viral injection directly into the rodent retina and brain (Davidson et al., 1993; Palella et al., 1989; Price et al., 1987). Furthermore, lipofectin-supported DNA transfection, which overcomes the electrostatic repulsion of DNA by the cell membrane, was also successfully performed by direct injection into the mouse brain (Ono et al., 1990). Subsequently, chemical polymers such as PEI were used to directly inject genetic material into the cortex, hippocampus (Abdallah et al., 1996), spinal cord (Shi et al., 2003), and SVZ (Lemkine et al., 2002) of rodents. Moreover, lipid vectors were also effectively injected in the ventricles of early postnatal mice (Hassani et al., 2005; Roessler and Davidson et al., 1994) for basic research or in rodent glioblastoma to investigate possible therapeutic approaches (Cikankowitz et al., 2017; Lagarce and Passirani, 2016; Pulkkanen and Yla-Herttuala, 2005). Currently, physical methods, such as IUE and EUE, are particularly suitable for studies of neurodevelopment, as DNA can be directly injected into the large ventricles of developing embryos and a strong electric field can be easily applied to the head of the embryos. Indeed, embryos have no bony skull, which guarantees high transfection efficiency (Saito, 2006; Szczurkowska et al., 2016). Moreover, the quick expression of transfected genetic material upon electroporation also contributes to the successful application of this technique for neurodevelopmental studies. On the other hand, for viral vectors, the main strategy used for their delivery in the brain remains the direct intraparenchymal infusion of viral particles. Indeed, ventricle injection requires a large quantity of viral material at high concentrations, which may be difficult to obtain, as well as costly. Thus, viral injection is more suitable for local transfection in the postnatal and adult brain. Moreover, unlike electroporation, which becomes difficult when the electric field needs to be delivered through the bony skull of an adult animal, small amounts of viral vectors can be delivered by direct stereotaxic injection in a specific brain region of adult animals, following a minor craniotomy. Thus, viral vectors are the technique of choice for the study of brain functionality at later postnatal ages, which is also compatible with the fact that these vectors may require days before driving efficient expression of the genetic material that they carry.

Since direct injection in the brain - especially when considered for translational applications - is still an invasive technique due to the procedure itself and the risks of possible side effects related to the surgical intervention, new strategies have been developed to bypass the BBB in recent years. In particular, lipids and polymers supplemented with helper lipids or functionalized with peptides to increase their BBB permeation were successfully used with intravenous injection. For example, dendrimers, PEI and nanoparticles have been functionalized with PEG and other organic molecules to enable them to cross the BBB (Zarebkohan et al., 2015). In addition, viral capsids have been engineered to be more BBB permeable (Choudhury et al., 2016a, c; Deverman et al., 2016; Zhang et al., 2011). Moreover, a portion of the produced AAV particles remain associated with cell membranes

Europe PMC Funders Author Manuscripts

Europe PMC Funders Author Manuscripts

(exosome-AAVs). Compared with AAVs, exosome-AAVs have a longer half-life in the blood and increased BBB permeability (Hudry et al., 2016; Maguire et al., 2012). Alternatively, nanoparticles have been conjugated to genetic material, and their small dimensions allow direct intranasal delivery; thus, this method guarantees direct brain access because it does not require BBB crossing (Yadav et al., 2016).

5.1.2 Transfection specificity in the brain—Another open issue to address when studying brain function and possibly conceiving new treatments for brain disorders is the complexity of brain networks: the ability to transfect a precise cell population among many others has always been a challenge. The possibility of directing the electric field and thus the DNA in a specific direction allowed the easy transfection of discrete populations of neuronal progenitors of specific brain areas by IUE and EUE (dal Maschio et al., 2012; Saito, 2006; Saito and Nakatsuji, 2001; Szczurkowska et al., 2016). Nevertheless, while this method is very useful for *in vivo* developmental studies, it is less suitable for studies performed in adult animals, where chemical methods or viruses are the method of choice. With these chemical or viral methods, the selection of an appropriate cell-specific promoter upstream of the gene of interest enables the transfection of discrete cell types (Murlidharan et al., 2014; Ojala et al., 2015). For this purpose, several neuron- and glial-specific promoters have been identified and tested for their ability to enable cell-specific transduction (Hashimoto et al., 1996; Miura et al., 1990; Morelli et al., 1999; Oellig and Seliger, 1990; Quinn, 1996). Nevertheless, the cell-specific promoters tend to be too large to be packaged into viral vectors, and the resulting gene expression is weaker than that driven by constitutive viral promoters (*e.g.*, CMV; Hioki et al., 2007; Shevtsova et al., 2005). Thus, novel, smaller hybrid promoters that are able to efficiently induce a strong, specific gene expression pattern have been generated (Gray et al., 2011; Hioki et al., 2007; Kugler, 2016).

5.1.3 Combinations of the diverse *in vivo* transfection methods—To try and further overcome the difficulties related to modulation of gene expression *in vivo* in the CNS in terms of brain accessibility, transfection efficiency and/or space and time specificity, coupling of the different delivery techniques has offered unquestionable advantages. For example, BBB opening by focused US was combined with systemic administration of DNA bound to nanoparticles, resulting in a noninvasive strategy for achieving safe, highly localized, robust, and sustained transgene expression in the CNS (Mead et al., 2016). Moreover, a combination of US with the intravenous administration of naked microbubbles - together with naked plasmid DNA (Shimamura et al., 2004), AAVs (Hsu et al., 2013; Wang et al., 2017), liposomal-plasmid DNA (Lin et al., 2015), liposome-shRNA-NGR complexes (Zhao et al., 2018), polyethylene glycol-modified lipid-based bubbles (Negishi et al., 2015), or folate-conjugated gene-carrying microbubbles (Fan et al., 2016) - can induce reversible openings in the BBB and can increase the transfection efficiency in rodents. Furthermore, a more efficient, brain area-specific infection was achieved by coupling adenoviral vectors with magnet-assisted transfection in the brain of rodent embryos *in utero* (Hashimoto and Hisano, 2011; Sapet et al., 2012).

5.1.4 Combinations of *in vivo* transfection methods with newly emerging techniques—The coupling of molecular biology tools, including newly emerging

Europe PMC Funders Author Manuscripts

Europe PMC Funders Author Manuscripts

techniques, with techniques for gene delivery *in vivo* also has tremendous potential. For example, to achieve a transfection that is better confined in time and space, IUE was coupled to the Cre/loxP system in the study of retinal development (Matsuda and Cepko et al., 2007), and AAV transfection was coupled to the tetracycline-controlled transcriptional activation system (tet-on/off) in the study of the structure of the neural circuits in the mouse neostriatum and primary somatosensory cortex (Sohn et al., 2017). Moreover, both viral vectors and/or IUE were successfully used to introduce optogenetic proteins, chemogenetic receptors or voltage sensors into specific cell-types, cortex layers or brain areas, allowing the study of neural circuits *in vivo* (Ghitani et al., 2015). Furthermore, CRISPR-Cas9 technology, which allows genome editing, regulation and visualization (Gilbert et al., 2013; Mali et al., 2013; Qi et al., 2013), was recently coupled to IUE to study the role of specific genes in brain development *in vivo* by knockout (Chen et al., 2015; Cheng et al., 2016; Kalebic et al., 2016; Rannals et al., 2016a, b; Shinmyo et al., 2016; Straub et al., 2014; Wang, 2018) or knock-in (Tsunekawa et al., 2016). CRISPR-Cas9 technology coupled to IUE also enabled the study of the subcellular localization of specific proteins by inserting a sequence for a fluorescent protein into their encoding gene (Mikuni et al., 2016). Moreover, CRISPR-Cas9, despite its large size, can be packaged in viral vectors for *in vivo* delivery, thus enabling robust transfection in the adult mouse brain (Chen and Goncalves, 2016; Chew et al., 2016; Ortinski et al., 2017; Schmidt and Grimm, 2015). Interestingly, to increase Cas9 editing efficiency and decrease the risks of off-target effects, different groups tested the delivery of a protein Cas9-guide RNA (gRNA) complex by nucleofection (Kim et al., 2014; Lin et al., 2014), cationic lipids (Zuris et al., 2015), lipid nanoparticles (Wang et al., 2016; Yu et al., 2016) and cell-penetrating peptides (Ramakrishna et al., 2014) in mammalian cells *in vitro*, thus opening the possibility of a new delivery strategy to be applied *in vivo*. Indeed, the protein Cas9/gRNA complex was recently coupled to IUE to study the effect of the Tbr2 knockout in mouse neocortical progenitors (Kalebic et al., 2016) and was injected in the hippocampus, dorsal striatum, primary somatosensory cortex and primary visual cortex of adult mice with a positive outcome (Staahl et al., 2017).

5.2 Specific challenges for translational research and possible therapeutic applications

Gene therapy is defined as the transfer of genetic materials to specific target cells of a patient with the final goal of preventing or rescuing a particular disease state (Mali, 2013). The main strategies for gene therapy utilized so far entail the introduction of a replacement allele into cells to compensate for the loss of function of a gene, the silencing of a dominant mutant pathological allele and the introduction of trophic factors or compensatory proteins (Choudhury et al., 2016c). The first gene delivery in the human brain was performed by stereotactic injection of retrovirus- and ADV-containing nuclear-targeted β-galactosidase cDNA in 10 patients with malignant glioma (Puumalainen et al., 1998). For the first time, this study evaluated the feasibility and safety of virus-mediated gene transfer in human glioma *in vivo*, and it showed a positive outcome (Puumalainen et al., 1998). Since then, due to the therapeutic benefits and the safety found in subsequent clinical trials, gene therapy has become a possible option for clinical intervention in some otherwise terminal or severely disabling conditions (Naldini, 2015). Indeed, in recent years, a large effort has been put into continuously improving gene-delivery methods, and currently, more than 2000 approved

Europe PMC Funders Author Manuscripts

Europe PMC Funders Author Manuscripts

gene-therapy clinical trials have been conducted or are ongoing worldwide (http://www.abedia.com/wiley/).

However, the vast majority of the gene-therapy clinical trials so far have addressed cancer (64,5%), with neurological diseases representing only 1.8% of the studies (http://www.abedia.com/wiley/). On the one hand, this scarcity may be because the neuropathological mechanisms underlying several neurological disorders are still poorly understood. In this respect, *in vivo* methods for gene delivery that have been discovered by emerging basic research may also hold great potential in the long run for increasing our understanding of brain pathology. On the other hand, the low number of gene-therapy clinical trials for brain disorders may be due to the low availability of safe and efficient delivery vectors that can cross the BBB or can be directly injected in the brain without major complications. Nevertheless, the increasing prevalence of some neurodevelopmental disorders (*e.g.*, autism spectrum disorders; Neggers, 2014) and of neurodegenerative disease (due to the increase in the average age of the population; Johnson, 2015), in combination with the identification of clearly causative mutations and the paucity of standard pharmacological treatments for these brain disorders, highlights the need to search for alternative therapeutic approaches, including gene therapy. Currently, AAV vectors have become the vehicle of choice for *in vivo* gene transfer in most of the clinical trials targeting the brain. Nevertheless, although some AAVs that are being currently tested in animal models can effectively cross the BBB (Choudhury et al., 2016b, c; Deverman et al., 2016; Zhang et al., 2011), so far, the AAVs used in clinical trials are less permeable. Therefore, these AAVs are commonly injected directly into the brain parenchyma, nevertheless enabling long-term, relatively safe expression (Choudhury et al., 2016c). For example, an ongoing phase I/II study is testing intraputaminal brain infusion of an AAV encoding human aromatic L-amino acid decarboxylase as a possible treatment in subjects with Parkinson's disease (http://www.abedia.com/wiley/). Interestingly, AAVs were recently engineered to be able to efficiently transduce neural stem cells (Choudhury et al., 2016b; Kotterman et al., 2015b). To avoid the risk of the surgery-related side effects of classic parenchymal injection for virus delivery, a less invasive method, such as administration into the cerebrospinal fluid *via* intracerebroventricular (ICV) or intrathecal (IT) injection, has also been proposed (Choudhury et al., 2016c). Nevertheless, these methods of application seem to be less effective in bypassing the BBB and less safe due to the activation of immunogenic responses (Choudhury et al., 2016c).

Despite the rapidly increasing usage of viruses for *in vivo* genetic manipulations, they still present drawbacks (*e.g.*, the possibility of mutagenesis following viral integration in the host genome with the risk of tumorigenesis, toxicity and immunogenicity, as well as the limited genomic capacity). Thus, considerable interest has been recently concentrated on the development of nonviral vectors (*e.g.*, lipids, nanoparticles and polymers) for translational purposes. Interestingly, some clinical trials based on the use of lipofection to treat glioblastoma are ongoing (http://www.abedia.com/wiley/), and the use of US combined with microbubbles to deliver nanoparticles carrying the tumor-suppressive miRNA-34a was recently evaluated in mice as a new possible treatment (Vega et al., 2016). Moreover, the C2-9r peptide delivering a siRNA against α-synuclein (Javed et al., 2016) and the US-mediated delivery of the GDNF plasmid (Fan et al., 2016) or of nanomicrobubbles

Europe PMC Funders Author Manuscripts

Europe PMC Funders Author Manuscripts

containing the factor Nrf2 (Long et al., 2017) were recently tested in rodents as a novel approach to treat Parkinson's disease.

Finally, development of the CRISPR-Cas9 tool has opened new avenues and possibilities for translational research and gene therapy. Recently, some groups have started to investigate the potential of CRISPR-Cas9 technology to recover mutations and correct monogenic disorders in both cultured and *in vivo* stem cells (Maeder and Gersbach, 2016; Prakash et al., 2016). Moreover, CRISPR-Cas9 technology has also been used to manipulate the cancer genome or epigenome for therapeutic purposes *in vivo*. These changes include loss- or gain-of-function mutations in oncogenes, tumor suppressor genes, and modulators of cellular transformation or drug response (Sanchez-Rivera and Jacks, 2015). Nevertheless, the application of CRISPR-Cas9 technology as a therapeutic approach for brain disorders has been slowed down, in part, by difficulties in delivery due to its large dimensions (Walters et al., 2015). Interestingly, recent promising results have been obtained in a Huntington mouse model by reducing the mutant Huntingtin (mHTT) gene expression through the injection of Cas9 and mHTT-gRNA packaged in an AAV vector in the striatum (Yang et al., 2017).

5.3 Concluding remarks

Starting from the first attempts to deliver DNA to the difficult-to-reach brain, much progress has been obtained in terms of the efficiency of transfection, target specificity and safety in the CNS. This issue is of great importance since the basic mechanisms of brain functions are far from being resolved and since most brain disorders are still lacking a cure. In this respect, the currently available variety of delivery methods, which can be chosen to meet different experimental needs, and the continuous effort to find new and/or more efficient and safer ways to perform gene delivery *in vivo* will possibly aid basic research on animal models and translational attempts. The coupling of different delivery systems, such as chemical, physical and viral methods, together with new technological revolutions, such as optogenetics, chemogenetics and CRISPR-Cas9 technology, will further advance the field to further broaden our understanding of the brain and address several neurological disorders with new possible treatment options.

Acknowledgments

This work was funded by the European Research Council (ERC) under the European Union's Horizon 2020 research and innovation program (725563 to LC) and by the Telethon Foundation (GGP13187 and No TCP15021).

Abbreviations

AAV	adeno-associated viruses
ADV	adenoviruses
ApoE	apolypoprotein E
BBB	blood brain barrier
cap	encapsulation
Cas9	CRISPR associated protein 9

Europe PMC Funders Author Manuscripts

Europe PMC Funders Author Manuscripts

cDNA	coding DNA
CMV	cytomegalovirus
CNS	central nervous system
CNT	carbon nanotubes
CRISPR	clustered regularly interspaced short palindromic repeats
DCX	doublecortin
DNA	deoxyribonucleic acid
DOPE	1,2-dioleoyl-phosphatidyl-ethanolamine
EGFP	enhanced green fluorescent protein
EUE	exo utero electroporation
EYFP	enhanced yellow fluorescent protein
gRNA	guide RNA
HBD	heparin-binding domain
HD-ADV	helper-dependent ADVs
HIV	human immunodeficiency virus
HSV	herpes simplex viruses
HV	helper virus
ICV	intracerebroventricular
iPS	induced pluripotent stem-cells
IT	intrathecal
IUE	*in utero* electroporation
LNE	lipid nanoemulsion
LPS	lipopolysaccharide
LRP	lipoprotein receptor-related protein
mHTT	mutant huntingtin
miRNA	micro-RNA
MNP	magnetic nanoparticles
mRNA	messenger RNA
PAMAM	polyamidoamine

Europe PMC Funders Author Manuscripts

Europe PMC Funders Author Manuscripts

PEG	polyethylene Glycol
PEI	polyethylenimine
rep	replication
RNA	ribonucleic acid
RVG	rabies virus glycoprotein
SF	spherical fullerenes
shRNA	short hairpin RNA
siRNA	small-interfering RNA
SLN	solid lipid nanoparticles
ssDNA	single-stranded DNA
SV40	simian virus 40
SVZ	subventricular zone
TMC	trimethylated chitosan
TNF-α	tumor necrosis factor alpha
US	ultrasound
VSV-G	vesicular stomatitis virus glycoprotein

References

Abdallah B, Hassan A, Benoist C, Goula D, Behr JP, Demeneix BA. A powerful nonviral vector for in vivo gene transfer into the adult mammalian brain: polyethylenimine. Hum Gene Ther. 1996; 7:1947–1954. [PubMed: 8930654]

Ahmad HI, Ahmad MJ, Asif AR, Adnan M, Iqbal MK, Mehmood K, Muhammad SA, Bhuiyan AA, Elokil A, Du X, et al. A review of CRISPR-based genome editing: survival, evolution and challenges. Curr Issues Mol Biol. 2018; 28:47–68. [PubMed: 29428910]

Akamatsu W, Okano HJ, Osumi N, Inoue T, Nakamura S, Sakakibara S, Miura M, Matsuo N, Darnell RB, Okano H. Mammalian ELAV-like neuronal RNA-binding proteins HuB and HuC promote neuronal development in both the central and the peripheral nervous systems. Proc Natl Acad Sci U S A. 1999; 96:9885–9890. [PubMed: 10449789]

Al-Jamal KT, Gherardini L, Bardi G, Nunes A, Guo C, Bussy C, Herrero MA, Bianco A, Prato M, Kostarelos K, et al. Functional motor recovery from brain ischemic insult by carbon nanotube-mediated siRNA silencing. Proc Natl Acad Sci U S A. 2011; 108:10952–10957. [PubMed: 21690348]

Andersen HB, Benveniste D, Bitsch-Larsen L, Carl P, Crawford M, Djernes M, Eriksen J, Grell AM, Henriksen H, Jansen E, et al. Long-term treatment with epidural opiates. A multicenter account of 125 patients. Ugeskr Laeger. 1982; 144:2633–2637. [PubMed: 6758261]

Artegiani B, Calegari F. Lentiviruses allow widespread and conditional manipulation of gene expression in the developing mouse brain. Development. 2013; 140:2818–2822. [PubMed: 23757413]

Atchison RW, Casto BC, Hammon WM. Adenovirus-associated defective virus particles. Science. 1965; 149:754–756. [PubMed: 14325163]

Europe PMC Funders Author Manuscripts

Azzouz M, Ralph S, Wong LF, Day D, Askham Z, Barber RD, Mitrophanous KA, Kingsman SM, Mazarakis ND. Neuroprotection in a rat Parkinson model by GDNF gene therapy using EIAV vector. Neuroreport. 2004; 15:985–990. [PubMed: 15076720]

Badyal DK, Desai C. Animal use in pharmacology education and research: the changing scenario. Indian J Pharmacol. 2014; 46:257–265. [PubMed: 24987170]

Bensadoun JC, Deglon N, Tseng JL, Ridet JL, Zurn AD, Aebischer P. Lentiviral vectors as a gene delivery system in the mouse midbrain: cellular and behavioral improvements in a 6-OHDA model of Parkinson's disease using GDNF. Exp Neurol. 2000; 164:15–24. [PubMed: 10877911]

Bharali DJ, Klejbor I, Stachowiak EK, Dutta P, Roy I, Kaur N, Bergey EJ, Prasad PN, Stachowiak MK. Organically modified silica nanoparticles: a nonviral vector for in vivo gene delivery and expression in the brain. Proc Natl Acad Sci U S A. 2005; 102:11539–11544. [PubMed: 16051701]

Bishop CJ, Tzeng SY, Green JJ. Degradable polymer-coated gold nanoparticles for co-delivery of DNA and siRNA. Acta Biomater. 2015; 11:393–403. [PubMed: 25246314]

Bonci D, Cittadini A, Latronico MV, Borello U, Aycock JK, Drusco A, Innocenzi A, Follenzi A, Lavitrano M, Monti MG, et al. Advanced' generation lentiviruses as efficient vectors for cardiomyocyte gene transduction in vitro and in vivo. Gene Ther. 2003; 10:630–636. [PubMed: 12692591]

Bonoiu AC, Mahajan SD, Ding H, Roy I, Yong KT, Kumar R, Hu R, Bergey EJ, Schwartz SA, Prasad PN. Nanotechnology approach for drug addiction therapy: gene silencing using delivery of gold nanorod-siRNA nanoplex in dopaminergic neurons. Proc Natl Acad Sci U S A. 2009; 106:5546–5550. [PubMed: 19307583]

Borrell V, Yoshimura Y, Callaway EM. Targeted gene delivery to telencephalic inhibitory neurons by directional in utero electroporation. J Neurosci Methods. 2005; 143:151–158. [PubMed: 15814147]

Bourdenx M, Dutheil N, Bezard E, Dehay B. Systemic gene delivery to the central nervous system using Adeno-associated virus. Front Mol Neurosci. 2014; 7:50. [PubMed: 24917785]

Boutin C, Diestel S, Desoeuvre A, Tiveron MC, Cremer H. Efficient in vivo electroporation of the postnatal rodent forebrain. PLoS One. 2008; 3:e1883. [PubMed: 18382666]

Breakefield XO, Geller AI. Gene transfer into the nervous system. Mol Neurobiol. 1987; 1:339–371. [PubMed: 3077063]

Burger C, Gorbatyuk OS, Velardo MJ, Peden CS, Williams P, Zolotukhin S, Reier PJ, Mandel RJ, Muzyczka N. Recombinant AAV viral vectors pseudotyped with viral capsids from serotypes 1, 2, and 5 display differential efficiency and cell tropism after delivery to different regions of the central nervous system. Mol Ther. 2004; 10:302–317. [PubMed: 15294177]

Cang J, Kaneko M, Yamada J, Woods G, Stryker MP, Feldheim DA. Ephrinas guide the formation of functional maps in the visual cortex. Neuron. 2005; 48:577–589. [PubMed: 16301175]

Chang DC, Reese TS. Changes in membrane structure induced by electroporation as revealed by rapid-freezing electron microscopy. Biophys J. 1990; 58:1–12. [PubMed: 2383626]

Chatterjee J, Haik Y, Chen CJ. Modification and characterization of polystyrene-based magnetic microspheres and comparison with albumin-based magnetic microspheres. J Magn Magn Mater. 2001; 225:21–29.

Chen F, Rosiene J, Che A, Becker A, LoTurco J. Tracking and transforming neocortical progenitors by CRISPR/Cas9 gene targeting and piggyBac transposase lineage labeling. Development. 2015; 142:3601–3611. [PubMed: 26400094]

Chen X, Goncalves MA. Engineered viruses as genome editing devices. Mol Ther. 2016; 24:447–457. [PubMed: 26336974]

Cheng M, Jin X, Mu L, Wang F, Li W, Zhong X, Liu X, Shen W, Liu Y, Zhou Y. Combination of the clustered regularly interspaced short palindromic repeats (CRISPR)-associated 9 technique with the piggybac transposon system for mouse in utero electroporation to study cortical development. J Neurosci Res. 2016; 94:814–824. [PubMed: 27317429]

Chesler AT, Le Pichon CE, Brann JH, Araneda RC, Zou DJ, Firestein S. Selective gene expression by postnatal electroporation during olfactory interneuron neurogenesis. PLoS One. 2008; 3:e1517. [PubMed: 18231603]

Europe PMC Funders Author Manuscripts

Europe PMC Funders Author Manuscripts

Chew WL, Tabebordbar M, Cheng JK, Mali P, Wu EY, Ng AH, Zhu K, Wagers AJ, Church GM. A multifunctional AAV-CRISPR-Cas9 and its host response. Nat Methods. 2016; 13:868–874. [PubMed: 27595405]

Choi JS, Nam K, Park JY, Kim JB, Lee JK, Park JS. Enhanced transfection efficiency of PAMAM dendrimer by surface modification with L-arginine. J Control Release. 2004; 99:445–456. [PubMed: 15451602]

Choudhury SR, Fitzpatrick Z, Harris AF, Maitland SA, Ferreira JS, Zhang Y, Ma S, Sharma RB, Gray-Edwards HL, Johnson JA, et al. In vivo selection yields AAV-B1 capsid for central nervous system and muscle Gene therapy. Mol Ther. 2016a; 24:1247–1257. [PubMed: 27117222]

Choudhury SR, Harris AF, Cabral DJ, Keeler AM, Sapp E, Ferreira JS, Gray-Edwards HL, Johnson JA, Johnson AK, Su Q, et al. Widespread central nervous system gene transfer and silencing after systemic delivery of novel AAV-AS vector. Mol Ther. 2016b; 24:726–735. [PubMed: 26708003]

Choudhury SR, Hudry E, Maguire CA, Sena-Esteves M, Breakefield XO, Grandi P. Viral vectors for therapy of neurologic diseases. Neuropharmacology. 2016c; 120:63–80. [PubMed: 26905292]

Cikankowitz A, Clavreul A, Tetaud C, Lemaire L, Rousseau A, Lepareur N, Dabli D, Bouchet F, Garcion E, Menei P, et al. Characterization of the distribution, retention, and efficacy of internal radiation of 188Re-lipid nanocapsules in an immunocompromised human glioblastoma model. J Neuro Oncol. 2017; 131:49–58.

Cockrell AS, Kafri T. Gene delivery by lentivirus vectors. Mol Biotechnol. 2007; 36:184–204. [PubMed: 17873406]

Connor EE, Mwamuka J, Gole A, Murphy CJ, Wyatt MD. Gold nanoparticles are taken up by human cells but do not cause acute cytotoxicity. Small. 2005; 1:325–327. [PubMed: 17193451]

Conrad S, Stimpfle F, Montazeri S, Oldekamp J, Seid K, Alvarez-Bolado G, Skutella T. RGMb controls aggregation and migration of Neogenin-positive cells in vitro and in vivo. Mol Cell Neurosci. 2010; 43:222–231. [PubMed: 19944164]

Costa PM, Bourgognon M, Wang JT, Al-Jamal KT. Functionalised carbon nanotubes: from intracellular uptake and cell-related toxicity to systemic brain delivery. J Control Release. 2016; 241:200–219. [PubMed: 27693751]

Crystal RG. Adenovirus: the first effective in vivo gene delivery vector. Hum Gene Ther. 2014; 25:3–11. [PubMed: 24444179]

Cui L, Jeong H, Borovecki F, Parkhurst CN, Tanese N, Krainc D. Transcriptional repression of PGC-1alpha by mutant huntingtin leads to mitochondrial dysfunction and neurodegeneration. Cell. 2006; 127:59–69. [PubMed: 17018277]

dal Maschio M, Ghezzi D, Bony G, Alabastri A, Deidda G, Brondi M, Sato SS, Zaccaria RP, Di Fabrizio E, Ratto GM, et al. High-performance and site-directed in utero electroporation by a triple-electrode probe. Nat Commun. 2012; 3:960. [PubMed: 22805567]

Dan N. Lipid-nucleic acid supramolecular complexes: lipoplex structure and the kinetics of formation. AIMS Biophys. 2015; 2:163–183.

Danhier F, Messaoudi K, Lemaire L, Benoit JP, Lagarce F. Combined anti-Galectin-1 and anti-EGFR siRNA-loaded chitosan-lipid nanocapsules decrease temozolomide resistance in glioblastoma: in vivo evaluation. Int J Pharm. 2015; 481:154–161. [PubMed: 25644286]

David LS, Aitoubah J, Lesperance LS, Wang LY. Gene delivery in mouse auditory brainstem and hindbrain using in utero electroporation. Mol Brain. 2014; 7:51. [PubMed: 25063346]

Davidson BL, Allen ED, Kozarsky KF, Wilson JM, Roessler BJ. A model system for in vivo gene transfer into the central nervous system using an adenoviral vector. Nat Genet. 1993; 3:219–223. [PubMed: 8387378]

De Vry J, Martinez-Martinez P, Losen M, Temel Y, Steckler T, Steinbusch HW, De Baets MH, Prickaerts J. In vivo electroporation of the central nervous system: a non-viral approach for targeted gene delivery. Prog Neurobiol. 2010; 92:227–244. [PubMed: 20937354]

Deverman BE, Pravdo PL, Simpson BP, Kumar SR, Chan KY, Banerjee A, Wu WL, Yang B, Huber N, Pasca SP, et al. Cre-dependent selection yields AAV variants for widespread gene transfer to the adult brain. Nat Biotechnol. 2016; 34:204–209. [PubMed: 26829320]

Dobrzanski G, Kossut M. Application of the DREADD technique in biomedical brain research. Pharmacol Rep. 2017; 69:213–221. [PubMed: 28092807]

Europe PMC Funders Author Manuscripts

Europe PMC Funders Author Manuscripts

Dodart JC, Marr RA, Koistinaho M, Gregersen BM, Malkani S, Verma IM, Paul SM. Gene delivery of human apolipoprotein E alters brain Abeta burden in a mouse model of Alzheimer's disease. Proc Natl Acad Sci U S A. 2005; 102:1211–1216. [PubMed: 15657137]

Duceppe N, Tabrizian M. Advances in using chitosan-based nanoparticles for in vitro and in vivo drug and gene delivery. Expert Opin Drug Deliv. 2010; 7:1191–1207. [PubMed: 20836623]

Duque S, Joussemet B, Riviere C, Marais T, Dubreil L, Douar AM, Fyfe J, Moullier P, Colle MA, Barkats M. Intravenous administration of self-complementary AAV9 enables transgene delivery to adult motor neurons. Mol Ther. 2009; 17:1187–1196. [PubMed: 19367261]

Eichman JD, Bielinska AU, Kukowska-Latallo JF, Baker JR Jr. The use of PAMAM dendrimers in the efficient transfer of genetic material into cells. Pharm Sci Technol Today. 2000; 3:232–245. [PubMed: 10884679]

Ekin A, Karatas OF, Culha M, Ozen M. Designing a gold nanoparticle-based nanocarrier for microRNA transfection into the prostate and breast cancer cells. J Gene Med. 2014; 16:331–335. [PubMed: 25331590]

Endoh M, Koibuchi N, Sato M, Morishita R, Kanzaki T, Murata Y, Kaneda Y. Fetal gene transfer by intrauterine injection with microbubble-enhanced ultrasound. Mol Ther. 2002; 5:501–508. [PubMed: 11991740]

Escoffre JM, Zeghimi A, Novell A, Bouakaz A. In-vivo gene delivery by sonoporation: recent progress and prospects. Curr Gene Ther. 2013; 13:2–14. [PubMed: 23157546]

Escudero-Francos MA, Cepas V, Gonzalez-Menedez P, Badia-Laino R, Diaz-Garcia ME, Sainz RM, Mayo JC, Hevia D. Cellular uptake and tissue biodistribution of functionalized gold nanoparticles and nanoclusters. J Biomed Nanotechnol. 2017; 13:167–179. [PubMed: 29377647]

Estelrich J, Escribano E, Queralt J, Busquets MA. Iron oxide nanoparticles for magnetically-guided and magnetically-responsive drug delivery. Int J Mol Sci. 2015; 16:8070–8101. [PubMed: 25867479]

Ewe A, Przybylski S, Burkhardt J, Janke A, Appelhans D, Aigner A. A novel tyrosine-modified low molecular weight polyethylenimine (P10Y) for efficient siRNA delivery in vitro and in vivo. J Control Release. 2016; 230:13–25. [PubMed: 27061141]

Fan CH, Chang EL, Ting CY, Lin YC, Liao EC, Huang CY, Chang YC, Chan HL, Wei KC, Yeh CK. Folate-conjugated gene-carrying microbubbles with focused ultrasound for concurrent blood-brain barrier opening and local gene delivery. Biomaterials. 2016; 106:46–57. [PubMed: 27544926]

Farson D, Harding TC, Tao L, Liu J, Powell S, Vimal V, Yendluri S, Koprivnikar K, Ho K, Twitty C, et al. Development and characterization of a cell line for large-scale, serum-free production of recombinant adeno-associated viral vectors. J Gene Med. 2004; 6:1369–1381. [PubMed: 15538729]

Fassler M, Weissberg I, Levy N, Diaz-Griffero F, Monsonego A, Friedman A, Taube R. Preferential lentiviral targeting of astrocytes in the central nervous system. PLoS One. 2013; 8:e76092. [PubMed: 24098426]

Fernandez ME, Croce S, Boutin C, Cremer H, Raineteau O. Targeted electroporation of defined lateral ventricular walls: a novel and rapid method to study fate specification during postnatal forebrain neurogenesis. Neural Dev. 2011; 6:13. [PubMed: 21466691]

Fischer AJ, Stanke JJ, Omar G, Askwith CC, Burry RW. Ultrasound-mediated gene transfer into neuronal cells. J Biotechnol. 2006; 122:393–411. [PubMed: 16309774]

Foust KD, Kaspar BK. Over the barrier and through the blood: to CNS delivery we go. Cell Cycle. 2009; 8:4017–4018. [PubMed: 19949299]

Foust KD, Nurre E, Montgomery CL, Hernandez A, Chan CM, Kaspar BK. Intravascular AAV9 preferentially targets neonatal neurons and adult astrocytes. Nat Biotechnol. 2009; 27:59–65. [PubMed: 19098898]

Fraley R, Subramani S, Berg P, Papahadjopoulos D. Introduction of liposome-encapsulated SV40 DNA into cells. J Biol Chem. 1980; 255:10431–10435. [PubMed: 6253474]

Freire JM, Santos NC, Veiga AS, Da Poian AT, Castanho MA. Rethinking the capsid proteins of enveloped viruses: multifunctionality from genome packaging to genome transfection. FEBS J. 2015; 282:2267–2278. [PubMed: 25808179]

Europe PMC Funders Author Manuscripts

Europe PMC Funders Author Manuscripts

Fukuchi-Shimogori T, Grove EA. Neocortex patterning by the secreted signaling molecule FGF8. Science. 2001; 294:1071–1074. [PubMed: 11567107]

Gao Y, Wang ZY, Zhang J, Zhang Y, Huo H, Wang T, Jiang T, Wang S. RVG-peptide-linked trimethylated chitosan for delivery of siRNA to the brain. Biomacromolecules. 2014; 15:1010–1018. [PubMed: 24547943]

Germano IM, Fable J, Humayun Gultekin SEA. Adenovirus/herpes simplex-thymidine kinase/ganciclovir complex: preliminary results of a Phase I trial in patients with recurrent malignant gliomas. J Neuro Oncol. 2003; 65(279)

Ghitani N, Bayguinov PO, Ma Y, Jackson MB. Single-trial imaging of spikes and synaptic potentials in single neurons in brain slices with genetically encoded hybrid voltage sensor. J Neurophysiol. 2015; 113:1249–1259. [PubMed: 25411462]

Gilbert LA, Larson MH, Morsut L, Liu Z, Brar GA, Torres SE, Stern-Ginossar N, Brandman O, Whitehead EH, Doudna JA, et al. CRISPR-mediated modular RNA-guided regulation of transcription in eukaryotes. Cell. 2013; 154:442–451. [PubMed: 23849981]

Glover DJ, Lipps HJ, Jans DA. Towards safe, non-viral therapeutic gene expression in humans. Nat Rev Genet. 2005; 6:299–310. [PubMed: 15761468]

Goff SP, Berg P. Construction of hybrid viruses containing SV40 and lambda phage DNA segments and their propagation in cultured monkey cells. Cell. 1976; 9:695–705. [PubMed: 189942]

Graham FL, van der Eb AJ. Transformation of rat cells by DNA of human adenovirus 5. Virology. 1973; 54:536–539. [PubMed: 4737663]

Gray SJ, Blake BL, Criswell HE, Nicolson SC, Samulski RJ, McCown TJ, Li W. Directed evolution of a novel adeno-associated virus (AAV) vector that crosses the seizure-compromised blood-brain barrier (BBB). Mol Ther. 2010; 18:570–578. [PubMed: 20040913]

Gray SJ, Foti SB, Schwartz JW, Bachaboina L, Taylor-Blake B, Coleman J, Ehlers MD, Zylka MJ, McCown TJ, Samulski RJ. Optimizing promoters for recombinant adeno-associated virus-mediated gene expression in the peripheral and central nervous system using self-complementary vectors. Hum Gene Ther. 2011; 22:1143–1153. [PubMed: 21476867]

Gribkoff VK, Kaczmarek LK. The need for new approaches in CNS drug discovery: why drugs have failed, and what can be done to improve outcomes. Neuropharmacology. 2017; 120:11–19. [PubMed: 26979921]

Grimm D, Lee JS, Wang L, Desai T, Akache B, Storm TA, Kay MA. In vitro and in vivo gene therapy vector evolution via multispecies interbreeding and retargeting of adeno-associated viruses. J Virol. 2008; 82:5887–5911. [PubMed: 18400866]

Gu J, Al-Bayati K, Ho EA. Development of antibody-modified chitosan nanoparticles for the targeted delivery of siRNA across the blood-brain barrier as a strategy for inhibiting HIV replication in astrocytes. Drug Deliv Transl Res. 2017; 7:497–506. [PubMed: 28315051]

Haddad-Tovolli R, Szabo NE, Zhou X, Alvarez-Bolado G. Genetic manipulation of the mouse developing hypothalamus through in utero electroporation. J Vis Exp. 2013; 24(77)

Hashemi M, Tabatabai SM, Parhiz H, Milanizadeh S, Amel Farzad S, Abnous K, Ramezani M. Gene delivery efficiency and cytotoxicity of heterocyclic amine-modified PAMAM and PPI dendrimers. Mater Sci Eng C Mater Biol Appl. 2016; 61:791–800. [PubMed: 26838910]

Hashimoto M, Aruga J, Hosoya Y, Kanegae Y, Saito I, Mikoshiba K. A neural cell-type-specific expression system using recombinant adenovirus vectors. Hum Gene Ther. 1996; 7:149–158. [PubMed: 8788166]

Hashimoto M, Hisano Y. Directional gene-transfer into the brain by an adenoviral vector tagged with magnetic nanoparticles. J Neurosci Methods. 2011; 194:316–320. [PubMed: 21074563]

Hassani Z, Lemkine GF, Erbacher P, Palmier K, Alfama G, Giovannangeli C, Behr JP, Demeneix BA. Lipid-mediated siRNA delivery down-regulates exogenous gene expression in the mouse brain at picomolar levels. J Gene Med. 2005; 7:198–207. [PubMed: 15515135]

Helmschrodt C, Hobel S, Schoniger S, Bauer A, Bonicelli J, Gringmuth M, Fietz SA, Aigner A, Richter A, Richter F. Polyethylenimine nanoparticle-mediated siRNA delivery to reduce alpha-synuclein expression in a model of Parkinson's disease. Mol Ther Nucleic Acids. 2017; 9:57–68. [PubMed: 29246324]

Europe PMC Funders Author Manuscripts

Europe PMC Funders Author Manuscripts

Higuchi Y, Kawakami S, Fumoto S, Yamashita F, Hashida M. Effect of the particle size of galactosylated lipoplex on hepatocyte-selective gene transfection after intraportal administration. Biol Pharm Bull. 2006; 29:1521–1523. [PubMed: 16819204]

Hioki H, Kameda H, Nakamura H, Okunomiya T, Ohira K, Nakamura K, Kuroda M, Furuta T, Kaneko T. Efficient gene transduction of neurons by lentivirus with enhanced neuron-specific promoters. Gene Ther. 2007; 14:872–882. [PubMed: 17361216]

Hsu PH, Wei KC, Huang CY, Wen CJ, Yen TC, Liu CL, Lin YT, Chen JC, Shen CR, Liu HL. Noninvasive and targeted gene delivery into the brain using microbubble-facilitated focused ultrasound. PLoS One. 2013; 8:e57682. [PubMed: 23460893]

Hu J, Hu K, Cheng Y. Tailoring the dendrimer core for efficient gene delivery. Acta Biomater. 2016; 35:1–11. [PubMed: 26923528]

Hu K, Chen X, Chen W, Zhang L, Li J, Ye J, Zhang Y, Zhang L, Li CH, Yin L, et al. Neuroprotective effect of gold nanoparticles composites in Parkinson's disease model. Nanomed : Nanotechnol, Biol, Med. 2018; 14:1123–1136.

Huang R, Ke W, Liu Y, Jiang C, Pei Y. The use of lactoferrin as a ligand for targeting the polyamidoamine-based gene delivery system to the brain. Biomaterials. 2008; 29:238–246. [PubMed: 17935779]

Huang RQ, Qu YH, Ke WL, Zhu JH, Pei YY, Jiang C. Efficient gene delivery targeted to the brain using a transferrin-conjugated polyethyleneglycol-modified polyamidoamine dendrimer. FASEB J. 2007; 21:1117–1125. [PubMed: 17218540]

Hudry E, Martin C, Gandhi S, Gyorgy B, Scheffer DI, Mu D, Merkel SF, Mingozzi F, Fitzpatrick Z, Dimant H, et al. Exosome-associated AAV vector as a robust and convenient neuroscience tool. Gene Ther. 2016; 23:819. [PubMed: 27808124]

Hwang DW, Son S, Jang J, Youn H, Lee S, Lee D, Lee YS, Jeong JM, Kim WJ, Lee DS. A brain-targeted rabies virus glycoprotein-disulfide linked PEI nanocarrier for delivery of neurogenic microRNA. Biomaterials. 2011; 32:4968–4975. [PubMed: 21489620]

Imamura F, Greer CA. Pax6 regulates Tbr1 and Tbr2 expressions in olfactory bulb mitral cells. Mol Cell Neurosci. 2013; 54:58–70. [PubMed: 23353076]

Immonen A, Vapalahti M, Tyynela K, Hurskainen H, Sandmair A, Vanninen R, Langford G, Murray N, Yla-Herttuala S. AdvHSV-tk gene therapy with intravenous ganciclovir improves survival in human malignant glioma: a randomised, controlled study. Mol Ther. 2004; 10:967–972. [PubMed: 15509514]

Inoh Y, Nagai M, Matsushita K, Nakanishi M, Furuno T. Gene transfection efficiency into dendritic cells is influenced by the size of cationic liposomes/DNA complexes. Eur J Pharm Sci. 2017; 102:230–236. [PubMed: 28323115]

Javed H, Menon SA, Al-Mansoori KM, Al-Wandi A, Majbour NK, Ardah MT, Varghese S, Vaikath NN, Haque ME, Azzouz M, et al. Development of nonviral vectors targeting the brain as a therapeutic approach for Parkinson's disease and other brain disorders. Mol Ther. 2016; 24:746–758. [PubMed: 26700614]

Jensen SA, Day ES, Ko CH, Hurley LA, Luciano JP, Kouri FM, Merkel TJ, Luthi AJ, Patel PC, Cutler JI, et al. Spherical nucleic acid nanoparticle conjugates as an RNAi-based therapy for glioblastoma. Sci Transl Med. 2013; 5:209ra.

Jin J, Bae KH, Yang H, Lee SJ, Kim H, Kim Y, Joo KM, Seo SW, Park TG, Nam DH. In vivo specific delivery of c-Met siRNA to glioblastoma using cationic solid lipid nanoparticles. Bioconjug Chem. 2011; 22:2568–2572. [PubMed: 22070554]

Johnson IP. Age-related neurodegenerative disease research needs aging models. Front Aging Neurosci. 2015; 7:168. [PubMed: 26388766]

Juffermans LJ, Dijkmans PA, Musters RJ, Visser CA, Kamp O. Transient permeabilization of cell membranes by ultrasound-exposed microbubbles is related to formation of hydrogen peroxide. Am J Physiol Heart Circ Physiol. 2006; 291:H1595–H1601. [PubMed: 16632548]

Kalebic N, Taverna E, Tavano S, Wong FK, Suchold D, Winkler S, Huttner WB, Sarov M. CRISPR/Cas9-induced disruption of gene expression in mouse embryonic brain and single neural stem cells in vivo. EMBO Rep. 2016; 17:338–348. [PubMed: 26758805]

Europe PMC Funders Author Manuscripts

Europe PMC Funders Author Manuscripts

Kamiya A. Animal models for schizophrenia via in utero gene transfer: understanding roles for genetic susceptibility factors in brain development. Prog Brain Res. 2009; 179:9–15. [PubMed: 20302813]

Kaur IP, Bhandari R, Bhandari S, Kakkar V. Potential of solid lipid nanoparticles in brain targeting. J Control Release. 2008; 127:97–109. [PubMed: 18313785]

Kay MA, Glorioso JC, Naldini L. Viral vectors for gene therapy: the art of turning infectious agents into vehicles of therapeutics. Nat Med. 2001; 7:33–40. [PubMed: 11135613]

Ke W, Shao K, Huang R, Han L, Liu Y, Li J, Kuang Y, Ye L, Lou J, Jiang C. Gene delivery targeted to the brain using an Angiopep-conjugated polyethyleneglycol-modified polyamidoamine dendrimer. Biomaterials. 2009; 30:6976–6985. [PubMed: 19765819]

Kim S, Kim D, Cho SW, Kim J, Kim JS. Highly efficient RNA-guided genome editing in human cells via delivery of purified Cas9 ribonucleoproteins. Genome Res. 2014; 24:1012–1019. [PubMed: 24696461]

Kim SS, Ye C, Kumar P, Chiu I, Subramanya S, Wu H, Shankar P, Manjunath N. Targeted delivery of siRNA to macrophages for anti-inflammatory treatment. Mol Ther. 2010; 18:993–1001. [PubMed: 20216529]

Kita Y, Kawakami K, Takahashi Y, Murakami F. Development of cerebellar neurons and glias revealed by in utero electroporation: Golgi-like labeling of cerebellar neurons and glias. PLoS One. 2013; 8:e70091. [PubMed: 23894597]

Kitamura K, Judkewitz B, Kano M, Denk W, Hausser M. Targeted patch-clamp recordings and single-cell electroporation of unlabeled neurons in vivo. Nat Methods. 2008; 5:61–67. [PubMed: 18157136]

Klein RL, Muir D, King MA, Peel AL, Zolotukhin S, Moller JC, Kruttgen A, Heymach JV Jr, Muzyczka N, Meyer EM. Long-term actions of vector-derived nerve growth factor or brain-derived neurotrophic factor on choline acetyltransferase and Trk receptor levels in the adult rat basal forebrain. Neuroscience. 1999; 90:815–821. [PubMed: 10218782]

Kneuer C, Sameti M, Bakowsky U, Schiestel T, Schirra H, Schmidt H, Lehr CM. A nonviral DNA delivery system based on surface modified silica-nanoparticles can efficiently transfect cells in vitro. Bioconjug Chem. 2000a; 11:926–932. [PubMed: 11087343]

Kneuer C, Sameti M, Haltner EG, Schiestel T, Schirra H, Schmidt H, Lehr CM. Silica nanoparticles modified with aminosilanes as carriers for plasmid DNA. Int J Pharm. 2000b; 196:257–261. [PubMed: 10699731]

Koonin EV, Senkevich TG, Dolja VV. The ancient virus world and evolution of cells. Biol Direct. 2006; 1:29. [PubMed: 16984643]

Kotterman MA, Chalberg TW, Schaffer DV. Viral vectors for gene therapy: translational and clinical outlook. Annu Rev Biomed Eng. 2015a; 17:63–89. [PubMed: 26643018]

Kotterman MA, Vazin T, Schaffer DV. Enhanced selective gene delivery to neural stem cells in vivo by an adeno-associated viral variant. Development. 2015b; 142:1885–1892. [PubMed: 25968319]

Krisky DM, Wolfe D, Goins WF, Marconi PC, Ramakrishnan R, Mata M, Rouse RJ, Fink DJ, Glorioso JC. Deletion of multiple immediate-early genes from herpes simplex virus reduces cytotoxicity and permits long-term gene expression in neurons. Gene Ther. 1998; 5:1593–1603. [PubMed: 10023438]

Kugler S. Tissue-specific promoters in the CNS. Methods Mol Biol. 2016; 1382:81–91. [PubMed: 26611580]

Lacerda L, Ali-Boucetta H, Herrero MA, Pastorin G, Bianco A, Prato M, Kostarelos K. Tissue histology and physiology following intravenous administration of different types of functionalized multiwalled carbon nanotubes. Nanomedicine (Lond.). 2008; 3:149–161. [PubMed: 18373422]

Lagarce F, Passirani C. Nucleic-acid delivery using lipid nanocapsules. Curr Pharm Biotechnol. 2016; 17:723–727. [PubMed: 27033510]

Lawlor PA, Bland RJ, Mouravlev A, Young D, During MJ. Efficient gene delivery and selective transduction of glial cells in the mammalian brain by AAV serotypes isolated from nonhuman primates. Mol Ther. 2009; 17:1692–1702. [PubMed: 19638961]

Europe PMC Funders Author Manuscripts

Europe PMC Funders Author Manuscripts

Lemkine GF, Mantero S, Migne C, Raji A, Goula D, Normandie P, Levi G, Demeneix BA. Preferential transfection of adult mouse neural stem cells and their immediate progeny in vivo with polyethylenimine. Mol Cell Neurosci. 2002; 19:165–174. [PubMed: 11860270]

Lentacker I, De Cock I, Deckers R, De Smedt SC, Moonen CT. Understanding ultrasound induced sonoporation: definitions and underlying mechanisms. Adv Drug Deliv Rev. 2014; 72:49–64. [PubMed: 24270006]

Lentz TB, Gray SJ, Samulski RJ. Viral vectors for gene delivery to the central nervous system. Neurobiol Dis. 2012; 48:179–188. [PubMed: 22001604]

Levy R, Shaheen U, Cesbron Y, See V. Gold nanoparticles delivery in mammalian live cells: a critical review. Nano Rev. 2010; 1

Li HL, Gee P, Ishida K, Hotta A. Efficient genomic correction methods in human iPS cells using CRISPR-Cas9 system. Methods. 2016; 101:27–35. [PubMed: 26525194]

Li M, Yuan Y, Hu B, Wu L. Study on lentivirus-mediated ABCA7 improves neurocognitive function and related mechanisms in the C57BL/6 mouse model of Alzheimer's disease. J Mol Neurosci. 2017; 61:489–497. [PubMed: 28124230]

Lin CY, Hsieh HY, Pitt WG, Huang CY, Tseng IC, Yeh CK, Wei KC, Liu HL. Focused ultrasound-induced blood-brain barrier opening for non-viral, non-invasive, and targeted gene delivery. J Control Release. 2015; 212:1–9. [PubMed: 26071631]

Lin S, Staahl BT, Alla RK, Doudna JA. Enhanced homology-directed human genome engineering by controlled timing of CRISPR/Cas9 delivery. eLife. 2014; 3:e04766. [PubMed: 25497837]

Linemann T, Thomsen LB, Jardin KG, Laursen JC, Jensen JB, Lichota J, Moos T. Development of a novel lipophilic, magnetic nanoparticle for in vivo drug delivery. Pharmaceutics. 2013; 5:246–260. [PubMed: 24300449]

Liu CH, Yu SY. Cationic nanoemulsions as non-viral vectors for plasmid DNA delivery. Colloids Surf B Biointerfaces. 2010; 79:509–515. [PubMed: 20541375]

Long L, Cai X, Guo R, Wang P, Wu L, Yin T, Liao S, Lu Z. Treatment of Parkinson's disease in rats by Nrf2 transfection using MRI-guided focused ultrasound delivery of nanomicrobubbles. Biochem Biophys Res Commun. 2017; 482:75–80. [PubMed: 27810365]

LoTurco J, Manent JB, Sidiqi F. New and improved tools for in utero electroporation studies of developing cerebral cortex. Cereb Cortex. 2009; 19(Suppl 1):i120–125. [PubMed: 19395528]

Lu L, Zeitlin PL, Guggino WB, Craig RW. Gene transfer by lipofection in rabbit and human secretory epithelial cells. Pflugers Arch. 1989; 415:198–203. [PubMed: 2594476]

Lu Y, Jiang C. Brain-targeted polymers for gene delivery in the treatment of brain diseases. Top Curr Chem (Cham). 2017; 375:48. [PubMed: 28397188]

Lungwitz U, Breunig M, Blunk T, Gopferich A. Polyethylenimine-based non-viral gene delivery systems. Eur J Pharm Biopharm. 2005; 60:247–266. [PubMed: 15939236]

Luo D, Saltzman WM. Nonviral gene delivery: thinking of silica. Gene Ther. 2006; 13:585–586. [PubMed: 17526071]

Ma B, Zhang S, Jiang H, Zhao B, Lv H. Lipoplex morphologies and their influences on transfection efficiency in gene delivery. J Control Release. 2007; 123:184–194. [PubMed: 17913276]

Maeda-Mamiya R, Noiri E, Isobe H, Nakanishi W, Okamoto K, Doi K, Sugaya T, Izumi T, Homma T, Nakamura E. In vivo gene delivery by cationic tetraamino fullerene. Proc Natl Acad Sci U S A. 2010; 107:5339–5344. [PubMed: 20194788]

Maeder ML, Gersbach CA. Genome-editing technologies for gene and cell therapy. Mol Ther. 2016; 24:430–446. [PubMed: 26755333]

Maguire CA, Balaj L, Sivaraman S, Crommentuijn MH, Ericsson M, Mincheva-Nilsson L, Baranov V, Gianni D, Tannous BA, Sena-Esteves M, et al. Microvesicle-associated AAV vector as a novel gene delivery system. Mol Ther. 2012; 20:960–971. [PubMed: 22314290]

Mah C, Byrne BJ, Flotte TR. Virus-based gene delivery systems. Clin Pharmacokinet. 2002a; 41:901–911. [PubMed: 12222993]

Mah C, Fraites TJ Jr, Zolotukhin I, Song S, Flotte TR, Dobson J, Batich C, Byrne BJ. Improved method of recombinant AAV2 delivery for systemic targeted gene therapy. Mol Ther. 2002b; 6:106–112. [PubMed: 12095310]

Europe PMC Funders Author Manuscripts

Europe PMC Funders Author Manuscripts

Mah CS, Zolotukhin I, Fraites T, Dobson J, Batich C. Microsphere-mediated delivery of recombinant AAV vectors in vitro and in vivo. Mol Ther. 2000; 1:S239.

Mali P, Esvelt KM, Church GM. Cas9 as a versatile tool for engineering biology. Nat Methods. 2013; 10:957–963. [PubMed: 24076990]

Mali S. Delivery systems for gene therapy. Indian J Hum Genet. 2013; 19:3–8. [PubMed: 23901186]

Manent JB, Wang Y, Chang Y, Paramasivam M, LoTurco JJ. Dcx re-expression reduces subcortical band heterotopia and seizure threshold in an animal model of neuronal migration disorder. Nat Med. 2009; 15:84–90. [PubMed: 19098909]

Matsuda T, Cepko CL. Controlled expression of transgenes introduced by in vivo electroporation. Proc Natl Acad Sci U S A. 2007; 104:1027–1032. [PubMed: 17209010]

Mead BP, Mastorakos P, Suk JS, Klibanov AL, Hanes J, Price RJ. Targeted gene transfer to the brain via the delivery of brain-penetrating DNA nanoparticles with focused ultrasound. J Control Release. 2016; 223:109–117. [PubMed: 26732553]

Menendez CM, Carr DJ. Defining nervous system susceptibility during acute and latent herpes simplex virus-1 infection. J Neuroimmunol. 2017; 308:43–49. [PubMed: 28302316]

Mikuni T, Nishiyama J, Sun Y, Kamasawa N, Yasuda R. High-Throughput, High-Resolution Mapping of Protein Localization in Mammalian Brain by In Vivo Genome Editing. Cell. 2016; 165:1803–1817. [PubMed: 27180908]

Mitani K. Gene targeting in human-induced pluripotent stem cells with adenoviral vectors. Methods Mol Biol. 2014; 1114:163–167. [PubMed: 24557902]

Miura M, Tamura T, Mikoshiba K. Cell-specific expression of the mouse glial fibrillary acidic protein gene: identification of the cis- and trans-acting promoter elements for astrocyte-specific expression. J Neurochem. 1990; 55:1180–1188. [PubMed: 2398353]

Mizuno H, Hirano T, Tagawa Y. Evidence for activity-dependent cortical wiring: formation of interhemispheric connections in neonatal mouse visual cortex requires projection neuron activity. J Neurosci. 2007; 27:6760–6770. [PubMed: 17581963]

Montellano A, Da Ros T, Bianco A, Prato M. Fullerene C(6)(0) as a multi-functional system for drug and gene delivery. Nanoscale. 2011; 3:4035–4041. [PubMed: 21897967]

Morelli AE, Larregina AT, Smith-Arica J, Dewey RA, Southgate TD, Ambar B, Fontana A, Castro MG, Lowenstein PR. Neuronal and glial cell type-specific promoters within adenovirus recombinants restrict the expression of the apoptosis-inducing molecule Fas ligand to predetermined brain cell types, and abolish peripheral liver toxicity. J Gen Virol. 1999; 80(Pt. 3): 571–583. [PubMed: 10091995]

Muramatsu T, Mizutani Y, Ohmori Y, Okumura J. Comparison of three non-viral transfection methods for foreign gene expression in early chicken embryos in ovo. Biochem Biophys Res Commun. 1997; 230:376–380. [PubMed: 9016787]

Murlidharan G, Samulski RJ, Asokan A. Biology of adeno-associated viral vectors in the central nervous system. Front Mol Neurosci. 2014; 7:76. [PubMed: 25285067]

Nakashima H, Nguyen T, Kasai K, Passaro C, Ito H, Goins WF, Shaikh I, Erdelyi R, Nishihara R, Nakano I, et al. Toxicity and efficacy of a novel GADD34-expressing oncolytic HSV-1 for the treatment of experimental glioblastoma. Clin Cancer Res. 2018 Mar 6.

Naldini L. Gene therapy returns to centre stage. Nature. 2015; 526:351–360. [PubMed: 26469046]

Naldini L, Blomer U, Gage FH, Trono D, Verma IM. Efficient transfer, integration, and sustained long-term expression of the transgene in adult rat brains injected with a lentiviral vector. Proc Natl Acad Sci U S A. 1996a; 93:11382–11388. [PubMed: 8876144]

Naldini L, Blomer U, Gallay P, Ory D, Mulligan R, Gage FH, Verma IM, Trono D. In vivo gene delivery and stable transduction of nondividing cells by a lentiviral vector. Science. 1996b; 272:263–267. [PubMed: 8602510]

Nayerossadat N, Maedeh T, Ali PA. Viral and nonviral delivery systems for gene delivery. Adv Biomed Res. 2012; 1:27. [PubMed: 23210086]

Neggers YH. Increasing prevalence, changes in diagnostic criteria, and nutritional risk factors for autism spectrum disorders. ISRN Nutr. 2014; 2014:514026. [PubMed: 24967269]

Negishi Y, Yamane M, Kurihara N, Endo-Takahashi Y, Sashida S, Takagi N, Suzuki R, Maruyama K. Enhancement of Blood-Brain Barrier Permeability and Delivery of Antisense Oligonucleotides or

Europe PMC Funders Author Manuscripts

Europe PMC Funders Author Manuscripts

Plasmid DNA to the Brain by the Combination of Bubble Liposomes and High-Intensity Focused Ultrasound. Pharmaceutics. 2015; 7:344–362. [PubMed: 26402694]

Neumann E, Schaefer-Ridder M, Wang Y, Hofschneider PH. Gene transfer into mouse lyoma cells by electroporation in high electric fields. EMBO J. 1982; 1:841–845. [PubMed: 6329708]

Ning J, Wakimoto H. Oncolytic herpes simplex virus-based strategies: toward a breakthrough in glioblastoma therapy. Front Microbiol. 2014; 5:303. [PubMed: 24999342]

Nouri F, Sadeghpour H, Heidari R, Dehshahri A. Preparation, characterization, and transfection efficiency of low molecular weight polyethylenimine-based nanoparticles for delivery of the plasmid encoding CD200 gene. Int J Nanomed. 2017; 12:5557–5569.

Oellig C, Seliger B. Gene transfer into brain tumor cell lines: reporter gene expression using various cellular and viral promoters. J Neurosci Res. 1990; 26:390–396. [PubMed: 2398515]

Oh J, Lee MS, Jeong JH, Lee M. Deoxycholic Acid-Conjugated Polyethylenimine for Delivery of Heme Oxygenase-1 Gene in Rat Ischemic Stroke Model. J Pharm Sci. 2017; 106:3524–3532. [PubMed: 28780392]

Ojala DS, Amara DP, Schaffer DV. Adeno-associated virus vectors and neurological gene therapy. Neuroscientist. 2015; 21:84–98. [PubMed: 24557878]

Ono T, Fujino Y, Tsuchiya T, Tsuda M. Plasmid DNAs directly injected into mouse brain with lipofectin can be incorporated and expressed by brain cells. Neurosci Lett. 1990; 117:259–263. [PubMed: 1710037]

Ortinski PI, O'Donovan B, Dong X, Kantor B. Integrase-Deficient Lentiviral Vector as an All-in-One Platform for Highly Efficient CRISPR/Cas9-Mediated Gene Editing. Mol Ther Methods Clin Dev. 2017; 5:153–164. [PubMed: 28497073]

Pack DW, Hoffman AS, Pun S, Stayton PS. Design and development of polymers for gene delivery. Nat Rev Drug Discov. 2005; 4:581–593. [PubMed: 16052241]

Palella TD, Hidaka Y, Silverman LJ, Levine M, Glorioso J, Kelley WN. Expression of human HPRT mRNA in brains of mice infected with a recombinant herpes simplex virus-1 vector. Gene. 1989; 80:137–144. [PubMed: 2551779]

Pantarotto D, Singh R, McCarthy D, Erhardt M, Briand JP, Prato M, Kostarelos K, Bianco A. Functionalized carbon nanotubes for plasmid DNA gene delivery. Angew Chem Int Ed Engl. 2004; 43:5242–5246. [PubMed: 15455428]

Parsi S, Pandamooz S, Heidari S, Naji M, Morfini G, Ahmadiani A, Dargahi L. A novel rat model of Alzheimer's disease based on lentiviral-mediated expression of mutant APP. Neuroscience. 2015; 284:99–106. [PubMed: 25270904]

Parveen A, Rizvi SH, Sushma, Mahdi F, Ahmad I, Singh PP, Mahdi AA. Intranasal exposure to silica nanoparticles induces alterations in pro-inflammatory environment of rat brain. Toxicol Ind Health. 2017; 33:119–132. [PubMed: 26431867]

Pathak K, Shankar R, Joshi M. An Update of Patents, Preclinical and Clinical Outcomes of Lipid Nanoparticulate Systems. Curr Pharm Des. 2017 Nov 21.

Peng LH, Huang YF, Zhang CZ, Niu J, Chen Y, Chu Y, Jiang ZH, Gao JQ, Mao ZW. Integration of antimicrobial peptides with gold nanoparticles as unique non-viral vectors for gene delivery to mesenchymal stem cells with antibacterial activity. Biomaterials. 2016; 103:137–149. [PubMed: 27376562]

Penrod RD, Wells AM, Carlezon WA Jr, Cowan CW. Use of Adeno-Associated and Herpes Simplex Viral Vectors for In Vivo Neuronal Expression in Mice. Curr Protoc Neurosci. 2015; 73(4):31–37.

Petschauer JS, Madden AJ, Kirschbrown WP, Song G, Zamboni WC. The effects of nanoparticle drug loading on the pharmacokinetics of anticancer agents. Nanomedicine (Lond.). 2015; 10:447–463. [PubMed: 25707978]

Pissuwan D, Niidome T, Cortie MB. The forthcoming applications of gold nanoparticles in drug and gene delivery systems. J Control Release. 2011; 149:65–71. [PubMed: 20004222]

Potrykus I, Paszkowski J, Saul MW, Petruska J, Shillito RD. Molecular and general genetics of a hybrid foreign gene introduced into tobacco by direct gene transfer. Mol Gen Gen. 1985; 199:169–177.

Europe PMC Funders Author Manuscripts

Europe PMC Funders Author Manuscripts

Potter H. Electroporation in biology: methods, applications, and instrumentation. Anal Biochem. 1988; 174:361–373. [PubMed: 3071177]

Prakash V, Moore M, Yanez-Munoz RJ. Current Progress in Therapeutic Gene Editing for Monogenic Diseases. Mol Ther. 2016; 24:465–474. [PubMed: 26765770]

Price J, Turner D, Cepko C. Lineage analysis in the vertebrate nervous system by retrovirus-mediated gene transfer. Proc Natl Acad Sci U S A. 1987; 84:156–160. [PubMed: 3099292]

Pulkkanen KJ, Yla-Herttuala S. Gene therapy for malignant glioma: current clinical status. Mol Ther. 2005; 12:585–598. [PubMed: 16095972]

Puumalainen AM, Vapalahti M, Agrawal RS, Kossila M, Laukkanen J, Lehtolainen P, Viita H, Paljarvi L, Vanninen R, Yla-Herttuala S. Beta-galactosidase gene transfer to human malignant glioma in vivo using replication-deficient retroviruses and adenoviruses. Hum Gene Ther. 1998; 9:1769–1774. [PubMed: 9721087]

Qi LS, Larson MH, Gilbert LA, Doudna JA, Weissman JS, Arkin AP, Lim WA. Repurposing CRISPR as an RNA-guided platform for sequence-specific control of gene expression. Cell. 2013; 152:1173–1183. [PubMed: 23452860]

Qiao WL, Hu HY, Shi BW, Zang LJ, Jin W, Lin Q. Lentivirus-mediated knockdown of TSP50 suppresses the growth of non-small cell lung cancer cells via G0/G1 phase arrest. Oncol Rep. 2016; 35:3409–3418. [PubMed: 27109614]

Quick KL, Ali SS, Arch R, Xiong C, Wozniak D, Dugan LL. A carboxyfullerene SOD mimetic improves cognition and extends the lifespan of mice. Neurobiol Aging. 2008; 29:117–128. [PubMed: 17079053]

Quinn JP. Neuronal-specific gene expression–the interaction of both positive and negative transcriptional regulators. Prog Neurobiol. 1996; 50:363–379. [PubMed: 9004350]

Ramakrishna S, Kwaku Dad AB, Beloor J, Gopalappa R, Lee SK, Kim H. Gene disruption by cell-penetrating peptide-mediated delivery of Cas9 protein and guide RNA. Genome Res. 2014; 24:1020–1027. [PubMed: 24696462]

Ramamoorth M, Narvekar A. Non viral vectors in gene therapy- an overview. J Clin Diagn Res. 2015; 9:GE01–GE06.

Rannals MD, Hamersky GR, Page SC, Campbell MN, Briley A, Gallo RA, Phan BN, Hyde TM, Kleinman JE, Shin JH, et al. Psychiatric Risk Gene Transcription Factor 4 Regulates Intrinsic Excitability of Prefrontal Neurons via Repression of SCN10a and KCNQ1. Neuron. 2016a; 90:43–55. [PubMed: 26971948]

Rannals MD, Page SC, Campbell MN, Gallo RA, Mayfield B, Maher BJ. Neurodevelopmental models of transcription factor 4 deficiency converge on a common ion channel as a potential therapeutic target for Pitt Hopkins syndrome. Rare Dis. 2016b; 4:e1220468. [PubMed: 28032012]

Reimsnider S, Manfredsson FP, Muzyczka N, Mandel RJ. Time course of transgene expression after intrastriatal pseudotyped rAAV2/1, rAAV2/2, rAAV2/5, and rAAV2/8 transduction in the rat. Mol Ther. 2007; 15:1504–1511. [PubMed: 17565350]

Remedios R, Huilgol D, Saha B, Hari P, Bhatnagar L, Kowalczyk T, Hevner RF, Suda Y, Aizawa S, Ohshima T, et al. A stream of cells migrating from the caudal telencephalon reveals a link between the amygdala and neocortex. Nat Neurosci. 2007; 10:1141–1150. [PubMed: 17694053]

Rivera VM, Gao GP, Grant RL, Schnell MA, Zoltick PW, Rozamus LW, Clackson T, Wilson JM. Long-term pharmacologically regulated expression of erythropoietin in primates following AAV-mediated gene transfer. Blood. 2005; 105:1424–1430. [PubMed: 15507527]

Roessler BJ, Davidson BL. Direct plasmid mediated transfection of adult murine brain cells in vivo using cationic liposomes. Neurosci Lett. 1994; 167:5–10. [PubMed: 8177529]

Ross PC, Hui SW. Lipoplex size is a major determinant of in vitro lipofection efficiency. Gene Ther. 1999; 6:651–659. [PubMed: 10476225]

Saba R, Nakatsuji N, Saito T. Mammalian BarH1 confers commissural neuron identity on dorsal cells in the spinal cord. J Neurosci. 2003; 23:1987–1991. [PubMed: 12657654]

Saito T. In vivo electroporation in the embryonic mouse central nervous system. Nat Protoc. 2006; 1:1552–1558. [PubMed: 17406448]

Saito T, Nakatsuji N. Efficient gene transfer into the embryonic mouse brain using in vivo electroporation. Dev Biol. 2001; 240:237–246. [PubMed: 11784059]

Europe PMC Funders Author Manuscripts

Samulski RJ, Muzyczka N. AAV-Mediated Gene Therapy for Research and Therapeutic Purposes. Annu Rev Virol. 2014; 1:427–451. [PubMed: 26958729]

Sanchez-Rivera FJ, Jacks T. Applications of the CRISPR-Cas9 system in cancer biology. Nat Rev Cancer. 2015; 15:387–395. [PubMed: 26040603]

Santos JL, Oliveira H, Pandita D, Rodrigues J, Pego AP, Granja PL, Tomas H. Functionalization of poly(amidoamine) dendrimers with hydrophobic chains for improved gene delivery in mesenchymal stem cells. J Control Release. 2010; 144:55–64. [PubMed: 20138937]

Sapet C, Pellegrino C, Laurent N, Sicard F, Zelphati O. Magnetic nanoparticles enhance adenovirus transduction in vitro and in vivo. Pharm Res. 2012; 29:1203–1218. [PubMed: 22146803]

Scherer F, Anton M, Schillinger U, Henke J, Bergemann C, Kruger A, Gansbacher B, Plank C. Magnetofection: enhancing and targeting gene delivery by magnetic force in vitro and in vivo. Gene Ther. 2002; 9:102–109. [PubMed: 11857068]

Schmidt F, Grimm D. CRISPR genome engineering and viral gene delivery: a case of mutual attraction. Biotechnol J. 2015; 10:258–272. [PubMed: 25663455]

Schwab LC, Richetin K, Barker RA, Deglon N. Formation of hippocampal mHTT aggregates leads to impaired spatial memory, hippocampal activation and adult neurogenesis. Neurobiol Dis. 2017; 102:105–112. [PubMed: 28286179]

Shevtsova Z, Malik JM, Michel U, Bahr M, Kugler S. Promoters and serotypes: targeting of adeno-associated virus vectors for gene transfer in the rat central nervous system in vitro and in vivo. Exp Physiol. 2005; 90:53–59. [PubMed: 15542619]

Sheyn D, Kimelman-Bleich N, Pelled G, Zilberman Y, Gazit D, Gazit Z. Ultrasound-based nonviral gene delivery induces bone formation in vivo. Gene Ther. 2008; 15:257–266. [PubMed: 18033309]

Shi L, Tang GP, Gao SJ, Ma YX, Liu BH, Li Y, Zeng JM, Ng YK, Leong KW, Wang S. Repeated intrathecal administration of plasmid DNA complexed with polyethylene glycol-grafted polyethylenimine led to prolonged transgene expression in the spinal cord. Gene Ther. 2003; 10:1179–1188. [PubMed: 12833127]

Shimamura M, Sato N, Taniyama Y, Yamamoto S, Endoh M, Kurinami H, Aoki M, Ogihara T, Kaneda Y, Morishita R. Development of efficient plasmid DNA transfer into adult rat central nervous system using microbubble-enhanced ultrasound. Gene Ther. 2004; 11:1532–1539. [PubMed: 15269716]

Shinmyo Y, Tanaka S, Tsunoda S, Hosomichi K, Tajima A, Kawasaki H. CRISPR/Cas9-mediated gene knockout in the mouse brain using in utero electroporation. Sci Rep. 2016; 6:20611. [PubMed: 26857612]

Singh R, Pantarotto D, McCarthy D, Chaloin O, Hoebeke J, Partidos CD, Briand JP, Prato M, Bianco A, Kostarelos K. Binding and condensation of plasmid DNA onto functionalized carbon nanotubes: toward the construction of nanotube-based gene delivery vectors. J Am Chem Soc. 2005; 127:4388–4396. [PubMed: 15783221]

Smith-Arica JR, Morelli AE, Larregina AT, Smith J, Lowenstein PR, Castro MG. Cell-type-specific and regulatable transgenesis in the adult brain: adenovirus-encoded combined transcriptional targeting and inducible transgene expression. Mol Ther. 2000; 2:579–587. [PubMed: 11124058]

Sohn J, Takahashi M, Okamoto S, Ishida Y, Furuta T, Hioki H. A Single Vector Platform for High-Level Gene Transduction of Central Neurons: Adeno-Associated Virus Vector Equipped with the Tet-Off System. PLoS One. 2017; 12:e0169611. [PubMed: 28060929]

Soma M, Aizawa H, Ito Y, Maekawa M, Osumi N, Nakahira E, Okamoto H, Tanaka K, Yuasa S. Development of the mouse amygdala as revealed by enhanced green fluorescent protein gene transfer by means of in utero electroporation. J Comp Neurol. 2009; 513:113–128. [PubMed: 19107806]

Sonego M, Zhou Y, Oudin MJ, Doherty P, Lalli G. In vivo postnatal electroporation and time-lapse imaging of neuroblast migration in mouse acute brain slices. J Vis Exp. 2013; (81)

Song G, Petschauer JS, Madden AJ, Zamboni WC. Nanoparticles and the mononuclear phagocyte system: pharmacokinetics and applications for inflammatory diseases. Curr Rheumatol Rev. 2014; 10:22–34. [PubMed: 25229496]

Europe PMC Funders Author Manuscripts

Song HP, Yang JY, Lo SL, Wang Y, Fan WM, Tang XS, Xue JM, Wang S. Gene transfer using self-assembled ternary complexes of cationic magnetic nanoparticles, plasmid DNA and cell-penetrating Tat peptide. Biomaterials. 2010; 31:769–778. [PubMed: 19819012]

Soto-Sanchez C, Martinez-Navarrete G, Humphreys L, Puras G, Zarate J, Pedraz JL, Fernandez E. Enduring high-efficiency in vivo transfection of neurons with non-viral magnetoparticles in the rat visual cortex for optogenetic applications. Nanomed : Nanotechnol, Biol, Med. 2015; 11:835–843.

Southgate T, Kroeger KM, Liu C, Lowenstein PR, Castro MG. Gene transfer into neural cells in vitro using adenoviral vectors. Curr Protoc Neurosci. 2008 (Unit 4), 23 Chapter 4.

Spaete RR, Frenkel N. The herpes simplex virus amplicon: a new eucaryotic defective-virus cloning-amplifying vector. Cell. 1982; 30:295–304. [PubMed: 6290080]

Staahl BT, Benekareddy M, Coulon-Bainier C, Banfal AA, Floor SN, Sabo JK, Urnes C, Munares GA, Ghosh A, Doudna JA. Efficient genome editing in the mouse brain by local delivery of engineered Cas9 ribonucleoprotein complexes. Nat Biotechnol. 2017; 35:431–434. [PubMed: 28191903]

Straub C, Granger AJ, Saulnier JL, Sabatini BL. CRISPR/Cas9-mediated gene knock-down in post-mitotic neurons. PLoS One. 2014; 9:e105584. [PubMed: 25140704]

Sun M, Zhang GR, Kong L, Holmes C, Wang X, Zhang W, Goldstein DS, Geller AI. Correction of a rat model of Parkinson's disease by coexpression of tyrosine hydroxylase and aromatic amino acid decarboxylase from a helper virus-free herpes simplex virus type 1 vector. Hum Gene Ther. 2003; 14:415–424. [PubMed: 12691607]

Szczurkowska J, Cwetsch AW, dal Maschio M, Ghezzi D, Ratto GM, Cancedda L. Targeted in vivo genetic manipulation of the mouse or rat brain by in utero electroporation with a triple-electrode probe. Nat Protoc. 2016; 11:399–412. [PubMed: 26844428]

Szczurkowska J, dal Maschio M, Cwetsch AW, Ghezzi D, Bony G, Alabastri A, Zaccaria RP, di Fabrizio E, Ratto GM, Cancedda L. Increased performance in genetic manipulation by modeling the dielectric properties of the rodent brain. Conf Proc IEEE Eng Med Biol Soc. 2013; 2013:1615–1618. [PubMed: 24110012]

Tabata H, Nakajima K. Efficient in utero gene transfer system to the developing mouse brain using electroporation: visualization of neuronal migration in the developing cortex. Neuroscience. 2001; 103:865–872. [PubMed: 11301197]

Tabata H, Nakajima K. Labeling embryonic mouse central nervous system cells by in utero electroporation. Dev Growth Differ. 2008; 50:507–511. [PubMed: 18482404]

Takeuchi I, Onaka H, Makino K. Biodistribution of colloidal gold nanoparticles after intravenous injection: Effects of PEGylation at the same particle size. Biomed Mater Eng. 2018; 29:205–215. [PubMed: 29457594]

Tan JK, Pham B, Zong Y, Perez C, Maris DO, Hemphill A, Miao CH, Matula TJ, Mourad PD, Wei H, et al. Microbubbles and ultrasound increase intraventricular polyplex gene transfer to the brain. J Control Release. 2016; 231:86–93. [PubMed: 26860281]

Tan VTY, Mockett BG, Ohline SM, Parfitt KD, Wicky HE, Peppercorn K, Schoderboeck L, Yahaya MFB, Tate WP, Hughes SM, et al. Lentivirus-mediated expression of human secreted amyloid precursor protein-alpha prevents development of memory and plasticity deficits in a mouse model of Alzheimer's disease. Mol Brain. 2018; 11:7. [PubMed: 29426354]

Tanaka DH, Maekawa K, Yanagawa Y, Obata K, Murakami F. Multidirectional and multizonal tangential migration of GABAergic interneurons in the developing cerebral cortex. Development. 2006; 133:2167–2176. [PubMed: 16672340]

Tanaka S, Uehara T, Nomura Y. Up-regulation of protein-disulfide isomerase in response to hypoxia/brain ischemia and its protective effect against apoptotic cell death. J Biol Chem. 2000; 275:10388–10393. [PubMed: 10744727]

Taniguchi Y, Young-Pearse T, Sawa A, Kamiya A. In utero electroporation as a tool for genetic manipulation in vivo to study psychiatric disorders: from genes to circuits and behaviors. Neuroscientist. 2012; 18:169–179. [PubMed: 21551077]

Taniyama Y, Morishita R. [Development of plasmid DNA-based gene transfer]. Yakugaku Zasshi. 2006; 126:1039–1045. [PubMed: 17077610]

Europe PMC Funders Author Manuscripts

Thomas CE, Ehrhardt A, Kay MA. Progress and problems with the use of viral vectors for gene therapy. Nat Rev Genet. 2003; 4:346–358. [PubMed: 12728277]

Titomirov AV, Sukharev S, Kistanova E. In vivo electroporation and stable transformation of skin cells of newborn mice by plasmid DNA. Biochim Biophys Acta. 1991; 1088:131–134. [PubMed: 1703441]

Tomita K, Kubo K, Ishii K, Nakajima K. Disrupted-in-Schizophrenia-1 (Disc1) is necessary for migration of the pyramidal neurons during mouse hippocampal development. Hum Mol Genet. 2011; 20:2834–2845. [PubMed: 21540240]

Towne C, Thompson KR. Overview on Research and Clinical Applications of Optogenetics. Curr Protoc Pharmacol. 2016; 75(11):1911–1921.

Tsunekawa Y, Terhune RK, Fujita I, Shitamukai A, Suetsugu T, Matsuzaki F. Developing a de novo targeted knock-in method based on in utero electroporation into the mammalian brain. Development. 2016; 143:3216–3222. [PubMed: 27578183]

Vega RA, Zhang Y, Curley C, Price RL, Abounader R. 370 Magnetic Resonance-Guided Focused Ultrasound Delivery of Polymeric Brain-Penetrating Nanoparticle MicroRNA Conjugates in Glioblastoma. Neurosurgery. 2016; 63(Suppl. 1):210.

Vomund S, Sapir T, Reiner O, Silva MA, Korth C. Generation of topically transgenic rats by in utero electroporation and in vivo bioluminescence screening. J Vis Exp. 2013:e50146. [PubMed: 24084570]

Walters BJ, Azam AB, Gillon CJ, Josselyn SA, Zovkic IB. Advanced In vivo Use of CRISPR/Cas9 and Anti-sense DNA Inhibition for Gene Manipulation in the Brain. Front Genet. 2015; 6:362. [PubMed: 26793235]

Wang K. Manipulating Potassium Channel Expression and Function in Hippocampal Neurons by In Utero Electroporation. Methods Mol Biol. 2018; 1684:1–5. [PubMed: 29058179]

Wang M, Zuris JA, Meng F, Rees H, Sun S, Deng P, Han Y, Gao X, Pouli D, Wu Q, et al. Efficient delivery of genome-editing proteins using bioreducible lipid nanoparticles. Proc Natl Acad Sci U S A. 2016; 113:2868–2873. [PubMed: 26929348]

Wang S, Karakatsani ME, Fung C, Sun T, Acosta C, Konofagou E. Direct brain infusion can be enhanced with focused ultrasound and microbubbles. J Cereb Blood Flow Metab. 2017; 37:706–714. [PubMed: 26969468]

Wang S, Ma N, Gao SJ, Yu H, Leong KW. Transgene expression in the brain stem effected by intramuscular injection of polyethylenimine/DNA complexes. Mol Ther. 2001; 3:658–664. [PubMed: 11356070]

Wang W, Xiong W, Wan J, Sun X, Xu H, Yang X. The decrease of PAMAM dendrimer-induced cytotoxicity by PEGylation via attenuation of oxidative stress. Nanotechnology. 2009; 20:105103. [PubMed: 19417510]

Widder KJ, Senyel AE, Scarpelli GD. Magnetic microspheres: a model system of site specific drug delivery in vivo. Proc Soc Exp Biol Med. 1978; 158:141–146. [PubMed: 674215]

Wijaya A, Hamad-Schifferli K. Ligand customization and DNA functionalization of gold nanorods via round-trip phase transfer ligand exchange. Langmuir. 2008; 24:9966–9969. [PubMed: 18717601]

Wollmann G, Tattersall P, van den Pol AN. Targeting human glioblastoma cells: comparison of nine viruses with oncolytic potential. J Virol. 2005; 79:6005–6022. [PubMed: 15857987]

Wu J. Temperature rise generated by ultrasound in the presence of contrast agent. Ultrasound Med Biol. 1998; 24:267–274. [PubMed: 9550185]

Yadav S, Gandham SK, Panicucci R, Amiji MM. Intranasal brain delivery of cationic nanoemulsion-encapsulated TNFalpha siRNA in prevention of experimental neuroinflammation. Nanomed : Nanotechnol, Biol, Med. 2016; 12:987–1002.

Yamada M, Seto Y, Taya S, Owa T, Inoue YU, Inoue T, Kawaguchi Y, Nabeshima Y, Hoshino M. Specification of spatial identities of cerebellar neuron progenitors by ptf1a and atoh1 for proper production of GABAergic and glutamatergic neurons. J Neurosci. 2014; 34:4786–4800. [PubMed: 24695699]

Yan Z, Zak R, Zhang Y, Engelhardt JF. Inverted terminal repeat sequences are important for intermolecular recombination and circularization of adeno-associated virus genomes. J Virol. 2005; 79:364–379. [PubMed: 15596830]

Europe PMC Funders Author Manuscripts

Europe PMC Funders Author Manuscripts

Yang R, Yang X, Zhang Z, Zhang Y, Wang S, Cai Z, Jia Y, Ma Y, Zheng C, Lu Y, et al. Single-walled carbon nanotubes-mediated in vivo and in vitro delivery of siRNA into antigen-presenting cells. Gene Ther. 2006; 13:1714–1723. [PubMed: 16838032]

Yang S, Chang R, Yang H, Zhao T, Hong Y, Kong HE, Sun X, Qin Z, Jin P, Li S, et al. CRISPR/Cas9-mediated gene editing ameliorates neurotoxicity in mouse model of Huntington's disease. J Clin Invest. 2017; 127:2719–2724. [PubMed: 28628038]

Yin H, Kanasty RL, Eltoukhy AA, Vegas AJ, Dorkin JR, Anderson DG. Non-viral vectors for gene-based therapy. Nat Rev Genet. 2014; 15:541–555. [PubMed: 25022906]

Yin WL, Yin WG, Huang BS, Wu LX. Neuroprotective effects of lentivirus-mediated cystathionine-beta-synthase overexpression against 6-OHDA-induced parkinson's disease rats. Neurosci Lett. 2017; 657:45–52. [PubMed: 28764908]

Yoon SO, Lois C, Alvirez M, Alvarez-Buylla A, Falck-Pedersen E, Chao MV. Adenovirus-mediated gene delivery into neuronal precursors of the adult mouse brain. Proc Natl Acad Sci U S A. 1996; 93:11974–11979. [PubMed: 8876247]

Yu X, Liang X, Xie H, Kumar S, Ravinder N, Potter J, de Mollerat du Jeu X, Chesnut JD. Improved delivery of Cas9 protein/gRNA complexes using lipofectamine CRISPRMAX. Biotechnol Lett. 2016; 38:919–929. [PubMed: 26892225]

Zarebkohan A, Najafi F, Moghimi HR, Hemmati M, Deevband MR, Kazemi B. Synthesis and characterization of a PAMAM dendrimer nanocarrier functionalized by SRL peptide for targeted gene delivery to the brain. Eur J Pharm Sci. 2015; 78:19–30. [PubMed: 26118442]

Zhang H, Yang B, Mu X, Ahmed SS, Su Q, He R, Wang H, Mueller C, Sena-Esteves M, Brown R, et al. Several rAAV vectors efficiently cross the blood-brain barrier and transduce neurons and astrocytes in the neonatal mouse central nervous system. Mol Ther. 2011; 19:1440–1448. [PubMed: 21610699]

Zhang L, Yu F, Cole AJ, Chertok B, David AE, Wang J, Yang VC. Gum arabic-coated magnetic nanoparticles for potential application in simultaneous magnetic targeting and tumor imaging. AAPS J. 2009; 11:693–699. [PubMed: 19842043]

Zhang Y, Petibone D, Xu Y, Mahmood M, Karmakar A, Casciano D, Ali S, Biris AS. Toxicity and efficacy of carbon nanotubes and graphene: the utility of carbon-based nanoparticles in nanomedicine. Drug Metab Rev. 2014; 46:232–246. [PubMed: 24506522]

Zhao G, Huang Q, Wang F, Zhang X, Hu J, Tan Y, Huang N, Wang Z, Wang Z, Cheng Y. Targeted shRNA-loaded liposome complex combined with focused ultrasound for blood brain barrier disruption and suppressing glioma growth. Cancer Lett. 2018; 418:147–158. [PubMed: 29339208]

Zhao MG, Toyoda H, Lee YS, Wu LJ, Ko SW, Zhang XH, Jia Y, Shum F, Xu H, Li BM, et al. Roles of NMDA NR2B subtype receptor in prefrontal long-term potentiation and contextual fear memory. Neuron. 2005; 47:859–872. [PubMed: 16157280]

Zhi D, Bai Y, Yang J, Cui S, Zhao Y, Chen H, Zhang S. A review on cationic lipids with different linkers for gene delivery. Adv Colloid Interface Sci. 2018; 253:117–140. [PubMed: 29454463]

Zuris JA, Thompson DB, Shu Y, Guilinger JP, Bessen JL, Hu JH, Maeder ML, Joung JK, Chen ZY, Liu DR. Cationic lipid-mediated delivery of proteins enables efficient protein-based genome editing in vitro and in vivo. Nat Biotechnol. 2015; 33:73–80. [PubMed: 25357182]

Europe PMC Funders Author Manuscripts

Europe PMC Funders Author Manuscripts

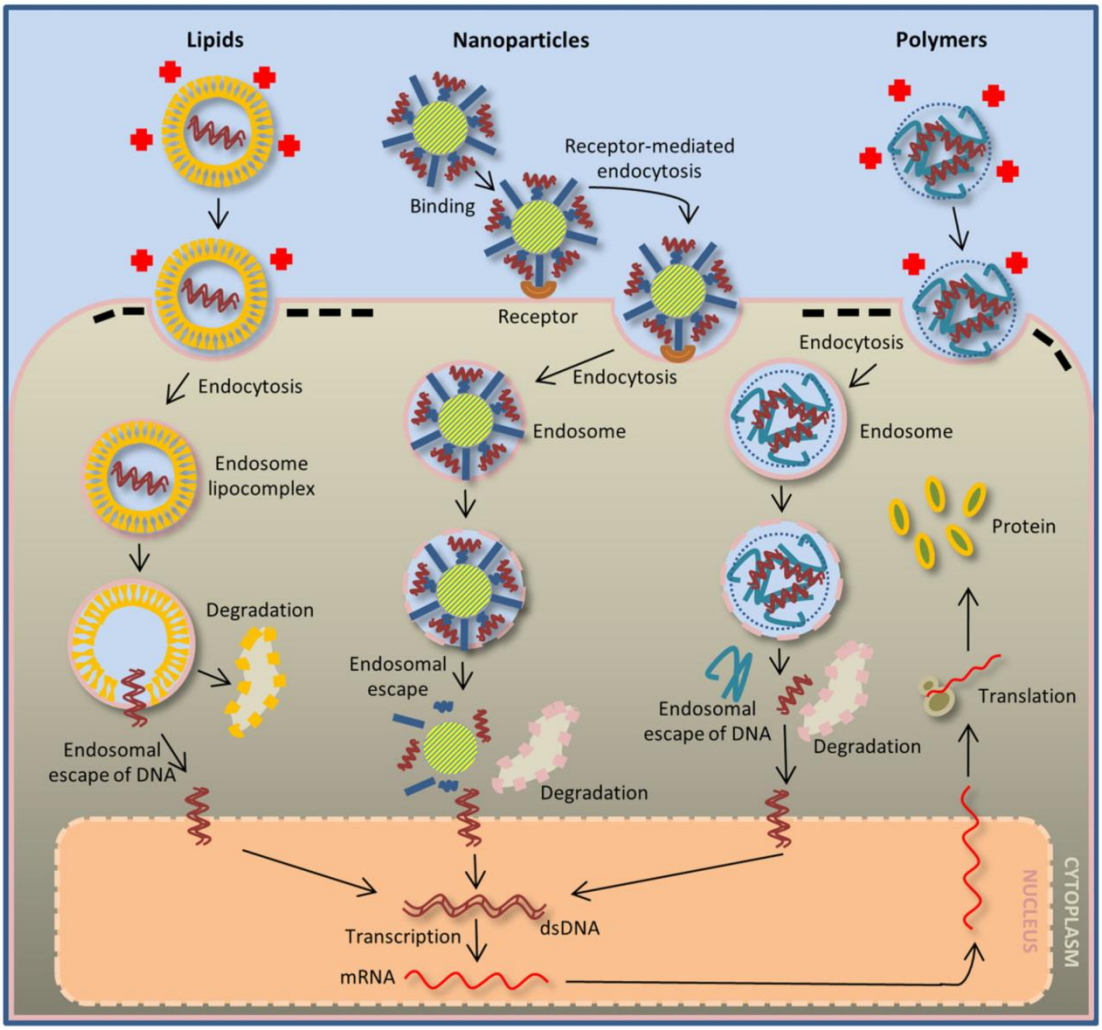

Fig. 1. Chemical methods of gene delivery.

Lipid-mediated gene transfer (left) occurs by the interaction between the positively charged surface of the carriers and the negatively charged cell membrane. This interaction promotes endocytosis, creating an endosome lipocomplex. The complex is then degraded in the cell cytoplasm, and the released DNA is transported to the nucleus. *Nanoparticle*-mediated gene transfer (middle) occurs by the nanoparticles binding to receptors on the cell surface, followed by endocytosis. During endosome degradation in the cell cytoplasm, the DNA attached to the core of the nanoparticles is released and transported to the nucleus. Similar to lipid-mediated gene transfer, *polymer*-mediated gene transfer (right) occurs *via* charge differences between the carriers and the cell membrane, which promotes binding and endocytosis. During endosome degradation, the DNA is released from the polymer structure

and is transported to the nucleus. After DNA transcription, the mRNA exits the nucleus, and it is translated into a protein in the cytoplasm.

Europe PMC Funders Author Manuscripts

Europe PMC Funders Author Manuscripts

Europe PMC Funders Author Manuscripts

Europe PMC Funders Author Manuscripts

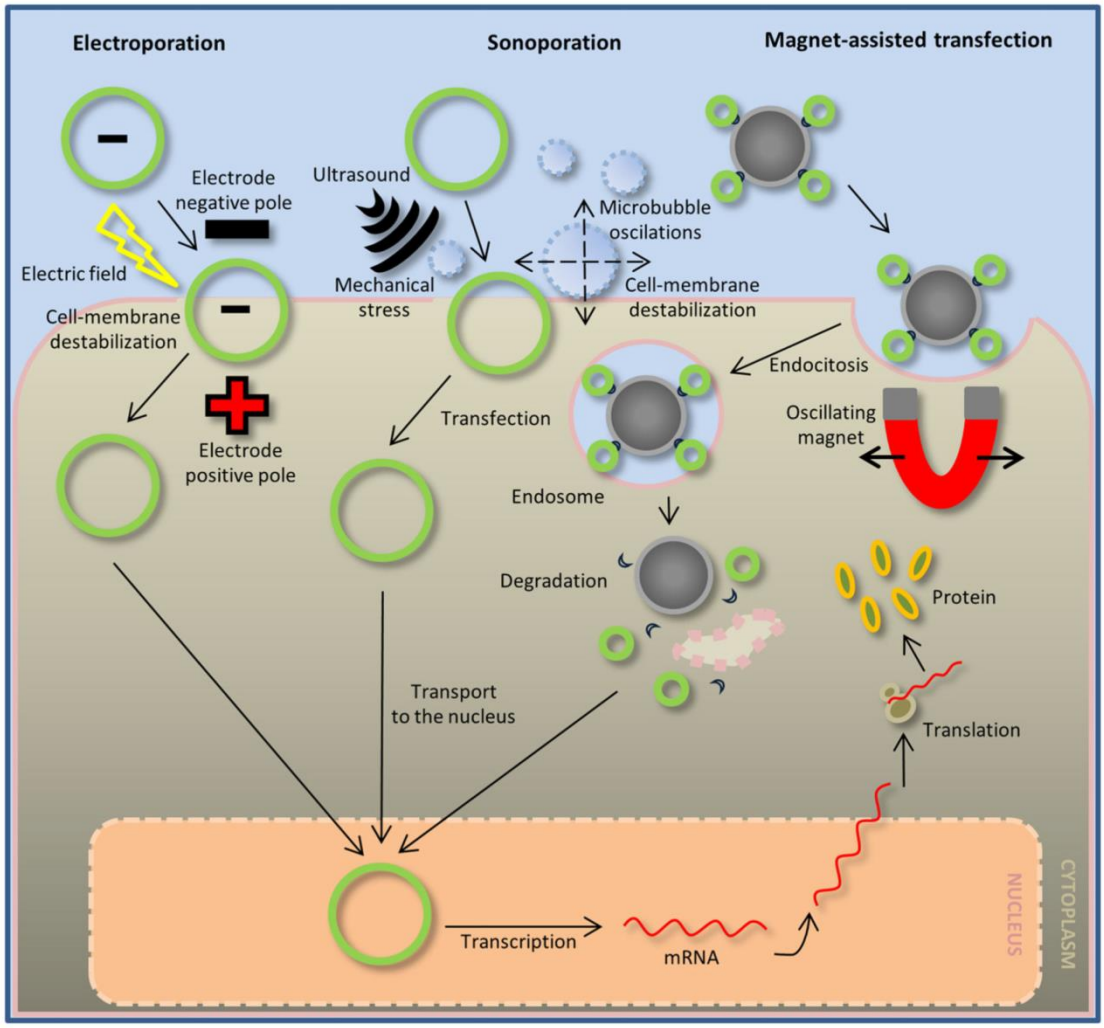

Fig. 2. Physical methods of gene delivery.

Electroporation-mediated gene transfer (left) enables the directional guidance of plasmids carrying the negatively charged DNA of interest towards the positive pole of the electrode. At the same time, electroporation causes destabilization of the structure of the cell membrane, creating temporary pores in its surface and allowing the plasmid to enter the cell. The plasmid is then transported to the nucleus. *Sonoporation*-mediated gene transfer (middle) occurs by ultrasound application, which promotes destabilization of the cell membrane in the presence of oscillating microbubbles. During this process, the plasmid contained in the microbubble mixture enters the cell and is then transported to the nucleus. *Magnet*-assisted transfection (right) is mediated by magnetic field oscillations that guide and promote endocytosis of the magnetic carriers with attached DNA. In the cytoplasm of the

cell, the endosome undergoes degradation and the released DNA enters the cell nucleus. After DNA transcription, the mRNA exits the nucleus, and it is translated into a protein in the cytoplasm.

Europe PMC Funders Author Manuscripts

Europe PMC Funders Author Manuscripts

Europe PMC Funders Author Manuscripts

Europe PMC Funders Author Manuscripts

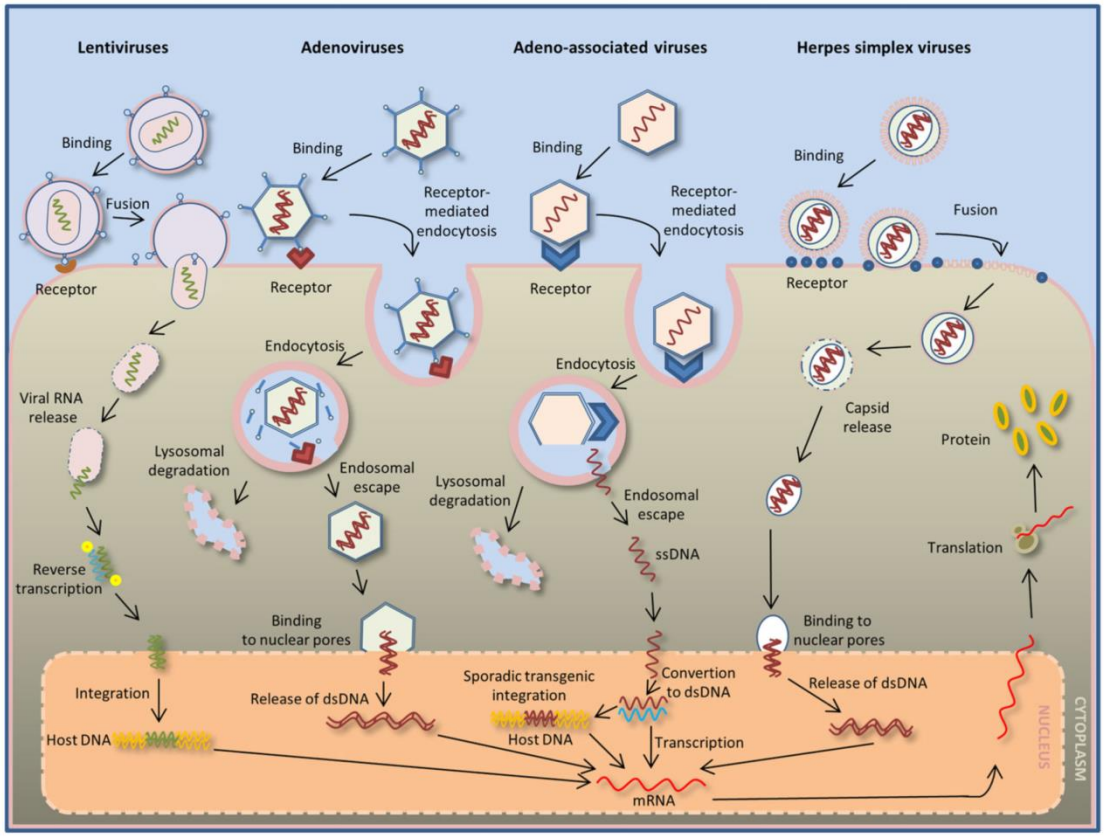

Fig. 3. Virus-mediated transduction.

A *lentivirus* (left) can carry RNA inside its capsid. Contact with cell-specific receptors induces the fusion of the capsid with the cell membrane, followed by RNA release. In the cell cytoplasm, the released RNA undergoes reverse transcription, and upon transport to the nucleus, the RNA is integrated with the host DNA. *Adenovirus* infection (middle left) is mediated by specific receptor binding on the cell membrane, followed by endocytosis. Endosome degradation then results in the release of the virus capsid and lysosomal degradation of the endosome. The released virus capsid binds to the nuclear pore of the infected-cell nucleus, allowing the introduction of the double-stranded DNA inside the nucleus. *Adeno-associated virus* infection (middle right) is mediated by receptor binding on the host-cell surface and endocytosis. Endosome degradation results in the release of single-stranded DNA. The single-stranded DNA enters the nucleus and undergoes a conversion to double-stranded DNA, which can be either integrated in the host DNA (and later transcribed) or can remain in the host cell nucleus as nonintegrated viral DNA. *Herpes simplex virus*-mediated gene delivery (right) is the result of receptor binding and fusion of the virus with the cell membrane of the host cell. Inside the cell, the released capsid binds to the nuclear pore and introduces double-stranded DNA into the nucleus to be transcribed. The

viral DNA in the host cell nucleus is transcribed into mRNA. The transcribed viral mRNA exits the nucleus, and it is translated into a protein in the cytoplasm of the host cell.

Europe PMC Funders Author Manuscripts

Europe PMC Funders Author Manuscripts

Europe PMC Funders Author Manuscripts
Europe PMC Funders Author Manuscripts

Table 1

Chemical methods for transfection.

Group	Type/Helper	Toxicity	*In vivo* delivery method	Efficiency/Stability	BBB accessibility	Most Prominent Applications (references)
Lipids	Liposomes	→	N/A	↓	N/A	Nayerossadat et al., 2012
	Cationic lipid mix/PEG	↓	Intraventricular injection	→	N/A	Hassani et al., 2005; Nayerossadat et al., 2012; Yin et al., 2014;Zhi et al., 2018
	Cationic lipid mix/DOPE	↓	Intraventricular injection, Intratumoral (glioblastoma) injection	↑	N/A	Roessler and Davidson et al., 1994; Hassani et al., 2005; Pulkkanen and Yla-Herttuala, 2005; Lagarce and Passirani, 2016;Cikankowitz et al., 2017
	Lipid Nanoemulsions	↓	Intranasal	↑	N/A	Ramamoorth and Narvekar, 2015; Yadav et al., 2016
	Solid lipid nanoparticles	↓	Intravenous injection	↑	Possibly	Jin et al., 2011; Pathak et al., 2017
Nanoparticles	Silica	↓	Subventricular injection, Intracortical injection	↑	N/A	Bharali et al., 2005; Luo and Saltzman, 2006
	Gold nanoparticles	↓	Systemic injection	→	+	Jensen et al., 2013; Escudero-Francos et al., 2017; Takeuchi et al., 2018; Hu et al., 2018
	Carbon Nanotubes	↓	Intraventricular injection	↑	N/A	Al-Jamal et al., 2011; Costa et al., 2016
Polymers	Polyethylenimine	↑	Intracortical injection	↓	(+ with PEG)	Abdallah et al., 1996; Lungwitz et al., 2005; Nouri et al., 2017
	Polyethylenimine/RVG	↑	Tail injection	↓	+	Hwang et al., 2011
	Chitosans/PEG	↓	Intratumoral (glioblastoma) injection	↑	–	Duceppe and Tabrizian, 2010; Danhier et al., 2015; Ramamoorth and Narvekar, 2015
	ChitosansTrimethylated/PEG + RVG	↓	Intravenous injection	↑	+	Gao et al., 2014
	Polyamidoamine (with various functionalizations)	↓	Tail injection, Systemic injection, Intravenous administration	↑	+	Huang et al., 2007;Huang et al., 2008;Ke et al., 2009;Zarebkohan et al., 2015

↓high / →medium / ↓low / +yes / -no / N/A-information not available.

Prog Neurobiol. Author manuscript; available in PMC 2018 September 01.

Europe PMC Funders Author Manuscripts

Europe PMC Funders Author Manuscripts

Table 2

Physical methods for transfection.

Group	Type/Helper	Toxicity	*In vivo* delivery method	Efficiency/Stability	BBB accessibility	Most Prominent Applications (references)
Electroporation	*In utero*	↓	Intraventricular injection	↑	N/A	Saito, 2006;Dal Maschio et al., 2012;Szczurkowska et al., 2016
	Exo utero	↓	Intraventricular injection	↑	N/A	Akamatsu et al., 1999; Saba et al., 2003
	Postnatal	↓	Intraventricular injection, Stereotaxic micro injection	↑	N/A	Boutin et al., 2008; Chesler et al., 2008;Kitamura et al., 2008
Sonoporation	Microbubbles	→	Systemic injection, Intraventricular injection	↓	–	Endoh et al., 2002;Tan et al., 2016
Magnet-assisted transfection	Magnetic nanoparticles/PEI	↓	Lumbar intrathecal injection, Stereotaxic injection	→	–	Song et al., 2010;Soto-Sanchez et al., 2015

↑high / →medium / ↓low / +yes / -no / N/A-information not available.

Europe PMC Funders Author Manuscripts

Europe PMC Funders Author Manuscripts

Table 3

Virus-mediated transduction.

Group	Type / Helper	Toxicity	*In vivo* delivery method	Efficiency /Stability	BBB accessibility	Most Prominent Applications (references)
Lentivirus	HIV / VSV-G	↓	Stereotaxic micro injection	↑	N/A	Naldini et al., 1996a; Mah et al., 2002b;Artegiani and Calegari et al., 2013
Adenovirus	Replication-defective ADV	↑	Stereotaxic micro injection, Intraventricular injection	↑	N/A	Yoon et al., 1996;Germano et al., 2003
Adeno-associated virus	AAV	↓	Stereotaxic micro injection	↑	N/A	Mah et al., 2000; Kay et al., 2001;Mah et al., 2002a
	AAV-DJ	↓	Stereotaxic micro injection, Intravenous injection	↑	+	Grimm et al., 2008; Duque et al., 2009; Foust et al., 2009Gray et al., 2010; Bourdenx et al., 2014
Herpes simplex virus	HSV / helper virus	→	Stereotaxic micro injection	↑	N/A	Spaete and Frenkel, 1982; Krisky et al., 1998; Sun et al., 2003

↑high / →medium / ↓low / +yes / -no / N/A-information not available.

APPENDIX III

***Activity-dependent expression of Channelrhodopsin at neuronal synapses*.**

Francesco Gobbo, Laura Marchetti, Ajesh Jacob, Bruno Pinto, Noemi Binini, Federico Pecoraro Bisogni, Claudia Alia, Stefano Luin, Matteo Caleo, Tommaso Fellin, Laura Cancedda, Antonino Cattaneo.

nature COMMUNICATIONS

ARTICLE

DOI: 10.1038/s41467-017-01699-7 OPEN

Activity-dependent expression of Channelrhodopsin at neuronal synapses

Francesco Gobbo[1,2], Laura Marchetti[1,2,3], Ajesh Jacob[1], Bruno Pinto[1,4], Noemi Binini[5], Federico Pecoraro Bisogni[5], Claudia Alia[1,6], Stefano Luin[2], Matteo Caleo[6], Tommaso Fellin[5], Laura Cancedda[4,7] & Antonino Cattaneo[1]

Increasing evidence points to the importance of dendritic spines in the formation and allocation of memories, and alterations of spine number and physiology are associated to memory and cognitive disorders. Modifications of the activity of subsets of synapses are believed to be crucial for memory establishment. However, the development of a method to directly test this hypothesis, by selectively controlling the activity of potentiated spines, is currently lagging. Here we introduce a hybrid RNA/protein approach to regulate the expression of a light-sensitive membrane channel at activated synapses, enabling selective tagging of potentiated spines following the encoding of a novel context in the hippocampus. This approach can be used to map potentiated synapses in the brain and will make it possible to re-activate the neuron only at previously activated synapses, extending current neuron-tagging technologies in the investigation of memory processes.

[1] Bio@SNS, Scuola Normale Superiore, piazza dei Cavalieri 7, 56126 Pisa, Italy. [2] NEST, Scuola Normale Superiore, piazza San Silvestro 12, 56127 Pisa, Italy. [3] Center for Nanotechnology Innovation @NEST, Istituto Italiano di Tecnologia, piazza San Silvestro 12, 56127 Pisa, Italy. [4] Department of Neuroscience and Brain Technologies, Istituto Italiano di Tecnologia, via Morego 30, 16163 Genoa, Italy. [5] Optical Approaches to Brain Function Laboratory, Department of Neuroscience and Brain Technologies, Istituto Italiano di Tecnologia, via Morego 30, 16163 Genova, Italy. [6] Istituto di Neuroscienze, Consiglio Nazionale delle Ricerche, via Moruzzi 1, 56124 Pisa, Italy. [7] Dulbecco Telethon Institute, via Varese 16b, 00185 Rome, Italy. Correspondence and requests for materials should be addressed to A.C. (email: antonino.cattaneo@sns.it)

Understanding the mnemonic processes is one of the greatest challenges in neuroscience. Long-lasting changes in the synaptic connectivity between neurons are generally accepted to be crucial for the establishment and maintenance of memories[1,2]. Similarities between synaptic and memory consolidation suggest shared mechanisms[3–5], and synaptic modifications have been shown to be critically involved in memory formation, strengthening, and recall[6,7]. Recently, it has become possible to define sets of neurons involved in specific memories by activity-dependent tagging[8–10]. However, many details remain to be worked out on the role of the modifications at the synapse level in the encoding and establishment of memories[6,11–13].

Whereas much progress in the understanding of neural circuits has been made using optogenetics[8,9], to date no direct modulation of specific synapses involved in the formation of memories has been possible using state-of-the-art optogenetic tools. Indeed, the current spatial resolution of opsin expression in activity-dependent tagging is the whole neuron. Cell-wide excitation does not take into account, for instance, the complexity of different incoming pathways converging onto the same postsynaptic neuron[14] and the synchronous activation of the whole cell may fail to mimic a physiological condition[14,15]. In recent attempts, subcellular localization of light-sensitive effectors has taken advantage of trafficking signals inserted into the opsin aminoacidic sequence[16–18]. For example, channelrhodopsin-2 (ChR2) and halorhodopsin were differentially targeted with protein-targeting signals to the soma and dendrites of retinal ganglion cells, to recreate antagonistic center-surround receptive fields[19], and fusion with a MyosinVa-binding domain targeted

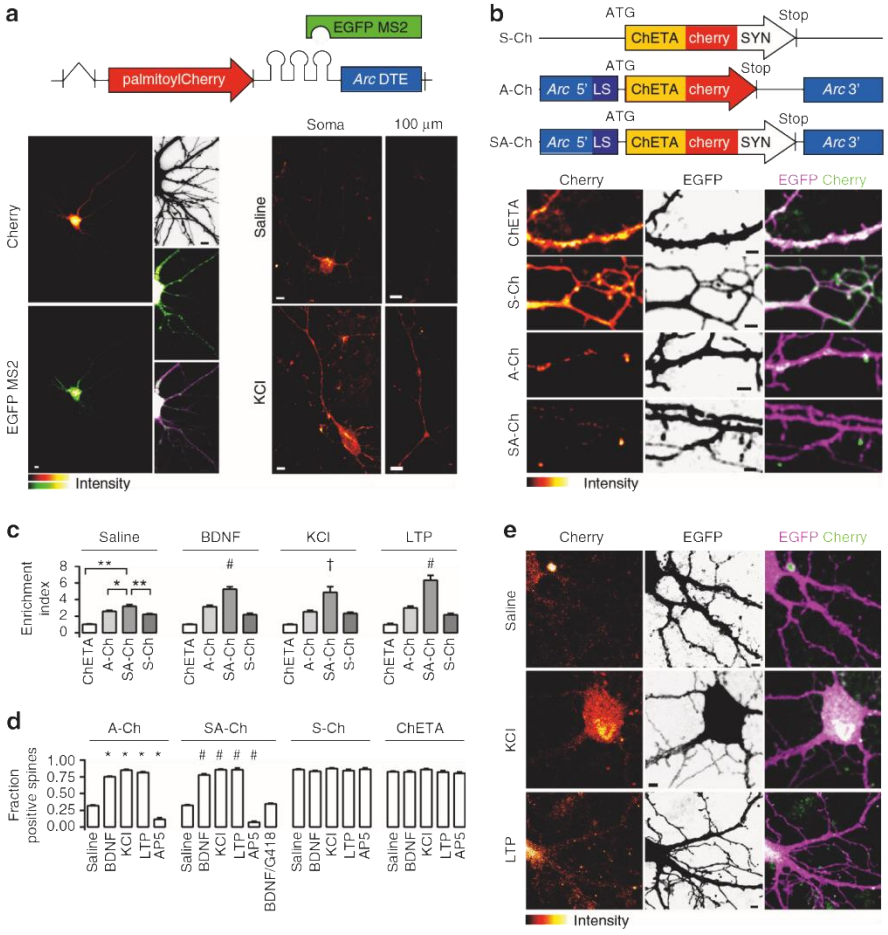

Fig. 1 Activity-dependent SA-Ch expression at spines. **a** Schematic construct of palmitoyl-Cherry/MS2 reporter. Left, Cherry (top) and EGFP-MS2 (bottom) distribution in living neurons under resting conditions. In the presence of *Arc* DTE, MS2/RNA signal is granular. Inset, top to bottom, neuron profile, EGFP-MS2, merge (stretched levels). Right, *Arc* DTE regulates reporter expression in response to neuron activity. Cherry expression in proximal dendrites ("soma") and 100 µm away from the soma ("100 µm") after 1 h saline (top) or 10 mM KCl (bottom) treatment. **b** Schematic S-Ch, A-Ch and SA-Ch constructs. Below, dendritic pattern of ChETA-Cherry expression (left), EGFP filler (centre) and merge (right) for unmodified ChETA-Cherry and the three constructs above. **c** Enrichment Index for the three constructs and unmodified ChETA-Cherry under different stimulation conditions (see Methods). $^{*}P < 0.01$ and $^{**}P < 0.001$, one-way ANOVA, Bonferroni comparison of means, within group. †$P < 0.05$ and #$P < 0.001$ to SA-Ch, saline treated, one-way ANOVA, Bonferroni comparison of means. **d** Fraction of ChETA-Cherry-expressing spines under different stimulation conditions, grouped for construct. $^{*}P < 0.001$ to A-Ch saline and #$P < 0.001$ to SA-Ch saline, one-way ANOVA, Bonferroni comparison of means. Differences within and between S-Ch and ChETA values are not significant at the 0.05 level. **e** Representative images of SA-Ch-expressing neurons under different treatment conditions. Following KCl or NMDA-dependent LTP, bright ChETA-Cherry puncta are evident along dendrites. Bars are mean ± SEM. Data in **d** and **e** are reported as boxplots in Supplementary Fig. 5. Scale bar (a) 5 µm, (b,e) 2 µm. *N* and replicate numbers for all figures are listed in Supplementary Table 1

ChR2 to the somatodendritic compartment of neurons in living mice[16]. These approaches can be useful to refine spatial stimulation specificity and to activate specific subcellular compartments[18]. However, tagging different subsets of synapses based on their activity in order to selectively stimulate them appear demanding tasks for this protein-based approach, as it is not straightforward to integrate it with activity-tagging methodologies. Indeed, synapses are at the same time a subcellular compartment of the neuron and the physical site of circuit connections, enabling them to undergo local modifications in an autonomous way[6]. Single-synapse optogenetics can be achieved by restricting illumination to single spines[20], but this requires *a priori* knowledge of the identity of the synapses involved in the circuit, in order to test their role in a memory process.

A functionally relevant reactivation of the incoming stimulus in an unbiased, synapse-specific way would require the tagging of activated synapses by locally expressing opsins. Towards this aim, here we describe a novel strategy, named SynActive (SA), for the expression of proteins at synapses in an input-specific, activity-dependent manner by combining RNA targeting elements and a short protein tag. The SA-Channelrhodopsin variant presented here is locally translated at synapses in vitro and in vivo, and the exploration of a novel context increases the number of hippocampal synapses expressing the opsin, revealing a non-random dist′ribution of the activated synapses along dendrites.

Results

***Arc* mRNA targeting element regulates translation**. We developed a dual RNA/protein reporter to compare possible RNA synaptic tags. Transcripts encode membrane-anchored fast-maturing fluorescent mCherry[21] and bear different dendritic or axonal targeting elements (DTEs and ATEs, see Supplementary Methods); MS2-binding sites in the 3′-untranslated region (UTR) bind EGFP-MS2 protein to visualize RNA[22]. *Arc* is transcribed in an activity-dependent manner and its messenger RNA localizes near synapses that experienced recent activity; in resting conditions, it is believed to be translationally repressed within ribonucleoparticle (RNP) granules[23]. We found that a minimal DTE from *Arc* 3′-UTR[24] determined a significantly lower level of mCherry expression in non-stimulated neurons than strong or constitutive DTEs from alphaCaMKII or MAP2 (Fig. 1a and Supplementary Fig. 1), whereas a discrete, granule-like *Arc*/MS2 signal was detected in the soma and along dendrites (Fig. 1a). KCl activation of neurons expressing the *Arc* DTE construct dramatically increased mCherry fluorescence in dendrites as far as 100 µm away from the soma in as little as 1 h (Fig. 1a), significantly increasing mCherry dendritic pool; conversely, the increase driven by alphaCaMKII DTE was less prominent (Supplementary Fig. 1).

Synergistic action of RNA and protein. To enrich opsin expression at synapses, we combined RNA- and protein-targeting sequences. We cloned fast-spiking ChETA-Cherry[25] between *Arc* 5′- and 3′-UTRs. Although 3′-UTR may contain DTEs, 5′-UTR and other parts of 3′-UTR generally regulate translation[26]. For instance *Arc* 5′-UTR has IRES (internal ribosome entry site)-like activity[27], a process involved in the synaptic translation associated to long-term potentiation (LTP)[26]. As ribosomes typically lie at the dendrite-spine junction, we reasoned that a protein tag interacting with postsynaptic components would improve spine retention and enrichment of the newly synthesized protein. We therefore fused to the C terminus of ChETA-Cherry a short bipartite tag (AAAASIESDVAAAAETQV, hereafter SYN tag) composed of the *N*-methyl-D-aspartate receptor (NMDAR) C terminus SIESDV and the PSD95-PDZ-binding consensus ETQV, which has been previously reported to enrich proteins at postsynaptic sites[28,29].

To compare the distinct contributions of the protein and RNA instructive signals, we generated three constructs and expressed them in primary neurons: (i) *Arc* 5′-ChETA-Cherry-MS2-*Arc* 3′-UTR (hereafter A-Ch); (ii) ChETA-Cherry-SYN tag-MS2 (S-Ch), and (iii) *Arc* 5′-ChETA-Cherry-SYN tag-MS2-*Arc* 3′-UTR (SA-Ch) (Fig. 1b). Neurons expressing the constructs were morphologically similar to each other or to neurons expressing enhanced green fluorescent protein (EGFP) alone; neither the modified SYN-ChETA nor *Arc* UTRs determined significant changes in spine number and morphology (Supplementary Fig. 2a–c). In addition, SA-Ch expression did not alter the ratio of surface NMDAR/AMPAR (Supplementary Fig. 2d).

Brain-derived neurotrophic factor (BDNF) administration, which causes a translation-dependent late form of LTP[30], induced dendritic expression of A-Ch, but not of S-Ch; following BDNF treatment, A-Ch signal in dendrites was significantly higher than that of EGFP, which lacks DTEs and is translated in the soma only (Supplementary Fig. 3a). Conversely, dendritic S-Ch distribution was quite similar to that of EGFP. This is consistent with previous observations that BDNF boosts the translation of transcripts bearing alphaCaMKII 3′-UTR, increasing the protein levels along dendrites as compared to the soma[31]. In addition, A-Ch and SA-Ch RNA in unstimulated neurons, identified by RNA-tethered EGFP-MS2, was prevalently granular along dendrites. Following KCl treatment, the RNA/MS2 signal became much more diffuse (Supplementary Fig. 4a, b), indicating RNA exit from granule, allowing local SA-Ch translation[26].

We then co-expressed the three ChETA-Cherry variants with EGFP in cortical neurons to compare their subcellular expression pattern. S-Ch was enriched at spines compared to unmodified ChETA-Cherry (Fig. 1b, c), but spines were labelled quite evenly. Conversely, A-Ch labelled spines in a sparse way (Fig. 1b). In many cases the base of the spine, rather than the head, was labelled most intensely, and Cherry fluorescence was also prominent on the dendritic shaft. SA-Ch recapitulated the sparse expression pattern typical of A-Ch, while more trustfully tagging spine heads (Fig. 1b).

A quantitative enrichment index (EI), the ratio of ChETA-fused Cherry intensity at the synapse to that measured in the dendritic shaft (1 to 2 µm from the spine junction), demonstrated effective SA-Ch accumulation at synapses. The EI calculated for SA-Ch was significantly higher than that for A-Ch or S-Ch, and all three constructs had higher EI than ChETA-Cherry (Fig. 1c).

Activity-dependent SA-Ch expression and synapse enrichment. We next characterized the activity-dependent regulation of SA-Ch expression at synapses. Treatment of cortical neurons with (i) BDNF, that induces L-LTP[26,30], (ii) KCl, and (iii) NMDA, under conditions that promote spine potentiation (NMDA-induced LTP) (see Methods and Supplementary Fig. 6) dramatically increased the number of SA-Ch-positive spines (Fig. 1d, e). Conversely, NMDAR inhibition with AP5 drastically reduced the number of SA-Ch-positive spines. Translation inhibition with G418 (geneticin) blocked BDNF effect on SA-Ch expression, demonstrating its dependence on novel protein synthesis. In terms of expressing spines, SA-Ch response to treatments was identical to that of A-Ch, whereas neither S-Ch nor ChETA-Cherry expression was affected by treatments that increased or decreased neural activity (Fig. 1d). Importantly, treatments that activate neurons or induce synaptic LTP significantly increase SA-Ch EI, relative to saline treatment (Fig. 1c), and A-Ch EI was only modestly responsive to treatments. We ascribe this last effect to the fact that, following translation, A-Ch can diffuse in the

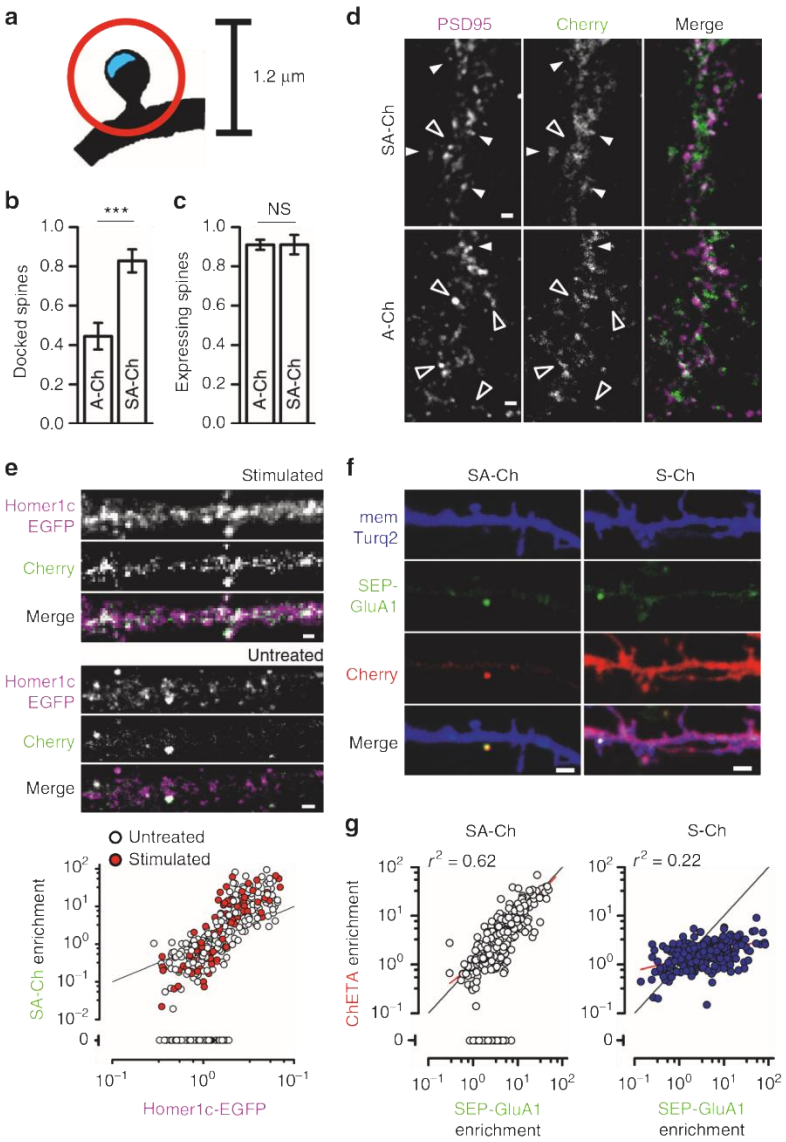

Fig. 2 Synergistic action of RNA and protein regulatory sequences. SYN tag confers synaptic localization of SA-Ch protein (**a**–**d**), whereas RNA sequences maps its expression to potentiated spines (**e**–**g**). **a** Schematic drawing for the determination of "docked" vs. positive but non-"docked" spines. Cherry fluorescence peaks within a circle of 1.2 µm diameter (red circle) centered on the postsynaptic density (PSD - blue area) for positive spines, and on the PSD for "docked" spines. Quantification of "docked" **b** and total positive spines (**c** following cLTP treatment (see Methods) for A-Ch and SA-Ch. Bars are mean ± SEM. $^{***}P < 0.001$ two-tailed Student's *t*-test. NS, not significant at the $\alpha = 0.05$ level. **d** Representative dendrites of neurons expressing the two constructs. White arrowheads indicate "docked" spines, empty arrowheads positive, non-"docked" spines. Another example is reported in Supplementary Fig. 7a. **e** SA-Ch co-localizes with PSD marker Homer1c-EGFP. In stimulated as well as in unstimulated neurons, SA-Ch was expressed at Homer1c-EGFP puncta (top). SA-Ch correlation with Homer1c-EGFP is supralinear, indicating that SA-Ch is preferentially enriched at spines with larger PSD (bottom graph). Spines that do not express SA-Ch are assigned a value of zero. White dots are spines from unstimulated neurons, red dots from stimulated ones, black line represents the diagonal. Because the plot has double-log scale, any linear correlation has unitary slope and is parallel to this line. **f** Comparison of SA-Ch and S-Ch expression: SA-Ch is only expressed at SEP-GluA1-tagged spines, whereas S-Ch has no preference for SEP-GluA1-positive spines. **g** SA-Ch (grey dots) significantly correlates with SEP-GluA1 expression in a linear fashion, whereas S-Ch (blue dots) does not. A proportion of SEP-GluA1-positive spines do not express SA-Ch and those spines are assigned an enrichment value of zero. Red lines indicate the regression lines. Scale bar, 1 µm (**d**, **e**) and 2 µm (**f**)

membrane both onto the spine head and along the dendritic shaft; conversely, the SYN tag helps retention of SA-Ch in the spine (Fig. 1c). The observed somatic SA-Ch protein (Fig. 1e and Supplementary Fig. 4) can probably be ascribed to the global level of the stimulations, which can signal the overexpressed transcript to be de-repressed also in the soma. In fact, in non-stimulated neurons somatic expression is much lower (Fig. 1e, first row and Supplementary Fig. 4a, second row), and can be further reduced by controlling promoter strength and localizing stimulation (see section "In vivo synaptic tagging with SA-Ch").

To probe the specificity of SA-Ch accumulation at synapses, we performed double immunofluorescence (IF) against Cherry and

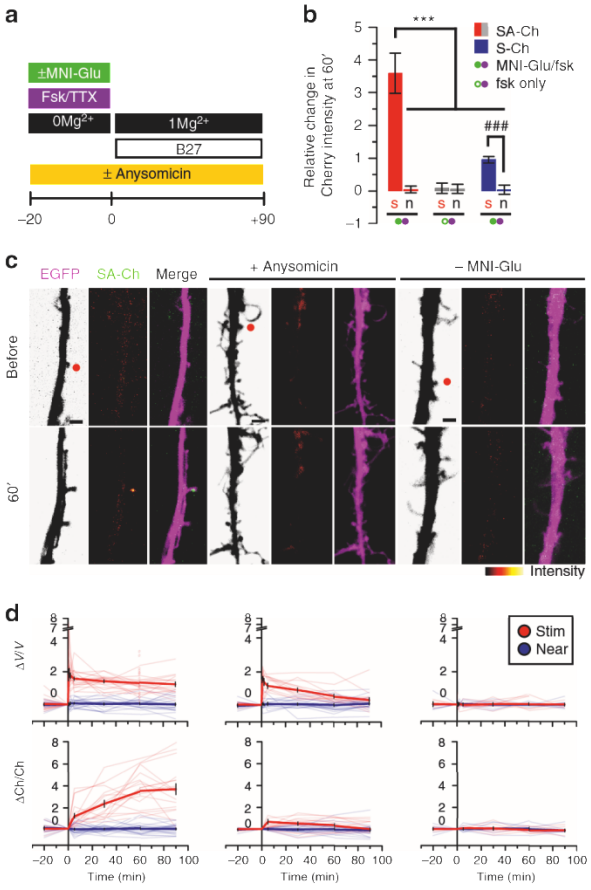

Fig. 3 Synapse specificity of SA-Ch expression at potentiated synapses. SA-Ch is specifically expressed at potentiated synapses. DIV 8-10 neurons were focally stimulated by uncaging glutamate in close proximity to selected spines. **a** Neurons were maintained in standard Mg^{2+}-free ACSF in the presence of forskolin and TTX for 20 min before uncaging with or without MNI-caged glutamate. Following two-photon uncaging, medium was changed to 1 mM Mg^{2+} ACSF supplemented with B27. **b** Local release of glutamate stimulates SA-Ch translation at stimulated (s), but not nearby (n) spines. This effect was specific to glutamate release, as it was absent when MNI-glutamate was not added to the medium. Following stimulation, S-Ch change was much lower and is an effect of spine enlargement. ***$P < 0.001$, one-way ANOVA, Bonferroni comparison of means. ### $P < 0.001$ unpaired samples Student's *t*-test, two-tailed. Bars are mean ± SEM. **c** Translation inhibition with anysomicin blocked SA-Ch accumulation at stimulated synapses. Representative images of stimulated dendrites in neurons transfected with SA-Ch. Red dots in the EGFP channel indicate the location of two-photon uncaging. Experimental conditions are indicated on top of images. Scale bar, 2 µm. **d** Time course of relative changes in volume ($\Delta V/V$, top graphs, measured by the EGFP intensity) and SA-Ch intensity ($\Delta Ch/Ch$, bottom graphs) following uncaging of stimulated (red) and near spines (blue). Stimulation induced a long-lasting volume change, paralleled by a slowly rising accumulation of SA-Ch; in the presence of anysomicin, volume change was transient and no accumulation of SA-Ch was evident. Bold lines represent mean ± EM, whereas narrow lines are single traces for depicted data for stimulated (light red) and nonstimulated (light blue) spines. **d** Corresponding conditions in **c** above: from left to right, samples with MNI-Glu/forskolin, MNI-Glu/forskolin/anysomicin, forskolin only/no MNI-Glu. Open circles are corresponding $\Delta V/V$ values at 60 min for SA-Ch spines in **b**

PSD95, a major component of the post-synaptic density (PSD), and compared the localization of A-Ch and SA-Ch, following NMDAR-dependent LTP. Spines were considered "docked" if mCherry signal coincided with that of PSD95, and positive, but not "docked", if it peaked outside the PSD, but within a circle of 0.6 µm radius centered on the PSD (Fig. 2a). About half of the spines expressing A-Ch were "docked" (44 ± 7%), whereas these constituted the vast majority (83 ± 6%) of SA-Ch spines (Fig. 2b). The total number of positive spines was the same for both constructs (Fig. 2c). Representative images are presented in Fig. 2d and in Supplementary Fig. 7a.

Above data demonstrate the strong dependence of SA-Ch expression on neural activity. This suggests that, in untreated cultures, positive spines received a sustained stimulation from the spontaneous activity of the culture, which could amplify basal NMDAR activation[32]. Consistently, blocking NMDAR activity with AP5 drastically reduces A-Ch and SA-Ch expression (Fig. 1d), and SA-Ch localized preferentially to larger PSDs, as indicated by the supralinear correlation between SA-Ch enrichment at synapses and Homer1c-EGFP content, an excellent indicator of spine volume and PSD size[33,34] (Fig. 2e). As spine enlargement strongly correlates with functional potentiation[35], this suggests SA-Ch expression at potentiated synapses; indeed, a significant proportion of spines with lower Homer1c content were devoid of any SA-Ch signal in non stimulated neurons. In addition, SA-Ch was preferentially expressed at synapses exposing the AMPAR-subunit 1 fused to superecliptic-EGFP (SEP-GluA1), a marker of functional potentiation[36] (SA-Ch-positive spines were 63 ± 3% of SEP-GluA1-positive spines, and 6 ± 2% of SEP-GluA1-negative spines, $P < 0.001$, χ^2-test). The relationship between SA-Ch and SEP-GluA1 enrichment was linear (Fig. 2f), indicating that SA-Ch is expressed at potentiated synapses. Notably, some of the spines with lower SEP-GluA1 enrichment did not express SA-Ch, most likely because they received a weaker stimulation. In fact, AMPAR exocytosis takes place during E-LTP phase, which has a lower threshold than translation-dependent L-LTP[3,36]. On the contrary, S-Ch enrichment only showed a modest dependence on SEP-GluA1 (Fig. 2g).

Experiments in hippocampal neuron cultures yield almost identical results to cortical neurons: SA-Ch co-localized with Homer1c-EGFP and NMDA-LTP strongly increased the number of SA-Ch-positive synapses (Supplementary Fig. 7b, c). Altogether, these data demonstrate the activity dependence of SA-Ch translation, as well as its preferential localization at postsynaptic sites.

Synapse-specificity of SA-Ch expression. We demonstrated synapse specificity of SA-Ch expression by focally stimulating selected synapses from neurons expressing EGFP and SA-Ch with two-photon glutamate uncaging in the presence of the protein kinase A(PKA) activator forskolin[37]. Tetrodotoxin (TTX) prevented potentiation from spontaneous activity under these elevated cAMP conditions, as well as synaptic capture. Glutamate uncaging induced SA-Ch expression at stimulated, but not at neighbor synapses or at other synapses on the same dendrite (Fig. 3). When caged glutamate was absent, no significant change in SA-Ch intensity was observed following focal illumination (Fig. 3b). Stimulated spines showed a sustained increase in volume (Fig. 3d), a structural rearrangement that parallels functional potentiation[35]. The increased Cherry intensity at stimulated spines observed for S-Ch, which is translated exclusively in the soma (Supplementary Fig. 3), is likely due to the PSD expansion following the volume change, and was significantly lower than what observed for SA-Ch (Fig. 3b).

It is unlikely that the increase in SA-Ch at the potentiated synapse is due to protein mobilization from surrounding regions, as no significant change in intensity in neighboring spines and in the dendritic shaft was apparent. The time course of SA-Ch increase also rules out this possibility, because it shows a slow rising phase following the stimulation that reaches a plateau between 30 and 60 min (Fig. 3d). Most importantly, translation inhibition with anysomicin blocked SA-Ch accumulation at stimulated spines (Fig. 3c, d) and the change in spine volume observed after stimulation slowly declined to pre-stimulation levels (Fig. 3d). Thus, synapse potentiation drives local SA-Ch expression in a protein-synthesis-dependent, synapse-specific way.

Optogenetic activation of SA-Ch-tagged synapses. Having established synapse specificity of SA-Ch expression, we asked whether the locally synthesized SA-Ch is effective in driving synaptic currents. Calcium influx is an established indicator of spine activation, both in vitro and in vivo[38–40]. We therefore co-expressed SA-Ch with the green calcium indicator GCaMP6s[38]. To minimize ChETA activation while imaging GCaMP6s, we stimulated SA-Ch spines with laser scanning at 488 nm wavelength and imaged GCaMP6s stimulating at 990 nm with two-photon excitation[41,42] in a region encompassing the base of the spine and the corresponding dendrite. We observed light-induced $\Delta F/F$ calcium transients in most stimulated spines, but not when blue light stimulation was omitted; consistently, TTX inhibition of presynaptic activity did not influence the recording of light-induced calcium transients (Fig. 4a). Channelrhodopsins are weakly permeable to calcium[43], but their stimulation could lead to the opening of voltage-gated calcium channels (VGCCs). Accordingly, blue light stimulation performed in the presence of VGCC inhibitors nifedipine, Ni^{2+}, and Zn^{2+} induced a markedly reduced response (Fig. 4a). In neurons expressing untargeted ChETA-Cherry, both the spine and the nearby dendrite could evoke light-dependent $\Delta F/F$ calcium transients when illuminated, in accordance with ref. [20]; on the contrary, only spines, and not dendrites, of SA-Ch-expressing neurons were responsive to blue light stimulation (Fig. 4b). SA-Ch expression does not appear to alter the normal synaptic transmission, as spontaneous $\Delta F/F$ calcium events that could be sometimes recorded from SA-Ch spines were not significantly different from those recorded from control neurons expressing palmitoyl-Cherry and GCaMP6s (Supplementary Fig. 8).

To see whether the activation of Channelrhodopsin-tagged synapses would mirror a physiological activation based on neurotransmitter release, we expressed SA-Ch or unmodified ChETA-Cherry in hippocampal neurons and determined CaMKII phosphorylation by IF 7.5 min after optogenetically stimulating them with a light pattern similar to *θ* burst stimuli used to induce LTP in the hippocampus (see Methods). In fact, sustained glutamate release activates synaptic CaMKII and determines its rapid phosphorylation that lasts for minutes[44]. To reduce background CaMKII phosphorylation, spontaneous activity was pharmacologically suppressed with TTX and glutamate receptors inhibitors, for the 3 h preceding light stimulation (Fig. 4c). During and after illumination, action potentials were inhibited with TTX. Light stimulation strongly increased phospho-CaMKII signal in SA-Ch-expressing neurons compared with neurons that were maintained in the dark. Light alone had no effect, as EGFP-only-expressing neurons were not affected by the stimulation and synaptic levels of phospho-CaMKII were comparable to those in unstimulated neurons expressing SA-Ch (Fig. 4c, d). Importantly, in optically stimulated neurons CaMKII phosphorylation was specific to SA-Ch-positive spines, as spines from the same neuron lacking Cherry signal did not differ from non-stimulated neurons. Indeed, physiologically, CaMKII activation is specific to stimulated spines[44]. Cell-wide activation of untargeted ChETA-Cherry also activated CaMKII, although the synaptic phospho-staining was lower than for SA-Ch (Fig. 4c). Interestingly, phospho-CaMKII staining was evident in the dendritic shaft of illuminated ChETA-Cherry, but not of SA-Ch neurons (Fig. 4d). A possible explanation is that, in ChETA-Cherry-expressing neurons, part of the CaMKII pool fails to translocate from the shaft into the spine due to concomitant extrasynaptic depolarization, as also data presented in Fig. 4b suggest; conversely, localized SA-Ch activation could more readily induce CamKII phosphorylation and mobilization, just as neurotransmitter-mediated synapse stimulation mobilizes CaMKII from the dendritic shaft and accumulates it at the spine head[44]. We conclude that large-field optical stimulation of synaptic SA-Ch is able to simulate an input-specific excitation onto the postsynaptic neuron; conversely, whole-cell activation of ChETA-Cherry has a different outcome on the neuron response at the subcellular level.

We next asked whether the optical activation of SA-Ch synapses could also drive global neuronal activation by illuminating cultured hippocampal neurons with blue light pulses as above and evaluating c-fos expression, an immediate early gene that is induced in neurons shortly after strong synaptic stimulation[45]. Light-stimulated neurons expressing SA-Ch and EGFP displayed evident nuclear c-fos staining 1 h after optogenetic activation (Supplementary Fig. 9). Conversely, c-fos staining was lower in control cells transfected with SA-Ch and EGFP that were maintained in the dark. Exposure to light alone had no effect on c-fos expression, as illuminated neurons that expressed EGFP only had lower levels of nuclear c-fos, comparable to those in SA-Ch, not stimulated neurons (Supplementary Fig. 9). Thus, optogenetic stimulation of neuronal cultures demonstrates that optical activation of SA-Ch-expressing synapses by large-field illumination is able to recapitulate key features of neuron-to-neuron communication.

***In vivo* synaptic tagging with SA-Ch**. Our work in culture demonstrates that SA-Ch is expressed at potentiated spines in cortical and hippocampal neurons. We next sought to investigate SA-Ch behavior in vivo, in order to (i) compare its somatic vs. synaptic expression and (ii) evaluate its expression following a natural stimulus such as the exploration of an unfamiliar environment, a paradigm that rapidly activates *c-fos*, as well as *Arc* expression in the hippocampus of mice and rats[45,46]. Blockage of *Arc* translation or of general protein synthesis with *Arc* antisense oligo-nucleotides or anysomicin inhibits context memory[3,47]. Indeed, a large body of evidence has identified populations of cells that are activated in the hippocampus when animals are presented a novel context[8,45]. We expressed SA-Ch under the Tet-responsive TRE promoter[48] in the hippocampus by means of triple-electrode *in utero* electroporation[49]. Mouse embryos were co-electroporated with constitutive transactivator rtTA and Tet-responsive EGFP. SA-Ch and EGFP transcription is induced with intraperitoneal administration of the tetracycline analog doxycycline, allowing us to restrict synapse tagging by SA-Ch to a defined time window. Control mice that did not receive doxycycline showed no expression. SA-Ch expression in the hippocampus in vivo showed a remarkable synaptic selectivity, as it was detected almost exclusively at spines of electroporated neurons, whereas somas were largely devoid of Cherry fluorescence (Fig. 5a and Supplementary Fig. 10). Conversely, untargeted ChR2 labeled intensely both dendrites in the stratum radiatum and stratum oriens, and somas in the stratum pyramidale (Supplementary Fig. 10c).

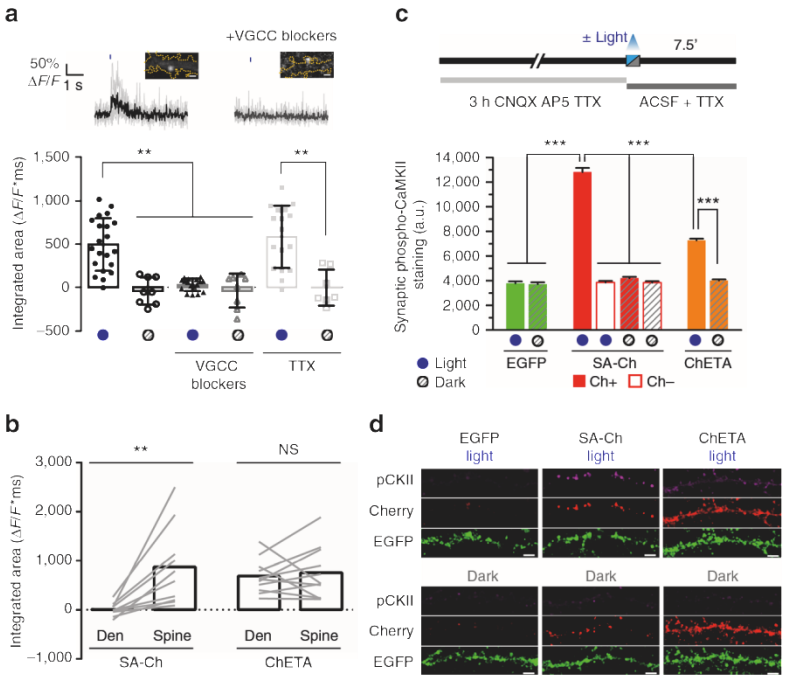

Fig. 4 Optogenetic activation of SA-Ch in neurons. **a** Activation of SA-Ch by means of 488 nm laser illumination drives calcium influx in the neuron. GCaMP6s was expressed along with SA-Ch and illuminated at 990 nm. Top, example of GCaMP6s $\Delta F/F$ time course following 10 ms light stimulation (blue mark above) in ACSF (left, black trace) or in ACSF with voltage-gated calcium channel (VGCC) blockers nifedipine, Ni^{2+}, and Zn^{2+} (right, gray trace). Single traces are in light gray and bold lines are the average. Above images show SA-Ch fluorescence in corresponding spines and yellow dotted trace shows neuron profile as inferred from GCaMP6s fluorescence; scale bar, 1 µm. Bottom, integrated area of $\Delta F/F$ against time plot after light stimulation for imaged spines with (blue dots below) or without (gray dots) light stimulation. SA-Ch neurons were recorded in standard ACSF (black, circles) or in ACSF in the presence of either VGCC inhibitors (dark gray, triangles) or TTX (light gray, squares); open symbols represent recordings in the same medium as corresponding filled symbols, without illumination. Data are values for single spines, each represents the average of trains on the same spine, bars are mean ± SD. $^{**}P < 0.01$, Kruskal–Wallis test, Dunn's *post-hoc* comparisons. **b** Illumination of spines in SA-Ch-expressing neurons drives calcium influx, but not when laser illumination is focused on the nearby dendrite. Conversely, ChETA neurons can be excited both by a spine-focused and a dendrite-focused laser beam. $^{**}P < 0.01$ paired Student's *t*-test, two-tailed. NS, not significant at the $\alpha = 0.05$ level. Lines connect single paired data points, bars are mean. **c** Outline of time course of the experiment. Cells were pretreated for 3 h with CNQX, AP5, and TTX, to reduce background CaMKII activation. Neurons were fixed 7.5 min after light stimulation and stained for phospho-CaMKII. Spines in SA-Ch-expressing neurons were subgrouped into Cherry-positive (filled bars) and Cherry-negative spines (empty bars). Light stimulation induced a significant increase of phospho-CaMKII staining in SA-Ch-expressing spines $^{***}P < 0.001$, one-way ANOVA, Bonferroni comparison of means. Bars are mean ± SEM. **d** Representative images of data shown in **c**. Panels show phospho-CaMKII immunofluorescence (p-CKII), anti-Cherry immunofluorescence (Cherry), and EGFP signal. Scale bar, 5 µm

To address possible concerns that targeting SA-Ch at the synapse may alter synaptic physiology, we electroporated mice as above, with TRE:SA-Ch, constitutive rtTA, and soluble mCherry, and we induced SA-Ch expression with doxycycline. We recorded AMPA- and NMDA-EPSCs in CA1 pyramidal neurons, while stimulating the Schaffer collateral with a bipolar electrode, and calculated the NMDA/AMPA ratio[50]. Importantly, the NMDA/AMPA ratio was not significantly different in CA1 neurons expressing the transgene (Cherry-positive cells) and in control non-electroporated CA1 neurons (Cherry-negative cells, Supplementary Fig. 11).

Next, electroporated mice with TRE:SA-Ch and TRE:EGFP were treated for 3 days with doxycycline and on the fourth day, while still on doxycycline, were exposed to a novel context with unfamiliar visual cues; control animals remained in the home cage. The exposure to a novel context significantly increased the number of SA-Ch spines in the CA1 and in the dentate gyrus (DG) regions (Fig. 5b, c). Interestingly, both in CA1 and in the DG, SA-Ch spines were closer to each other than what we calculated by randomly shuffling their positions along dendrites (Fig. 5d); consistently, the closest non-expressing spine was located at a greater distance than what would be expected by chance (Supplementary Fig. 12a). Not only the first neighbor spine, but also the second and third neighbor spines were significantly more likely to express SA-Ch than what would happen by chance (Fig. 5e). This implies the existence of clusters of SA-Ch-expressing spines and, hence, of potentiated synapses. We defined a cluster of potentiated synapses as a set of SA-Ch synapses comprising at least two spines separated by no more than 2 µm, i.e., two spines belong to the same cluster if their interdistance is <2 µm. In home-caged animals, 86% and 85% of spines in CA1 and DG, respectively, belonged to a cluster and the exposure to a novel context increased this proportion to 95% and 94%, respectively. As clusters ranged from 2 to 13 spines, context exploration significantly increased the average dimension of spine units, i.e. clusters and single spines taken together, both in the CA1 and in the DG (Fig. 5f).

SA-Ch spines also appeared to be non-randomly distributed across different dendrites: some dendrites had a higher density of potentiated synapses than nearby dendrites. This was more

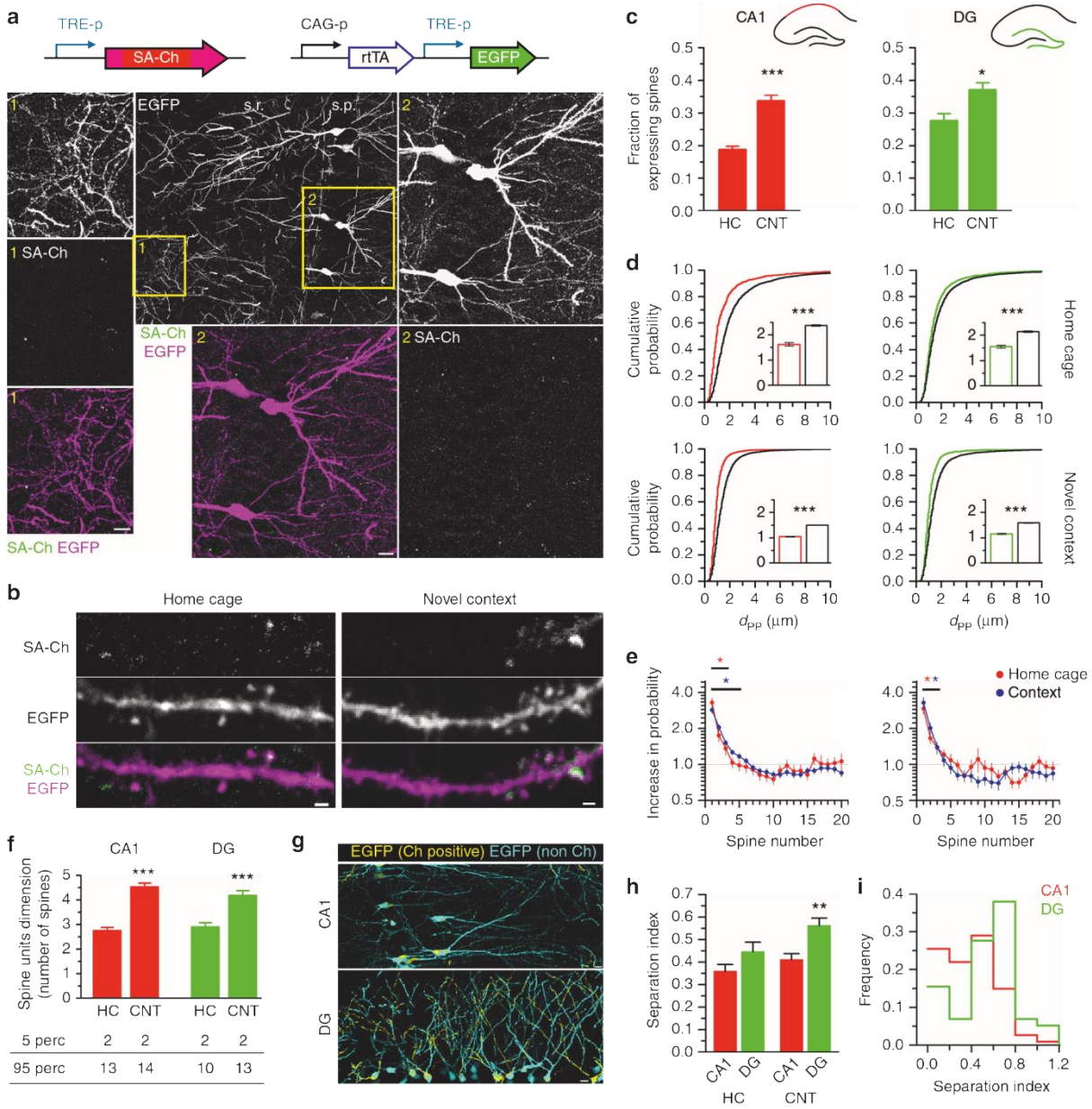

Fig. 5 *In vivo* synaptic tagging. **a** Constructs expressed in the hippocampus of electroporated mice. TRE-p is the tetracycline-responsive promoter. Expression of SA-Ch in mouse CA1 after 2d intraperitoneal doxycycline injection. Dendritic (1) and somatic (2) regions (yellow squares in the large-field image) are magnified, showing EGFP, SA-Ch, and merge channels (SA-Ch: green, EGFP: magenta). s.p. stratum pyramidale, s.r. stratum radiatum. **b** Dendrites expressing SA-Ch in pyramidal neurons in CA1 from animals held in the home cage or exposed to a novel context (see text). **c** Average fractions of SA-Ch-positive spines in CA1 and DG neurons in home cage (HC) and novel context (CNT) groups. $^{*}P < 0.05$, $^{***}P < 0.001$, Student's *t*-test, two-tailed. **d** Distribution of first neighbor distance (d_{PP}) for two potentiated spines in CA1 (left) and in the DG (right). Graphs on the top represent data from home-caged animals, bottom graphs from animals exposed to a novel context. Black lines are the corresponding distributions after randomly shuffling positive/negative assignments to the original spine positions. Insets show, with corresponding colors, first neighbor distance mean ± SEM. $^{***}P < 0.001$ Kruskal–Wallis test, followed by Dunn's comparison. **e** Measured increase in estimated probability to be potentiated themselves for the first 20 neighbors of a potentiated spines in CA1 (left panel) and DG (right panel) neurons. Under the assumption of random distribution of potentiated spines, this value should be 1 uniformly. $^{*}P < 0.01$, *z*-test from the reference value of 1. Points are mean ± SEM. **f** Mean number of spines per unit (cluster and single spines). Bottom table represents the 5th and 95th percentiles of cluster dimension. $^{***}P < 0.001$ Kruskal–Wallis test, Dunn's comparison. Bars are mean ± SEM. **g** Localization of SA-Ch-positive regions (yellow) and SA-Ch-negative region (cyan). Original images are in Supplementary Fig. 12. **h** Separation index (see text for details). A large separation index value indicates that the number of potentiated spine in the dendrite strongly deviates from the expected value if potentiated spines were equally distributed in neurons from the same slice. $^{**}P < 0.01$ Kruskal–Wallis test, Dunn's comparison. **i** Separation index distribution of dendrites in CA1 and the DG in context-exposed animals. Scale bar, 10 μm (**a**, **g**) and 1 μm (**b**)

strikingly observed in the DG granule cells, whereas CA1 pyramidal neurons were more uniform (Fig. 5g and Supplementary Fig. 12b). We calculated the difference between the number of SA-Ch spines in each dendrite and the number that would be expected if potentiated spines were uniformly distributed in dendrites in the same region of the slice (Separation Index, see Methods). We found that in the new context-exposed mice the dendrites of DG granule cells had a significantly higher Separation Index (SI) than CA1 pyramidal neurons (Fig. 5h). In addition, the majority of DG neurons had a high SI, implying that, in the DG, neurons were divided in two populations with either a high or a low number of potentiated synapses (Fig. 5i).

Discussion

The current paradigm in memory studies, based on theoretical and experimental data, points to synaptic ensembles underlying the generation and storage of new memories[6,12,13]. Accordingly, learning different tasks involves different sets of spines, which further supports the idea that spines, and not whole neurons, are the more relevant entities for information storage in the brain[51,52]. At the same time, methods for activity mapping and causally probing memories heavily rely on promoters from immediate early genes[9,13].

We propose here the SA approach to refine the investigation on memory (and other) circuits to map brain activity at the synaptic scale. pSA plasmids combine activity-dependent translation at potentiated synapses with *Arc* mRNA regulatory sequences and a protein tag to drive synaptic expression of any desired gene (including, but not limited to, opsins).

Our findings are consistent with most observations implying a role for *Arc* in synapse potentiation[23,53]. SA-Ch is preferentially found at larger spines (Fig. 2e) and is expressed at focally stimulated spines (Fig. 3). We tested regulatory sequences and DTEs from other mRNAs, including BDNF, which is also targeted to dendrites in an activity-dependent manner[54]. However, the BDNF splice variants that we employed (exons IIa, IIc, and VI), out of the many BDNF transcripts[54], were much less responsive to neural activity, either due to high basal translation (IIa and IIc) or to almost undetectable translation competence (VI form). The *Arc* sequences that we tested gave the best results; however, we envisage that background expression can be further lowered to increase synaptic enrichment; in any case, the use of less strong or tunable promoters (as the TRE promoter) can also be helpful, as our data in vivo suggest. This would also help further reducing the residual somatic expression.

Current imaging techniques to label synapses, such as mGRASP, can be modified to restrict synapse mapping to determinate regions, projections or cellular types with long-established genetic or tracing technologies[55]. On the other hand, efforts in the implementation of activity sensors have made it possible to record real-time synapse activity in response to sensory stimulations[40,56]. However, activity alone does not imply the involvement in the storage of a defined status and not all active synapses become potentiated[39,56]. Recently, activity reporter SEP-GluA1, which labels synapses incorporating fluorescent AMPA receptor subunit 1 on the membrane surface, has been proposed as a marker for synapse potentiation[36,57]. AMPA receptors are rapidly exposed on the surface of spines that undergo sustained stimulation[57], which is generally accepted to be responsible for the increased currents following potentiation. However, potentiation comprises dissociable events, and different forms of potentiation exist[58]. Some do not last indefinitely and AMPA receptors incorporation may be transient[33]. Instead, our strategy can act as reporter of a late-phase, translation-dependent LTP (L-LTP)[58] and can be used to map potentiated synapses across a population of neurons in memory tasks, thus enabling to identify candidate "synaptic engrams." Indeed, SA-Ch significantly correlates with SEP-GluA1 accumulation on postsynaptic sites; however, spines with lower SEP-GluA1 enrichment were also in many cases devoid of SA-Ch (Fig. 2f), suggesting that SA proteins would tag the subpopulation of SEP-GluA1-expressing spines that undergo L-LTP, a likely candidate for memory storage unit in the brain[13].

Work in acute hippocampal slices identified potentiated spines in CA1 with the incorporation of fluorescent phalloidin[59]. Recently, the incorporation of fluorescently tagged AMPA receptors has been observed in vivo in the mouse barrel cortex following whisker stimulation[60], providing the first observation of potentiated spines in vivo. Here we demonstrate the usefulness of the SA approach by labeling synapses that underwent translational-dependent potentiation in the hippocampus of live mice exploring a novel context. Exposure to a novel environment has been linked to an increase in active neurons, as identified by c-fos staining or catFISH technique[46,47], but no parallel has been done so far with long-lasting synaptic changes such as translation-dependent LTP.

Previous work identified functional clusters of synapses in cortical areas and hippocampal slices (spines with correlated activity)[36,40,61]; clustering has been proposed in models for cooperative integration of synaptic activity in neuron computation, sensory integration, and memory formation[62–64]. We identified clusters of potentiated synapses in hippocampal regions CA1 and DG, which comprised most of the potentiated spines. It must be noted that the exact number of spines in each cluster is dependent on the chosen cutoff (2 µm) in our working definition. However, we consider this choice reasonable, when taking into account the physical dimensions of a typical mushroom spine. Indeed, the range (2–13 spines) that we calculated for the cluster dimension (Fig. 5f) is in accordance to what reported for functional clusters identified by calcium imaging of synaptic activity (2–12 synapses)[61].

Our approach enabled us to map potentiated synapses across different dendrites, highlighting differences in the distribution between the DG and the CA1 regions (Fig. 5h, i). Our data suggest that single dendrites of granule cells function as a highly homogeneous unit in terms of activity integration and plasticity, supporting a role of the DG for pattern separation[15,65]. According to this model, DG cells encode highly orthogonal contextual information, whereas downstream CA3 and CA1 complete and process this information. Consistently, whole-cell optogenetic activation of engram cells in the DG, but not in CA1, served as an effective contextual stimulus in the fear conditioning protocol[9], despite other experiments clearly advocating a role for CA1 in the encoding of contextual information[66].

In order to highlight the role of potentiated synapses in a memory recall framework, it is necessary to envisage an experimental strategy to selectively act on them, but cell-wide neuron activation also recruits other learning-related mechanisms at the cellular level[67]. Although subcellular optogenetic stimulation can be achieved by restricting the illumination pattern down to single spines[20], this requires *a priori* knowledge of the sites to be stimulated, which are not always known. Moreover, the feasible number and sparseness of distinct illumination spots heavily depend on technological aspects. On the other hand, the biologically achieved spatial restriction of Channelrhodopsin expression presented here, would allow unbiased excitation of recently activated synapses with standard experimental setups for wide-field illumination. In this scenario, light power should be adjusted so that the effect of the optical stimulation is similar to physiological synaptic events; from our results in culture, we have found that although blue light reactivation of the locally expressed SA-

Ch is able to elicit calcium transients in a specific manner, these evoked calcium signals look somewhat smaller than calcium events occurring in the same spines spontaneously (Supplementary Fig. 9). However, it must be noted that ChETA itself does not have the greatest photocurrents among the opsin family[25,68] and a number of ChR2 variants now exists with larger photocurrents[69]. The majority of these variants differ from the parental ChR2 by a few point mutations[68], so we expect that the substitution of ChETA complementary DNA to encode an opsin with a higher photoconductance would replicate the key expression features of SA-Ch in tagging potentiated synapses. Changing the fluorescent proteins attached to SA-Ch could also increase photocurrents, as Cherry-fused ChR2 have been sometimes reported to have a reduced trafficking to the plasma membrane than fusion proteins of the GFP family[70].

SA-Ch application (or any of its relatives) could help clarifying the role of synaptic potentiation in the formation and recall of encoded memories. Synapse re-excitation could be performed more physiologically than what existing technologies used to tag and reactivate whole neurons can achieve. For instance, the work presented in this paper lays the ground for the use of SA-Ch to test the hypothesis of a "synaptic engram," parallel to the identified "population engram"[6,12,13]. It is likely to be that the two activity-tagging approaches (cellular vs. synaptic) would give similar results where there is large identity overlap between the unit of plasticity and the single neuron, as in the DG[15,63,71]. On the other hand, CA1 neurons receive multiple converging inputs whose crosstalk, following activation by current whole-cell optogenetic protocols, is likely to result in memory occlusion[9].

Taking advantage of *Arc* RNA regulatory sequences, we were able to express a Channelrhodopsin variant at synapses undergoing potentiation, establishing a novel tool to map and reactivate these sites. Recently, a novel approach towards the development of "synaptic optogenetic" strategies was proposed[72]; by expressing a photoactivable form of Rac1 in the motor cortex, Kasai and colleagues[72] demonstrated that the light-induced shrinkage of recently potentiated spines severely impairs motor learning. That study emphasizes the necessity of controlling selected inputs, rather than a selected population of neurons, underscoring the interest of synaptic optogenetic approaches, such as the one presented here. However, by dramatically altering actin dynamics, such approach determined a drastic alteration of the spine structure; therefore, the interference with the memory trace could not be reverted. Accordingly, it was not possible to perform a memory recall task, as the intervention was purely destructive. Although establishing a first important step in highlighting, and interfering with, established engrams at the synaptic level, the sufficiency of those potentiated synaptic inputs for memory encoding remains to be addressed. Our approach allows, in principle, to re-excite those synapses. In addition, it is likely to be naturally extended to any variant opsin family, thus enabling the bidirectional interference of the synaptic inputs involved in circuit traces and memories.

Methods

Constructs. Palmitoyl-Cherry-MS2 was generated by cloning palmitoylation sequence MLCCMRRTKQ from GAP43 to Cherry N-terminal, whereas MS2 sequence was derived from plasmid pSL-MS2 12X (Addgene 27119). *Arc* DTE comprises nucleotides 2035–2701 of *Arc* transcript (NCBI NM_019361.1), in accordance to ref. [24]. EGFP-MS2 coat protein-NLS was constructed and cloned into pcDNA3.1(+) (Invitrogen) from plasmid Cherry-MS2 coat protein-NLS (a gift from A. Marcello, ICGEB Trieste). ChETA-Cherry cDNA was PCR amplified from plasmid pAAV-CaMKII-hChR2 (E123A)-mCherry-WPRE[25]. ChETA-Cherry-SYN (S-Ch) was generated by cloning 5′-GCCGCCGCTGCTTCAATTGAAAGT-GACGTGGCCGCAGCTGCCGAAACCCAGGTGTAATAA-3′ oligo sequence (IDT Technologies) in frame to ChETA-Cherry using unique site BglII site at 3′-end of Cherry cDNA. A-Ch and SA-Ch constructs were generated by inserting *Arc* 5′- and 3′-UTRs before and after ChETA-Cherry and S-Ch cDNA, respectively. *Arc* UTRs were amplified from plasmid pCMV-ArcF encompassing whole 5′-UTR and first 13 nucleotides of *Arc* CDS, where start ATG was mutated to ACG, and whole 3′-UTR[24]. MS2 sequence was inserted downstream STOP codon before 3′-UTR. Constructs were cloned into plasmid pcDNA3.1(+) (Invitrogen) under cytomegalovirus (CMV) promoter. EGFP was expressed from plasmid pN1-EGFP (Clontech). Homer1c-EGFP was kindly provided by D. Choquet, Institut interdisciplinaire de Neurosciences CNRS, Université Bordeaux 2. Palmitoyl-Turquoise2 is Addgene plasmid 36209. GCaMP6s was expressed from pGP-CMV-GCaMP6s (Addgene 40753). SEP-GluA1 was expressed from Addgene plasmid 64942. For *in utero* electroporation, SA-Ch was inserted downstream of third-generation TRE promoter[48] in a plasmid containing the minimal CK0.4 promoter driving the expression of rtTA2S-M2 transactivator amplified from vector TMPrtTA[73], yielding pTRE3-SA-CK-rtTA. Parental plasmid was custom synthesised by Life Technologies (USA). It was cotransfected with plasmid pCAGGS-rtTA-TRE-EGFP, which was generated by cloning rtTA2S-M2 and TRE-EGFP sequences into plasmid pCAGGS[49]. TRE-EGFP was amplified by PCR from plasmid pSIN-TRE-EGFP, provided by Dr L. Marchetti. pCAGGS-rtTA-IRES-mCherry was generated analogously and IRES sequence was derived from pCAGGS[49].

Cell culture. Primary cortical and hippocampal neurons were extracted from P0 B6129 mice as follows: after surgery and tissue isolation, tissue was triturated in cold calcium-free Hank's balanced salt solution with 100 U ml^{-1} penicillin, 0.1 mg ml^{-1} streptomycin, and digested in 0.1% trypsin, followed by inactivation in 10% fetal bovine serum (FBS) Dulbecco's modified Eagle's medium (Invitrogen) 100 U ml^{-1} DNase. Neurons were seeded on previously poly-D-lysine-coated glass coverslips or plasma-treated poly-D-lysine-coated Willco dishes. For initial plating, neurons were maintained in Neurobasal-A medium (Invitrogen) supplemented with 4.5 g l^{-1} D-glucose, 10% FBS, 2% B27 (Invitrogen), 1% Glutamax (Invitrogen), 1 mM pyruvate, 4 µM reduced glutathione, and 12.5 µM glutamate. From the following day on, neurons were grown in Neurobasal-A medium (Invitrogen) supplemented with 2% B27 (Invitrogen), 1% Glutamax (Invitrogen), and 1–10 µg ml^{-1} gentamicin. Medium was refreshed every 2–4 days. For experiments in Fig. 1a and Supplementary Fig. 1, div 12 neurons were used. All other experiments employed div 17–19 neurons. Neurons were transfected with calcium phosphate method the day before experiment. The procedure was approved by the National Council for Research Ethical Committee.

Treatments. Neurons as in Fig. 1 were treated for 1 h with either KCl to a final concentration of 10 mM, or with saline, added to bath. Otherwise, treatments are (i) BDNF: hBDNF (Alomone) 100 ng ml^{-1} 90′; (ii) KCl: KCl 10 mM 90′; (iii) LTP: 20′ in 2 mM $CaCl_2$, 1 mM $MgCl_2$ ACSF (artificial cerebrospinal fluid: 136 mM NaCl, 2.5 mM KCl, 10 mM glucose, 2 mM sodium pyruvate, 1 mM ascorbic acid, 0.5 mM myo-inositol, 10 mM HEPES pH 7.3, with 2 mM $CaCl_2$ and 1 mM $MgCl_2$ unless otherwise indicated) followed by 10′ in 2 mM $CaCl_2$/Mg^{2+}-free ACSF, 5.4 mM KCl, 100 µM NMDA (Sigma-Aldrich, Saint Louis, MO), 20 µM glycine (Sigma-Aldrich), and 0.1 µM rolipram (Sigma-Aldrich) as described[74], followed by 90′ in culture medium; (iv) AP5: 50 µM AP5 (Sigma-Aldrich) from transfection to analysis (17–20 h). See also Supplementary Fig. 6 for temporal outline of treatments. Stimulated neurons in Fig. 2e are treated with 20′ 2 mM CaCl2, 1 mM $MgCl_2$ ACSF followed by 5′ in 2 mM $CaCl_2$/Mg^{2+}-free ACSF, 60 mM KCl, 100 µM NMDA (Sigma-Aldrich), 20 µM glycine (Sigma-Aldrich), and fixed after 90′ (see below).

Immunofluorescence. Neurons expressing A-Ch or SA-Ch were fixed in 2% formaldehyde 5% sucrose phosphate-buffered saline (PBS) and permeabilized in 0.1% Triton X-100. After PBS washing, samples were blocked in 1% bovine serum albumin (BSA) PBS, and primary antibodies anti-Cherry (GeneTex GTX59788, 1:500) and anti-PSD95 (Abcam ab9909, 1:600) were used in 0.5% BSA PBS. After washing, primary antibodies were detected with anti-rabbit-TRITC (Sigma-Aldrich T6778, 1:200) and anti-mouse-Alexa647 (Thermo Fisher A32728, 1:200) in 0.5% BSA PBS. Coverslips were mounted in Fluoroshield (Sigma-Aldrich) mounting medium. Hippocampal neurons expressing EGFP, ChETA/EGFP, S-Ch/EGFP, or SA-Ch/EGFP for 24 h were processed as above. Primary antibody was 1:2,500 anti-MAP2 (Abcam ab5392) and it was detected with anti-chicken-Alexa647 (Abcam ab150171, 1:250). For surface NMDAR/AMPAR immunostaining, div 9 neurons were transfected with SA-Ch and palmitoyl-Turquoise2, or palmitoyl-Turquoise2 alone; on the third day from transfection, neurons were fixed in 4% formaldehyde, 5% sucrose PBS and washed, blocked in 5% BSA PBS, and stained with 1:500 anti-GluR1-NT (Millipore MAB2263) and 1:500 anti-GluN1 (Alomone AGC-001), and followed by 1:200 anti-mouse-Alexa488 (Thermo Fisher A32723)/1:200 anti-rabbit-Alexa647 (Thermo Fisher A32733) and mounting.

Microscopy. Optical sections (512 × 512 pixels) were acquired with a confocal microscope (Leica TCS SP5 SMD on an inverted DM6000 microscope) using an oil objective HCX PL APO CS 40 × (numerical aperture NA = 1.25), and pinhole was set to 1.47 AU. Digital zoom was adjusted for sampling spines correctly. For whole-cell reconstruction, *z*-stacks were acquired every 0.5 µm. Sequential illumination

with HeNe 633, Ar 561, Ar 488, Ar 458, and diode (Picoquant, Berlin, Germany) 405 laser lines was used for Alexa647, TRITC and Cherry, EGFP and Alexa488, Turquoise2 and 4′,6-diamidino-2-phenylindole (DAPI), respectively. Neurons in Fig. 1a and Supplementary Fig. 1 were acquired with the same acquisition parameters.

For two-photon uncaging, images were acquired using an Olympus FV1000 confocal module on an inverted IX81 microscope with immersion oil objective UPLSAPO 60× (NA = 1.35) and pinhole was set to 180 µm. Digital zoom was set to 8x. Used laser lines were Ar 488 and HeNe 543 for EGFP and Cherry excitation, respectively. For two-photon uncaging, 720 nm line was set on a tunable Chameleon Vision II Ti:Sapphire pulsed laser (Coherent, 80 MHz). Green and red channels were acquired before 720 nm stimulation (−5′ time point) and 60′ after medium change (see the following two-photon uncaging section).

Two-photon uncaging. DIV 8–10 cortical neurons were seeded on plasma-treated, poly-D-lysine-coated Willco dishes, and transfected the day before experiment. Neurons were maintained in Mg^{2+}-free ACSF (in mM, 136 NaCl, 2.5 KCl, 2 $CaCl_2$ 10 D-glucose, 10 HEPES, 2 pyruvate, 1 ascorbic acid, 0.5 myo-inositol) with 10 µM forskolin (Tocris BioSciences), 1 µM TTX (Tocris BioSciences) and, where indicated, 2.5 mM MNI-caged glutamate (Tocris BioSciences, Bristol, UK) for 20′ before uncaging. Following EGFP and Cherry acquisition, 30 pulses (720 nm, 9–13 mW at the objective lens) of 7 ms were delivered at 0.5 Hz at 0.5–1 µm from spine head as in ref. [37]. After 5′, medium was changed to 1 mM $MgCl_2$ ACSF supplemented with 2% B27 and the same dendrite was imaged after 60′. The mock stimulation was conducted in the same way, except that MNI-glutamate was not added in the medium. For time-course experiments, red and green channels were acquired 20′ and 5′ before the uncaging start. Green channel was acquired at 0.5′, 1′, 2′, 5′, 30′, 60′, and 90′ following uncaging, and red channel was acquired at 5′, 30′, 60′, and 90′. Throughout the whole protocols, neurons were maintained at 37 °C under humidified 5% CO_2 atmosphere. In experiments with translation inhibitors, 5 µM anysomicin (Sigma) was present in the medium all the time staring from the 20′ preincubation.

Calcium imaging. Div 7-11 cortical neurons grown on glass-bottom coverslip, expressing GCaMP6s and SA-Ch were imaged using an Olympus FV1000 confocal module on an inverted IX81 microscope with immersion oil objective UPLSAPO 60× (NA = 1.35). Neurons were maintained in ACSF containing 2 mM $CaCl_2$, 1 mM $MgCl_2$ at 37 °C under humidified atmosphere. In a parallel sets of experiments, we included (i) VGCC inhibitors nifedipine 5 µM (Sigma), Ni^{2+} (as $NiSO_4$) 500 µM, and Zn^{2+} (as $ZnCl_2$) 500 µM, or (ii) 1 µM TTX (Tocris Biosciences). SA-Ch was imaged at 543 nm and GCaMP6s was excited with Chameleon Vision II Ti: Sapphire pulsed laser (Coherent, 80 MHz) tuned at 990 nm (actual peak was detected at 988 ± 2 nm), to minimize Channelrhodopsin excitation[42]. Selected spines were identified comparing the 543 nm and the two-photon channel. A rectangular imaging region of interest (ROI) was defined on the dendrite immediately under the selected spine, whereas the excitation ROI was set on the spine. We acquired 500 frames every 20 ms by exciting at 990 nm using RM690 filter; GCaMP6s fluorescence was acquired in the 500–600 nm range. The size and dimension of the ROIs were maintained constant in all experiments. After 50 frames, we stimulated the spine with a 10 ms pulse of the 488 nm laser line in spiral scanning mode in the excitation ROI and continued imaging. Laser power (488 nm) was measured to be 8.9–10.7 µW upon steady illumination[41] and 990 nm laser power was 2.5–3.7 mW. Randomly between stimulations, trains were performed identically, except the 488 nm laser line was kept switched off. After dark frame subtraction, $\Delta F/F$ values were integrated for the first 200 frames following stimulation.

For the recording of low-frequency spontaneous events, two-photon GCaMP6s imaging of a region under a defined spine was performed as above, except the duration of each recording session was extended up to 40 s. Neurons transfected with palmitoyl-Cherry-MS2 or SA-Ch, and GCaMP6s were recorded in ACSF; spontaneous events from SA-Ch were derived from long recording sessions without stimulation of SA-Ch expressing spines that were responsive to light (see above).

Neurons in Fig. 4b expressing SA-Ch or ChETA-Cherry and GCaMP6s were recorded as described above. The recording ROI under the spine was maintained constant across recording sessions, whereas the excitation ROI was set on the spine or on the dendrite adjacent to the imaging ROI; for each session, both recordings with spine-centered and dendrite-centered excitation ROIs were performed. The position of the excitation ROI for the first recording of a session (i.e., spine or dendrite) was chosen randomly.

Culture optogenetics. DIV 17–19 hippocampal neurons were grown on poly-D-lysine-coated glass coverslips in 24 wells. The day after transfection, neurons expressing SA-Ch and EGFP, ChETA-Cherry and EGFP, or EGFP alone, were put in standard 2 mM $CaCl_2$ 1 mM $MgCl_2$ ACSF and illuminated with single-channel PlexBright LED Module 450 nm connected to an optical fiber (THORLABS, 200 µM diameter, 0.39 NA, ceramic ferrule) at 1–3 mW peak power (measured at the end of the fiber). Ten trains of 13 pulses at 100 Hz were repeated at 0.5 Hz; 4 stimulations at different positions were performed on each culture, in order to evenly illuminate the whole culture area. In a first set of experiments, neurons were pre-treated for 3 h with 40 µM CNQX, 100 µM AP5, and 1 µM TTX. Medium was changed to ACSF, 2 mM $CaCl_2$, 1 mM $MgCl_2$, and 1 µM TTX, and cultures were light stimulated or maintained in the dark; 7.5 min after stimulation, neurons were fixed for 15 min in 2% formaldehyde, 5% sucrose PBS supplemented with 1 mM Na_2VO_4 (Sigma-Aldrich), and 1 mM NaF (Sigma-Aldrich) to inhibit phosphatases; after permeabilization in ice-cold methanol, neurons were blocked in 5% BSA, 1 mM Na_2VO4, 1 mM NaF PBS, and subsequently incubated overnight with 1:100 mouse anti-phosphoCaMKII (Thermo Fisher MA1-047 clone 22B1) and 1:300 rabbit anti-Cherry (GeneTex GTX59788) in 2% BSA PBS. Secondary antibodies were 1:100 anti-rabbit-TRITC (Sigma-Aldrich T6778) and 1:100 anti-mouse-Alexa647 (Thermo Fisher A32728) in 2% BSA PBS. In the second set of experiments, neurons were light-stimulated in ACSF, 2 mM $CaCl_2$, and 1 mM $MgCl_2$; after stimulation, neurons were put back into culture medium; parallel cultures did not undergo such a treatment and were maintained in the dark. After 1 h, cells were fixed in 2% formaldehyde, 5% sucrose PBS, and permeabilized in 0.5% Triton X-100; after PBS washing, cells were blocked in 4% BSA PBS and hybridized with 1:100 rabbit polyclonal anti c-fos (Santa Cruz sc-52) in 2% BSA and 0.05% Triton X-100 PBS. Secondary antibody was 1:100 anti-rabbit-Alexa647 (Thermo Fisher A32733). Samples were mounted in Fluoroshield with DAPI (Sigma-Aldrich).

***In utero* electroporation and animal experiments**. Animal care and experimental procedures were approved by the IIT and CIBIO licensing, as well as with the Italian Ministry of Health. Hippocampal *in utero* electroporation was performed as described in ref. [49]: E15.5 timed-pregnant CD1 mice (Charles River SRL, Italy) were used. Time-pregnant matings were performed on the evening; the day after mating was defined as E0.5 and the day of birth was defined as P0. The plasmids pTRE3-SA-CK-rtTA and pCAGGS-rtTA-TRE-EGFP (or, alternatively, pTRE3-SA-CK-rtTA and pCAGGS-rtTA-IRES-mCherry) were used at 1 µg µl^{-1} with Fast Green dye (0.3 mg ml^{-1}; Sigma) to allow visualization. Briefly, the dam was anesthetized with isofluorane (induction, 4.0%; surgery, 2.0%) and the uterine horns were exposed by laparotomy. Each embryo was injected (3–4 µl) through the uterine wall unilaterally with a 30 G needle (Pic indolor, Grandate, Italy). For the electroporation, 6 electrical pulses (amplitude, 30 V; duration, 50 ms; intervals, 1) were delivered with a square-wave electroporation generator (CUY21EDIT; Nepa Gene). Then, the uterine horns were returned into the abdominal cavity and embryos were allowed to continue their normal development. Mice from both sexes were P24–P26 on the day of the experiment. A first group of mice received 0.5 mg doxycycline (1 mg per 30 g BW) in saline solution intraperitoneally once a day for 2 days; on the third day, brains were fixed by transcardial perfusion of 4% formaldehyde. A second group of mice received an additional intraperitoneal injection (1 mg per mouse) on day 3 and brains were fixed on day 4. On day 4, mice of the novel context group were put separately in a different cage (novel context). Two of the walls had visual cues (3 cm black/white vertical stripes and 3 × 3 cm black/white dashboard); one object was put in the cage (a blue 50 ml Falcon tube)[57]. After 3 h, brains were fixed by 4% formaldehyde transcardial perfusion. Home-cage animals received the same doses of doxyxycline and were kept in their cage until perfusion. After perfusion, brains were post-fixed overnight in 4% formaldehyde in PBS, then cryoprotected in 30% sucrose PBS. Sixty micrometers of coronal sections were cut with a cryostat. Slices were mounted in Vectashield or Fluoroshield with DAPI (Sigma) and native fluorescence was imaged with Leica SP5 (see above) with 1.5 AU pinhole; stacks encompassing the whole section were acquired every 0.5 µm. To calculate intensity profiles in CA1 large fields (Supplementary Fig. 10), IF was performed on free floating slices. Slices were blocked 1 h in 0.3% Triton X-100 in 10% normal goat serum (NGS, Sigma-Aldrich) PBS, then incubated overnight in 1:500 anti-GFP (Abcam ab38689), 1:500 anti-Cherry (Abcam ab16743), in 0.3% Triton X-100, and 10% NGS PBS at 4 °C, washed three times (10′ each), and incubated in secondary antibodies (1:100 anti-mouse-Alexa488 (Thermo Fisher A32723) and 1:100 anti-rabbit-Alexa647 (Thermo Fisher A32733)), 1:200 in 0.3% Triton X-100, and 10% NGS for 1 h. After three washes in PBS, slices were mounted in Fluoroshield with DAPI (Sigma-Aldrich).

Brains from Thy1-ChR2-YFP (line 18) mice (B6.Cg-Tg(Thy1-COP4/EYFP) 9Gfng/J, Jackson Laboratory, stock 007612) strongly expressing ChR2 in CA1 and only modestly in CA3 and DG, were fixed with 4% formaldehyde transcardial perfusion. Brains were post-fixed overnight in 4% formaldehyde in PBS, then cryoprotected in 30% sucrose PBS. Coronal sections of 60 µm were cut with a cryostat and mounted in Fluoroshield with DAPI.

Slice electrophysiology and analysis. Acute coronal slices from the mouse neocortex were prepared at postnatal day 21–25. Slices were cut from animals previously electroporated at E15.5 with pCAGGS-rtTA-IRES-Cherry and pTRE3-SA-CK-rtTA (for details regarding *in utero* electroporation, see previous section) and kept for 4 days on doxycycline (intraperitoneal injection, 0.5 mg per day). Mice were anesthetized with urethane (1.65 g kg^{-1}) and the brain was quickly dissected and placed in an ice-cold cutting solution containing: 130 mM K-gluconate, 15 mM KCl, 0.2 mM EGTA, 20 mM HEPES, and 25 mM glucose, pH adjusted to 7.4 with NaOH. The solution was constantly oxygenated. Slices (thickness: 300 µm) were first cut with a vibratome (VT1000S, Leica Microsystems, GmbH, Wetzlar, Germany) and immersed for 1 min in solution at room temperature (RT) containing: 225 mM D-mannitol, 25 mM glucose, 2.5 mM KCl, 1.25 mM NaH_2PO_4, 26 mM

$NaHCO_3$, 0.8 mM $CaCl_2$, 8 mM $MgCl_2$, pH 7.4 with 95% O_2/5% CO_2. Slices were then incubated for 30 min at 35 °C in sACSF composed of: 125 mM NaCl, 2.5 mM KCl, 25 mM $NaHCO_3$, 1.25 mM NaH_2PO_4, 2 mM $MgCl_2$, 1 mM $CaCl_2$, 25 mM glucose, pH 7.4 with 95% O_2/ 5% CO_2. After incubations slices were maintained in sACSF at RT until use. During experiments, slices were positioned in a submerged recording chamber (RC-26, Warner Instruments, Hamden, CT, USA) and continuously perfused with fresh bathing solution (125 mM NaCl, 2.5 mM KCl, 25 mM $NaHCO_3$, 1.25 mM NaH_2PO_4, 2 mM $MgCl_2$, 2 mM $CaCl_2$, 25 mM glucose, pH 7.4 with 95 %O_2/5 % CO_2) including the $GABA_A$-receptor antagonist picrotoxin (0.1 mM, Sigma-Aldrich) and maintained at 30–32 °C by an inline solution heater (TC-344B, Warner Instruments). Pipettes (resistance: 3-4 MΩ) were filled with intracellular solution containing: 8 mM NaCl, 145 mM Cs-methanesulfonate, 10 mM HEPES, 10 mM phosphocreatine di(tris) salt, 2 mM Na_2ATP, 0.5 mM NaGTP, 0.3 mM EGTA, 5 mM lidocaine *N*-ethyl bromide, and 10 mM tetraethylammonium chloride, pH adjusted to 7.25 with CsOH. Only recordings with series resistance < 20 MΩ were included in the analysis. Series resistance was not compensated and data were not corrected for the liquid junction potential. Electrical signals were amplified by a Multiclamp 700B, low-pass filtered at 2 kHz, digitized at 50 kHz with a Digidata 1440 and acquired with pClamp 10 (Molecular Device, Sunnyvale, CA). Electrophysiological traces were analyzed using Clampfit 10.4 software (Molecular Device).

Synaptic responses were recorded in the same animal in whole-cell voltage-clamp configuration from Cherry-positive CA1 pyramidal cells of the electroporated hemisphere and from Cherry-negative CA1 pyramidal cells of the non electroporated hemisphere. To evoke synaptic responses, Schaffer collaterals were stimulated at 0.1 Hz (stimulus duration: 100 µs) with a bipolar metal electrode placed in the CA1 stratum radiatum, about 100–200 µm from the recording site. Stimulus intensity was adjusted to obtain half-maximal AMPA receptor-mediated excitatory postsynaptic currents (AMPA-EPSCs, average stimulating current: 129 ± 34 µA). AMPA-EPSCs were recorded at $V_m = -80$ mV and completely blocked in bathing solution containing 2,3-Dioxo-6-nitro-1,2,3,4-tetrahydrobenzo[f] quinoxaline-7-sulfonamide disodium salt (NBQX, 10 µM, Tocris Bioscience). NMDA receptor-mediated EPSCs (NMDA-EPSCs) were recorded at $V_m = +40$ mV in the presence of 10 µM NBQX. The NMDA/AMPA ratio was computed as the ratio of the NMDA-EPSC peak amplitude to the AMPA-EPSC peak amplitude (both measured on a mean trace obtained averaging ten consecutive traces) in the same cell.

Data quantification. Spine number and subclass for neurons in Supplementary Fig. 3 were assigned manually based on established nomenclature. Short spines with no apparent neck are classified as stubby; elongated spines whose head and neck diameters are similar are classified as thin and spines with a defined neck and a prominent head are classified as mushroom. Filopodia were few in number across all samples and were excluded from analysis. For the calculation of surface NMDAR/AMPAR ratio, ROIs were defined on dendrites from expressing neurons (SA-Ch/palmitoyl-Turquoise2 or palmitoyl-Turquoise2), and mean sGluR1/Alexa488 and sGluN1/Alexa647 intensities were calculated after background subtraction. The calculated value is the ratio of the two means.

EI was calculated as the ratio between the Cherry average intensity on the spine region (identified using the EGFP channel) and the average intensity calculated on the dendritic shaft between 1 and 2 µm away from the spine junction, after background subtraction. For the EI calculation, only expressing spines were included in the analysis. Homer1c-EGFP content was quantified by integrating EGFP intensity in correspondence to the PSD and normalized by the mean intensity on the dendrite. SEP-GluA1 enrichment was calculated in an analogous manner to Cherry EI; for the comparison of the two EIs, the same regions were considered in the two channels.

For two-photon stimulation experiments, spines were identified in the EGFP filler channel, Cherry fluorescence was integrated in the corresponding channel after background subtraction. Intensity was calculated for images acquired immediately before photouncaging and after 60′ for stimulated and neighboring spines. The relative change in Cherry intensity (I_c) at time point i was calculated as the difference, normalized for the initial intensity as follows: $[I_c(i) - I_c(-5')]/I_c(-5')$. Volume change was calculated in an analogous way as $[I_g(i) - I_g(-5')]/I_g(-5')$, where I_g is the spine integrated density in the EGFP channel, normalized by the mean value in the dendrite underneath.

For the intensity profiles shown in Supplementary Fig. 10, 1,024 × 1,024, 0.5 µm stacks of immunostained slices were acquired by centering the field on the CA1 region above the DG upper blade. For each channel, slices were summed to generate the projection image. After background subtraction, linear profiles of 325 µm (80 µm thick) were measured starting from the stratum oriens toward the stratum lacunosum-moleculare in correspondence to all detected EGFP-positive neurons. Profiles were aligned in the DAPI channel by setting the start of the stratum pyramidale, identified as the stratum with packed soma, at 100 µm. For EGFP and Cherry channels, baseline was subtracted and resulting profiles were averaged. Baseline was evaluated in the non-electroporated hemisphere in an analogous manner. To reduce noise, resulting data were smoothened with SigmaPlot v12 (SYSTAT) with the median method (0.01 sampling) in Supplementary Fig. 10b. To compare SA-Ch profiles and Thy1:ChR2-YFP profiles, first values were averaged in a 5 µm window. Resulting profile data were averaged and normalized on the highest value, and two-way analysis of variance (ANOVA) was performed (factor A: SA-Ch/Thy1-YFP, factor B: distance).

For in vivo experiments, spine distance was calculated as the euclidean distance as $[(x_1\text{-}x_2)^2 + (y_1\text{-}y_2)^2 + (z_1\text{-}z_2)^2]^{1/2}$ where (x,y,z) are the spine coordinates in micrometers. Distances were calculated for each SA-Ch-positive spine to all other SA-Ch-positive spines and all SA-Ch-negative spines with a custom-made program in R (version 3.3.1, available at http://www.R-project.org). Distance to first potentiated neighbor and to first non-potentiated neighbor are defined as the minima of the two sets, respectively. The distances to first potentiated and first non-potentiated neighbor were also calculated for randomly shuffled data by using the "sample" module in R to randomly assign the identity of spines to the (x,y,z) positions; for every dendrite, five shuffled datasets were considered.

Probability data were calculated as follows with a custom made program in R: for each SA-Ch-positive spine we considered the first 20 neighbor spines (both directions along the dendrite were considered). For each dendrite, this gave a set of N sequences of 20 spines that could be aligned from position 1 to position 20 generating a N×20 matrix. For each i-th column, we counted the number of positive spines and divided it by the number of rows N. The resulting value is the probability of finding a potentiated spine in position i. To calculate the increase in probability, for each dendrite probability data were divided by the expected probability of finding a potentiated spine in the corresponding position if they were randomly arranged. Thus, calculated values were divided by $(p\text{-}1)/(T\text{-}1)$, where p and T are the number of potentiated spines and the total number of spines in each dendrite, respectively.

Clusters of SA-Ch-positive spines were calculated with the "Hierarchical cluster analysis" function in R (contributed to STATLIB by F. Murtagh) with the "single linkage" method with a 2 µm threshold. Thus, two spines belong to a cluster if their distance (calculated as above) is lower than 2 µm. Together, spine clusters and single spines (spines that do not have another SA-Ch-positive spine within 2 µm and could therefore be regarded as cluster with dimension = 1) constitute spine units. Accordingly, spine unit dimension was calculated as the number of members for each unit.

To calculate the SI, the average fraction of potentiated spines (f) was calculated for each slice as the sum of SA-Ch-positive spines in dendrites belonging to the slice divided by the total number of spines. Then, for each dendrite, the expected number of potentiated spine p^* was calculated as $f \times T$, where T is the number of spines in the dendrite. SI was calculated as the absolute value of $(p\text{-}p^*)/p^*$, where p is the number of potentiated spines in the dendrite.

Statistics. Image analysis was performed using ImageJ. Statistical analysis was performed with OriginPro v9.0 or GraphPad Prism 6. Differences between two groups were evaluated with two-tailed Student's t-test. Residues (Supplementary Fig. 3) distributions were compared with Kolmogorov-Smirnov test. Multiple comparisons were made by one-way ANOVA followed by *post-hoc* Bonferroni test, unless otherwise stated. Significance was set at $\alpha = 0.05$. One hundred and thirty neurons were analyzed in Supplementary Fig. 2a–c; 106 dendrites from 35 neurons were analyzed in Supplementary Fig. 2d. Seven hundred and fifty-six frames (21,564 spines) were used for ChETA constructs expression calculation. A total of 1,493 spines was analyzed for EI calculation. For PSD95/ChETA-Cherry co-localization, a total of 2,251 spines from 44 neurons were analyzed. For Homer1c-EGFP/SA-Ch correlation, 369 spines from 37 neurons were analyzed; for SEP-GluA1 experiments, 737 spines from 108 neurons were analyzed.

For two-photon uncaging experiments, a total of 48 samples were analyzed, and a total of 118 spines were considered. For the time-course experiments in two-photon uncaging, we considered the following number of spines: uncaging, 18 stimulated and 24 nearby spines; uncaging with anysomicin, 15 stimulated and 21 nearby spines; without MNI-caged glutamate, 8 stimulated and 8 nearby spines.

For GCaMP6s imaging, 55 spines were stimulated, out of which 17 in presence of VGCC inhibitors and 17 in the presence of TTX. For in vivo analysis, the following number of dendrites (spines/slices/animals) were considered: CA1 home cage 93 (6703/8/4), DG home cage 52 (4157/9/4), CA1 novel context 111 (10223/8/3), and DG novel context 58 (4865/8/3). Thirteen dendrites were excluded from the calculation of the increase in probability according to pre-established criteria, because (i) the fraction of positive spine was below the defined threshold of 0.05 or (ii) it was not possible to define a whole set of 20 neighbors. Data were analyzed from two researchers; spine notation was performed by a blind researcher to condition (home cage/context) but not to hippocampal region (CA1/DG). No statistical method has been used to pre-determine sample size. Animals were distributed randomly between groups. Animals where the hippocampus was not electroporated (due to electrodes misalignment during electroporation) were excluded from the analysis, as established before the analysis ($n = 1$).

Comparisons between groups when distributions were not normal, or requirements for parametric tests were not met, were performed with Kruskal–Wallis test, followed by Dunn's test for pairwise comparison. Non-parametric comparisons between two samples were performed with Mann–Whitey test. Parametric test used were Student's t-test (two-tailed) (paired tests were used to compare sets of coupled values in Fig. 4b), or Bonferroni correction following one-way ANOVA for multiple comparisons.

All information is summarized in Supplementary Table 1.

Data availability. Data supporting the findings of this study are available within the paper and its supplementary information file. Reagents will be made freely available upon request and the exchange of materials will be regulated by an MTA. All R codes are freely available upon request.

Received: 17 September 2016 Accepted: 6 October 2017
Published online: 20 November 2017

References

1. Yuste, R. & Denk, W. Dendritic spines as basic functional units of neuronal integration. *Nature* **375**, 682–684 (1995).
2. Redondo, R. L. & Morris, R. G. M. Making memories last: the synaptic tagging and capture hypothesis. *Nat. Rev. Neurosci.* **12**, 17–30 (2011).
3. Kelleher, R. J. III, Govindarajan, A., Jung, H.-Y., Kang, H. & Tonegawa, S. Translational control by MAPK signaling in long-term synaptic plasticity and memory. *Cell* **116**, 467–479 (2004).
4. Moncada, D. & Viola, H. Induction of long-term memory by exposure to novelty requires protein synthesis: evidence for a behavioral tagging. *J. Neurosci.* **27**, 7476–7481 (2007).
5. Takeuchi, T., Duszkiewicz, A. J. & Morris, R. G. The synaptic plasticity and memory hypothesis: encoding, storage and persistence. *Phil. Trans. R. Soc. B* **369**, 20130288 (2014).
6. Rogerson, T. et al. Synaptic tagging during memory allocation. *Nat. Rev. Neurosci.* **15**, 157–169 (2014).
7. Nabavi, S. et al. Engineering a memory with LTD and LTP. *Nature* **511**, 348–352 (2014).
8. Liu, X. et al. Optogenetic stimulation of a hippocampal engram activates fear memory recall. *Nature* **484**, 381–385 (2012).
9. Ramirez, S. et al. Creating a false memory in the hippocampus. *Science* **341**, 387–391 (2013).
10. Mayford, M. The search for a hippocampal engram. *Philos. Trans. R. Soc. Lond. B Biol. Sci.* **369**, 20130161 (2014).
11. Hübener, M. & Bonhoeffer, T. Searching for engrams. *Neuron* **67**, 363–371 (2010).
12. Poo, M. et al. What is memory? The present state of the engram. *BMC Biol.* **14**, 1 (2016).
13. Neves, G., Cooke, S. F. & Bliss, T. V. Synaptic plasticity, memory and the hippocampus: a neural network approach to causality. *Nat. Rev. Neurosci.* **9**, 65–75 (2008).
14. Häusser, M. & Mel, B. Dendrites: bug or feature? *Curr. Opin. Neurobiol.* **13**, 372–383 (2003).
15. Rebola, N., Carta, M. & Mulle, C. Operation and plasticity of hippocampal CA3 circuits: implications for memory encoding. *Nat. Rev. Neurosci.* **18**, 209–221 (2017).
16. Lewis, T. L. J., Mao, T., Svoboda, K. & Arnold, D. B. Myosin-dependent targeting of transmembrane proteins to neuronal dendrites. *Nat. Neurosci.***12**, 568–576 (2009).
17. Lewis, T. L. J., Mao, T. & Arnold, D. B. A role for myosin VI in the localization of axonal proteins. *PLoS Biol.* **9**, e1001021 (2011).
18. Lin, J. Y. et al. Optogenetic inhibition of synaptic release with chromophore-assisted light inactivation (CALI). *Neuron* **79**, 241–253 (2013).
19. Greenberg, K. P., Pham, A. & Werblin, F. S. Differential targeting of optical neuromodulators to ganglion cell soma and dendrites allows dynamic control of center-surround antagonism. *Neuron* **69**, 713–720 (2011).
20. Packer, A. M. et al. Two-photon optogenetics of dendritic spines and neural circuits. *Nat. Methods* **9**, 1202–1205 (2012).
21. Shaner, N. C. et al. Improved monomeric red, orange and yellow fluorescent proteins derived from Discosoma sp. red fluorescent protein. *Nat. Biotechnol.* **22**, 1567–1572 (2004).
22. Fusco, D. et al. Single mRNA molecules demonstrate probabilistic movement in living mammalian cells. *Curr. Biol.***13**, 161–167 (2003).
23. Steward, O., Farris, S., Pirbhoy, P. S., Darnell, J. & Driesche, S. J. V. Localization and local translation of Arc/Arg3.1 mRNA at synapses: some observations and paradoxes. *Front. Mol. Neurosci.* **7**, 101 (2015).
24. Kobayashi, H., Yamamoto, S., Maruo, T. & Murakami, F. Identification of a cis-acting element required for dendritic targeting of activity-regulated cytoskeleton-associated protein mRNA. *Eur. J. Neurosci.* **22**, 2977–2984 (2005).
25. Gunaydin, L. A. et al. Ultrafast optogenetic control. *Nat. Neurosci.***13**, 387–392 (2010).
26. Kindler, S., Wang, H., Richter, D. & Tiedge, H. RNA transport and local control of translation. *Annu. Rev. Cell Dev. Biol.* **21**, 223 (2005).
27. Pinkstaff, J. K., Chappell, S. A., Mauro, V. P., Edelman, G. M. & Krushel, L. A. Internal initiation of translation of five dendritically localized neuronal mRNAs. *Proc. Natl Acad. Sci. USA* **98**, 2770–2775 (2001).
28. Kornau, H.-C., Schenker, L. T., Kennedy, M. B. & Seeburg, P. H. Domain interaction between NMDA receptor subunits and the postsynaptic density protein PSD-95. *Science* **269**, 1737–1740 (1995).
29. Gradinaru, V. et al. Targeting and readout strategies for fast optical neural control in vitro and in vivo. *J. Neurosci.* **27**, 14231–14238 (2007).
30. Panja, D. & Bramham, C. R. BDNF mechanisms in late LTP formation: a synthesis and breakdown. *Neuropharmacology* **76**, 664–676 (2014).
31. Aakalu, G., Smith, W. B., Nguyen, N., Jiang, C. & Schuman, E. M. Dynamic visualization of local protein synthesis in hippocampal neurons. *Neuron* **30**, 489–502 (2001).
32. Espinosa, F. & Kavalali, E. T. NMDA receptor activation by spontaneous glutamatergic neurotransmission. *J. Neurophysiol.* **101**, 2290–2296 (2009).
33. Constals, A. et al. Glutamate-induced AMPA receptor desensitization increases their mobility and modulates short-term plasticity through unbinding from stargazin. *Neuron* **85**, 787–803 (2015).
34. Meyer, D., Bonhoeffer, T. & Scheuss, V. Balance and stability of synaptic structures during synaptic plasticity. *Neuron* **82**, 430–443 (2014).
35. Matsuzaki, M., Honkura, N., Ellis-Davies, G. C. & Kasai, H. Structural basis of long-term potentiation in single dendritic spines. *Nature* **429**, 761–766 (2004).
36. Makino, H. & Malinow, R. Compartmentalized versus global synaptic plasticity on dendrites controlled by experience. *Neuron* **72**, 1001–1011 (2011).
37. Hill, T. C. & Zito, K. LTP-induced long-term stabilization of individual nascent dendritic spines. *J. Neurosci.* **33**, 678–686 (2013).
38. Chen, T.-W. et al. Ultrasensitive fluorescent proteins for imaging neuronal activity. *Nature* **499**, 295–300 (2013).
39. Winnubst, J., Cheyne, J. E., Niculescu, D. & Lohmann, C. Spontaneous activity drives local synaptic plasticity *in vivo*. *Neuron* **87**, 399–410 (2015).
40. Lee, K. F., Soares, C., Thivierge, J.-P. & Béïque, J.-C. Correlated synaptic inputs drive dendritic calcium amplification and cooperative plasticity during clustered synapse development. *Neuron* **89**, 784–799 (2016).
41. Schoenenberger, P., Grunditz, Å., Rose, T. & Oertner, T. G. Optimizing the spatial resolution of Channelrhodopsin-2 activation. *Brain Cell Biol.* **6**, 119–127 (2008).
42. Paluch-Siegler, S. et al. All-optical bidirectional neural interfacing using hybrid multiphoton holographic optogenetic stimulation. *Neurophotonics* **2**, 031208–031208 (2015).
43. Schneider, F., Gradmann, D. & Hegemann, P. Ion selectivity and competition in channelrhodopsins. *Biophys. J.* **105**, 91–100 (2013).
44. Lisman, J., Yasuda, R. & Raghavachari, S. Mechanisms of CaMKII action in long-term potentiation. *Nat. Rev. Neurosci.* **13**, 169–182 (2012).
45. Guzowski, J. F., Setlow, B., Wagner, E. K. & McGaugh, J. L. Experience-dependent gene expression in the rat hippocampus after spatial learning: a comparison of the immediate-early genesArc, c-fos, and zif268. *J. Neurosci.* **21**, 5089–zif5098 (2001).
46. Rinaldi, A. & Romeo, S. Agust'/in-Pavón, C., Oliverio, A. & Mele, A. Distinct patterns of Fos immunoreactivity in striatum and hippocampus induced by different kinds of novelty in mice. *Neurobiol. Learn. Memory* **94**, 373–381 (2010).
47. Guzowski, J. F. Insights into immediate-early gene function in hippocampal memory consolidation using antisense oligonucleotide and fluorescent imaging approaches. *Hippocampus* **12**, 86–104 (2002).
48. Sato, T., Muroyama, Y. & Saito, T. Inducible gene expression in postmitotic neurons by an in vivo electroporation-based tetracycline system. *J. Neurosci. Methods* **214**, 170–176 (2013).
49. Szczurkowska, J. et al. Targeted in vivo genetic manipulation of the mouse or rat brain by in utero electroporation with a triple-electrode probe. *Nat. Protoc.* **11**, 399–412 (2016).
50. Gabernet, L. et al. Enhancement of the NMDA receptor function by reduction of glycine transporter-1 expression. *Neurosci. Lett.* **373**, 79–84 (2004).
51. Xu, T. et al. Rapid formation and selective stabilization of synapses for enduring motor memories. *Nature* **462**, 915–919 (2009).
52. Yang, G., Pan, F. & Gan, W.-B. Stably maintained dendritic spines are associated with lifelong memories. *Nature* **462**, 920–924 (2009).
53. Minatohara, K., Akiyoshi, M. & Okuno, H. Role of immediate-early genes in synaptic plasticity and neuronal ensembles underlying the memory trace. *Fronti. Mol. Neurosci.* **8**, 78 (2015).
54. Baj, G., Leone, E., Chao, M. V. & Tongiorgi, E. Spatial segregation of BDNF transcripts enables BDNF to differentially shape distinct dendritic compartments. *Proc. Natl Acad. Sci. USA* **108**, 16813–16818 (2011).
55. Feng, L., Kwon, O., Lee, B., Oh, W. C. & Kim, J. Using mammalian GFP reconstitution across synaptic partners (mGRASP) to map synaptic connectivity in the mouse brain. *Nat. Protoc.* **9**, 2425–2437 (2014).
56. Cichon, J. & Gan, W.-B. Branch-specific dendritic Ca2 + spikes cause persistent synaptic plasticity. *Nature* **520**, 180–185 (2015).
57. Tanaka, H. & Hirano, T. Visualization of subunit-specific delivery of glutamate receptors to postsynaptic membrane during hippocampal long-term potentiation. *Cell Rep.* **1**, 291–298 (2012).

58. Park, P. et al. NMDA receptor-dependent long-term potentiation comprises a family of temporally overlapping forms of synaptic plasticity that are induced by different patterns of stimulation. *Phil. Trans. R. Soc. B* **369**, 20130131 (2014).
59. Kramár, E. A. et al. Synaptic evidence for the efficacy of spaced learning. *Proc. Natl Acad. Sci. USA* **109**, 5121–5126 (2012).
60. Zhang, Y., Cudmore, R. H., Lin, D.-T., Linden, D. J. & Huganir, R. L. Visualization of NMDA receptor-dependent AMPA receptor synaptic plasticity in vivo. *Nat. Neurosci.* **18**, 402–407 (2015).
61. Takahashi, N. et al. Locally synchronized synaptic inputs. *Science* **335**, 353–356 (2012).
62. Govindarajan, A., Kelleher, R. J. & Tonegawa, S. A clustered plasticity model of long-term memory engrams. *Nat. Rev. Neurosci.* **7**, 575–583 (2006).
63. Govindarajan, A., Israely, I., Huang, S.-Y. & Tonegawa, S. The dendritic branch is the preferred integrative unit for protein synthesis-dependent LTP. *Neuron* **69**, 132–146 (2011).
64. Kastellakis, G., Cai, D. J., Mednick, S. C., Silva, A. J. & Poirazi, P. Synaptic clustering within dendrites: An emerging theory of memory formation. *Prog. Neurobiol.* **126**, 19–35 (2015).
65. Knierim, J. J. & Neunuebel, J. P. Tracking the flow of hippocampal computation: Pattern separation, pattern completion, and attractor dynamics. *Neurobiol. Learn. Memory* **129**, 38–49 (2016).
66. Ohkawa, N. et al. Artificial association of pre-stored information to generate a qualitatively new memory. *Cell Rep.* **11**, 261–269 (2015).
67. Josselyn, S. A., Köhler, S. & Frankland, P. W. Finding the engram. *Nat. Rev. Neurosci.* **16**, 521–534 (2015).
68. Mattis, J. et al. Principles for applying optogenetic tools derived from direct comparative analysis of microbial opsins. *Nat. Methods* **9**, 159–172 (2011).
69. Dawydow, A. et al. Channelrhodopsin-2-XXL, a powerful optogenetic tool for low-light applications. *Proc. Natl Acad. Sci. USA* **111**, 13972–13977 (2014).
70. Asrican, B. et al. Next-generation transgenic mice for optogenetic analysis of neural circuits. *Front. Neural Circuits* **7**, 160 (2013).
71. Chavlis, S., Petrantonakis, P. C. & Poirazi, P. Dendrites of dentate gyrus granule cells contribute to pattern separation by controlling sparsity. *Hippocampus* **27**, 89–110 (2017).
72. Hayashi-Takagi, A. et al. Labelling and optical erasure of synaptic memory traces in the motor cortex. *Nature* **525**, 333–338 (2015).
73. Barde, I. et al. Efficient control of gene expression in the hematopoietic system using a single Tet-on inducible lentiviral vector. *Mol. Ther.* **13**, 382–390 (2006).
74. Palida, S. F. et al. PKMζ, but Nnt PKCλ, is rapidly synthesized and degraded at the neuronal synapse. *J. Neurosci.* **35**, 7736–7749 (2015).

Acknowledgements

We thank Dr S.Kindler (Uni Hamburg) for useful discussion and for providing MAP2 and alphaCaMKII cDNA, to amplify DTEs, Dr A. Riccio (UCL) for IMPA1 ATE cDNA, Dr A. Marcello (ICGEB Trieste) for plasmids pSL-MS2 12X and Cherry-MS2 coat protein-NLS, and Dr D. Choquet (CNRS Bordeaux) for making plasmid Homer1c-EGFP available. We thank G. Testa (Scuola Normale Superiore, Pisa) for help with animal perfusion and slice preparation for IF. We thank C. Rizzi and N.M. Carucci (Scuola Normale Superiore, Pisa) for help with cortex and hippocampus dissections. The work was financially supported by institutional funding from Scuola Normale Superiore and by the E.U. flagship Human Brain Project (grant number 604602).

Author contributions

A.C. conceived the project. F.G. and A.C. designed research. F.G., L.M., A.J., B.P., N.B., F.P.B. and C.A. performed experiments and analyzed data. M.C. supervised and provided expertise on the optogenetic experiments in culture. S.L. supervised two-photon uncaging experiments. T.F. supervised and provided expertise on the measurement of synaptic glutamatergic transmission in *ex vivo* hippocampal slices. L.C. supervised and provided expertise on the *in utero* electroporation. A.C. provided expertise and discussion on the in utero data. F.G., L.M., S.L. and A.C. wrote the manuscript.

Additional information

Supplementary Information accompanies this paper at doi:10.1038/s41467-017-01699-7.

Competing interests: The authors declare no competing financial interests.

Reprints and permission information is available online at http://npg.nature.com/reprintsandpermissions/

Publisher's note: Springer Nature remains neutral with regard to jurisdictional claims in published maps and institutional affiliations.

Open Access This article is licensed under a Creative Commons Attribution 4.0 International License, which permits use, sharing, adaptation, distribution and reproduction in any medium or format, as long as you give appropriate credit to the original author(s) and the source, provide a link to the Creative Commons license, and indicate if changes were made. The images or other third party material in this article are included in the article's Creative Commons license, unless indicated otherwise in a credit line to the material. If material is not included in the article's Creative Commons license and your intended use is not permitted by statutory regulation or exceeds the permitted use, you will need to obtain permission directly from the copyright holder. To view a copy of this license, visit http://creativecommons.org/licenses/by/4.0/.

© The Author(s) 2017

APPENDIX IV

APache Is an AP2-Interacting Protein Involved in Synaptic Vesicle Trafficking and Neuronal Development.

Piccini A, Castroflorio E, Valente P, Guarnieri FC, Aprile D, Michetti C, Bramini M, Giansante G, Pinto B, Savardi A, Cesca F, Bachi A, Cattaneo A, Wren JD, Fassio A, Valtorta F, Benfenati F, Giovedì S.

Article

Cell Reports

APache Is an AP2-Interacting Protein Involved in Synaptic Vesicle Trafficking and Neuronal Development

Graphical Abstract

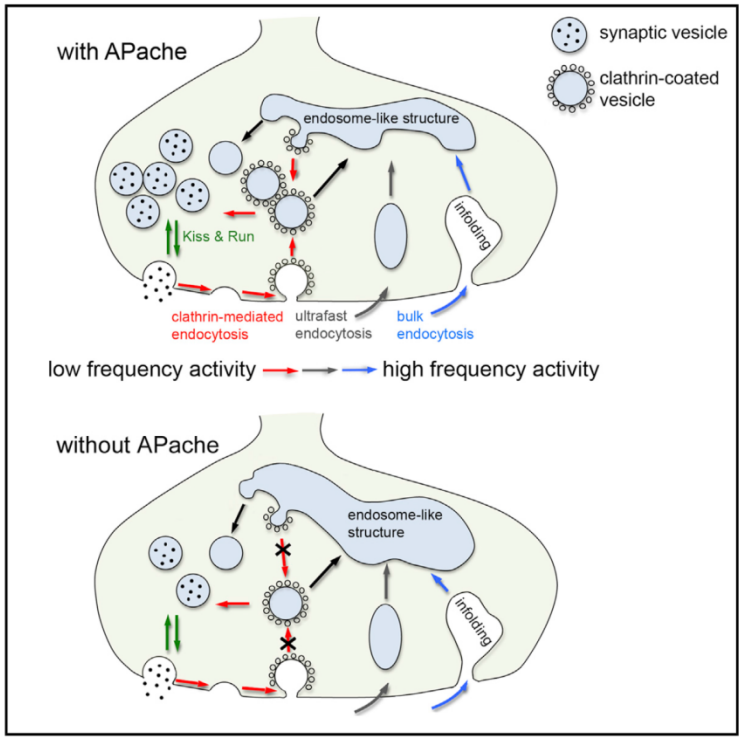

Highlights

- APache is a presynaptic AP2 interactor on clathrin-coated vesicles
- APache silencing affects the early neuronal development *in vitro* and *in vivo*
- APache-silenced synapses exhibit a marked endocytic phenotype
- APache silencing impairs clathrin-mediated endocytosis and synaptic function

Authors

Alessandra Piccini, Enrico Castroflorio, Pierluigi Valente, ..., Flavia Valtorta, Fabio Benfenati, Silvia Giovedì

Correspondence

fabio.benfenati@iit.it (F.B.), silvia.giovedi@unige.it (S.G.)

In Brief

Piccini et al. uncovered the AP2-interacting protein APache that acts in the clathrin-mediated endocytic machinery and synaptic vesicle trafficking. They found that silencing APache impairs neuronal development and neurotransmitter release during repetitive stimulation by markedly reducing vesicle recycling.

Piccini et al., 2017, Cell Reports *21*, 3596–3611
December 19, 2017 © 2017 The Authors.
https://doi.org/10.1016/j.celrep.2017.11.073

CellPress

OPEN ACCESS
CellPress

Cell Reports
Article

APache Is an AP2-Interacting Protein Involved in Synaptic Vesicle Trafficking and Neuronal Development

Alessandra Piccini,[1] Enrico Castroflorio,[2] Pierluigi Valente,[1] Fabrizia C. Guarnieri,[3] Davide Aprile,[1] Caterina Michetti,[2] Mattia Bramini,[2] Giorgia Giansante,[1] Bruno Pinto,[4,5] Annalisa Savardi,[1,4] Fabrizia Cesca,[2] Angela Bachi,[6] Angela Cattaneo,[6] Jonathan D. Wren,[7] Anna Fassio,[1,2] Flavia Valtorta,[3] Fabio Benfenati,[1,2,8,*] and Silvia Giovedì[1,8,9,*]
[1]Department of Experimental Medicine, University of Genova, 16132 Genova, Italy
[2]Center for Synaptic Neuroscience and Technology, Istituto Italiano di Tecnologia, 16132 Genova, Italy
[3]San Raffaele Scientific Institute and Vita Salute University, 20132 Milano, Italy
[4]Local Micro-environment and Brain Development Laboratory, Istituto Italiano di Tecnologia, 16163 Genova, Italy
[5]Bio@SNS, Scuola Normale Superiore, 56126 Pisa, Italy
[6]IFOM, FIRC Institute of Molecular Oncology, 20132 Milano, Italy
[7]Department of Arthritis and Clinical Immunology, Oklahoma Medical Research Foundation, Oklahoma City, OK 73104-5005, USA
[8]These authors contributed equally
[9]Lead Contact
*Correspondence: fabio.benfenati@iit.it (F.B.), silvia.giovedi@unige.it (S.G.)
https://doi.org/10.1016/j.celrep.2017.11.073

SUMMARY

Synaptic transmission is critically dependent on synaptic vesicle (SV) recycling. Although the precise mechanisms of SV retrieval are still debated, it is widely accepted that a fundamental role is played by clathrin-mediated endocytosis, a form of endocytosis that capitalizes on the clathrin/adaptor protein complex 2 (AP2) coat and several accessory factors. Here, we show that the previously uncharacterized protein KIAA1107, predicted by bioinformatics analysis to be involved in the SV cycle, is an AP2-interacting clathrin-endocytosis protein (APache). We found that APache is highly enriched in the CNS and is associated with clathrin-coated vesicles via interaction with AP2. APache-silenced neurons exhibit a severe impairment of maturation at early developmental stages, reduced SV density, enlarged endosome-like structures, and defects in synaptic transmission, consistent with an impaired clathrin/AP2-mediated SV recycling. Our data implicate APache as an actor in the complex regulation of SV trafficking, neuronal development, and synaptic plasticity.

INTRODUCTION

High-frequency and sustained neurotransmitter release is dependent on the correct reformation of exocytosed synaptic vesicles (SVs) by efficient endocytosis. During physiological activity, clathrin-mediated endocytosis (CME) represents the best-characterized pathway for recycling of fully fused SVs (Heuser and Reese, 1973; Granseth et al., 2006; Dittman and Ryan, 2009; Saheki and De Camilli, 2012), although the precise mechanisms of SV membrane retrieval and functional SV reconstitution remain highly controversial (Soykan et al., 2016; Cousin, 2017).

At the plasma membrane, the most abundant adaptor coordinating coat recruitment and cargo selection into endocytic pits is the heterotetrameric adaptor protein complex 2 (AP2), comprised of two large α and β2 subunits, a medium-size μ2 subunit, and a small δ2 subunit. Among the numerous accessory proteins believed to control the internalization pathway (Slepnev and De Camilli, 2000), clathrin and AP2 constitute the two main protein interaction hubs, around which an extensive and highly dynamic endocytic network is organized to achieve clathrin-coated vesicle (CCV) formation (Schmid and McMahon, 2007). However, other alternate clathrin-associated sorting proteins (CLASP) have recently been identified for the internalization of selected cargo membrane proteins (Traub and Bonifacino, 2013). Thus, synapses have evolved distinct mechanisms to maintain membrane homeostasis and the dominant mode for SV recycling may depend on the type of neuron and its activity pattern (Valtorta et al., 2001; Kononenko and Haucke, 2015; Park et al., 2016). Despite intense research, much remains to be learned about the exact molecular components of the endocytic pathways.

Here, we characterize the highly conserved AP2-interacting clathrin-endocytosis protein APache (NP_001007575.2) and investigate its physiological role in neuronal development and synaptic function. APache is a neuron-specific protein, expressed in axonal processes and presynaptic terminals, that specifically interacts with AP2 on CCVs. Our data indicate that APache plays a role in neuronal development and is required to maintain normal SV recycling in mature neurons. APache can thus be considered an important actor of the clathrin-mediated endocytic machinery at the synapse that is required for normal synaptic transmission.

 © 2017 The Authors.
This is an open access article under the CC BY-NC-ND license (http://creativecommons.org/licenses/by-nc-nd/4.0/).

OPEN ACCESS
CellPress

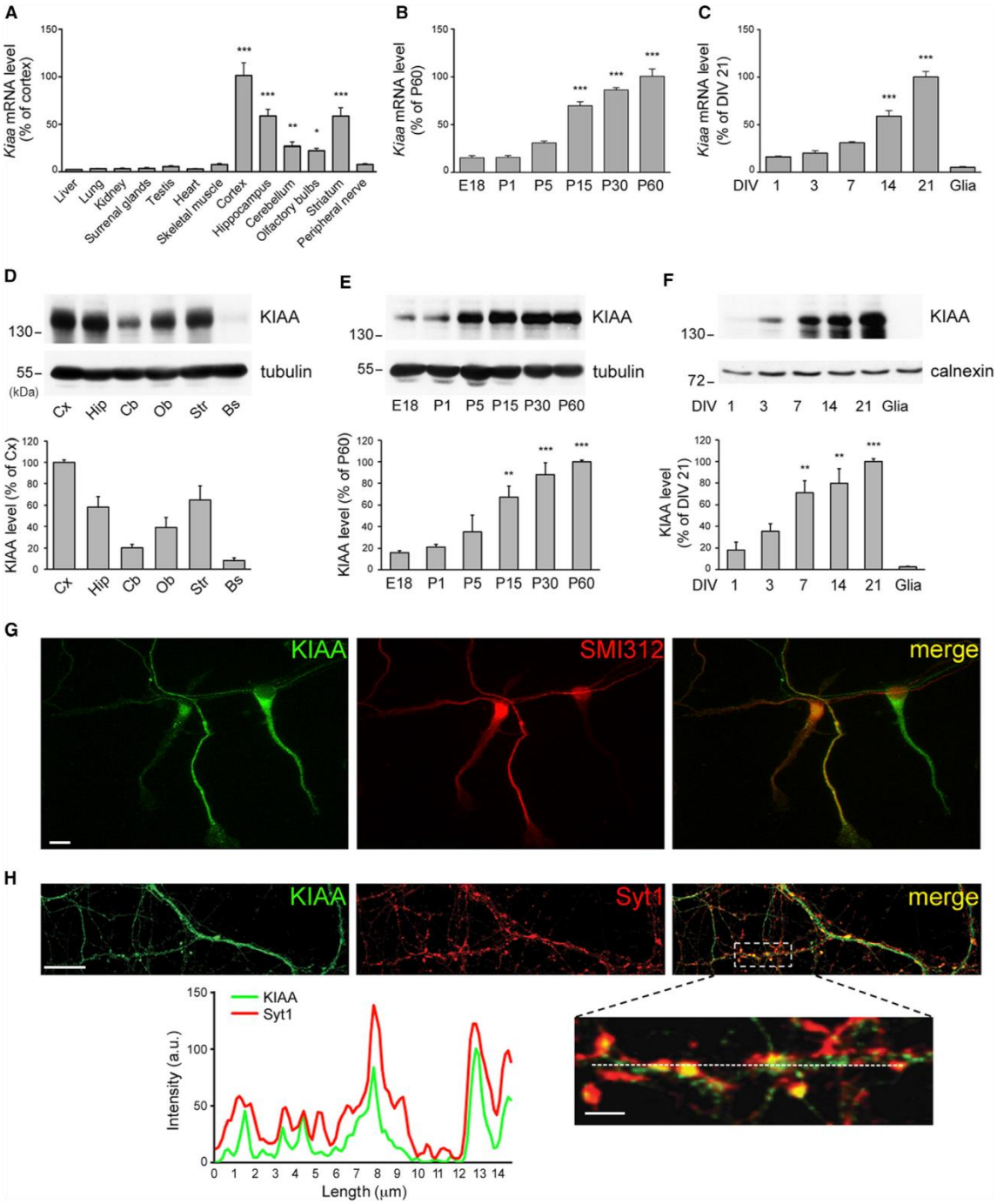

Figure 1. Expression and Localization of Endogenous KIAA1107 in Neurons

(A) Real-time PCR analysis of *Kiaa1107* mRNA levels in various mouse tissues. Means ± SEM of n = 3 animals; one-way ANOVA/Bonferroni's multiple comparison test; *p < 0.05; **p < 0.01; ***p < 0.001 versus liver.

(legend continued on next page)

RESULTS

Identification of KIAA1107 by GAMMA

Global Microarray Meta-Analysis (GAMMA) is a program previously developed to identify highly correlated transcripts within microarray experiments, which can then be used to infer function, phenotype, genetic network, and disease relevance for uncharacterized genes (Wren, 2009). GAMMA was used to search for uncharacterized genes associated with SV recycling, and KIAA1107 was the highest scoring gene without prior publications. The predicted phenotypes associated with KIAA1107 disruption, predicted disease relevance, and predicted cellular/anatomical structures of relevance to KIAA1107 activity are shown in Figure S1.

KIAA1107 is evolutionarily conserved from zebrafish to human. The murine *Kiaa1107* gene (official symbol: A830010M20Rik) is located on chromosome 5 (forward strand). According to the Ensembl database, the gene gives rise to five differentially spliced transcripts, four of which are predicted to be protein coding. Conversely, the NCBI database includes only two splicing variants (NCBI Refseq NM_001007574.2 and NM_001168557.1, corresponding to ENSMUST00000112671.8 and ENSMUST00000060553.7, respectively, in the Ensembl database). Among these two, one transcript codes for a protein of 1,088 amino acids (aas) and is considered the main isoform, whereas the other codes for a smaller protein of 443 aas. We cloned the major isoform, with an expected molecular mass of 117 kDa, and will refer to it as KIAA1107 throughout. No significant similarity with other proteins could be identified with a BLAST search of the murine KIAA1107 against the *Mus musculus* RefSeq protein database. No conserved protein domains were predicted using bioinformatics tools, such as SMART and InterProScan, but one coiled-coil region was predicted at aa position 820–841 with COILS2 (probability 62.9% with window 21; MTIDK matrix; no weights). Hence, the sequence of KIAA1107 does not reveal any particular information about its possible function or localization, but the GAMMA predictions on its involvement in synaptic function were really strong and persuaded us to investigate it further.

To characterize KIAA1107, we first generated a polyclonal antibody directed against a conserved region comprising aas 732–894 of the mouse ortholog (Figure S2A). The affinity-purified antibody recognized both overexpressed and endogenous KIAA1107 as a band of ~140 kDa in immunoblotting assays (Figures S2B and S2C). Its specificity was further proved by preadsorbing the primary antibody with a molar excess of the recombinant immunizing peptide (Figure S2D).

To silence KIAA1107 expression, we designed 3 short hairpin RNAs (shRNAs) based on the coding sequence (shRNA#1) and the 3′ UTR (shRNA#2 and #3) of the mouse *Kiaa1107* transcript, inserted them into a bicistronic lentiviral vector expressing the fluorescent reporter mCherry, and validated their specificity and efficacy by immunoblotting (Figures S2B and S2C). shRNA#2 was chosen for the subsequent studies, being the most active in knocking down the endogenous KIAA1107 expression. The specificity of the KIAA1107 antibody was subsequently demonstrated by immunocytochemistry of silenced neurons (Figure S2E).

KIAA1107 Is a Neuron-Specific and Developmentally Regulated Protein

We evaluated *Kiaa1107* mRNA and protein levels in various tissues and brain areas of adult mice and determined its developmental expression profile in the intact mouse cortex and primary neuronal cultures (Figures 1A–1F). KIAA1107 was primarily expressed in brain, with the highest mRNA and protein levels in the cerebral cortex, hippocampus, and striatum (Figures 1A and 1D). It was already present in the mouse brain at prenatal and early postnatal stages (embryonic day 18 [E18]–postnatal day 5 [P5]), and its expression increased during postnatal development to reach a plateau at 1 month of age (Figures 1B and 1E). A similar pattern was reproduced in primary cortical neurons, where *Kiaa1107* mRNA and protein levels were discernible at early stages of development (1–3 days in vitro [DIV]) and were greatly enhanced between 7 and 21 DIV (Figures 1C and 1F). Consistent with the strictly neuron-specific expression of the protein, KIAA1107 was not detected in primary astroglial cultures.

To examine the localization of KIAA1107 in neurons during development, 5 and 17 DIV primary cortical neurons were analyzed by immunocytochemistry. In early stages of *in vitro* development, KIAA1107 was expressed in the cell body and growing processes, including the axon, as shown by the colocalization with the pan-axonal neurofilament marker SMI312

(B) Real-time PCR analysis of *Kiaa1107* mRNA expression in the cerebral cortex of developing mice (from embryonic day 18 [E18] to postnatal day 60 [P60]). Means ± SEM of n = 3 animals/developmental stage; one-way ANOVA/Bonferroni's multiple comparison test; ***p < 0.001 versus E18.
(C) Real-time PCR analysis of *Kiaa1107* mRNA expression in primary cultures of cortical neurons at various stages of development (from 1 to 21 DIV). Means ± SEM of n = 3 independent cultures/developmental stage; one-way ANOVA/Bonferroni's multiple comparison test; ***p < 0.001 versus DIV 1.
(D) Regional expression of KIAA1107 in the adult mouse brain. Representative immunoblot (top) and relative densitometric quantification normalized on βIII tubulin levels (bottom) are shown. Means ± SEM of n = 4 animals. Bs, brain stem; Cb, cerebellum; Cx, cortex; Hip, hippocampus; Ob, olfactory bulb; Str, striatum.
(E) Temporal expression profile of KIAA1107 in the developing mouse cerebral cortex (from E18 to P60). Representative immunoblot of KIAA1107 levels (top) and relative densitometric quantification normalized on βIII tubulin (bottom) are shown. Means ± SEM of n = 3 animals/developmental stage; one-way ANOVA/Bonferroni's multiple comparison test; **p < 0.01; ***p < 0.001 versus E18.
(F) Temporal expression profile of KIAA1107 in primary cortical neurons at various stages of development (from 1 to 21 DIV). Representative immunoblot of KIAA1107 levels (top) and relative densitometric quantification normalized on calnexin (bottom) are shown. Means ± SEM of n = 3 independent neuronal cultures/developmental stage; one-way ANOVA/Bonferroni's multiple comparison test; **p < 0.01; ***p < 0.001 versus DIV 1.
(G and H) Localization of KIAA1107 in cultured neurons during development. Representative images of cortical neurons fixed and double stained for KIAA1107 (green) and SMI312 (red) at 5 DIV (G) or for KIAA1107 (green) and synaptotagmin-1 (Syt1) (red) at 17 DIV (H) are shown. The scale bars represent 10 μm. In the bottom panel, linear intensity profiles of KIAA1107 (green) and Syt1 (red) fluorescence (measured along the dashed lines as indicated in the merge field) illustrate the presynaptic localization of KIAA1107 in mature neurons. The scale bar represents 2 μm.
See also Figures S1 and S2.

(Figure 1G). In mature neurons, the antibody also revealed a punctate nerve terminal pattern that partially colocalized with the presynaptic marker synaptotagmin-1 (Figure 1H). These data indicate that KIAA1107 is a developmentally regulated, widely expressed neuron-specific protein, mainly present at axonal and presynaptic terminal levels.

KIAA1107 Is an AP2 Interactor

In order to identify KIAA1107 protein-interacting partners, we employed a mass spectrometry (MS) approach using FLAG-KIAA1107, purified from SH-SY5Y human neuroblastoma or COS-7 cells, as a bait to pull-down KIAA1107 interactors from SH-SY5Y cell or subcellular fractions of mouse brain extracts (Figure 2A). The bands of interest were excised from the Coomassie-blue-stained gels, analyzed by liquid chromatography (LC)-MS/MS, and the MS/MS spectra were assigned to peptides with a >95% confidence level. In two independent preparations, a total of 163 proteins were reproducibly identified as specific KIAA1107-binding partners (MSdataSHSY5Y_XTandem.sf3 and MSdataCOS7_XTandem.sf3 in Data S1), seven of which resulted to be in common between the human and murine cellular models (Figure 2B). These included AP2 (α1 and β subunits) and AP3 (β2 and δ1 subunits) found in CCVs that traffic cargoes from the plasma membrane and between the endosomal and lysosomal systems, respectively (Robinson, 2004); Numb-like protein (NUMBL) involved in neural development and clathrin-dependent endocytosis (Sestan et al., 1999; Nishimura et al., 2003; Santolini et al., 2000); Bcl-2-associated transcription factor that interacts with antiapoptotic members of the Bcl-2 family (Kasof et al., 1999); V-type proton ATPase catalytic subunit A, a component of vacuolar ATPase (van Hille et al., 1993); and dynactin subunit1 (DCTN1) involved in organelle transport (Schroer, 2004).

We first focused our attention on AP2, the main adaptor protein responsible for CME (Conner and Schmid, 2003) and proceeded to co-immunoprecipitation assays to validate the potential interaction with KIAA1107. After verifying by MS analysis that the ~140-kDa protein band immunoprecipitated from mouse brain extract with the KIAA1107 polyclonal antibody was indeed the endogenous 1,088-aa KIAA1107 isoform, we found that both AP2 α and β subunits were specifically co-immunoprecipitated with endogenous KIAA1107 from mouse brain extracts (Figure 2C), whereas no interaction of KIAA1107 with clathrin was observed under the same conditions in which the AP2/clathrin binding was evident (Figure 2D). Interestingly, KIAA1107 was also co-immunoprecipitated from mouse brain extracts with anti-AP2α antibodies (Figure 2D), demonstrating the reciprocity of the interaction between KIAA1107 and AP2.

To restrict the part of the protein that interacts with AP2, we performed additional pull-down assays in mouse brain extracts using FLAG-KIAA1107 full-length, N- and C-terminal fragments. Interestingly, AP2α and AP2β were affinity purified only by the N-terminal fragment, whereas no interactions were observed with the C-terminal fragment (Figures S3A and S3B). In addition, the possibility of a nonspecific immunoprecipitation of AP2 was excluded by performing analogous co-immunoprecipitation assays in mouse liver extracts, a tissue that expresses AP2, but not KIAA1107 (Figure S3C).

We then combined the KIAA1107 binding proteins detected in our study with the results of another large proteomic study (Hein et al., 2015) that also identified KIAA1107 as a potential NUMBL interactor. Thus, we searched for additional shared interactions and overlaps with genes that GAMMA predicted to be relevant to KIAA1107 to infer a potential genetic neighborhood for KIAA1107 (Figure 2E). Such a predictive study revealed connections between KIAA1107 and clusters of genes playing key roles in exocytosis (SNAP25, syntaxin, syntaxin-binding protein, VAMP, NSF, and synaptotagmin-1), endocytosis (dynamin1, AP2, AP3, and Eps15), and neuronal development (Notch1, NUMB, and NUMBL).

KIAA1107 Is Expressed at Nerve Terminals and Associates with CCVs

As AP2 is one of the major coat proteins of CCVs, it was important to determine whether KIAA1107 is associated with CCVs. We isolated a CCV-enriched fraction from cultured rat neurons, successively stripped it and analyzed by immunoblotting the various fractions. The CCV preparation was highly enriched in the coat proteins clathrin and AP2, which were efficiently stripped from the purified vesicles, and in the integral vesicle membrane proteins synaptotagmin-1 and synaptophysin, which were not stripped (Figure 3A). In contrast, an accessory protein of CME, such as dynamin, was neither enriched on CCVs nor stripped, indicating that it does not function as classical clathrin adaptor (Slepnev and De Camilli, 2000). KIAA1107 was significantly enriched in the CCV fraction, although to a lesser extent than clathrin, and could be stripped by treatment with Tris buffer (Figure 3A). These data show that KIAA1107 is a protein associated with the coat component and not with the vesicle fraction.

In subcellular fractions prepared from rat forebrain, KIAA1107 immunoreactivity was mostly associated with the S2 fraction, consistent with the widespread localization of the protein in neurons (Figure 3B). However, it co-enriched with AP2 in the nerve-terminal-derived fractions LS1 and LP2, containing SVs and endosomal membranes, and its distribution roughly paralleled that of AP2 in other fractions (Figure 3B). Consistent with the biochemical data, a close colocalization of endogenous KIAA1107 with the essential components of the endocytic machinery AP2 and dynamin1 was observed in primary cortical neurons (17 DIV; Figure 3C). Notably, dynamin1 was identified as an indirect KIAA1107 interactor in a recent proteomics study (Gorini et al., 2010). These data suggest that KIAA1107 is closely associated with intracellular vesicular structures and binds specifically to AP2 on CCVs.

KIAA1107 Silencing Affects the Early Neuronal Development

CME controls cell surface expression of receptors, including those for axon guidance cues (Tojima et al., 2010), and AP2 plays a key role in directed cell migration (Raman et al., 2014). To interrogate the role of KIAA1107 in neuronal development, we acutely downregulated KIAA1107 expression in primary cortical neurons by RNAi with KIAA1107 shRNA#2

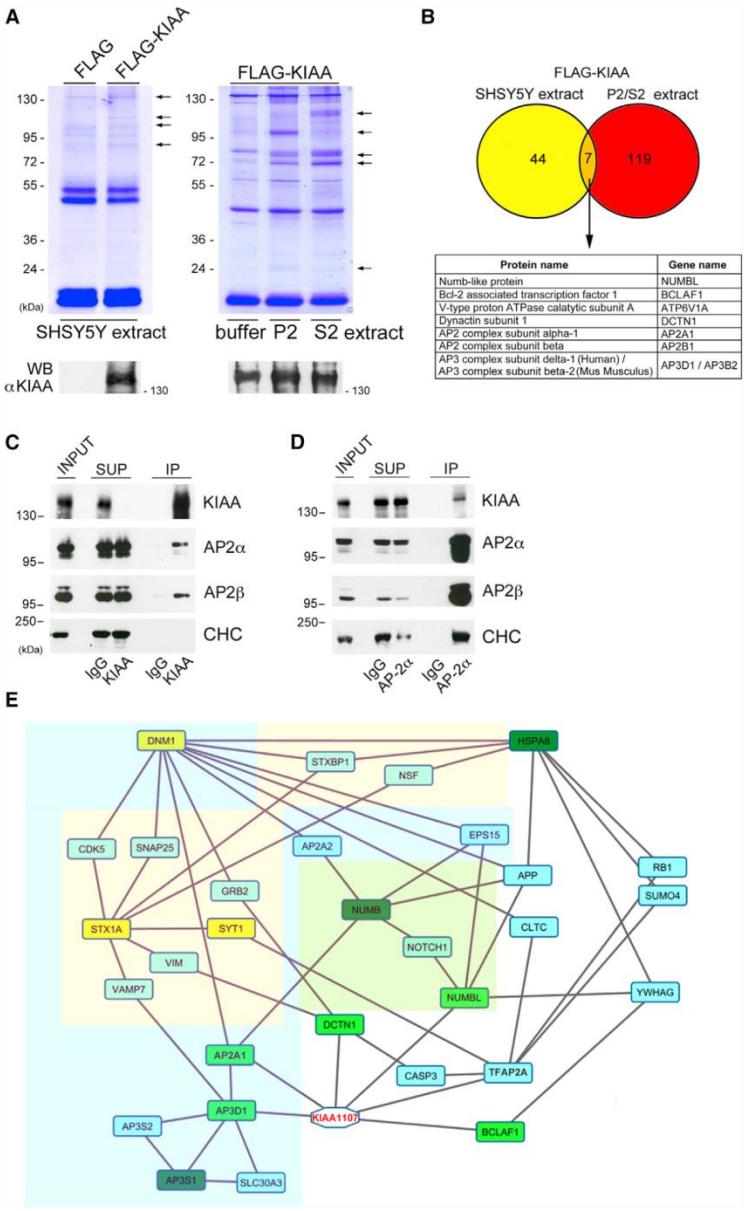

Figure 2. Identification of AP2 as a Specific KIAA1107 Interactor

(A and B) MS analysis of KIAA1107 interactors.

(A, top) Coomassie blue stained SDS-PAGE gels for proteins affinity purified by pull-down with overexpressed FLAG-KIAA1107 or FLAG-control in extracts of either SH-SY5Y cells (left panel) or subcellular fractions of mouse brain (cytosolic/microsomal S2 fraction or synaptosomal P2 fraction; right panel) are shown. Selected gel bands (arrows) were excised from the gels and analyzed by LC-MS/MS. (Bottom) KIAA1107 expression and specific precipitation in the samples was confirmed by western blotting (WB). The procedure was repeated twice with independent preparations.

(B) Venn diagram of the number of proteins identified by LC-MS/MS analysis exclusively in FLAG-KIAA1107 samples. The result showed 7 proteins (orange area) shared by both experimental models (protein and gene names are listed in the table) within 44 (yellow area) and 119 (red area) specific proteins for SH-SY5Y cells and mouse brain, respectively.

(C and D) Co-immunoprecipitation of KIAA1107 and AP2. Mouse brain extracts were subjected to immunoprecipitation (IP) with anti-KIAA1107 polyclonal antibodies (C), anti-AP2α monoclonal antibodies (D), or control immunoglobulin Gs (IgGs). Equal aliquots (2% of total) of the starting material (INPUT) and the supernatants (SUP) together with the IP samples were subjected to immunoblotting with the indicated antibodies (CHC [clathrin heavy chain]). The same membranes were stripped and re-probed for AP2α and β. The IPs were performed three times with similar results.

(E) Putative KIAA1107 genetic neighborhood based upon protein-protein interactions (PPIs). Our data (light green) were combined with PPIs found in a large proteomics study by Hein et al. (2015; dark green). Then, we searched for their shared PPIs (blue), as documented in Entrez Gene, and looked for overlap with GAMMA-predicted genes that fit into this network (yellow) to infer a potential genetic neighborhood for KIAA1107. Exocytic (yellow area), endocytic (blue area), and developmental (green area) clusters of genes are highlighted.

See also Figure S3 and Data S1.

(Figure S4). Cell morphology analysis revealed that silenced neurons displayed a significant impairment in neuronal development in terms of neurite number and length at early stages *in vitro* (3 and 5 DIV) compared to cells treated with control shRNA (shRNActr) (Figures 4A–4C). Interestingly, silenced neurons also showed a reduced expression level of AP2 (Figure S4), potentially due to partial degradation of the protein in the absence of complex formation with KIAA1107. The defective neurite outgrowth was completely rescued by the expression of EGFP-KIAA1107, a construct intrinsically resistant to shRNA#2 (Figures 4A–4C), indicating that the developmental impairment was specifically due to the downregulation of endogenous KIAA1107 and not to shRNA-mediated off-target effects. Moreover, KIAA1107 overexpression per se did not affect neuronal maturation, as length and number of processes did not differ between control and EGFP-KIAA1107-overexpressing neurons at both 3 and 5 DIV.

To further investigate the role of KIAA1107 in neocortical development *in vivo*, we downregulated its expression by in

OPEN ACCESS
CellPress

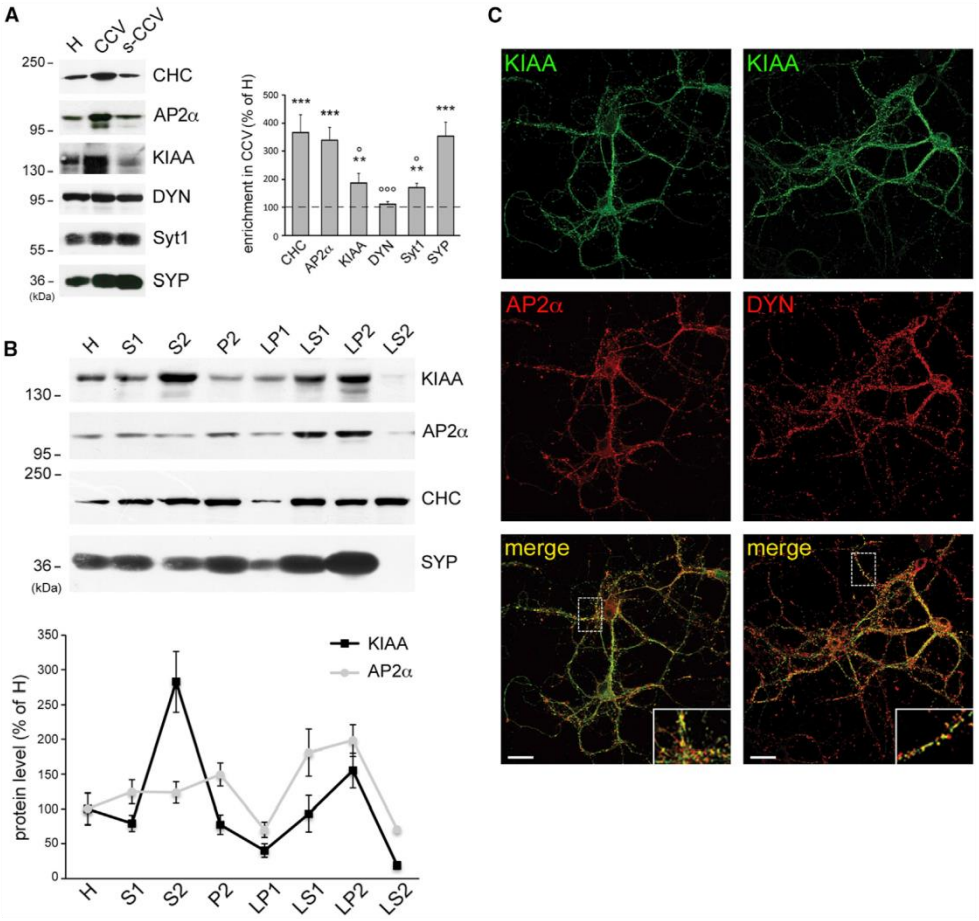

Figure 3. KIAA1107 Is a CCV-Associated Protein

(A) KIAA1107 is enriched in CCVs. (Left) The distribution of KIAA1107 immunoreactivity is compared with that of components of clathrin coats (CHC and AP2α), SVs (Syt1 and synaptophysin [SYP]), and CCV accessory proteins (dynamin1 [DYN]). Representative immunoblots are shown. Equal amounts of protein were loaded. H, total homogenate; s-CCV, stripped-CCV. (Right) Densitometric quantification of protein levels in the CCV-enriched fraction expressed as mean (±SEM) percentages of H is shown (n = 3 independent experiments); $^{**}p < 0.01$, $^{***}p < 0.001$ versus H, unpaired Student's t test; $^{\circ}p < 0.05$, $^{\circ\circ\circ}p < 0.001$ versus CHC, one-way ANOVA/Bonferroni's multiple comparison test.

(B) KIAA1107 co-fractionates with AP2. (Top) Subcellular fractions of rat forebrain were analyzed by immunoblotting using KIAA1107, AP2α, and CHC antibodies. The distribution of the specific SV marker SYP in the same fractions is shown for comparison. LP1, crude synaptic plasma membranes; LP2, crude SVs; LS1, SV-enriched supernatant fraction; LS2, synaptosol; P2, crude synaptosomes; S1, post-nuclear supernatant; S2, cytosolic and microsomal fraction. (Bottom) Densitometric quantification of KIAA1107 and AP2α immunoreactivities in the various subcellular fractions is shown. Data are expressed in percent of the relative H value (means ± SEM of n = 4 independent experiments).

(C) KIAA1107 colocalizes with the endocytic network. Representative confocal images of mature cortical neurons (17 DIV) double stained for KIAA1107 (green) and AP2α (red, left panels) or dynamin1 (DYN) (red, right panels) showing a largely overlapping staining of the proteins (magnified in the insets) are shown. The scale bars represent 10 μm (4.2 μm in the insets). Pearson's correlation coefficient is 0.846 ± 0.041 and 0.796 ± 0.039 for KIAA1107/AP2α and KIAA1107/DYN, respectively (n = 25 images obtained from n = 2 independent experiments were used for each protein).

utero electroporation (IUE) at E15.5 and analyzed the development of newly generated cortical pyramidal neurons (PNs) derived from shRNA#2-positive progenitors at P7. Whereas the knockdown (KD) of KIAA1107 did not affect radial migration of neural progenitors to layer II/III of the somatosensory cortex (Figures 4D and 4E), it significantly impaired maturation of PNs that exhibited an aberrant morphology with a significant reduction of total number and length of neurites (Figures 4F and 4G).

These data suggest a crucial role of KIAA1107 in the early stages of *in vitro* and *in vivo* neuronal development, when active SV exo/endocytotic activity at the growth cone is essential for

OPEN ACCESS
CellPress

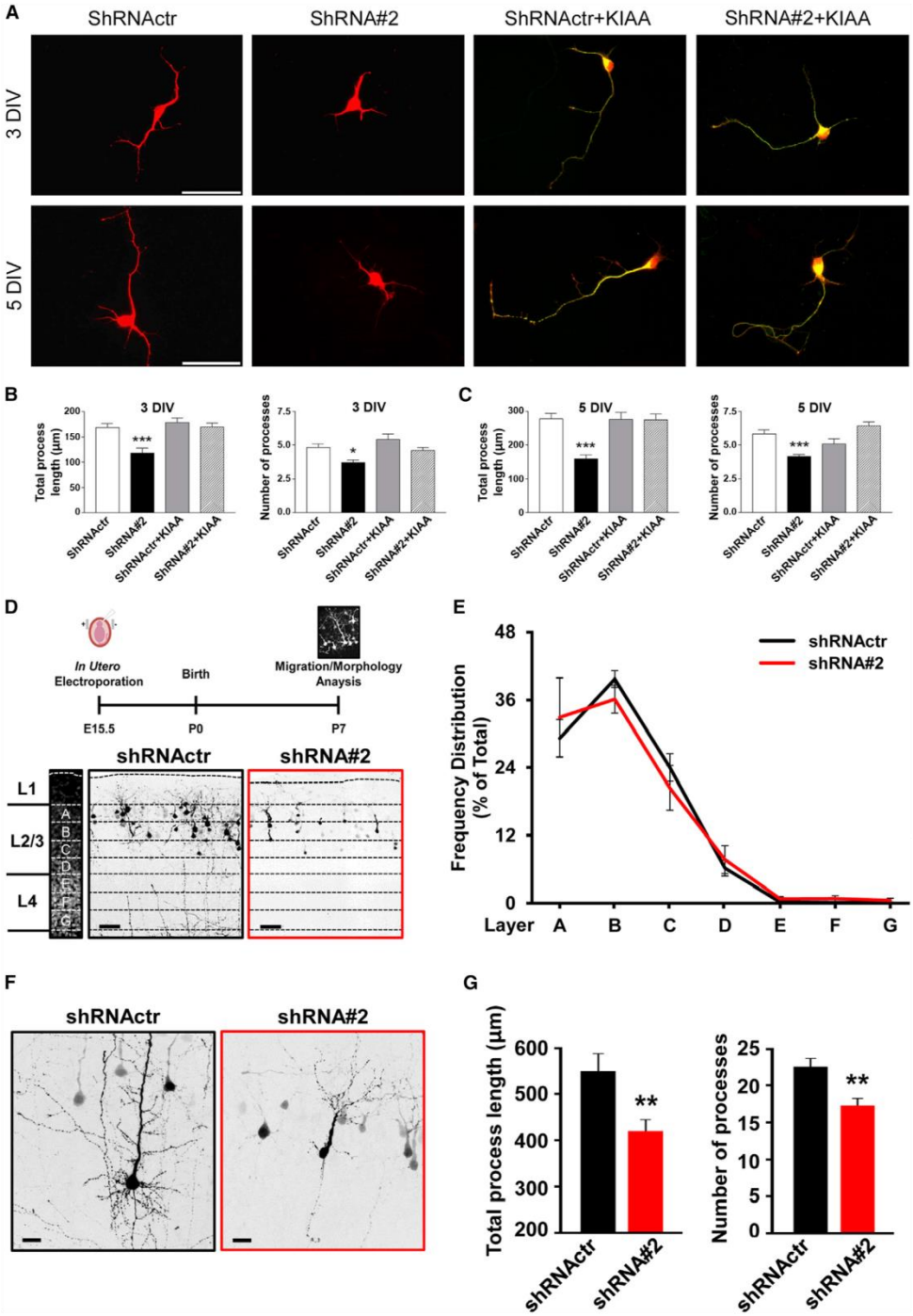

(legend on next page)

process outgrowth (Matteoli et al., 1992; Sabo and McAllister, 2003).

KIAA1107 Markedly Alters the Synaptic Ultrastructure

In view of the potential implication of KIAA1107 in SV endocytosis at mature synapses, we examined the presynaptic ultrastructure of KIAA1107-KD neurons by performing conventional transmission electron microscopy (TEM). Mouse cortical neurons were transduced with a lentiviral vector driving the expression of shRNA#2 or shRNActr at 12 DIV. After 5 days, KIAA1107 became undetectable (Figure S5A), whereas no difference in viability was observed between uninfected (ctr) and infected cells (Figure S5B). Notably, KIAA1107-KD synapses were characterized by a markedly reduced density of total SVs (~50% reduction; Figures 5A and 5B), whereas synaptic area, active zone (AZ) length, density of docked SVs, and distribution of SVs with respect to the AZ were comparable to control synapses (Figure 5C). These data were corroborated by a reduced expression level of synaptophysin and AP2 in KIAA1107-KD neurons compared to control (~40% reduction; Figure S5A). Moreover, the density of CCVs was dramatically reduced in silenced synapses (Figure 5B). Finally, KIAA1107-KD synapses displayed enlarged endosome-like structures (~50% increase in size) but with a preserved endosome density (Figure 5B), as confirmed by the increased immunoreactivity of the endosomal marker Rab5 at KIAA1107-KD synapses (Figures S6A and S6B).

To analyze in greater detail the morphology of synaptic terminals, we performed serial sectioning followed by 3D reconstruction of control and KIAA1107-KD synapses (Figure 5D). The morphometric analysis confirmed the severe reduction in the number of SVs and the parallel depletion of CCVs in silenced synapses compared to control (Figure 5E) and revealed that the enlarged endosome-like structures were fully separated from the plasma membrane (Figure 5D). Notably, the ultrastructural effects of KIAA1107 KD were reversible; the silencing phenotype was completely rescued by coinfection of the neurons with EGFP-KIAA1107 (Figures 5D and 5E) resistant to shRNA#2 silencing (Figure S5C). These results show that KIAA1107-silenced synapses, in spite of a normal gross morphology, display severe ultrastructural defects that are consistent with an important role of KIAA1107 in the regulation of SV recycling and in the maintenance of SV pools.

Clathrin/AP2-Mediated Endocytosis Is Impaired in KIAA1107-Silenced Synapses

Mutations in the genes that encode AP2 and other adaptor-like proteins, which are intrinsic components of the clathrin coat and are implicated in the early steps of SV recovery, lead to ultrastructural phenotypes that are similar to that induced by KIAA1107 silencing (González-Gaitán and Jäckle, 1997; Fergestad et al., 1999; Zhang et al., 1998).

To uncover whether SV recycling is impaired in KIAA1107-KD synapses, we imaged shRNActr- and shRNA#2-infected neurons by electron microscopy upon action potential (AP) firing in the presence of soluble horseradish peroxidase (HRP) to visualize the formation of endocytic intermediates.

We first analyzed synapses under conditions of low-frequency stimulation, when compensatory during-stimulus membrane retrieval largely (but not exclusively) occurs through CME (Granseth et al., 2006; Dittman and Ryan, 2009; Kononenko et al., 2014). Samples were fixed under basal conditions, immediately at the end of the field stimulation (200 APs at 5 Hz) or after 2- and 20-min wash in the absence of HRP. At the end of the stimulus, a significantly decreased density of HRP-positive (HRP^+) SVs, HRP^+ CCVs, and HRP^+ endosome-like structures, all representative of active cycling during stimulation, was observed in KIAA1107-KD terminals compared to control (Figures 6A and 6B). Moreover, the percentage of synapses displaying HRP^+ CCVs at the end of the stimulus versus total synapses was decreased by about 75% in silenced neurons compared to control (40.9% ± 2.7% and 10.3% ± 6.9% for shRNActr and shRNA#-2-infected neurons, respectively). After 2-min wash in the absence of HRP, a significant impairment in the formation of HRP^+ SVs was still evident in KIAA1107-KD terminals, whereas the formation of HRP^+ endosomal vacuoles recovered to control levels. Finally, after 20-min wash in the absence of HRP, SVs and endosomal structures lost their HRP content in both experimental groups, indicating an active and complete recovery. These results indicate that, in KIAA1107-KD synapses, the recovery of SVs, budding either directly from the plasma membrane or from endosome-like structures, was delayed during mild stimulation. The formation of HRP^+ endosomal structures derived from either homotypic fusion of CME-derived vesicles or fusion of such vesicles with early endosomes (Heuser and Reese, 1973; Rizzoli et al., 2006; Hoopmann et al., 2010) was

Figure 4. KIAA1107-Silenced Cortical Neurons Display an Impaired Maturation at Early Stages of *In Vitro* and *In Vivo* Development

(A) Representative merged images of 3 and 5 DIV cortical neurons nucleofected before plating with either ShRNActr or ShRNA#2 (red) and Sh-resistant EGFP-KIAA1107 (green). The scale bars represent 50 μm.

(B and C) Quantification of total process length and number of processes at 3 (B) and 5 (C) DIV using ImageJ. Data are means ± SEM (n = 101 and 83 for ShRNActr neurons; n = 98 and 105 for ShRNA#2 neurons; n = 74 and 89 for ShRNActr+KIAA1107 neurons; n = 66 and 61 for ShRNA#2+KIAA1107 neurons; at 3 and 5 DIV, respectively, from n = 3 independent experiments). *p < 0.05; ***p < 0.001 versus ShRNActr neurons; one-way ANOVA/Bonferroni's multiple comparison test.

(D–G) KIAA1107-silencing *in vivo* does not impair radial migration but causes impairment in pyramidal neurons' morphology.

(D, top) Cartoon depicting the experimental design of the *in vivo* experiments is shown. (Bottom) Representative images of GFP fluorescence in neurons transfected with either ShRNActr (black) or ShRNA#2 (red) in the somatosensory cortex are shown. The slices were counterstained with DAPI to allow the visualization of cortical layers 2/3/4 (L2/3 and L4), here divided in 8 sub-layers (named from A to G, left). The scale bars represent 50 μm.

(E) Quantification of the percentage of total transfected cells in each layer is shown. Data are means ± SEM (n = 8 animals per condition, 1 slice per animal).

(F) Representative high-magnification images of GFP fluorescence in neurons transfected with either ShRNActr (black) or ShRNA#2 (red) in layer II/III of the somatosensory cortex are shown. The scale bars represent 15 μm.

(G) Quantification of total process length (left) and number (right) using ImageJ is shown. Data are means ± SEM (n = 21 cells from 8 different animals for ShRNActr; n = 23 cells from 8 different animals for ShRNA#2); **p < 0.01; unpaired Student's t test.

See also Figure S4.

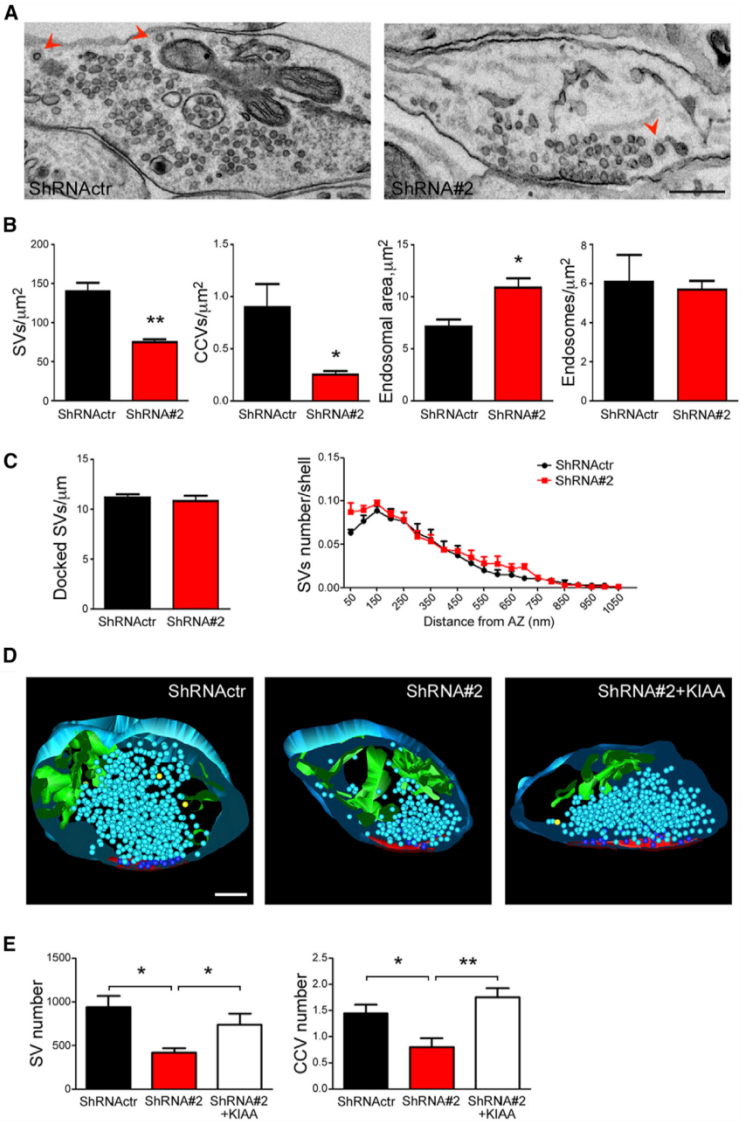

Figure 5. Reduced SV Density and Increased Size of Endosome-like Structures at KIAA1107-Silenced Cortical Synapses

(A) Representative TEM images of nerve terminals from cultured cortical neurons transduced with either ShRNActr or ShRNA#2 at 12 DIV and processed at 17 DIV. Note the reduced SV density in the KIAA1107-KD synapse compared to control (CCVs, red arrowheads). The scale bar represents 200 nm.

(B) Morphometric analysis from serial ultrathin sections obtained from ShRNActr- (black bars) and ShRNA#2- (red bars) treated synapses revealed (from left to right) a reduction in the density of total SVs and CCVs and an increase in the area of endosome-like structures in KIAA1107-KD synapses compared to control. *$p < 0.05$; **$p < 0.01$; unpaired Student's t test.

(C) No changes were observed in the density of AZ-docked SVs and in the spatial distribution of SVs in the nerve terminals of KIAA1107-KD neurons compared to control. The density of SVs located within successive 50-nm shells from the AZ was normalized for the total SV content of each terminals and is given as a function of the distance from the AZ. Nerve terminal areas (0.716 ± 0.059 μm^2 and 0.800 ± 0.024 μm^2 for ShRNActr and ShRNA#2-infected neurons, respectively) and AZ lengths (0.350 ± 0.016 µm and 0.335 ± 0.007 µm for ShRNActr and ShRNA#2-infected neurons, respectively) were similar in the two experimental groups. Data are means ± SEM (n = 157 and n = 160 synapses for ShRNActr and ShRNA#2-infected neurons, respectively, from n = 4 independent preparations).

(D) Representative 3D reconstructions of synaptic terminals from 60-nm-thick serial sections obtained from cortical neurons confirmed the severe reduction in SV (light blue spheres) and CCV (yellow spheres) number in ShRNA#2-treated neurons, which was completely rescued in ShRNA#2+KIAA1107-treated neurons. Endosomal structures (green), not connected with the plasma membrane, are also visible. The AZ and AZ-docked SVs are shown in red and blue, respectively. The scale bar represents 200 nm.

(E) Morphometric analysis of the number of SVs and CCVs in 3D-reconstructed synapses from neurons transduced with ShRNActr (black bars), ShRNA#2 (red bars), or ShRNA#2+KIAA1107 (white bars). Docked SVs (19.3 ± 2.38, 14.57 ± 2.37, and 20.37 ± 4.15 for ShRNActr, ShRNA#2, and ShRNA#2+KIAA1107-infected neurons, respectively) were similar in the three experimental groups. Data are means ± SEM (n = 10 synapses per genotype from n = 3 independent preparations). *$p < 0.05$; **$p < 0.01$; one-way ANOVA/Bonferroni's multiple comparison test.

See also Figures S5 and S6.

also delayed in silenced terminals compared to controls. The increased endosomal size observed in silenced synapses both under basal conditions (Figures 5B, S6A, and S6B) and after stimulation (Figure S6C) is compatible with a longer retention of SVs at endosomal level, strongly suggesting an impaired clathrin-mediated SV reformation from endosomal structures.

When neurons were stimulated at higher frequency (200 APs at 40 Hz), i.e., a frequency known to trigger fast membrane retrieval via endocytic intermediates upstream of clathrin-coat assembly (Clayton et al., 2008; Cheung et al., 2010; Kononenko et al., 2014; Watanabe et al., 2013, 2014), a decreased density of HRP^+ SVs was observed only at the end of the stimulus in KIAA1107-KD terminals compared to control (Figure 6C), evidence of a moderate impairment of SV reformation at this intense activity level. HRP^+ CCVs were nearly absent in both genotypes, consistent with the idea that CME is largely dispensable for

OPEN ACCESS
CellPress

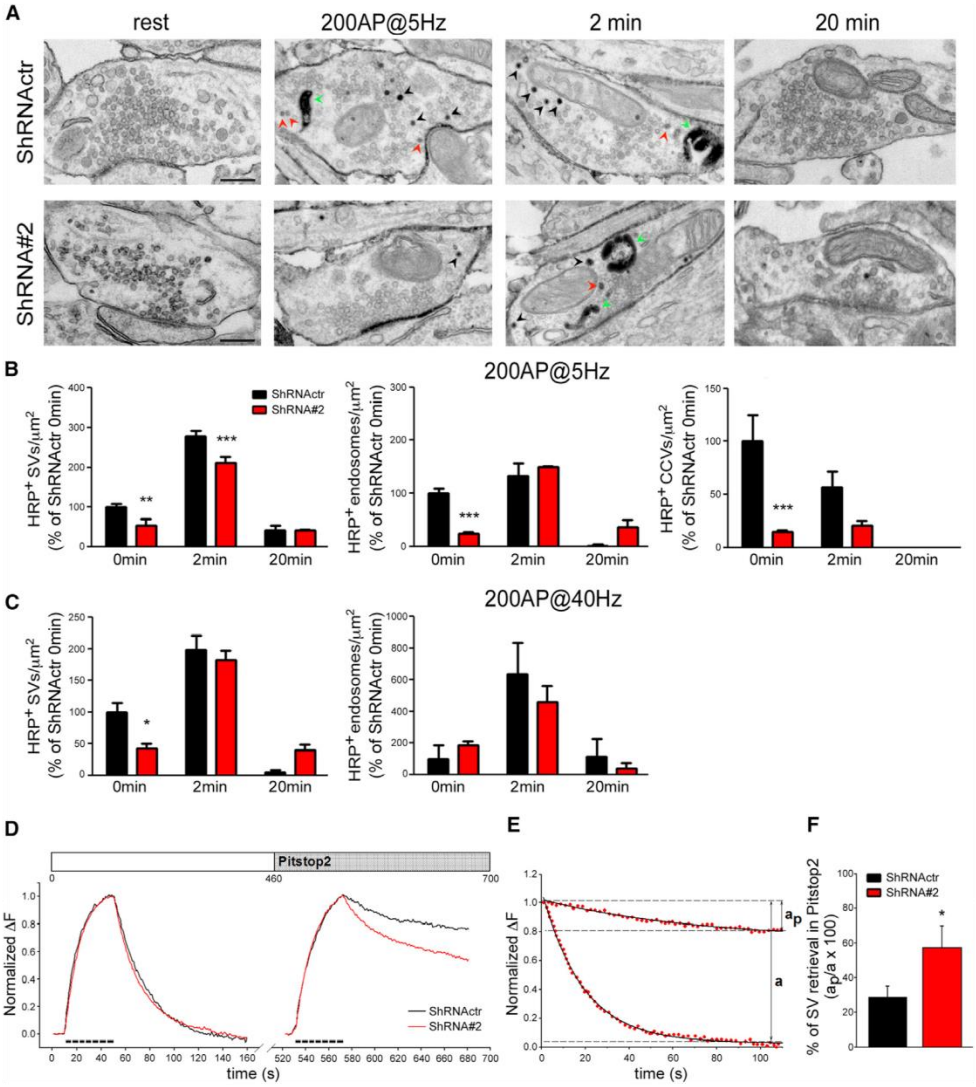

Figure 6. KIAA1107 Knockdown Impairs Clathrin-Mediated Endocytosis in Cortical Synapses

(A) Representative TEM images of presynaptic terminals from control (ShRNActr) and KIAA1107-KD (ShRNA#2) neurons infected at 12 DIV and stimulated at 17 DIV with 200 APs at 5 Hz in the presence of soluble HRP. Synaptic ultrastructure was evaluated by fixing neurons under basal conditions (rest), immediately after the stimulus (0 min), and after 2 or 20 min of recovery in the absence of HRP (HRP$^+$ SVs, black arrowheads; HRP$^+$ CCVs, red arrowheads; HRP$^+$ endosomes, green arrowheads). The scale bars represent 200 nm.

(B and C) Morphometric analysis of HRP-labeled structures after the train stimulation at 5 (B) and 40 (C) Hz (200 APs). The density of HRP-positive (HRP$^+$) SVs, HRP$^+$ endosome-like structures, and HRP$^+$ CCVs in control (black bars) and KIAA1107-KD (red bars) neurons are reported as mean (±SEM) percentages of the respective values observed in the control (ShRNActr) group at 0 min (5 Hz: ShRNActr HRP$^+$SVs, 3.15 ± 0.25; ShRNActr HRP$^+$CCVs, 0.90 ± 0.23; ShRNActr HRP$^+$endosomes, 1.11 ± 0.17; 40 Hz: ShRNActr HRP$^+$SVs, 1.54 ± 0.23; ShRNActr HRP$^+$endosomes, 0.1 ± 0.07). n = 150 and n = 120 images per genotype for the 5- and 40-Hz protocols, respectively, from n = 4 independent preparations. *p < 0.05; **p < 0.01; ***p < 0.001 across genotype, two-way ANOVA/Bonferroni's multiple comparison test.

(D) Ensemble average normalized traces of SypHy fluorescence plotted for control (black trace, n = 8) and KIAA1107-KD (red trace, n = 5) neurons sequentially stimulated with 200 APs at 5 Hz (dotted line) in the absence or presence of 30 µM Pitstop-2.

(E) Representative control data points (red dots) and relative fitting (black traces) by a single exponential function ($y = y_0+a^{-bx}$). The *a* values in the absence (*a*) or presence (a_p) of Pitstop-2 are shown.

(legend continued on next page)

plasma membrane retrieval at this stimulation frequency (Kononenko et al., 2014; Park et al., 2016). In addition, the density of HRP^+ endosomal vacuoles was not altered in silenced synapses (Figure 6C), although their size was increased also at this stimulation frequency (Figure S6D).

We then used Synaptophysin-pHluorin (SypHy) (Tagliatti et al., 2016), co-expressed in hippocampal neurons transduced with either shRNActr or shRNA#2, to further assay membrane recycling following low-frequency stimulation (200 APs at 5 Hz). Surprisingly, no differences in the fluorescence increase, indicative of the rate of release, as well as in the fluorescence decay, representative of post-stimulus endocytosis, were observed in KIAA1107-KD synapses compared to control synapses (Figure 6D). The inability of the SypHy assay to detect an endocytic phenotype in silenced terminals could in principle be due either to a compensatory SV membrane retrieval contributed by clathrin-independent endocytosis (CIE) or, alternatively, to a major involvement of KIAA1107 in SV budding from endosomes rather than from the presynaptic membrane. To sort this out, we challenged neurons with the clathrin inhibitor Pitstop-2 (von Kleist et al., 2011; Figure 6D). The inhibitory effect of Pitstop-2 on endocytosis was severe in both control and KIAA1107-KD synapses, despite the presence of a modest compensation mediated by CIE in the latter (Figures 6D–6F). This suggests that KIAA1107 silencing does not primarily impair SV membrane retrieval or vesicle reacidification but rather SV reformation from endosomes.

In summary, these functional data provide strong evidence that KIAA1107 plays an important role both in CME at the plasma membrane and in the reformation of SVs by clathrin coats budding from endosomes. The kinetics of SV reformation, especially under conditions of low-frequency activity when CME is the predominant pathway for SV recycling, is affected by KIAA1107 silencing. Based on these data, we named the KIAA1107 protein APache, for AP2-interacting clathrin-endocytosis protein.

APache-Silenced Autaptic Neurons Exhibit Impaired Presynaptic Function

To determine whether APache plays a role in synaptic transmission, we performed whole-cell patch-clamp recordings in autaptic hippocampal neurons silenced for APache at 6 DIV and analyzed 5 or 6 days after infection. We preliminarily analyzed the effects of APache silencing on the autapse density and found that the density of synaptic contacts was preserved in APache-KD autaptic neurons (Figure S7A).

Then, we proceeded to the analysis of synaptic transmission. Neurons were stimulated with paired stimuli (50-ms interpulse interval) to evaluate evoked excitatory postsynaptic current (eEPSC) amplitude and paired-pulse facilitation, a presynaptic form of short-term plasticity and an indirect measure of the release probability (Pr) (Fioravante and Regehr, 2011). APache-KD neurons displayed a significant reduction of eEPSC amplitude in response to single stimuli but no changes in paired-pulse facilitation (Figures 7A and 7B). To investigate which of the quantal parameters of release was responsible for the decreased synaptic strength in APache-KD synapses, the cumulative eEPSC amplitude analysis was performed by subjecting neurons to high-frequency trains (2 s at 40 Hz) that induce a complete depletion of the readily releasable pool of SVs (RRP) (Figures 7C–7E). Under this condition, the depression during the steady-state phase is limited by the constant recycling of SVs so that an equilibrium is reached between released and recycled SVs (Schneggenburger et al., 1999). The analysis showed that the RRP size was significantly decreased in APache-KD neurons, to the same extent of the reduction in eEPSC amplitude, whereas Pr was not affected (Figure 7F). This suggests that the impairment in evoked release in APache-KD neurons is likely to involve the constant replenishment of the RRP by the recycling SV pool. Despite the change in RRP, the dynamics of facilitation and depression during the 2-s train at 40 Hz were not significantly affected in silenced neurons compared to control (Figure 7D). Because the various endocytic mechanisms are known to be recruited in a frequency-dependent manner, autaptic neurons were challenged with short 2-s trains at frequencies ranging from 5 to 20 Hz and with a long 30-s train at 10 Hz to analyze the expression of facilitation/depression over time (Figures 7G, 7H, S7B, and S7C). APache-silenced neurons exhibited a more pronounced depression that was tightly dependent on the stimulus frequency. Synaptic depression was faster, more intense, and prolonged in APache-KD synapses during 5-Hz stimulation (Figures 7G and 7H) and progressively attenuated with the increase in stimulation frequency (Figure S7B). The strong increase in synaptic depression at 5 Hz, consistent with the RRP depletion and inactivation of release sites (Fioravante and Regehr, 2011), is likely due, similarly to other endocytic mutants (Milosevic et al., 2011), to the impaired clathrin-mediated recycling of SVs. APache silencing was also associated with an accelerated kinetics of depression evoked by long trains (30 s at 10 Hz; Figure S7C). In addition, post-tetanic potentiation (PTP), a form of short-term plasticity evoked after a short high-frequency stimulation and contributed by increases in both Pr and RRP (Valente et al., 2012), was also impaired in APache-KD neurons (~35% reduction; Figure S7D), consistent with the SV depletion observed upon APache silencing.

DISCUSSION

In the present study, using the bioinformatics GAMMA program to search for uncharacterized genes associated with SVs and presynaptic physiology, we identified KIAA1107 with the highest score. The mouse KIAA1107 main isoform is a protein of 1,088 aas lacking both structural data and known function. Our results demonstrate that KIAA1107 is an AP2 interactor that plays a role in early neuronal development and in CME at mature

(F) The a_P/a ratio, representing the percentage of retrieved SVs in the presence of Pitstop-2 versus the retrieved SVs in its absence, is plotted for control (black bar, n = 8) and KIAA1107-KD (red bar, n = 5) synapses. Data are means ± SEM from the indicated number of coverslips from n = 3 independent preparations. *$p < 0.05$; unpaired Student's t test.
See also Figure S6.

OPEN ACCESS
CellPress

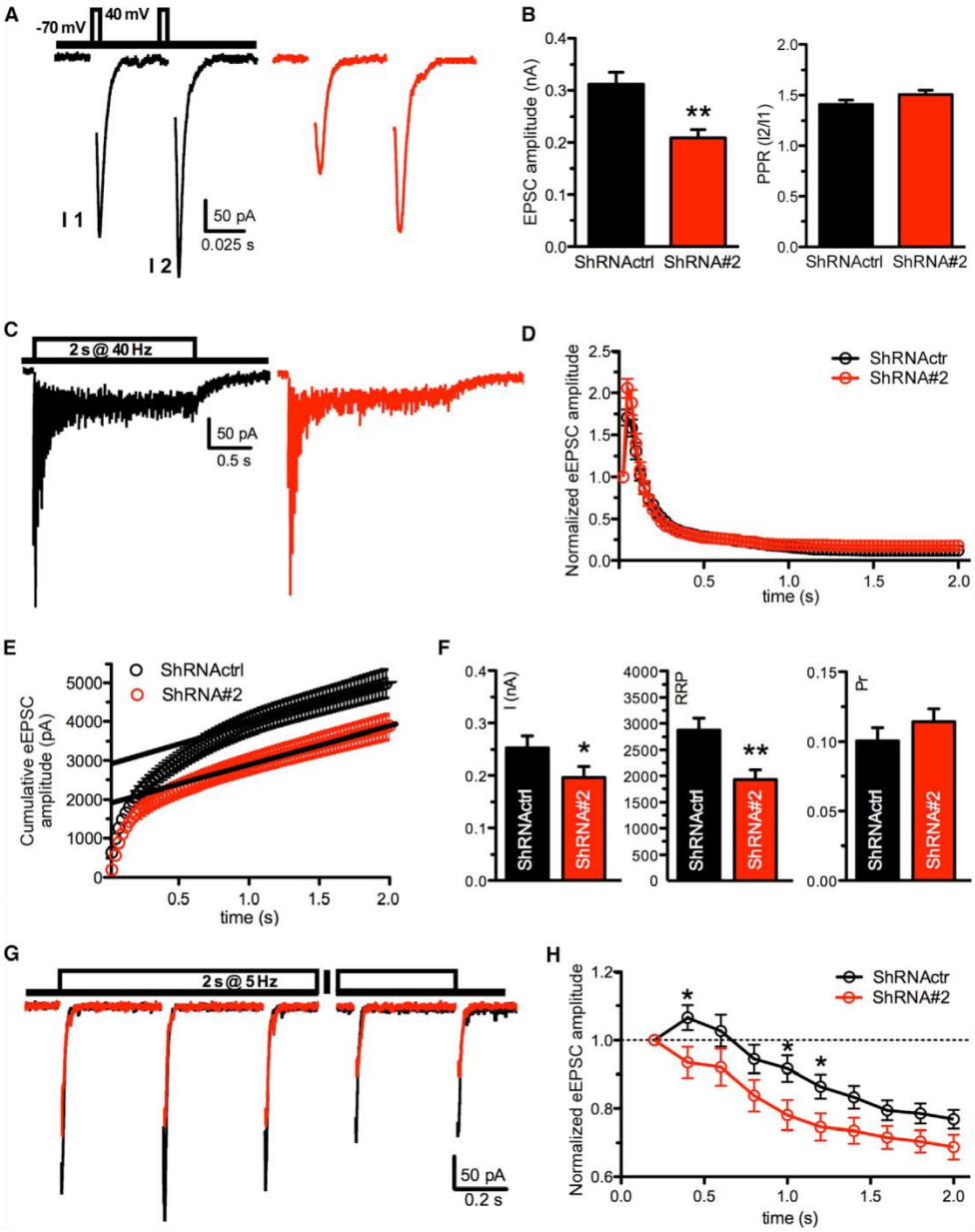

Figure 7. KIAA1107 Silencing Decreases Evoked Excitatory Synaptic Transmission and Enhances Synaptic Depression in Autaptic Hippocampal Neurons

(A) Representative eEPSCs recorded in autaptic neurons transduced with either ShRNActr (black traces, n = 67) or ShRNA#2 (red traces, n = 63). eEPSCs were elicited by clamping the cell at −70 mV and stimulating it with two voltage steps to + 40 mV lasting 0.5 ms at an inter-stimulus interval of 50 ms (inset).

(B) eEPSC amplitude evoked by the first pulse (I1, left) and paired-pulse ratio (PPR) (I2/I1, right) recorded under the same conditions of (A).

(C) Representative recordings of eEPSC evoked by a 2-s tetanic stimulation at 40 Hz in autaptic neurons transduced with ShRNActr (black) or ShRNA#2 (red).

(D) Normalized values of eEPSC amplitude showing the time course of synaptic facilitation and depression in autaptic neurons stimulated as in (C).

(E) Cumulative mean amplitude profiles for eEPSCs during the tetanic stimulation shown in (C) in neurons infected with ShRNActr (black trace, n = 40) or ShRNA#2 (red trace, n = 37). Data points in the 1- to 2-s range were fitted by linear regression and backextrapolated to time 0 (solid lines) to estimate the RRP.

(legend continued on next page)

synapses. We named the protein APache and consider it a molecular component of the clathrin/AP2-dependent endocytic machinery that regulates the fate of endocytosed SVs.

CME has a range of different functions that also include sampling the cell environment for growth and guidance cues and bringing nutrients into cells in developing neurons. An active SV exo/endocytosis in the growth cone has been demonstrated in cultured neurons (Matteoli et al., 1992; Sabo and McAllister, 2003). The present data suggest that, in developing neurons, APache may function in vesicle trafficking events. APache is expressed since the early stages of neuronal development and is present in axonal processes and growth cones, where it promotes neuronal maturation and process outgrowth both *in vitro* and *in vivo*. Moreover, the expression level of AP2 is reduced in developing silenced neurons. It is tempting to speculate that the developmental role of APache is obtained through the clathrin-mediated trafficking pathways that control axon and dendrite outgrowth in developing neurons that are characterized by abundant CCVs (Roos and Kelly, 1999). Intriguingly, AP180 and CALM, two clathrin assembly proteins involved in CME, also play critical roles in controlling the outgrowth of axons and dendrites in embryonic hippocampal neurons (Bushlin et al., 2008), and their silencing elicits morphological phenotypes reminiscent of those of APache-depleted cortical neurons.

Other potential interactors detected in the MS scans can contribute to the effects of APache in neuronal development. NUMBL, an endocytic adaptor binding to the AP2 complex and Eps15 and implicated in CME and neurite outgrowth (Santolini et al., 2000; Sestan et al., 1999; Nishimura et al., 2003) was identified as an APache interactor in our study as well as in a recent proteomic study (Hein et al., 2015). Dynactin, a direct AP2-binding partner that regulates bidirectional transport of vesicles in mammalian neurons, microtubule advance during growth cone remodeling (Kwinter et al., 2009; Grabham et al., 2007), and trafficking of BDNF-TrkB signaling endosomes (Kononenko et al., 2017; Zhou et al., 2012) was also identified as an APache interactor. Thus, in addition to its role in endocytosis at the plasma membrane, APache may also play a role in the internal vesicular/endosomal transport.

Several lines of evidence suggest a potential role for APache in CME at mature synapses. APache is most abundant in brain and, in mature synapses, is concentrated at presynaptic terminals, where it colocalizes with synaptotagmin-1, AP2, and dynamin-1. We have identified AP2 as an APache interactor with the following evidence: (1) APache co-immunoprecipitates with AP2α and β subunits from brain extracts, suggesting that it may participate in the complex network of interactions regulating CME and SV recycling; (2) APache is enriched in CCVs to levels comparable to the coat proteins AP2 and clathrin and at a much larger extent than CME accessory proteins, such as dynamin, synaptojanin, amphiphysin, or endophilin; and (3) APache can be stripped from purified CCVs by treatment with Tris buffer, a well-established procedure to remove coat components from SVs. Synapses that lack APache display the typical features of endocytic mutants. The ultrastructural changes include a severe depletion of SVs and CCVs and the presence of enlarged endosome-like structures. The morpho-functional phenotype of APache silencing consists in a global impairment of SV recycling and synaptic strength that peaks under conditions of low-frequency activity.

Mature synapses use multiple activity-dependent SV recycling mechanisms that operate in parallel and influence neurotransmitter release and synaptic plasticity: "kiss and run"; CME; and clathrin-independent mechanisms (i.e., ultrafast or bulk endocytosis). Whereas the retrieval of the majority of fully fused SVs during mild electrical activity occurs through CME, with vesicles reforming directly from the plasma membrane or from endosomal structures (Hoopmann et al., 2010; Uytterhoeven et al., 2011), during intense high-frequency activity, SV membranes are mostly retrieved through CIE.

The experimental evidence indicates that APache is required to maintain normal SV recycling and RRP refilling at the synapse under conditions of mild stimulation by acting in the clathrin/AP2-mediated regeneration of SVs both from the cell surface and from internalized endosomal structures. The latter mechanism seems to be the predominant one, given the lack of effect of APache silencing on SV reacidification in the SypHy assay. Consistent with this, enlarged endosomal vacuoles accumulate at silenced synapses and may contribute to the depression of neurotransmitter release. On the other hand, APache is dispensable for plasma membrane retrieval at high frequencies, although it may be required for the clathrin-mediated SV reformation from endosomal vacuoles generated by CIE. This model is consistent with prior data demonstrating that silencing or conditional knockout of either AP2 (Kim and Ryan, 2009; Kononenko et al., 2014) or AP2-associated endocytic adaptor proteins (Fergestad et al., 1999; Kononenko et al., 2013) significantly slows down, but does not abolish, SV endocytosis and validates the view that alternative molecules or different mechanisms that normally operate in conjunction with AP2 are required to ensure efficient SV and cargo retrieval over a wide range of stimulation frequencies.

Although further structure function studies will be needed to unravel the precise molecular mechanisms that mediate the described APache functions, the identification of an additional molecular component of the complex endocytic pathway is a

(F) Quantal analysis of release in neurons infected with ShRNActr (black bars) or ShRNA#2 (red bars). From left to right, amplitude of the first eEPSC, RRP size, and probability of release (Pr) are shown.

(G) Representative recordings of eEPSC evoked by a 2-s tetanic stimulation at 5 Hz in autaptic neurons transduced with either ShRNActr (black, n = 31) or ShRNA#2 (red, n = 21).

(H) Normalized values of eEPSC amplitude showing the time course of synaptic facilitation and depression in autaptic neurons stimulated as in (G). In all graphed currents, stimulation artifacts were blanked for clarity. Data are means ± SEM from the indicated numbers of cells recorded at least from n = 3 independent cell culture preparations. *p < 0.05; **p < 0.01; unpaired Student's t test or Mann-Whitney U test.

See also Figure S7.

step forward for getting insights into fundamental aspects of SV recycling in the healthy and diseased brain.

EXPERIMENTAL PROCEDURES

C57BL/6J mice and Sprague-Dawley rats of either sex were from Charles River Laboratories (Calco, Italy). All experiments, conducted at various stages of development (from E18 to adult mice), were carried out in accordance with the guidelines established by the European Communities Council (directive 2010/63/EU of March 4, 2014) and were approved by the Italian Ministry of Health. The standard procedures for western blotting, CCV purification, pull-down and co-immunoprecipitation assays, immunocytochemistry, real-time PCR, and cultures of low-density and autaptic neurons are reported in detail in the Supplemental Experimental Procedures.

GAMMA

GAMMA relies on identifying gene-gene expression correlations using thousands of publicly available microarray datasets available from the GEO repository. Additional data are reported in the Supplemental Experimental Procedures.

KIAA1107 Antibodies and Constructs

A polyclonal KIAA1107-specific antibody was raised in the rabbit against a conserved region comprising aas 732–894 of mouse KIAA1107. cDNA of *Kiaa1107* was amplified from total mRNA extracted from mouse brain and inserted into the p3XFLAG-CMV-14 or p277.pCCLsin.cPPT.hPGK.eGFP.WPRE vector. shRNAs#1–3 and control shRNA were inserted into the pLKO.1-CMV-mCherry lentiviral vector and used to knockdown the endogenous KIAA1107 in neurons. For detailed description of antibodies, constructs, and neuronal and cellular transfection, see the Supplemental Experimental Procedures.

MS Analysis

Sample preparation, LC-MS/MS analysis, database searching, and criteria for protein identification were conducted as reported in details in the Supplemental Experimental Procedures.

IUE

Standard IUE was performed as previously described (Szczurkowska et al., 2016). The images were acquired using a confocal laser-scanning microscope (TCS SP5; Leica Microsystem) or an epifluorescence microscope equipped with Neurolucida (MicroBrightField) software. For detailed procedures and reagents, see the Supplemental Experimental Procedures.

TEM

Low-density cultures of cortical neurons were infected at 12 DIV with either control shRNA or KIAA1107 shRNA and processed for TEM. For detailed procedures, see the Supplemental Experimental Procedures.

Live Imaging and Patch-Clamp Experiments

Optical recordings with Syphy fluorescent probe were performed at 17 DIV (5 days postinfection). Whole-cell patch-clamp recordings were made from autaptic neurons grown on microislands infected at 6 DIV with either control shRNA or KIAA1107 shRNA. For detailed procedures, see the Supplemental Experimental Procedures.

Statistical Analysis

Data with normal distribution were analyzed by one- or two-way ANOVA followed by the Bonferroni's multiple comparison test or the unpaired Student's t test. Non-normally distributed data were analyzed by the Mann-Whitney's U test. Statistical analysis was carried out using Prism (GraphPad Software, La Jolla, CA, USA) and OriginPro-8 (OriginLab, Northampton, MA, USA) software. Significance level was preset to $p < 0.05$. Data were expressed as means ± SEM for number of samples/cells (n) as detailed in the figure legends.

SUPPLEMENTAL INFORMATION

Supplemental Information includes seven figures and one data file and can be found with this article online at https://doi.org/10.1016/j.celrep.2017.11.073.

ACKNOWLEDGMENTS

We thank Dr. Silvia Casagrande (University of Genova, Italy) for assistance in the preparation of primary cultures, Dr. Elena Monzani (San Raffaele Scientific Institute, Milan, Italy) for preparation of lentiviral constructs, and Prof. Luigi Naldini (TIGET, San Raffaele Scientific Institute, Milan, Italy) for the kind supply of the lentiviral vector. This study was supported by research grants from the Italian Ministry of University and Research (FIRB 2010 "Futuro in Ricerca" to S.G.), CARIPLO Foundation (2013 0879 to F.V. and F.B.), and Compagnia di San Paolo (2015.0546 to F.B.). The support of Telethon-Italy (GGP13033 to F.B.) is also acknowledged and NIH grant number 5P20GM103636 (to J.D.W.).

AUTHOR CONTRIBUTIONS

A.P. participated in the design of the experiments and performed research. E.C. performed and analyzed the ultrastructural experiments. F.C.G. and F.C. ran the developmental studies and provided experimental tools. P.V. and G.G. performed the electrophysiological experiments and analyzed the data. D.A. performed the live imaging experiments. M.B. participated in image acquisition. C.M., B.P., and A.S. performed IUE, slice histology, and image acquisition and analysis. A.B. and A.C. performed the MS analysis. A.F. supervised the live imaging experiments. J.D.W. performed the bioinformatic analysis. F.V. contributed to the research design. S.G. performed research, analyzed data, and made the figures. S.G. and F.B. designed and supervised the research and wrote the paper. All authors revised the manuscript.

DECLARATION OF INTERESTS

The authors declare no competing interests.

Received: April 24, 2017
Revised: October 23, 2017
Accepted: November 20, 2017
Published: December 19, 2017

REFERENCES

Bushlin, I., Petralia, R.S., Wu, F., Harel, A., Mughal, M.R., Mattson, M.P., and Yao, P.J. (2008). Clathrin assembly protein AP180 and CALM differentially control axogenesis and dendrite outgrowth in embryonic hippocampal neurons. J. Neurosci. *28*, 10257–10271.

Cheung, G., Jupp, O.J., and Cousin, M.A. (2010). Activity-dependent bulk endocytosis and clathrin-dependent endocytosis replenish specific synaptic vesicle pools in central nerve terminals. J. Neurosci. *30*, 8151–8161.

Clayton, E.L., Evans, G.J., and Cousin, M.A. (2008). Bulk synaptic vesicle endocytosis is rapidly triggered during strong stimulation. J. Neurosci. *28*, 6627–6632.

Conner, S.D., and Schmid, S.L. (2003). Regulated portals of entry into the cell. Nature *422*, 37–44.

Cousin, M.A. (2017). Integration of synaptic vesicle cargo retrieval with endocytosis at central nerve terminals. Front. Cell. Neurosci. *11*, 234.

Dittman, J., and Ryan, T.A. (2009). Molecular circuitry of endocytosis at nerve terminals. Annu. Rev. Cell Dev. Biol. *25*, 133–160.

Fergestad, T., Davis, W.S., and Broadie, K. (1999). The stoned proteins regulate synaptic vesicle recycling in the presynaptic terminal. J. Neurosci. *19*, 5847–5860.

Fioravante, D., and Regehr, W.G. (2011). Short-term forms of presynaptic plasticity. Curr. Opin. Neurobiol. *21*, 269–274.

González-Gaitán, M., and Jäckle, H. (1997). Role of Drosophila alpha-adaptin in presynaptic vesicle recycling. Cell *88*, 767–776.

Gorini, G., Ponomareva, O., Shores, K.S., Person, M.D., Harris, R.A., and Mayfield, R.D. (2010). Dynamin-1 co-associates with native mouse brain BKCa channels: proteomics analysis of synaptic protein complexes. FEBS Lett. *584*, 845–851.

Grabham, P.W., Seale, G.E., Bennecib, M., Goldberg, D.J., and Vallee, R.B. (2007). Cytoplasmic dynein and LIS1 are required for microtubule advance during growth cone remodeling and fast axonal outgrowth. J. Neurosci. *27*, 5823–5834.

Granseth, B., Odermatt, B., Royle, S.J., and Lagnado, L. (2006). Clathrin-mediated endocytosis is the dominant mechanism of vesicle retrieval at hippocampal synapses. Neuron *51*, 773–786.

Hein, M.Y., Hubner, N.C., Poser, I., Cox, J., Nagaraj, N., Toyoda, Y., Gak, I.A., Weisswange, I., Mansfeld, J., Buchholz, F., et al. (2015). A human interactome in three quantitative dimensions organized by stoichiometries and abundances. Cell *163*, 712–723.

Heuser, J.E., and Reese, T.S. (1973). Evidence for recycling of synaptic vesicle membrane during transmitter release at the frog neuromuscular junction. J. Cell Biol. *57*, 315–344.

Hoopmann, P., Punge, A., Barysch, S.V., Westphal, V., Bückers, J., Opazo, F., Bethani, I., Lauterbach, M.A., Hell, S.W., and Rizzoli, S.O. (2010). Endosomal sorting of readily releasable synaptic vesicles. Proc. Natl. Acad. Sci. USA *107*, 19055–19060.

Kasof, G.M., Goyal, L., and White, E. (1999). Btf, a novel death-promoting transcriptional repressor that interacts with Bcl-2-related proteins. Mol. Cell. Biol. *19*, 4390–4404.

Kim, S.H., and Ryan, T.A. (2009). Synaptic vesicle recycling at CNS snapses without AP-2. J. Neurosci. *29*, 3865–3874.

Kononenko, N.L., and Haucke, V. (2015). Molecular mechanisms of presynaptic membrane retrieval and synaptic vesicle reformation. Neuron *85*, 484–496.

Kononenko, N.L., Diril, M.K., Puchkov, D., Kintscher, M., Koo, S.J., Pfuhl, G., Winter, Y., Wienisch, M., Klingauf, J., Breustedt, J., et al. (2013). Compromised fidelity of endocytic synaptic vesicle protein sorting in the absence of stonin 2. Proc. Natl. Acad. Sci. USA *110*, E526–E535.

Kononenko, N.L., Puchkov, D., Classen, G.A., Walter, A.M., Pechstein, A., Sawade, L., Kaempf, N., Trimbuch, T., Lorenz, D., Rosenmund, C., et al. (2014). Clathrin/AP-2 mediate synaptic vesicle reformation from endosome-like vacuoles but are not essential for membrane retrieval at central synapses. Neuron *82*, 981–988.

Kononenko, N.L., Claßen, G.A., Kuijpers, M., Puchkov, D., Maritzen, T., Tempes, A., Malik, A.R., Skalecka, A., Bera, S., Jaworski, J., and Haucke, V. (2017). Retrograde transport of TrkB-containing autophagosomes via the adaptor AP-2 mediates neuronal complexity and prevents neurodegeneration. Nat. Commun. *8*, 14819.

Kwinter, D.M., Lo, K., Mafi, P., and Silverman, M.A. (2009). Dynactin regulates bidirectional transport of dense-core vesicles in the axon and dendrites of cultured hippocampal neurons. Neuroscience *162*, 1001–1010.

Matteoli, M., Takei, K., Perin, M.S., Südhof, T.C., and De Camilli, P. (1992). Exo-endocytotic recycling of synaptic vesicles in developing processes of cultured hippocampal neurons. J. Cell Biol. *117*, 849–861.

Milosevic, I., Giovedi, S., Lou, X., Raimondi, A., Collesi, C., Shen, H., Paradise, S., O'Toole, E., Ferguson, S., Cremona, O., and De Camilli, P. (2011). Recruitment of endophilin to clathrin-coated pit necks is required for efficient vesicle uncoating after fission. Neuron *72*, 587–601.

Nishimura, T., Fukata, Y., Kato, K., Yamaguchi, T., Matsuura, Y., Kamiguchi, H., and Kaibuchi, K. (2003). CRMP-2 regulates polarized Numb-mediated endocytosis for axon growth. Nat. Cell Biol. *5*, 819–826.

Park, J., Cho, O.Y., Kim, J.A., and Chang, S. (2016). Endosome-mediated endocytic mechanism replenishes the majority of synaptic vesicles at mature CNS synapses in an activity-dependent manner. Sci. Rep. *6*, 31807.

Raman, D., Sai, J., Hawkins, O., and Richmond, A. (2014). Adaptor protein2 (AP2) orchestrates CXCR2-mediated cell migration. Traffic *15*, 451–469.

Rizzoli, S.O., Bethani, I., Zwilling, D., Wenzel, D., Siddiqui, T.J., Brandhorst, D., and Jahn, R. (2006). Evidence for early endosome-like fusion of recently endocytosed synaptic vesicles. Traffic *7*, 1163–1176.

Robinson, M.S. (2004). Adaptable adaptors for coated vesicles. Trends Cell Biol. *14*, 167–174.

Roos, J., and Kelly, R.B. (1999). The endocytic machinery in nerve terminals surrounds sites of exocytosis. Curr. Biol. *9*, 1411–1414.

Sabo, S.L., and McAllister, A.K. (2003). Mobility and cycling of synaptic protein-containing vesicles in axonal growth cone filopodia. Nat. Neurosci. *6*, 1264–1269.

Saheki, Y., and De Camilli, P. (2012). Synaptic vesicle endocytosis. Cold Spring Harb. Perspect. Biol. *4*, a005645.

Santolini, E., Puri, C., Salcini, A.E., Gagliani, M.C., Pelicci, P.G., Tacchetti, C., and Di Fiore, P.P. (2000). Numb is an endocytic protein. J. Cell Biol. *151*, 1345–1352.

Schmid, E.M., and McMahon, H.T. (2007). Integrating molecular and network biology to decode endocytosis. Nature *448*, 883–888.

Schneggenburger, R., Meyer, A.C., and Neher, E. (1999). Released fraction and total size of a pool of immediately available transmitter quanta at a calyx synapse. Neuron *23*, 399–409.

Schroer, T.A. (2004). Dynactin. Annu. Rev. Cell Dev. Biol. *20*, 759–779.

Sestan, N., Artavanis-Tsakonas, S., and Rakic, P. (1999). Contact-dependent inhibition of cortical neurite growth mediated by notch signaling. Science *286*, 741–746.

Slepnev, V.I., and De Camilli, P. (2000). Accessory factors in clathrin-dependent synaptic vesicle endocytosis. Nat. Rev. Neurosci. *1*, 161–172.

Soykan, T., Maritzen, T., and Haucke, V. (2016). Modes and mechanisms of synaptic vesicle recycling. Curr. Opin. Neurobiol. *39*, 17–23.

Szczurkowska, J., Cwetsch, A.W., dal Maschio, M., Ghezzi, D., Ratto, G.M., and Cancedda, L. (2016). Targeted in vivo genetic manipulation of the mouse or rat brain by in utero electroporation with a triple-electrode probe. Nat. Protoc. *11*, 399–412.

Tagliatti, E., Fadda, M., Falace, A., Benfenati, F., and Fassio, A. (2016). Arf6 regulates the cycling and the readily releasable pool of synaptic vesicles at hippocampal synapse. eLife *5*, e10116.

Tojima, T., Itofusa, R., and Kamiguchi, H. (2010). Asymmetric clathrin-mediated endocytosis drives repulsive growth cone guidance. Neuron *66*, 370–377.

Traub, L.M., and Bonifacino, J.S. (2013). Cargo recognition in clathrin-mediated endocytosis. Cold Spring Harb. Perspect. Biol. *5*, a016790.

Uytterhoeven, V., Kuenen, S., Kasprowicz, J., Miskiewicz, K., and Verstreken, P. (2011). Loss of skywalker reveals synaptic endosomes as sorting stations for synaptic vesicle proteins. Cell *145*, 117–132.

Valente, P., Casagrande, S., Nieus, T., Verstegen, A.M., Valtorta, F., Benfenati, F., and Baldelli, P. (2012). Site-specific synapsin I phosphorylation participates in the expression of post-tetanic potentiation and its enhancement by BDNF. J. Neurosci. *32*, 5868–5879.

Valtorta, F., Meldolesi, J., and Fesce, R. (2001). Synaptic vesicles: is kissing a matter of competence? Trends Cell Biol. *11*, 324–328.

van Hille, B., Richener, H., Evans, D.B., Green, J.R., and Bilbe, G. (1993). Identification of two subunit A isoforms of the vacuolar H(+)-ATPase in human osteoclastoma. J. Biol. Chem. *268*, 7075–7080.

von Kleist, L., Stahlschmidt, W., Bulut, H., Gromova, K., Puchkov, D., Robertson, M.J., MacGregor, K.A., Tomilin, N., Pechstein, A., Chau, N., et al. (2011). Role of the clathrin terminal domain in regulating coated pit dynamics revealed by small molecule inhibition. Cell *146*, 471–484.

Watanabe, S., Rost, B.R., Camacho-Pérez, M., Davis, M.W., Söhl-Kielczynski, B., Rosenmund, C., and Jorgensen, E.M. (2013). Ultrafast endocytosis at mouse hippocampal synapses. Nature *504*, 242–247.

OPEN ACCESS
CellPress

Watanabe, S., Trimbuch, T., Camacho-Pérez, M., Rost, B.R., Brokowski, B., Söhl-Kielczynski, B., Felies, A., Davis, M.W., Rosenmund, C., and Jorgensen, E.M. (2014). Clathrin regenerates synaptic vesicles from endosomes. Nature *515*, 228–233.

Wren, J.D. (2009). A global meta-analysis of microarray expression data to predict unknown gene functions and estimate the literature-data divide. Bioinformatics *25*, 1694–1701.

Zhang, B., Koh, Y.H., Beckstead, R.B., Budnik, V., Ganetzky, B., and Bellen, H.J. (1998). Synaptic vesicle size and number are regulated by a clathrin adaptor protein required for endocytosis. Neuron *21*, 1465–1475.

Zhou, B., Cai, Q., Xie, Y., and Sheng, Z.-H. (2012). Snapin recruits dynein to BDNF-TrkB signaling endosomes for retrograde axonal transport and is essential for dendrite growth of cortical neurons. Cell Rep. *2*, 42–51.